

UNIVERSITÉ DE GENÈVE
Département de physique
nucléaire et corpusculaire

FACULTÉ DE SCIENCES
Dr. Alessandra Lombardi et
Prof. Alain Blondel

Study of particle production and capture for a Neutrino Factory

THÈSE

présentée à la Faculté des sciences de l'Université de Genève
pour obtenir le grade de Docteur ès sciences, mention physique

par

Simone Silvano Gilardoni

d'Italie

Thèse N° 3536

GENÈVE

2004



FACULTÉ DES SCIENCES



UNIVERSITÉ DE GENÈVE

**Doctorat ès sciences
mention physique**

Thèse de *Monsieur Simone Silvano GILARDONI*

intitulée :

**" Study of particle production and capture
for a Neutrino Factory "**

La Faculté des sciences, sur le préavis de Monsieur A. BLONDEL, professeur ordinaire et directeur de thèse (Département de physique nucléaire et corpusculaire), et de Madame A. LOMBARDI, docteur et co-directrice de thèse (Accelerators and Beams Division - CERN - Genève, Suisse), et de Messieurs A. CLARK, professeur ordinaire, (Département de physique nucléaire et corpusculaire), V. PALLADINO, professeur (Università degli Studi di Napoli Federico II - Istituto Nazionale di Fisica Nucleare, sezione di Napoli - Naples, Italie) et H. HASEROTH, docteur (Accelerators and Beams Division - CERN - Genève, Suisse) autorise l'impression de la présente thèse, sans exprimer d'opinion sur les propositions qui y sont énoncées.

Genève, le 6 juillet 2004

Thèse - 3536 -

P. Spierer

Le Doyen, Pierre SPIERER

to Silvia, Nicola and my parents

The beam never lies. (M. Placidi)

Contents

1	Introduction to the Neutrino Factory	1
1.1	Neutrino birth	1
1.2	Neutrino physics	2
1.2.1	Neutrino Oscillations	3
1.2.2	Phenomenology of neutrino oscillations	3
1.2.3	Neutrino oscillation theory	4
1.2.4	Two-neutrino oscillation	7
1.2.5	Three family oscillations	8
1.2.6	Matter Effect	12
1.2.7	CP violation in the leptonic sector	14
1.3	Neutrino sources and detectors	16
1.3.1	Solar Neutrinos	16
1.3.2	Reactor (Anti)Neutrinos	20
1.3.3	The atmospheric neutrino anomaly	21
1.3.4	The LSND caveat	24
1.3.5	Short experimental summary	25
1.4	The Neutrino Factory	25
1.4.1	Oscillation signature: wrong sign muons	26
1.4.2	Machine parameters choice	28
1.5	Overview of the Neutrino Factory acceleration complex	29
1.5.1	Proton driver	29
1.5.2	Target	32
1.5.3	Horn	34
1.5.4	Decay channel and phase rotation	34
1.5.5	Cooling	35
1.5.6	Acceleration and storage ring	36
1.5.7	Detector and far location	36
1.6	Superbeam	36
1.7	Beta Beam	39

2	Target	41
2.1	Target material for pion production	41
2.2	Target proposals	47
2.3	Mercury Pros and Cons	50
2.4	Experimental measurement of Mercury explosion	53
2.5	Conclusion	57
2.6	A non conventional target concept: pulsed target	60
2.6.1	Target parameters	60
2.6.2	Particle production	64
2.6.3	Technological aspects	65
2.6.4	Conclusion	66
2.7	Converter target for isotope production	67
2.7.1	Converter target	68
2.7.2	Converter Simulation	70
2.7.3	Converter target for ${}^6\text{He}$ production	72
3	Horn	77
3.1	Horn	77
3.1.1	Horn design	82
3.2	The solenoid	88
3.3	Simulation and results	89
3.4	Conclusions	91
3.5	Horn power supply	93
3.5.1	Basics of dumped current circuit	93
3.5.2	Layout of the prototype power supply	94
3.5.3	Horn lifetime estimate	96
3.5.4	Cost of installation	108
3.6	Horn vibration measurements	110
3.6.1	Generalities of the acoustic method	110
3.6.2	Technical description of the method	110
3.6.3	Validation of the method: CNGS and AA horn mea- surements	111
3.6.4	Nufact Horn	114
3.6.5	Laser vibrometer measurements	117
3.6.6	Conclusions of the vibration measurements	124
3.7	Microphone Specifications	125
3.8	Introduction to four horn capture scheme	126
3.8.1	Proposed scheme	126
3.8.2	Results	129
3.8.3	Conclusions	129

4	SuperBeam	131
4.1	Introduction to the SuperBeam	131
4.2	Features of the CERN low energy neutrino SuperBeam	133
4.3	Optics design	135
4.4	Beam time structure	137
4.5	Decay tunnel length	139
4.6	Conclusions	140
5	Solenoidal channel stability	143
5.1	Matrix representation of a solenoid	143
5.2	Solenoidal periodic channel	146
5.2.1	Periodic channel with a drift	148
5.3	Stability versus energy acceptance	151
5.4	Hard edge and fieldmap equivalence for the stability	153
5.5	Conclusions	155
6	Phase Rotation	159
6.1	Phase Rotation	159
6.2	CERN Reference Scenario	162
6.2.1	Geometry and materials implemented in the simulation	164
6.2.2	Interactions of particles with materials	164
6.3	Results of the simulations	165
6.4	Energy deposition in the superconducting solenoids	168
6.5	Discussion and conclusions	169
6.6	Appendix: Introduction to GEANT4	169

Chapter 1

Introduction to the Neutrino Factory

Neutrino history is full of puzzles and surprises. Neutrinos were invented by Pauli to solve the puzzle of the electron spectrum emitted in beta decay, but his regret was the invention of a particle that cannot be experimentally observed. Nowadays, after 50 years of experimental neutrino physics, in spite of the Pauli's worries, the discovery of neutrino oscillation opened a new era for physics beyond the Standard Model.

A number of intriguing questions are still waiting for an answer. Why are neutrino masses so small compared to those of other leptons? Why are the mixing angles so large compared to those of quarks? Is there CP violation in the leptonic sector?

1.1 Neutrino birth

The official history of neutrinos started the 4 December 1930 when Pauli wrote this letter to a meeting in Tübingen[1]:

Dear Radioactive Ladies and Gentlemen,

As the bearer of these lines, to whom I graciously ask you to listen, will explain to you in more detail, how because of the "wrong" statistics of the N and ${}^6\text{Li}$ nuclei and the continuous beta spectrum, I have hit upon a desperate remedy to save the "exchange theorem" of statistics and the law of conservation of energy. Namely, the possibility that there could exist in the nuclei electrically neutral particles, that I wish to call neutrons, which have spin $1/2$ and obey the exclusion principle and which further differ from light quanta in that they do not travel with the velocity of light. The mass of the neutrons should be of the same order of magnitude as the electron mass

and in any event not larger than 0.01 proton masses. The continuous beta spectrum would then become understandable by the assumption that in beta decay a neutron is emitted in addition to the electron such that the sum of the energies of the neutron and the electron is constant [...].

I agree that my remedy could seem incredible because one should have seen those neutrons very earlier if they really exist. But only the one who dare can win and the difficult situation, due to the continuous structure of the beta spectrum, is lighted by a remark of my honored predecessor, Mr Debye, who told me recently in Bruxelles: "Oh, It's well better not to think to this at all, like new taxes". From now on, every solution to the issue must be discussed. Thus, dear radioactive people, look and judge. Unfortunately, I cannot appear in Tübingen personally since I am indispensable here in Zurich because of a ball on the night of 6/7 December. With my best regards to you, and also to Mr Back.

*Your humble servant
W. Pauli*

The famous physicist was trying to solve one of the most puzzling problems of the époque, the continuous spectrum of the electron produced in beta decay. At that time only the alpha decay had found an explication, since every element participating in the reaction is detected. Being a two-body decay, the energy of the alpha emitted is more or less fixed. However, in the beta decay, the energy of the particle emitted and detected, the electron, has a continuous spectrum. This is impossible without admitting the presence of a third particle, which escapes detection: the neutron invented by Pauli. Today the neutron is the particle discovered by Chadwick in 1932 and it is the partner of the proton as constituent of the nucleus, while E. Fermi introduced the name of neutrino for Pauli's particle. The first (anti)neutrino was detected by F. Reines and C.L. Cowan in 1956 using as source the Savannah River nuclear reactor[2]. The exciting history of this particular particle had started, and still today reserves surprises.

1.2 Neutrino physics

Neutrinos have always been considered as elusive particles. They have no electric charge and they interact only via weak currents, either charged or neutral, making their detection incredibly difficult.

From experimental evidence, neutrinos are left handed particles while antineutrinos are right handed particles.

Neutrinos are accommodated in the Standard Model in doublets together with their lepton partners, the electron, the muon and the tau. The only way to identify the neutrino flavour is via a charged current weak interaction, in which the lepton partner can be identified. Somehow, neutrinos have no other identity than that transmitted by the lepton which appears when they are created or detected. Moreover, as described in the following, this identity seems to be a quantity which is not conserved at different points in space or at different time.

1.2.1 Neutrino Oscillations

From the experimental results, and as described in the following sections, it is proven that during their propagation neutrinos of one flavor transform in neutrinos of another flavor. The first implication is already quite impressive: neutrinos have mass. In the Standard Model neutrinos had been assumed to have strictly zero masses.

The second implication is also new for the Standard Model. In any process observed, the number of leptons belonging to the same weak doublet, the lepton number, is a quantity experimentally so far always conserved, while in case of neutrino oscillations this is no more valid, since a neutrino of one doublet transform into a neutrino of another doublet. This violates lepton number conservation.

Moreover, flavour seems to become an ambiguous quantity to identify a neutrino, since it can vary with time or the distance between the neutrino source and the detector location. The discovery of neutrinos transforming into each other forces a drastic revision of the theoretical ideas in particle physics.

1.2.2 Phenomenology of neutrino oscillations

The flavor changing process of neutrino oscillations is possible if the neutrino mass eigenstates, which describe the propagation in space, are different from the weak flavor eigenstates, which describe the weak interaction of neutrinos in the Standard Model. This is similar to what happens for quarks.

At the time $t_0 = 0$, when a neutrino is created by weak interaction such as $W^\pm \rightarrow l_\alpha^\pm + \nu_\alpha(\bar{\nu}_\alpha)$ in a weak decay, it is produced in one of the possible flavor states ν_α ($\alpha = e, \mu, \tau$), namely in a given mix of mass states ν_i ($i = 1, 2, 3$), together with its lepton partner l_α ($l_\alpha = e, \mu, \tau$). A neutrino flavour state ν_α is hence expressed in terms of mass states in quantum mechanics as:

$$|\nu_\alpha\rangle = \sum_i U_{\alpha i} |\nu_i\rangle \quad (1.1)$$

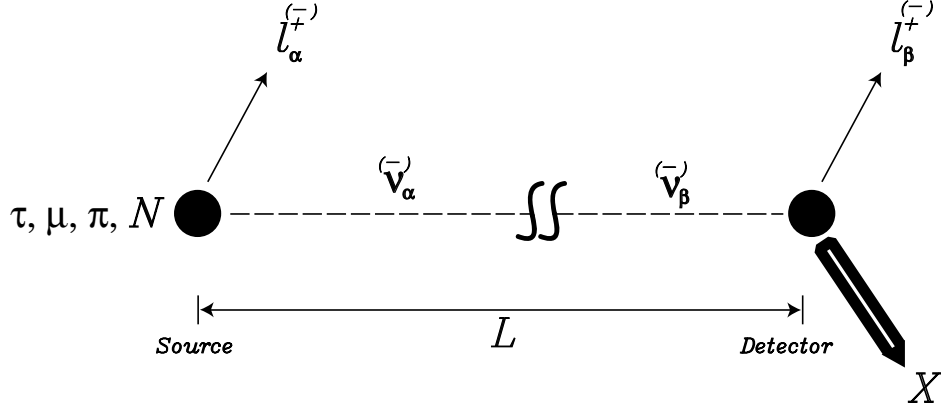


Figure 1.1: Sketch of the neutrino production, propagation and detection.

considering $|\nu_\alpha\rangle$ and $|\nu_i\rangle$ quantum mechanics states and with U the matrix of the coefficient which mix different quantum states. Once the neutrino propagates, the mass states m_i ($i = 1, 2, 3$) will evolve according to the Schrödinger equation differently, since the masses are different, and acquire different phases.

At a distance L , where the detector is placed, or at the time $t > t_0$, the mixing between the mass states could be different and the flavor of the neutrino could be different.

Then the experiment, which identifies the neutrino flavor via the lepton produced by a weak interaction, which creates a lepton of the same flavor of the neutrino (see figure 1.1 for a sketch of the oscillation process), will observe the initial flavour with a reduced probability.

1.2.3 Neutrino oscillation theory

The process of flavor transformation can be described by neutrino oscillations as invented by Pontecorvo in 1969 [3]. His idea was based on the development of a former hypothesis he expressed about the neutrino-antineutrino oscillation, during the years when the only neutrino flavour known was the electron neutrino.

As was proven by the measurements at LEP by the Z peak shape fitting, the light neutrino eigenflavours are three (ν_e, ν_μ, ν_τ) in the Standard Model. They form with e, μ and τ three leptonic $SU(2)_L$ weak doublets.

The minimum number of mass states required to explain the observed oscillation pattern is three (m_1, m_2, m_3). In the standard scenario with 3 weak lepton doublets, the mass eigenstates ν_i and the flavor eigenstates ν_α are

related via a 3×3 unitary mixing matrix U :

$$U = \begin{pmatrix} c_{12}c_{13} & s_{12}c_{13} & s_{13}e^{-i\delta} \\ -s_{12}c_{23} - c_{12}s_{23}s_{13}e^{i\delta} & c_{12}c_{23} - s_{12}s_{23}s_{13}e^{i\delta} & s_{23}c_{13} \\ s_{12}s_{23} - c_{12}c_{23}s_{13}e^{i\delta} & -c_{12}s_{23} - s_{12}c_{23}s_{13}e^{i\delta} & c_{23}c_{13} \end{pmatrix} \quad (1.2)$$

with $c_{ij} = \cos \theta_{ij}$, $s_{ij} = \sin \theta_{ij}$, θ_{ij} defined as the mixing angles, and δ a CP violating phase. The matrix U mixes the different mass eigenstates into a given a flavor eigenstate. Every weak neutrino eigenstate is hence a linear combination of the mass eigenstates according to:

$$|\nu_\alpha\rangle = \sum_i U_{\alpha i} |\nu_i\rangle \quad (1.3)$$

When the neutrino is created by a weak interaction at the point in space \vec{x}_0 its flavor state can be written as:

$$|\nu_\alpha\rangle = |\nu(\vec{x}_0, 0)\rangle = \sum_i U_{\alpha i} |\nu_i(\vec{x}_0, 0)\rangle = \sum_i U_{\alpha i} e^{i\vec{p}_i \cdot \vec{x}_0} |\nu_i\rangle \quad (1.4)$$

where p_i is the momentum associated to $|\nu_i\rangle$ in the laboratory frame. The neutrino flavour state is defined by the lepton flavour produced in the weak reaction. In particular $|\nu_e\rangle$ is a neutrino generated either by a β decay such as

$$p \rightarrow n + \nu_e + e^+$$

or, in general for a nucleus $A(Z, N)$, by:

$$A(Z, N) \rightarrow A(Z - 1, N + 1) + e^+ + \nu_e$$

A muon neutrino state $|\nu_\mu\rangle$ is produced by pion or muon decay:

$$\begin{aligned} \pi^+ &\rightarrow \mu^+ + \nu_\mu \\ \mu^+ &\rightarrow e^+ + \bar{\nu}_\mu + \nu_e \end{aligned}$$

Finally, a tau neutrino state $|\nu_\tau\rangle$ is produced by τ decays:

$$\begin{aligned} \tau^- &\rightarrow \nu_\tau + W^- \\ &\rightarrow \nu_\tau + e^- + \bar{\nu}_e \\ &\rightarrow \nu_\tau + \mu^- + \bar{\nu}_\mu \\ &\rightarrow \nu_\tau + \text{hadrons} \end{aligned}$$

The production of antineutrinos is obtained reversing the charges and transforming particle into their antiparticles in those processes.

After generation, the neutrino propagates to the new \vec{x} position according to the Schrödinger equation[†], and the previous state is multiplied by the time-evolution propagator:

$$|\nu(\vec{x}, t)\rangle = \sum_i U_{\alpha i} e^{i\vec{p}_i \cdot \vec{x}} e^{-iE_i t} |\nu_i\rangle \quad (1.5)$$

with E_i the energy of the ν_i mass state.

As the neutrino masses do not exceed few eV, neutrinos can be always considered as ultrarelativistic particles, and the approximation $m_i \ll p_i$ for which:

$$E_i = \sqrt{m_i^2 + p_i^2} \approx p_i + \frac{m_i^2}{2p_i} \quad (1.6)$$

can be applied together with $t \approx x$. As further approximation one considers that ν_α has been produced with a defined momentum p , and all the mass eigenstates are supposed to have all the same momentum p but different energies.

Then the neutrino propagation state can be rewritten as:

$$|\nu(x)\rangle = \sum_i U_{\alpha i} e^{-i\frac{m_i^2}{2p}x} |\nu_i\rangle \quad (1.7)$$

Expressing a mass state in terms of flavor eigenstates β , one gets:

$$|\nu_i\rangle = \sum_\beta U_{\beta i}^* |\nu_\beta\rangle \quad (1.8)$$

and the propagated state $|\nu(x)\rangle$ becomes:

$$|\nu(x)\rangle = \sum_\beta \left[\sum_i U_{\beta i}^* U_{\alpha i} e^{-i\frac{m_i^2}{2p}x} \right] |\nu_\beta\rangle \quad (1.9)$$

The neutrino flavor ν_α , propagating to \vec{x} as $|\nu(x)\rangle$ has become a combination of different neutrino flavor eigenstates $|\nu_\beta\rangle$. Considering a detector located at a distance $x = L$ from the neutrino source, the probability to find the neutrino of original flavour α to have the flavour β is:

$$P(\nu_\alpha \rightarrow \nu_\beta) = \left| A_{(\alpha \rightarrow \beta)}(L) \right|^2 \quad (1.10)$$

[†]Here and in the following $\hbar = c = 1$ and hence $t \approx x$

where the amplitude $A_{(\alpha \rightarrow \beta)}(L)$ is:

$$A_{(\alpha \rightarrow \beta)}(L) = \langle \nu_\beta | \nu(x) \rangle \quad (1.11)$$

which is the usual collapse of a quantum-mechanics state into one of the eigenstates. Then the probability can be expressed as:

$$\begin{aligned} P(\nu_\alpha \rightarrow \nu_\beta) &= \delta_{\alpha\beta} \\ &- 4 \sum_{i>j} \text{Re} \left(U_{\alpha i} U_{\beta i}^* U_{\alpha j}^* U_{\beta j} \sin^2 \left(\frac{\Delta m_{ij}^2 L}{4 E} \right) \right) \\ &+ 2 \sum_{i>j} \text{Im} \left(U_{\alpha i} U_{\beta i}^* U_{\alpha j}^* U_{\beta j} \sin^2 \left(\frac{\Delta m_{ij}^2 L}{2 E} \right) \right) \end{aligned} \quad (1.12)$$

where $\Delta m_{ij}^2 = m_i^2 - m_j^2$ is the mass splitting between two mass eigenstates i and j and can be either positive or negative, E is the energy [†] of the neutrino flavor α computed as the weighted average energy of the mass states.

From this formulation it is clear that neutrino oscillations exist only if

- all the masses are different and at least two of them are non-vanishing;
- the neutrino mixing matrix U has non diagonal elements different from zero.

1.2.4 Two-neutrino oscillation

The mixing matrix U can be rewritten in blocks of 2×2 matrices, obtaining:

$$U = \begin{pmatrix} 1 & 0 & 0 \\ 0 & c_{23} & s_{23} \\ 0 & -s_{23} & c_{23} \end{pmatrix} \begin{pmatrix} c_{13} & 0 & s_{13} e^{-i\delta} \\ 0 & 1 & 0 \\ -s_{13} e^{-i\delta} & 0 & c_{13} \end{pmatrix} \begin{pmatrix} c_{12} & s_{12} & 0 \\ -s_{12} & c_{12} & 0 \\ 0 & 0 & 1 \end{pmatrix} \quad (1.13)$$

The central submatrix contains the angle θ_{13} , which has been experimentally shown to be small, and it can be considered diagonal as first approximation. In this case the matrix U describes two rotations in two orthogonal planes (1,2) and (1,3) and the oscillation probabilities have a simplified expression. For reasons of simplicity let assume to have only two neutrino flavours, $|\nu_e\rangle$ and $|\nu_\mu\rangle$, and only two mass eigenstates, $|\nu_1\rangle$ and $|\nu_2\rangle$. Then every flavor eigenstate can be expressed via a rotation of the mass eigenstates (see figure 1.2):

$$\begin{aligned} |\nu_e\rangle &= \cos \theta |\nu_1\rangle + \sin \theta |\nu_2\rangle \\ |\nu_\mu\rangle &= -\sin \theta |\nu_1\rangle + \cos \theta |\nu_2\rangle \end{aligned} \quad (1.14)$$

[†]the theory reported in this section is consistent with [15]

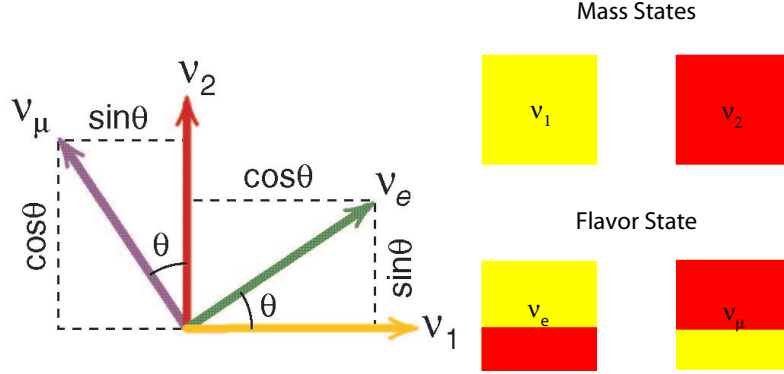


Figure 1.2: The relation between mass eigenstates and flavor eigenstates can be seen as a rotation or a misalignment between the two basis (left). Every flavor state contains a different contribution from one of the mass states (right).

The oscillation probability $P(\nu_\mu \rightarrow \nu_e)$ is reduced to:

$$P(\nu_\mu \rightarrow \nu_e) = \sin^2(2\theta) \sin^2\left(\frac{\Delta m_{12}^2 L}{4E}\right) \quad (1.15)$$

where $\Delta m_{12}^2 = m_1^2 - m_2^2$. The oscillation formula can be rewritten in different units as:

$$P(\nu_\mu \rightarrow \nu_e) = \sin^2(2\theta) \sin^2\left(\frac{1.27 \Delta m_{12}^2 L}{E}\right) \quad (1.16)$$

with Δm_{12}^2 expressed in eV^2 , the distance L in km and the energy in GeV . The factor 1.27 comes from the re-introduction of \hbar and c in the formulas, and $1/(4\hbar c) = 1.27 GeV/(km eV^2)$.

The experimental results are usually presented as plots on the plane Δm^2 versus $\sin^2(2\theta)$. The collection of pairs of those parameters, compatible with the observed data, describes the allowed regions of neutrino oscillation on this plane.

1.2.5 Three family oscillations

The simplified two family picture can be applied for most of the experiments. However, it is interesting to investigate what happens with 3 families. New phenomena appear, such as the CP violation in the leptonic sector.

In the complete formulation the mixing matrix can be seen as a rotation in a 3D space (see figure 1.3), and the oscillation probabilities are described

by six independent parameters: three mixing angles ($\theta_{12}, \theta_{13}, \theta_{23}$), two mass splittings ($\Delta m_{12}^2, \Delta m_{23}^2$) and the CP violating phase δ , following the same fashion as for quarks. Moreover, two cases are possible for the sign of the

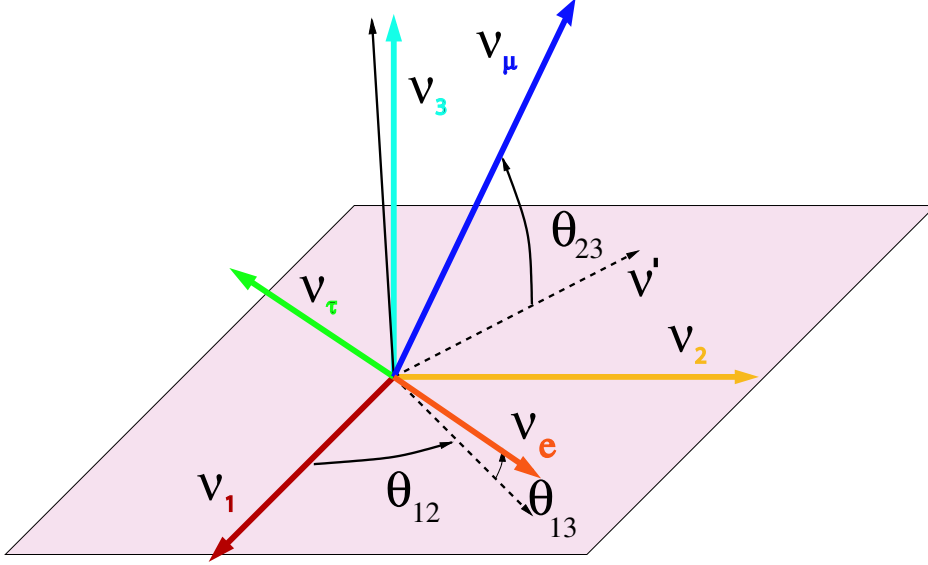


Figure 1.3: In the 3×3 approach, the mixing matrix represent a misalignment in the 3D space between mass states and flavor states which can be describe by three angles.

mass splitting Δm_{23}^2 (see figure 1.4) remembering that the small one, Δm_{12}^2 , dominates the solar neutrinos oscillations has a positive sign as suggested by the Solar experiments (section 1.3.1), and the large one, Δm_{23}^2 , governs the atmospheric neutrinos (section 1.3.3). The third mass state m_3 could be heavier than the other two (hierarchical spectrum) and the Δm_{23}^2 would be negative, or the inverse situation, where m_3 would be the lightest (degenerate spectrum).

In this approach the mass eigenstates are numbered according to their ν_e content: ν_1 is the mass states with the largest ν_e contribution while ν_3 is the one with the smallest contribution.

In the 3×3 scenario, the oscillation probability $P(\nu_e \rightarrow \nu_\mu)$, for example, takes the following form:

$$\begin{aligned}
 P(\nu_e \rightarrow \nu_\mu) &= 4c_{13}^2 \sin^2(\Delta_{23}) s_{12}^2 s_{13}^2 s_{23}^2 \\
 &+ 4c_{13}^2 c_{12}^2 (\sin^2(\Delta_{13}) s_{13}^2 s_{23}^2 + \sin^2(\Delta_{12}) s_{12}^2 (1 - (1 + s_{13}^2) s_{23}^2)) \\
 &- \frac{1}{4} |\tilde{J}| \cos \delta [\cos(2\Delta_{13}) - \cos(2\Delta_{23}) - 2 \cos(2\theta_{12}) \sin^2 \Delta_{12}]
 \end{aligned}$$

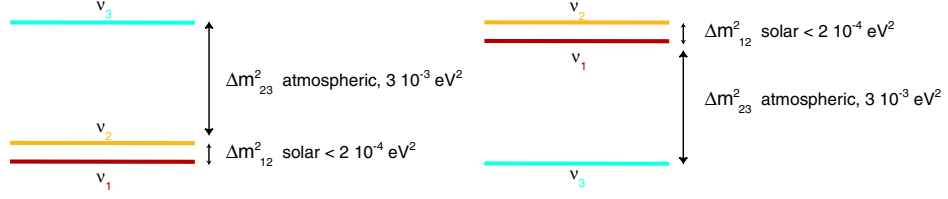


Figure 1.4: *Two possible mass splitting scenarios coming from the two different possible signs for the atmospheric splitting.*

$$+ \frac{1}{4} |\tilde{J}| \sin \delta [\sin(2\Delta_{12}) - \sin(2\Delta_{13}) + \sin(2\Delta_{23})] \quad (1.17)$$

where $\Delta_{ij} = \Delta m_{ij}^2 L / (4E)$ and $\tilde{J} = c_{13} \sin(2\theta_{12}) \sin(2\theta_{13}) \sin(2\theta_{23}) e^{i\delta}$.

Moreover CPT is assumed to be conserved, with the consequence that $P(\nu_e \rightarrow \nu_\mu) = P(\bar{\nu}_\mu \rightarrow \bar{\nu}_e)$. However, if CP is violated, namely if the mixing matrix is complex, which corresponds to $\delta \neq 0$, then $P(\nu_e \rightarrow \nu_\mu) \neq P(\bar{\nu}_e \rightarrow \bar{\nu}_\mu)$ or, considering T violation, the condition $P(\nu_e \rightarrow \nu_\mu) \neq P(\nu_\mu \rightarrow \nu_e)$ could also occur. Those probabilities are different since the transformation from neutrinos to antineutrinos implies the change of the sign of the phase δ in the mixing matrix U , and the same happens under the T transformation. It is clear that if CP is violated also T is violated in order to conserve CPT.

The observation of CP violation requires that all mixing angles have to be different from zero, or $\tilde{J} \neq 0$.

Equation 1.17 can be further simplified considering that θ_{13} is small and $\Delta m_{12}^2 \ll \Delta m_{13}^2 \approx \Delta m_{23}^2$ and rewritten as:

$$P(\nu_e \rightarrow \nu_\mu) = s_{13}^2 s_{23}^2 \sin^2(\Delta_{23}) + c_{23}^2 \sin^2(2\theta_{12}) \sin^2(\Delta_{12}) + |\tilde{J}| \cos(\delta - \Delta_{23}) \sin(\Delta_{12}) \sin(\Delta_{23}) \quad (1.18)$$

The contribution given by the CP violating term is small compared to the other two and a precise determination of δ requires a precise knowledge, at the same time, of the atmospheric term, that contains θ_{23} and Δm_{23}^2 , and the solar term, driven by θ_{12} and Δm_{12}^2 .

An even more simplified oscillation expression, much similar to the 2 family approach, can be derived considering $\Delta m_{12}^2 \approx 0$, which is meaningful since it is about thirty times smaller than Δm_{23}^2 .

The new approximate oscillation probability becomes:

$$P(\nu_e \rightarrow \nu_\mu) = \sin^2(2\theta_{13}) \sin^2(\theta_{23}) \sin^2\left(\frac{1.27 \Delta m_{23}^2 L}{E}\right) \quad (1.19)$$

expressing L in km , E in GeV and Δm_{23}^2 in eV^2 .

The CP violating term disappears because there is only one mass splitting

as in the 2×2 case. The other limitation to this formulation is that at low neutrino energy or for long distances, the contribution Δm_{12}^2 becomes important. This is shown in figure 1.5 and the effect of the modulation of the oscillation pattern over long distances due to the Δm_{12}^2 term becomes even more striking in figure 1.6. These plots have been calculated with the following values for the different mixing angles:

$$\theta_{12} = 31.7^\circ, \theta_{23} = 45^\circ, \theta_{13} = 2.8^\circ$$

and these mass splittings:

$$\Delta m_{12}^2 = 7 \cdot 10^{-5} \text{ eV}^2, \Delta m_{23}^2 = 2.5 \cdot 10^{-3} \text{ eV}^2$$

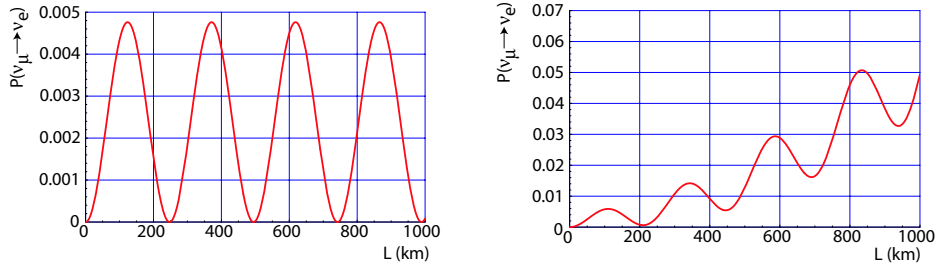


Figure 1.5: Oscillation probability calculated for a fixed energy $E=250 \text{ MeV}$ as a function of distance with the approximate formula (left) and the complete formula (right).

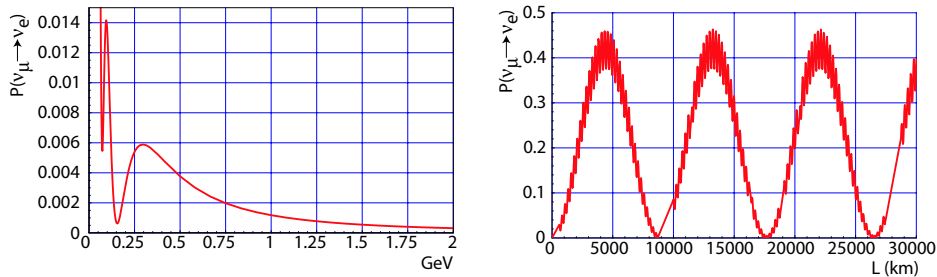


Figure 1.6: Oscillation probability calculated using the complete formula for a fixed distance $L=130 \text{ km}$ as a function of the energy (left) and calculated for a fixed energy $E=250 \text{ MeV}$ as a function of the distance (right).

1.2.6 Matter Effect

The influence of the passage through matter on the probability oscillation is known as matter effect or MSW effect (Mikheyev, Smirnov, Wolfenstein). As described above, the neutrino oscillation is due to a different propagation of the mass eigenstates in vacuum. However, once a neutrino passes through matter the electron neutrino component of a mass state has a different propagation than the other two flavors. This is due to the fact that electron neutrinos can interact with the electrons in the matter via neutral and charged current while all the other flavors only by neutral current (see figures 1.7).

For reasons of simplicity let consider only the 2 generation case, and take

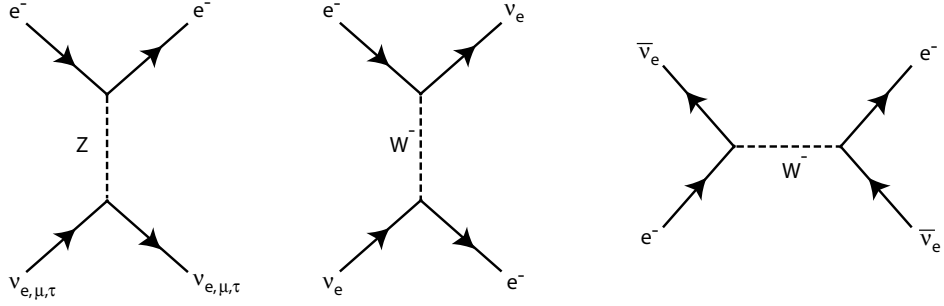


Figure 1.7: *Neutral current neutrino scattering (left) and charged current neutrino scattering (center) together with antielectron neutrino charged current interaction.*

$|\nu_e\rangle$ and $|\nu_\mu\rangle$ as flavour states. The passage through the matter induces an extra potential seen by neutrino during the propagation which equals to:

$$\begin{aligned} V_e &= \sqrt{2}G_F(N_e - \frac{N_n}{2}) \\ V_\mu &= -\sqrt{2}G_F\frac{N_n}{2} \end{aligned} \quad (1.20)$$

with G_F the Fermi constant, N_e the electron density and N_n the neutron density which are considered constant in space.

The Schrödinger equation for the neutrino propagation takes the matrix form of:

$$i\frac{d}{dt} \begin{pmatrix} \nu_e \\ \nu_\mu \end{pmatrix} = \begin{pmatrix} -\frac{\Delta m^2}{4E} \cos 2\theta + \sqrt{2}G_F N_e & \frac{\Delta m^2}{4E} \sin 2\theta \\ \frac{\Delta m^2}{4E} \sin 2\theta & \frac{\Delta m^2}{4E} \cos 2\theta \end{pmatrix} \begin{pmatrix} \nu_e \\ \nu_\mu \end{pmatrix} \quad (1.21)$$

after neglecting all the common phases and the phases coming from the neutral current which do not introduce a relative phase shift in the oscillation

probabilities.

The new mass eigenstates of the above propagation matrix can be expressed in function of the flavor eigenstates as:

$$\begin{aligned} |\nu_1^{MSW}\rangle &= \cos \theta_{MSW} |\nu_e\rangle + \sin \theta_{MSW} |\nu_\mu\rangle \\ |\nu_2^{MSW}\rangle &= -\sin \theta_{MSW} |\nu_e\rangle + \cos \theta_{MSW} |\nu_\mu\rangle \end{aligned} \quad (1.22)$$

considering that the mixing angle θ_{MSW} is different from the vacuum mixing angle θ , and given by the equation:

$$\sin^2 2\theta_{MSW} = \frac{\left(\frac{\Delta m^2}{4E}\right)^2 \sin^2 2\theta}{\left(\frac{\Delta m^2}{4E} \cos 2\theta - \sqrt{2}G_F N_e\right)^2 + \left(\frac{\Delta m^2}{4E}\right)^2 \sin^2 2\theta} \quad (1.23)$$

The oscillation probability takes the same form as the probability in vacuum:

$$P(\nu_e \rightarrow \nu_\mu) = \sin^2 2\theta_{MSW} \sin^2 \left(\pi \frac{L}{\lambda_{MSW}} \right) \quad (1.24)$$

with λ_{MSW} the oscillation wave length equals to:

$$\lambda_{MSW} = \frac{2\pi}{\sqrt{\left(\frac{\Delta m^2}{2E} \cos \theta - \sqrt{2}G_F N_e\right)^2 + \left(\frac{\Delta m^2}{2E}\right)^2 \sin^2 2\theta}} \quad (1.25)$$

The mixing of neutrinos traversing the matter can be large even if it would be very small in vacuum propagation, in particular, the maximum mixing can be reached when the condition:

$$\sqrt{2}G_F N_e = \frac{\Delta m^2}{2E} \cos \theta \quad (1.26)$$

is fulfilled. Since $N_e > 0$, this condition can be realized only if $\Delta m^2 \cos \theta > 0$. This implies that, for a given mixing angle in vacuum, there is only one sign of Δm^2 which enhances the oscillation probabilities. Moreover, for antineutrinos, the matter induced potential changes sign. This is due to the fact that the antineutrino charged current interaction with electron occurs in the s channel and not in the t channel (see figure 1.7). Thus the condition to obtain the enhancement of the oscillation probability is opposite comparing the neutrino and antineutrino cases: the same Δm^2 cannot increase the oscillation probabilities for neutrino and antineutrinos at the same time.

This effect, as described in section 1.4.2, or the comparison of the number of oscillated events for a beam composed of neutrinos and a beam composed by antineutrinos for a fixed distance, can be used in beams of sufficient energy and flux, such as in a Neutrino Factory, to discriminate the sign of Δm_{23}^2 .

1.2.7 CP violation in the leptonic sector

A number of experiments in the next ten years will try to observe the oscillation $\nu_\mu \rightarrow \nu_e$, which has never been observed, and to measure θ_{13} . In figure

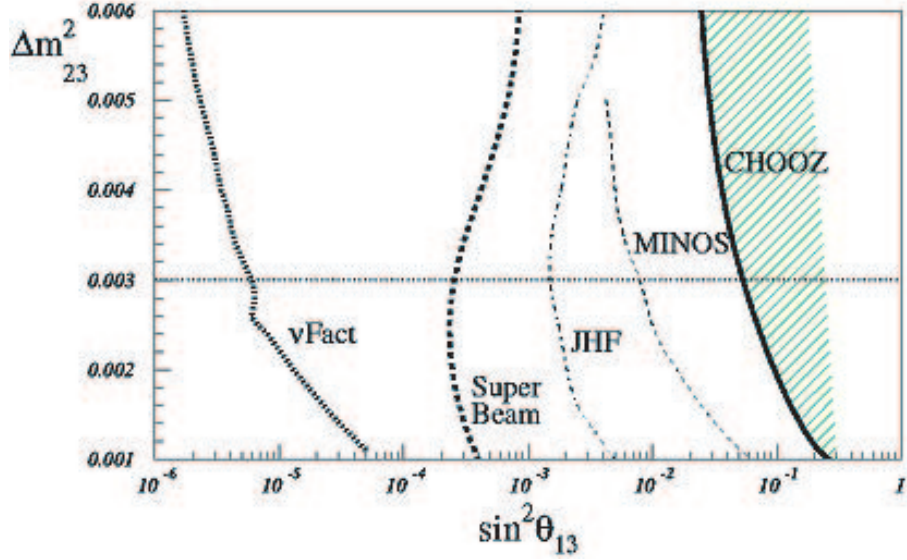


Figure 1.8: Sensitivity to $\sin^2 \theta_{13}$ for different future neutrino beam experiment[17].

1.8[17] the comparison of future neutrino experiments sensitivities to θ_{13} is presented.

Why this number is so important for the theory? $\sin \theta_{13}$ multiplies in the mixing matrix the term that contains the CP violating phase δ , and if it is too small or zero, there is no hope to observe CP violation in the leptonic sector from neutrino oscillations.

CP violation is one of the necessary ingredients to explain the asymmetry in the universe between matter and antimatter, and CP violation in the hadronic sector alone is not enough to explain this asymmetry. The leptonic CP violation could be the solution of the problem, but it can be discovered only if θ_{13} is non-zero or not too small (below 0.1 degrees): δ is the final "Holy Grail" for all the future neutrino experiment.

If it is non zero, the leptonic CP violation can be observed in an appearance experiment where, at different times, the two probabilities, $P(\nu_e \rightarrow \nu_\mu)$, $P(\bar{\nu}_e \rightarrow \bar{\nu}_\mu)$ are measured. The asymmetry:

$$A_{CP} = \frac{P(\nu_e \rightarrow \nu_\mu) - P(\bar{\nu}_e \rightarrow \bar{\nu}_\mu)}{P(\nu_e \rightarrow \nu_\mu) + P(\bar{\nu}_e \rightarrow \bar{\nu}_\mu)} \propto \frac{\sin \delta \sin(\Delta m_{12}^2)L/(4E) \sin \theta_{12}}{\sin \theta_{13} + \text{small Solar terms}} \quad (1.27)$$

if non null will give the access to δ once all the other parameters are sufficiently well known. Leptonic CP violation can be discovered only with an

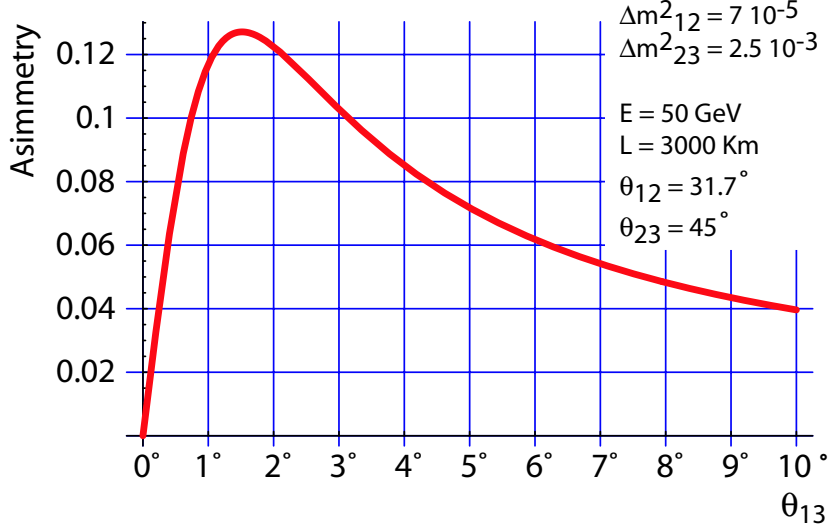


Figure 1.9: *Asimmetry in function of the angle θ_{13} .*

appearance experiment, which measures the appearance of a new flavour in a neutrino beam of another flavour, since a disappearance experiment, as the one using a nuclear reactors as source, measures the survival probability $P(\nu_e \rightarrow \nu_e)$, which is clearly time reversal symmetric. Since CPT has to be conserved, $P(\nu_e \rightarrow \nu_e)$ has to be equal to its CP conjugate $P(\bar{\nu}_e \rightarrow \bar{\nu}_e)$ and the asymmetry is hence zero.

In the case of an appearance experiment which measures $\nu_e(\bar{\nu}_e) \rightarrow \nu_\mu(\bar{\nu}_\mu)$, A_{CP} can be large if LMA (Large Mixing Angle, see section 1.3.1) is the solution for the solar neutrinos, as it is measured by Kamland and SNO (see next sections), and if $\sin\theta_{13}$ is small, in order of few degrees as shown in figure 1.9. However $\sin\theta_{13}$ should not be too small otherwise the oscillation probabilities become too small and the statistics error becomes too large to distinguish δ from 0.

It is hence fundamental to produce ν_e and $\bar{\nu}_e$ at high energy under the same controlled conditions and this is possible only in an artificial source that can accelerate alternatively both positive and negative muons such as a Neutrino Factory.

1.3 Neutrino sources and detectors

1.3.1 Solar Neutrinos

Neutrinos were introduced to solve the puzzle of the beta decay, and their masses were introduced to solve the solar neutrino puzzle. This second puzzle was born just a few years after the measurement of the first neutrinos.

R. Davis proposed and realized in the late 60's in the Homestake mine the first experiment[4] to measure the neutrino flux coming from the sun.

The power of the sun is produced by different fusion reactions (see figure 1.10, top), which produce only ν_e with an energy spectrum shown in figure 1.10 on the bottom. The typical ν_e flux reaching the earth equals $10^8 \nu_e/s/m^2$.

The experiment proposed and ran by Davies is able to detect only ν_e by inverse beta decay reaction in a pool of 400 m³ of C_2Cl_4 (tetrachlor ethene, which is a common cleaning liquid). Then the counting of the number of Ar nuclei produced by the reaction $Cl + \nu_e \rightarrow Ar + e^-$ gives the electron neutrino flux.

The result was already surprising after a few years, in the early 70's, and became even more striking by its confirmation after 30 years of continuous data taking: the ν_e detected from the sun are only one third of that expected by the theoretical prediction of the Standard Solar Model (SSM)[5].

The possible solutions proposed to solve this puzzle indicate to possible errors: the SSM calculation could be wrong or the experimental results could be wrong, but both doubts have presently been ruled out. The SSM predicts perfectly the power emitted from the sun in form of visible light, which is produced by the same fusion processes generating neutrinos[†]. The same SSM predicts also the vibration modes of the solar surface, again in agreement with the observations. Moreover, several experiments have measured the lack of neutrinos using different techniques: Homestake, Gallex, Sage and GNO use the inverse beta decay and Kamiokande and Super-Kamiokande are water Cerenkov detectors (see figure 1.11 for a summary of the experimental results).

The new generation of solar neutrino experiments tried to verify the results of the Davis experiment, but using different detectors. The Davis's experiment can measure solar neutrinos with an energy greater than 0.8 MeV. However, as shown in figure 1.10, most of the solar flux is produced by the pp fusion reaction with an energy below 0.5 MeV, and they cannot be de-

[†]One can point out that neutrinos, once created by fusion reactions, reach the earth in ≈ 8 minutes without any delay in the transport, while a photon produced in the core of the Sun takes 10^6 years to reach the Sun surface. The SSM is based on the hypothesis that the Sun is a stable star with unvaried characteristics on a time scale of 10^8 years.

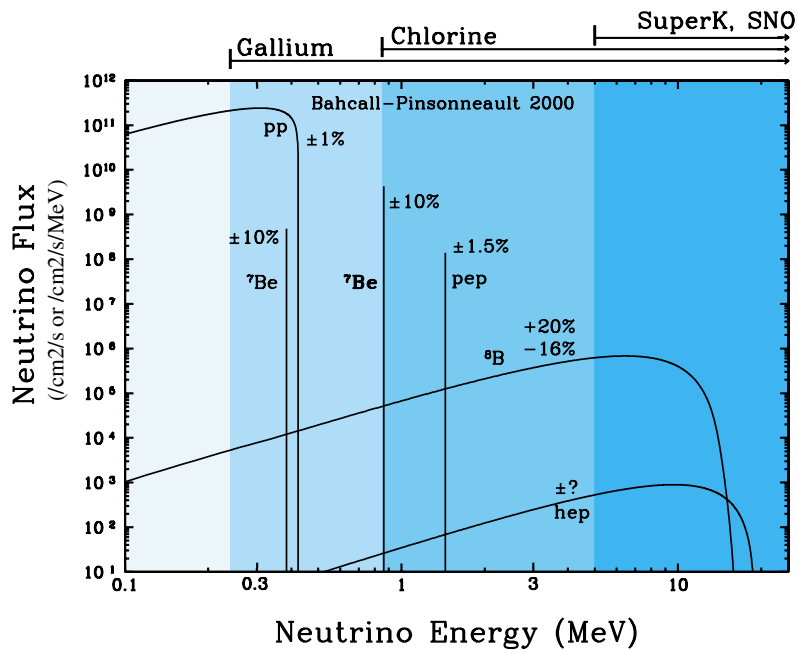
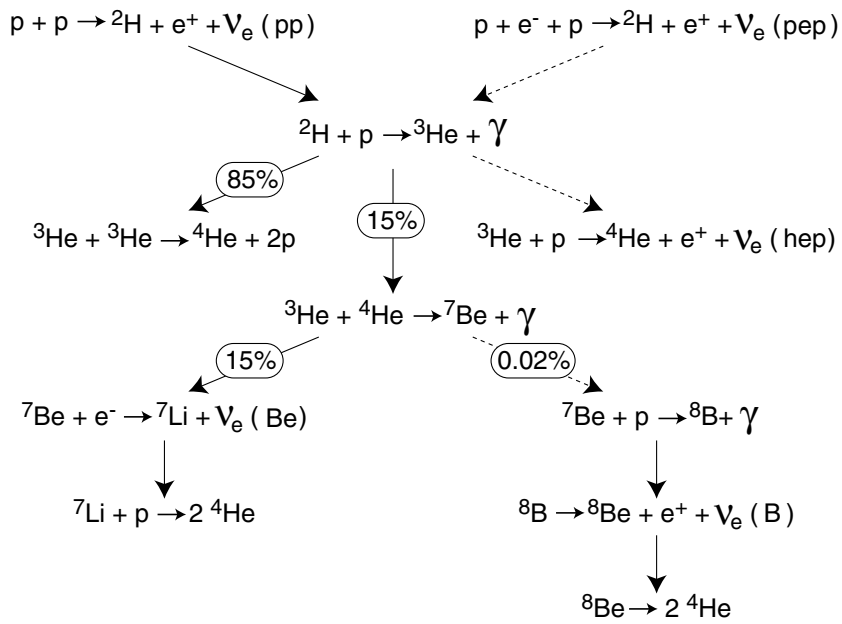


Figure 1.10: The different fusion reactions in the Sun (top) produces the neutrino spectrum on the bottom [5]

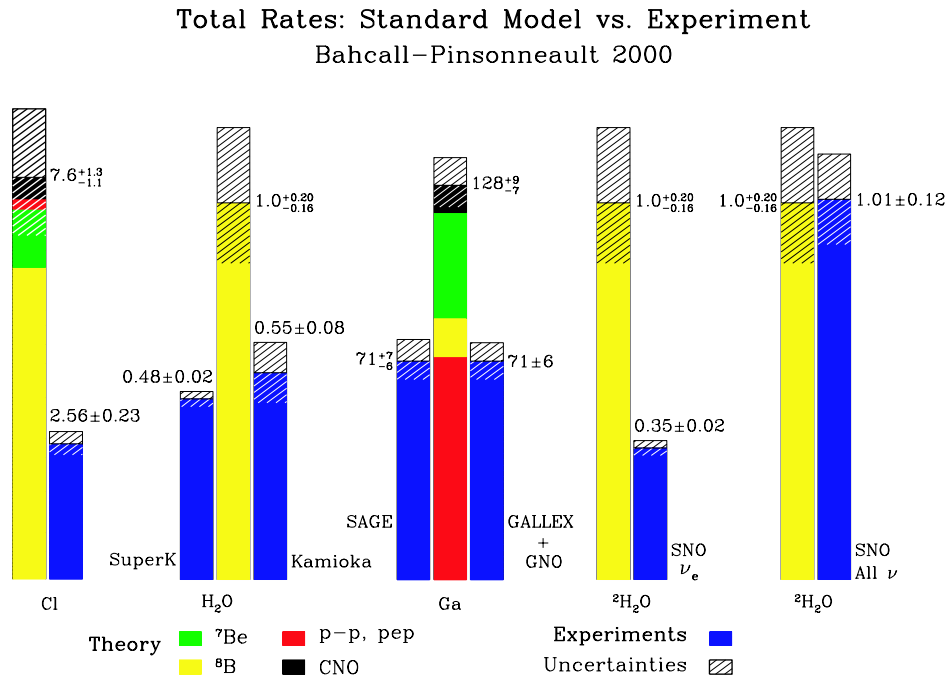


Figure 1.11: *Solar neutrino fluxes in SNU (1 Solar Neutrino Units = 10^{-36} captures per second and per absorber nucleus) for different experiments compared to the SSM (Standard Solar Model) prediction[5]. The last column shows the total ⁸B flux as computed by the SSM and compared to the total solar neutrino flux, composed by ν_e , ν_μ and ν_τ , measured with the NC reaction by SNO.*

tected by C_2Cl_4 .

The following generation of detectors, Gallex, Sage and GNO, uses Gallium as target. The Gallium threshold for the reaction ${}^{71}\text{Ga} + \nu_e \rightarrow {}^{71}\text{Ge} + e^+$ is 0.233 MeV, giving access to the largest solar neutrino flux.

Surprisingly, their results confirmed the Davis's solar puzzle, albeit with a different result: the neutrinos measured are the 55% of those expected for the SSM.

Even more striking, the Kamiokande experiment followed by Super-Kamiokande, based on Cerenkov light detection in water (see next section), confirmed again the lack of solar neutrinos.

The only solution left to explain the mystery of the missing solar neutrinos is that ν_e transform into something else, which is not detectable by an inverse beta decay detector.

As seen in section 1.2.3, neutrino oscillation would just do that, transforming a ν_e into one or the other known neutrinos, ν_μ or ν_τ , thus conserving the total

Reaction	Flux Measured
$\nu_{e,\mu,\tau} d \rightarrow \nu n p (NC)$	$\phi_{NC} = \phi_{\nu_e} + \phi_{\nu_\mu} + \phi_{\nu_\tau}$
$\nu_{e,\mu,\tau} e \rightarrow \nu e (ES)$	$\phi_{ES} = \phi_{\nu_e} + 0.15 (\phi_{\nu_\mu} + \phi_{\nu_\tau})$
$\nu_e d \rightarrow e p p (CC)$	$\phi_{CC} = \phi_{\nu_e}$

Table 1.1: Reaction of neutrinos in heavy water with the extrapolated fluxes

neutrino flux. The breakthrough would be an experiment able to prove the total neutrino flux conservation.

Although little doubt remained by then, the solution to the Solar neutrino puzzle was elegantly and definitely established in 2002 by the SNO Canadian experiment. SNO is a heavy water (D₂O or ²H₂O) Cerenkov detector[6], whose great innovation is the sensitivity to three different neutrino interactions in D₂O, which involve all neutrino flavors:

- Elastic Scattering (ES). A neutrino of any flavor can scatter on an electron which, being at high energy, radiates Cherenkov light.
- Charged Current (CC) interaction. The electron neutrino interacts with one of the quarks in the Deuterium neutron and produces a proton causing the dissociation of the nucleus. The electron produced in the weak interaction is detected via Cherenkov light.
- Neutral Current (NC) interaction. Neutrinos of any flavor can interact equally with Deuterium dissociating the nucleus. The free neutron is then detected.

This reaction is the key-point of the experiment, since it measures the total solar neutrino flux.

SNO can measure neutrinos produced mainly by the ⁸B reaction because the detection energy threshold is at ≈ 6 MeV.

The presence in the solar neutrino flux of neutrinos other than ν_e 's can be identified by comparing the neutrino flux extracted from the CC events, ϕ_{CC} , and the ES events, ϕ_{ES} , or the CC events and the NC events, ϕ_{NC} . If the ratio between the fluxes ϕ_{CC} and ϕ_{ES} is smaller than one and the ratio between ϕ_{CC} and ϕ_{NC} is also smaller than one this implies that there are neutrinos other than electron neutrinos in the solar flux. Table 1.1 summarizes of how the different reactions contribute to the different fluxes which have been measured as[8]:

$$\begin{aligned}\phi_{CC} &= 1.70 \pm 0.07(stat)_{-0.10}^{+0.09}(syst) 10^6 \frac{\nu}{cm^2 s} \\ \phi_{ES} &= 2.13_{-0.28}^{+0.29}(stat)_{-0.08}^{+0.15}(syst) 10^6 \frac{\nu}{cm^2 s}\end{aligned}$$

$$\phi_{NC} = 4.90 \pm 0.24(stat)_{-0.27}^{+0.29}(syst) 10^6 \frac{\nu}{cm^2 s}$$

This set of measurements clearly demonstrates that solar neutrinos, born as ν_e , arrive on the earth as a mix of ν_e , ν_μ and ν_τ , of which ν_e are only one third: this is the final clarification of the solar neutrino puzzle.

1.3.2 Reactor (Anti)Neutrinos

Nuclear reactors are a powerful source of $\bar{\nu}_e$ coming from β^- decay of neutron-rich isotopes produced by fission reactions. The neutrino flux and energy spectrum can be calculated with relatively high precision (around 3% as systematic error on final neutrino event rate [9]) knowing the composition and the burn-up of the reactor fuel.

The neutrino energy spectrum is in the same range of a few MeV as the solar neutrino. For this reason, a reactor experiment located at a sufficiently long distance has sensitivity to measure the solar oscillation parameters, for some of the allowed regions.

Until recently, reactor neutrino experiments were always located too close to the reactor source and gave negative results for the oscillations. A summary of these results is shown in figure 1.12, in which the antineutrino fluxes produced from different nuclear reactors match perfectly the flux measured by the detectors, $N_{obs}/N_{exp}=1$, meaning that no oscillations are observed. Nevertheless, there is one point which does not follow the no-oscillation line, the Kamland experiment result, which will be discussed in the following.

Before the Kamland experiment, the next to last experiment to be mentioned is CHOOZ[9]. CHOOZ produced the most significant limit on the angle θ_{13} . The detector was located in France, about 1 km away from two nuclear reactors which generate a total thermal power of ≈ 8.5 GW. The neutrinos generated from the fission decays have a typical average energy of 3 MeV.

The results of CHOOZ ruled out from the possible explanation of the atmospheric neutrino anomaly, described in the next section, the oscillation $\nu_e \rightarrow \nu_\mu$ and provided the limit for $\theta_{13} < 10^\circ$ for $\Delta m_{13}^2 \approx 3 \cdot 10^{-3} eV^2$.

The last most important experiment for nuclear reactors is Kamland[10]. Kamland is located in Japan and detects $\bar{\nu}_e$ produced by 16 reactors situated at an average distance of 160 km. The result (see figure 1.13, right, for the oscillation parameter phase space) of Kamland confirms the disappearance of $\bar{\nu}_e$ according to solar neutrino oscillation (see figure 1.13, left) prediction. Moreover the uncertainty on the solar oscillation parameter measurements is reduced once the results of Kamland are combined with other experiments results, in particular of SNO, as it is presented in figure 1.13, confirming the

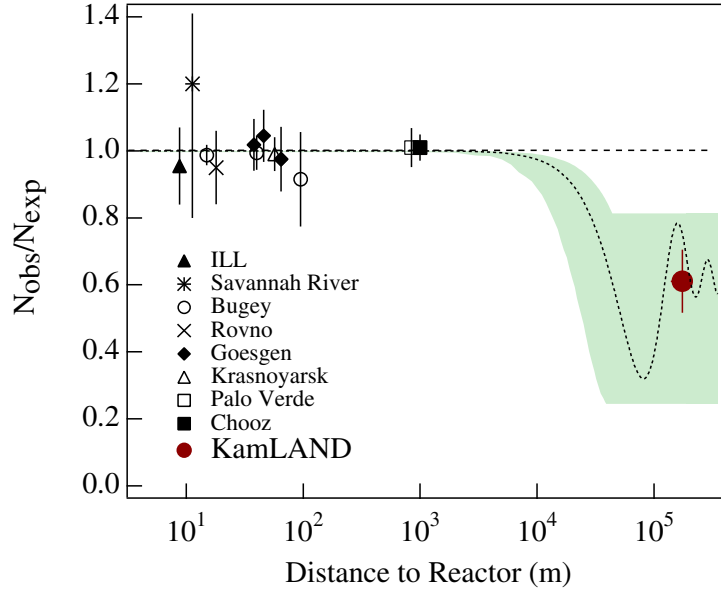


Figure 1.12: *Ratio of measured neutrinos over expected neutrinos versus the distance for different reactor antineutrino experiments. The red point is the KamLAND measurements, in agreement with the disappearance predicted by neutrino oscillations[10].*

LMA (Large Mixing Angle) solution as the preferred one. Even more important is the fact that the Kamland results are not affected by the matter effect as is the case for Solar neutrinos. The distance of hundreds kilometer between the reactors and the detector is too short, thus the oscillation probabilities are the same as in vacuum. Nevertheless the solution found is consistent with the solar oscillation.

1.3.3 The atmospheric neutrino anomaly

After the sun, the other main natural source of neutrinos is the earth atmosphere.

A very intense flux of cosmic rays impinges on the high atmosphere and produces a huge number of secondaries, in particular, pions of both sign decays in flight via $\pi^\pm \rightarrow \mu^\pm + \nu_\mu(\bar{\nu}_\mu)$. The muons again decay to $\mu^\pm \rightarrow e^\pm + \bar{\nu}_\mu(\nu_\mu) + \nu_e(\bar{\nu}_e)$. The typical energy spectrum of atmospheric neutrinos starts at about hundred MeV and extends up to several GeV.

The measurement of the atmospheric neutrino oscillation requires a different technique from that used for solar neutrinos, mainly because the atmosphere cannot be considered as a point-like source at fixed distance. Neutrinos can

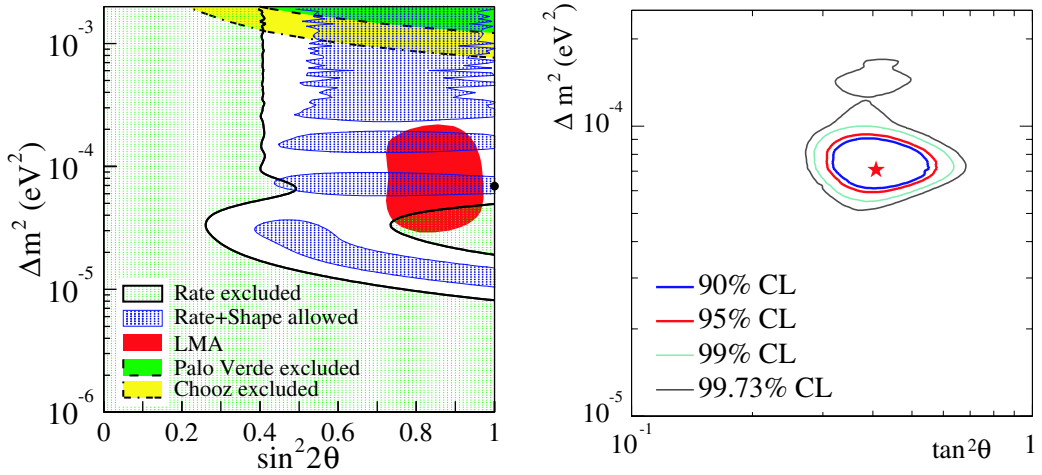


Figure 1.13: Allowed zone for the oscillation parameters resulting from the Kamland measurements (left)[10]. Solar oscillation parameter phase space (Δm_{12} vs θ_{12}) considering the results from SNO, Superkamiokande, inverse beta decay experiments and Kamland results (right)[8]

be generated in any point in the atmosphere, thus neutrinos of the same energy born at the same time can travel very different distances before reaching the detector hence with different oscillation probabilities (see figure 1.14).

For this reason the water-Cerenkov technique proved to be most effective

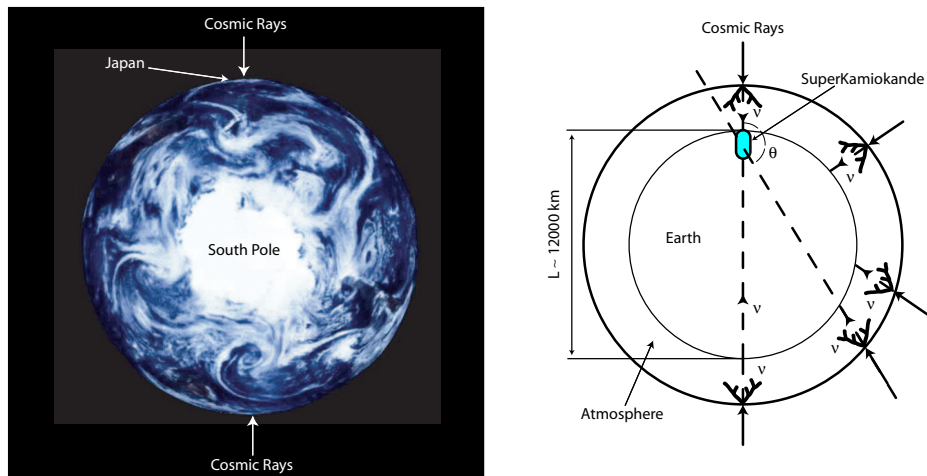


Figure 1.14: Picture taken from the Galileo satellite from the zenith at the South Pole[11](left). The sketch on the right shows the measurement setup of Super-Kamiokande.

for atmospheric neutrino detection, since it provides the information about the direction of each neutrino detected, thus about the distance it traveled. When neutrinos interact with matter they generate leptons. In particular, if they interact in water and if the lepton energy is above the water Cerenkov threshold, which is 0.77 MeV for electrons and 157 MeV for muons, a light cone is created by the lepton itself.

The typical water Cerenkov detector is composed by a huge water tank equipped with an array of phototube mounted on its wall used to record the Cerenkov light. The choice of water as material is based on three simple considerations: its low cost, high transparencies and reachable purity.

The amount of Cerenkov light is used to determine the energy of the lepton, and hence of its neutrino parent. Moreover muons and electrons can be separated by the shape of their Cerenkov rings, giving in this way also the flavour of the primary neutrino. Muons, being minimum-ionising particles, generate a ring with a boundary more defined than electrons (see figure 1.15).

The first detector that used this technology on a large scale was Kamiokande. Kamiokande was located where nowadays is set Kamland and its main physics aim was the discovery of proton decay, the physics of solar neutrinos being second. Kamiokande showed for the first time, thanks to the capability to recognize the direction of neutrinos, that the solar neutrinos were really coming from the Sun, and that the Solar Neutrino puzzle was not a fault of the inverse beta decay detectors (see figure 1.11).

The successor of Kamiokande is Super-Kamiokande[12], a 40 kT Cerenkov detector. In addition to the solar neutrinos Super-Kamiokande observes atmospheric neutrinos, separating the neutrino flux for different directions (see figure 1.14). The experiment counts ν_e and ν_μ in bins of the zenith angle θ ($\cos\theta = 1$ for the neutrinos coming from the top and $\cos\theta = -1$ from the bottom, see figure 1.16). The result is striking: the ν_μ coming from the bottom, hence traversing the earth diameter, are nearly half of those coming from the top. At a first glance the easiest explanation would sound like: neutrinos have interacted with the earth. But there are two caveats: the first is that from figure 1.16 the asymmetry doesn't appear for ν_e , and the second is that the earth is practically transparent for neutrinos of less than few GeV energy. The conclusion is that atmospheric ν_μ transform into another neutrino flavor, which is not ν_e , because there is no excess in the ν_e flux coming from the opposite side of the Earth.

The experimental results of Super-Kamiokande presented in 1998 were considered as the definite proof of neutrino oscillations: a convincing support of the oscillation hypothesis was the fact that the same theory could explain both solar and atmospheric puzzles.

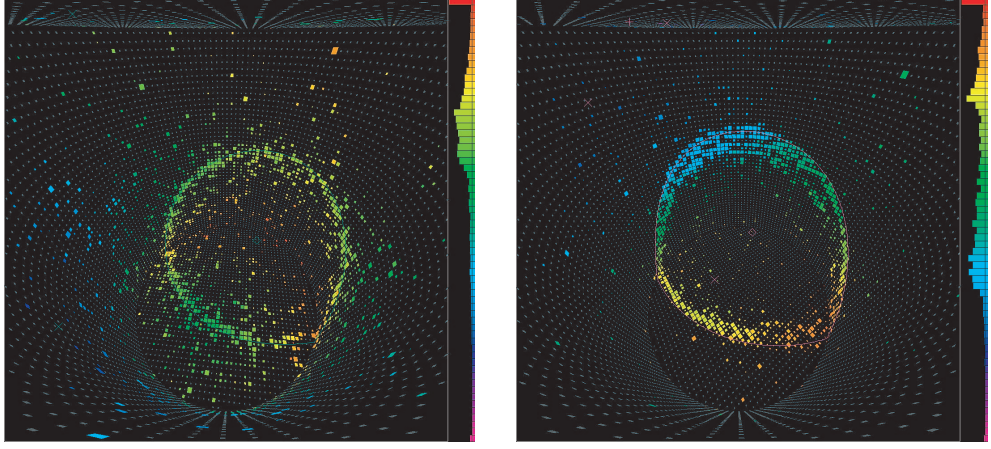


Figure 1.15: *Electron event (left) and muon event (right) in Super-Kamiokande[12].*

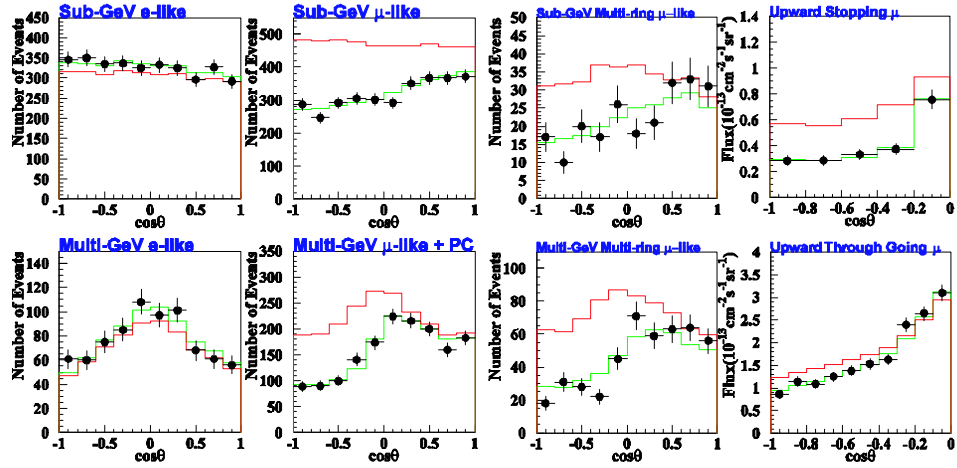


Figure 1.16: *Super-Kamiokande measurement. The neutrino fluxes are measured in bins of the zenith angle θ and divided in two categories, muon events created by a ν_μ scattering, and electron events, created by ν_e interaction. A further division is done according to the energy of the single event[12].*

1.3.4 The LSND caveat

In the previous discussion, the results of an experiment, LSND, have been excluded.

LSND[13] is an accelerator short base-line experiment which claimed to measure the oscillation $\bar{\nu}_\mu \rightarrow \bar{\nu}_e$. The Δm^2 found for this transition equals $\approx 1 \text{ eV}^2$ and this oscillation remains unconfirmed and not disproved by

other experiments.

The explication of the LSND data and the consistency of the other experimental results require a fourth mass state, thus a fourth neutrino flavor. The existence of the latter was never proven because this neutrino cannot couple to the W boson, since it doesn't have a charged lepton partner, and it cannot couple to the Z boson, since it was not observed at LEP. This kind of neutrino, defined as sterile, has been neglected, since disfavoured by the atmospheric neutrinos oscillations.

More exotic explications could be found supposing that CPT is not conserved by Nature. In any case the Miniboone[14] experiment should test the validity of the LSND results[†]

1.3.5 Short experimental summary

In the framework of the two family oscillation pattern, the state of the art for neutrino oscillation experimental picture can be summarized in the following points:

- the atmospheric neutrino anomaly has been solved by Super-Kamiokande. ν_μ oscillate into ν_τ and not into ν_e . The mixing angles θ_{23} is large $\approx 45^\circ$ and $\Delta m_{23}^2 \approx 2.7 \cdot 10^{-3} eV^2$;
- the solar neutrinos puzzle has been solved by SNO and Super-Kamiokande. ν_e oscillate into ν_x ($x = \mu$ or τ), the angle θ_{12} is large $\approx 32^\circ$ (LMA, Large Mixing Angle, solution with MSW is the preferred) and Δm_{12}^2 is around $7 \cdot 10^{-5} eV^2$;
- the angle θ_{13} is not larger than 10° as measured by CHOOZ. However this value is only an upper limit, and the lower limit could be zero.

The measurements of two oscillation parameters, θ_{13} and the CP violating phase δ , require a new powerful neutrino source: a Neutrino Factory.

1.4 The Neutrino Factory

The aim of a Neutrino Factory (NuFact) is the production of high energy, highly collimated (anti)electron and (anti)muon neutrino beams from muon decay:

$$\mu^- \rightarrow e^- + \bar{\nu}_e + \nu_\mu \quad (1.28)$$

[†]This thesis has been written at the beginning of the Miniboone data taking.

or

$$\mu^+ \rightarrow e^+ + \nu_e + \bar{\nu}_\mu \quad (1.29)$$

The objective is to achieve a neutrino flux of the order of several times 10^{20} neutrinos per year (1 year is assumed to be 10^7 seconds).

This powerful neutrino source will allow to reach the prefixed physics goals, which are:

- to measure the mixing angle θ_{13} by the oscillation probability $P(\nu_e \rightarrow \nu_\mu)$ with a precision of 10^{-3} or setting a limit to 10^{-6} degrees;
- to determine, via the MSW effect, the sign of Δm_{23}^2 ;
- to discover and measure leptonic CP violation.

A possible baseline scheme of a neutrino factory is the following: a high power proton beam (4 MW) impinges on a mercury target to produce pions. Pions around 200 MeV are focused by a magnetic lens (a horn) or captured by a 20 T solenoid and injected into a solenoidal decay channel. At the end of the channel muons produced by pion decay have a large energy spread and an enormous transverse emittance. Such kind of beam cannot be injected directly into a traditional accelerator without being essentially lost. The first step is the reduction of the muon energy spread in the phase rotation. Then ionisation cooling reduces the transverse phase space. The resulting beam can be accelerated by two recirculating linacs placed one after the other to reach the final energy of typically 20-50 GeV. The last step is to store the muons in a triangular decay ring, with two straight section pointing to two locations placed at different distances (figure 1.17).

The typical neutrino spectrum produced by the NuFact is shown in figure 1.19. The NuFact is quite different from traditional neutrino beams produced by accelerators, where neutrinos are not produced from accelerated parents. One example of traditional neutrino beam is shown in figure 1.18, the CERN neutrino beam produced for the experiment CHORUS and NOMAD.

1.4.1 Oscillation signature: wrong sign muons

Let suppose that the NuFact accelerates and stores μ^- . They decay via $\mu^- \rightarrow e^- + \bar{\nu}_e + \nu_\mu$.

If $\bar{\nu}_e$ oscillate into $\bar{\nu}_\mu$, the charged current interaction of $\bar{\nu}_\mu$ in the detector will create a μ^+ , while the interaction of ν_μ from the NuFact beam will generate a μ^- . The $\bar{\nu}_e$ oscillation signature is the detection of a *wrong sign muon*, a muon of charge opposite to that of the muons stored in the decay ring.

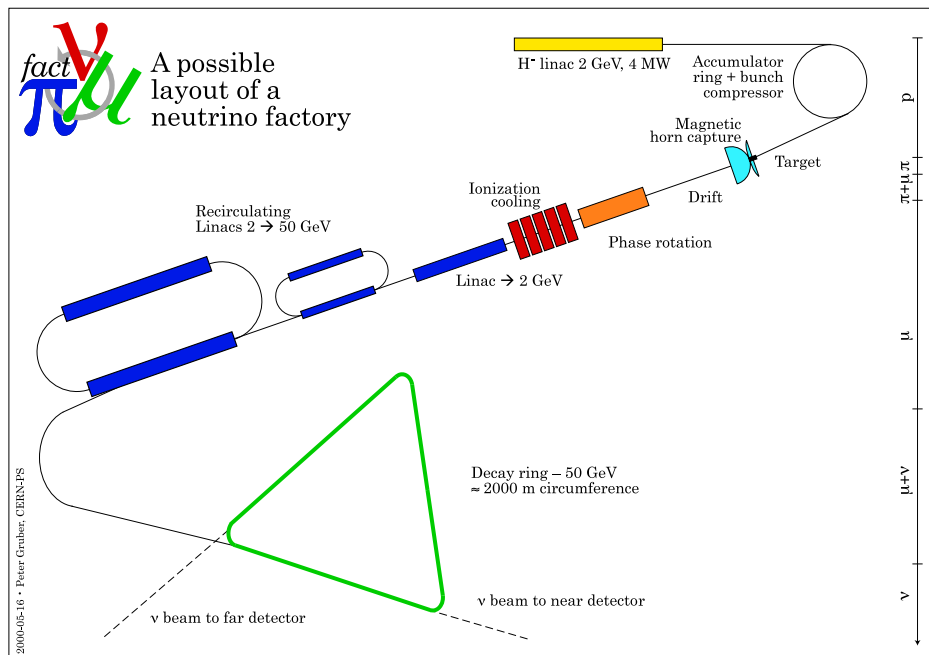


Figure 1.17: *CERN Neutrino Factory accelerator complex layout (not to scale).*

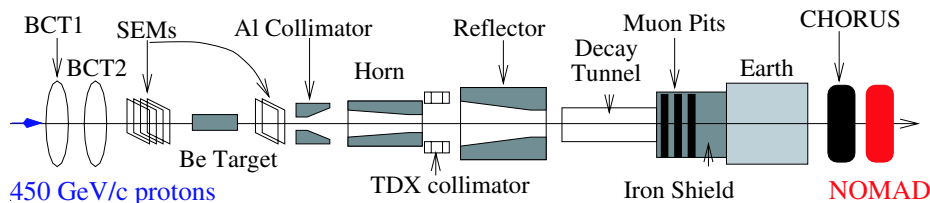


Figure 1.18: *Neutrino beamline scheme of the WANF (West Area Neutrino Facility) at CERN.*

The charge separation between wrong sign muons is possible using a large magnetized detector[17]. This signature is much more difficult in traditional human-made neutrino beams produced by pion and kaon decay because those beams contain a large fraction of the two flavors neutrinos and antineutrinos at the same time (see figure 1.19) and the fraction of $\bar{\nu}_e$ is very small compared to the other flavour in the beam.

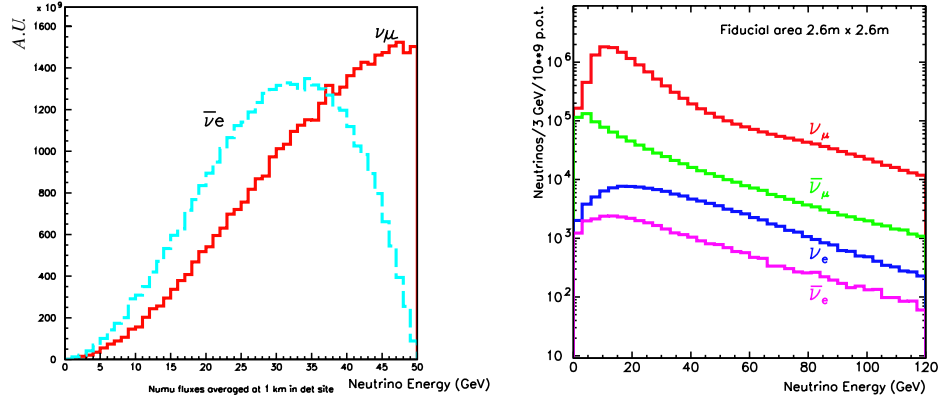


Figure 1.19: *NuFact flux (right) compared to the WNF neutrino beam[16] (plots in different scales).*

1.4.2 Machine parameters choice

The challenging physics requirements set stringent limits for the accelerator design and constraints on different NuFact parameters, which are discussed in the following.

The first two parameters are the neutrino energy and the neutrino flux

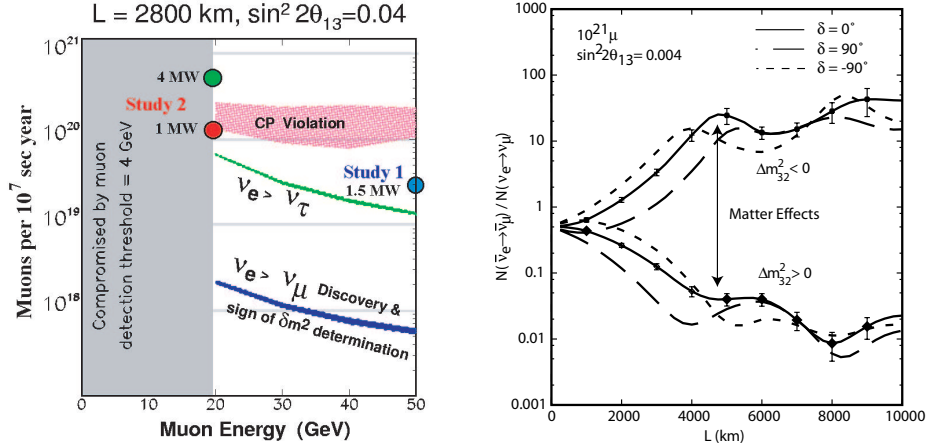


Figure 1.20: *Physics reach versus beam intensity and energy (left, [18]) and baseline influence on the mass splitting recognition and CP measurements (right)[17]*

intensity. Both are limited by technology and costs, while from the physics point of view they should be as high as possible: figure 1.20 (the left side[18]) describes the different physics possibility for different combinations of neu-

trino energy and neutrino flux. The observation of the CP violation requests a machine that can provide at least a few 10^{20} muons per year of energy greater than 20 GeV.

The third important parameter is the distance of the far detector, first because the detector should be placed far enough to have a large oscillation probability, second because the neutrino interaction with matter will discriminate the sign of Δm_{23}^2 , finally because the magnitude of CP violating asymmetry is distance dependent.

As described in section 1.2.6, ν_e interacts differently from the other neutrino flavors since ordinary matter contains electrons, but no muons or taus. An electron neutrino can interact with proton, neutrons and electrons via neutral current, as the other flavours, but it can interact also with the electrons via charged current. This picture corresponds to the case of propagation of polarised light (the polarisation component corresponds to a neutrino flavor) into a medium that has a different refraction index for the different polarisation components. The light enters the medium with a given polarisation and emerges with a different polarisation; for the neutrino propagation in matter this corresponds to a different oscillation probability between traversing matter (MSW effect) or going through vacuum.

The variation of the oscillation probability depends on the sign of Δm_{23}^2 and it is different for neutrinos and antineutrinos. In figure 1.20 is represented as function of distance, the ratio between the $\bar{\nu}_e \rightarrow \bar{\nu}_\mu$ and the $\nu_e \rightarrow \nu_\mu$ oscillation probabilities. This ratio changes with the distance and with the sign of Δm_{23}^2 and this ratio constitutes the CP violation. As shown in ref.[17], an appropriate distance to disentangle the CP violation from the sign of Δm_{23}^2 is between 2000 and 4000 km because at longer distances CP violation is obscured by matter effects. Furthermore such distances require an unacceptable slope for the muon storage ring straight sections.

Considering for example the CERN site for the neutrino factory, possible detector locations are shown in figure 1.21. One far detector could be placed at the Gran Sasso Laboratories at a distance of ≈ 700 km and the far one in the Canary Island or in the North Pole region.

1.5 Overview of the Neutrino Factory acceleration complex

1.5.1 Proton driver

The first element of the NuFact is the proton driver. In the CERN scheme H^- ions are accelerated using a Superconducting Proton Linac (SPL) to a

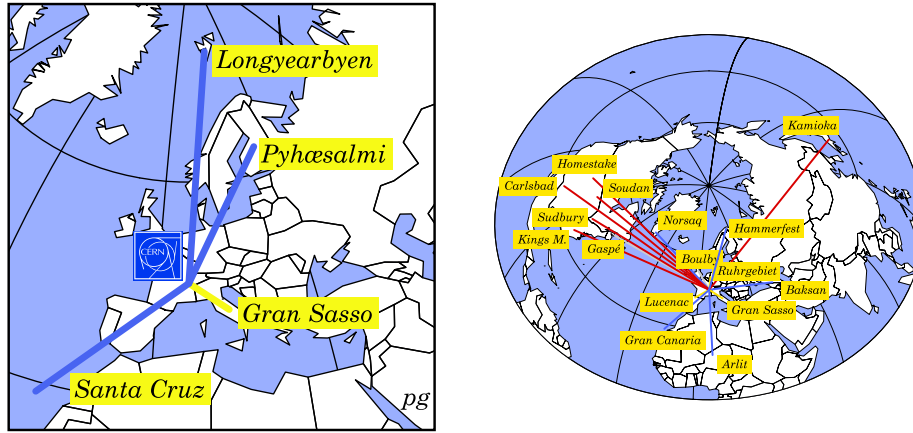


Figure 1.21: Different detector locations are already identified in Europe around CERN, but after all the entire world could be a nice playground.

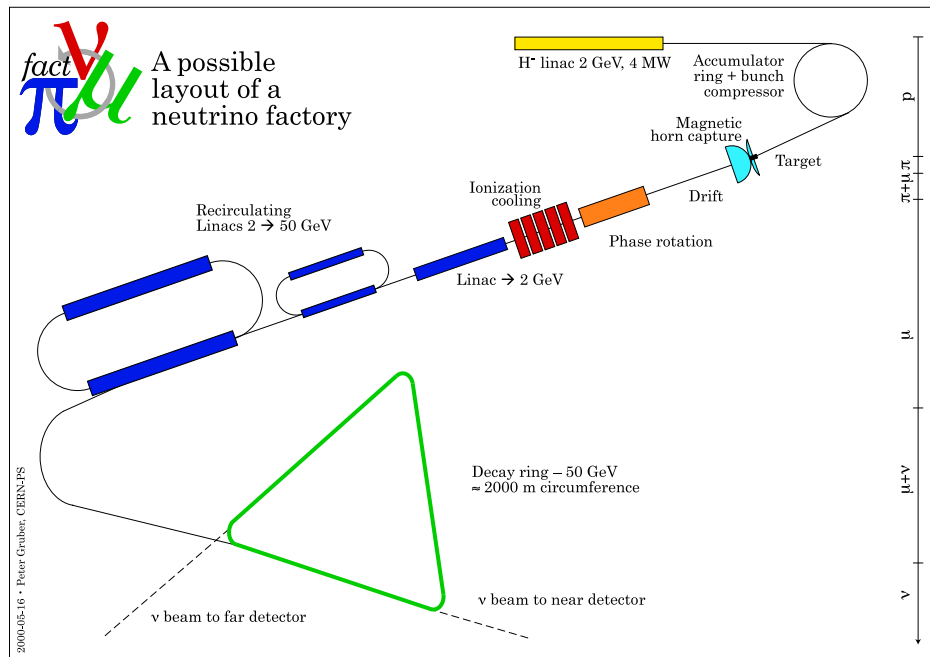


Figure 1.22: Neutrino Factory accelerator complex layout (not to scale).

kinetic energy of 2.2 GeV[13]. The maximum reasonable proton beam power technically feasible is around 4 MW, even if the SPL in continuous mode could possibly reach ≈ 20 MW. However the 4 MW is considered to be the reasonable upper limit for the realization of the target station. This power corresponds to $\approx 10^{16}$ protons per second or $\approx 10^{23}$ protons per year at 2.2 GeV. The typical rate proton/muon conversion is around 1% and

1.5. OVERVIEW OF THE NEUTRINO FACTORY ACCELERATION COMPLEX³¹

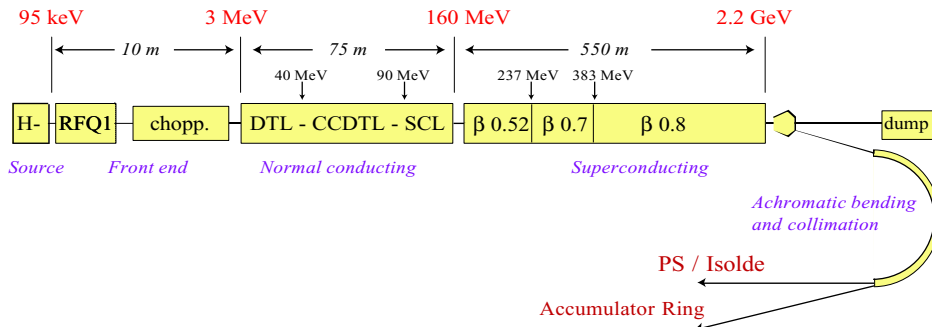


Figure 1.23: *Conceptual design of the SPL.*

the flux of neutrinos from muon decay for the oscillation experiments is estimated around 10^{20} neutrinos per year.

The SPL (see figure 1.23) is composed of a room-temperature low energy section (until 160 MeV), followed by a series of superconducting acceleration modules to reach 2.2 GeV. The SPL injects the stripped H^- into two rings, the first to accumulate protons and the second to compress them in 1 ns (1σ) bunches before the interaction with the target.

The proton driver time structure is a key point in the design of the proton driver. Protons are divided in micro-bunches which form a series of macrobunches (see figure 1.24). The length of a macrobunch is defined by the

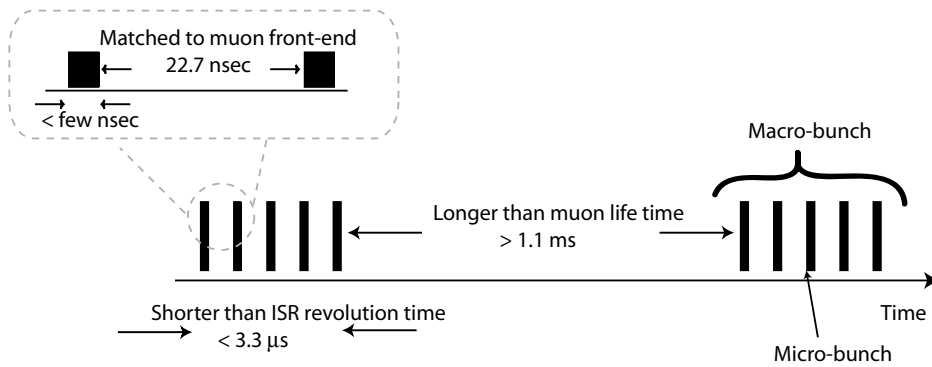


Figure 1.24: *Sketch of the proton driver time structure.*

length of the shortest circular accelerator. The shortest rings in the NuFact accelerator chain are the accumulator and compressor of the proton driver, which have to fit in the 1 km circumference ISR tunnel. The time for a revolution in this tunnel is $\approx 3.3 \mu\text{s}$, which is then chosen as the macro-bunch

length.

The distance between two different macro-bunches is defined by the muon life time in the decay ring. The muon life time at rest is $\approx 2.197 \mu\text{s}$ that is increased by the Lorentz boost at 50 GeV, which is the muon final energy, to $\approx 1.1 \text{ ms}$. The distance between the first micro-bunch of two successive macro-bunches has been chosen to be twenty times more the muon life time, 20 ms which implies that the repetition rate of the accelerator complex is 50 Hz.

The time structure of the micro-bunches which composes every macro-bunch has to be matched to the muon frontend. In the CERN reference scenario, as described in the following, the chosen frequency for the muon longitudinal phase space manipulation is 44 MHz. The micro-bunches are then spaced by 22.7 nsec, which means that in a macro-bunch 3.2 μs long there is space for 146 micro-bunches, 6 of which are left empty and used for the kicker rising time.

Every micro-bunch has a length, after the accumulator ring, of 15-17 nsec (4σ) which has to be reduced to minimize the longitudinal emittance of the pion and muon beam. The role of the second ring, the compressor, is to compress the time spread to 6 nsec (4σ), by a proton phase rotation (see chapter 6 for the definition of the phase rotation process). Figure 1.25 summarize the proton time structure.

1.5.2 Target

Protons impinge on a target to produce pions. The main challenge of this system is to sustain 4 MW and a high proton pulse repetition rate in a volume that cannot exceed the one of roughly a pint of beer (L=30 cm and 1 cm radius) since a bigger target will decrease considerably the efficiency of the pion collection system. The baseline material chosen is mercury because it has a high Z, which means high pion production per unit of length, it is liquid at room temperature and it can be easily replaced at every proton shot (50 Hz, see figure 1.25 for the proton time structure), while a solid will not survive more than few proton pulses impacts. A number of experiments have been performed to measure the speed of the mercury explosion induced by the proton energy deposition [22] (see figure 1.26). The speed required to change the target for every shot is estimated around 20 m/s, and the transverse speed of the Mercury drops generated by the explosion is around 30 m/s.

The integration between target and the focusing system is still a design issue for the target station. Another major difficulty in evaluating the best target material comes from the large uncertainty on the pion production and in-

1.5. OVERVIEW OF THE NEUTRINO FACTORY ACCELERATION COMPLEX³³

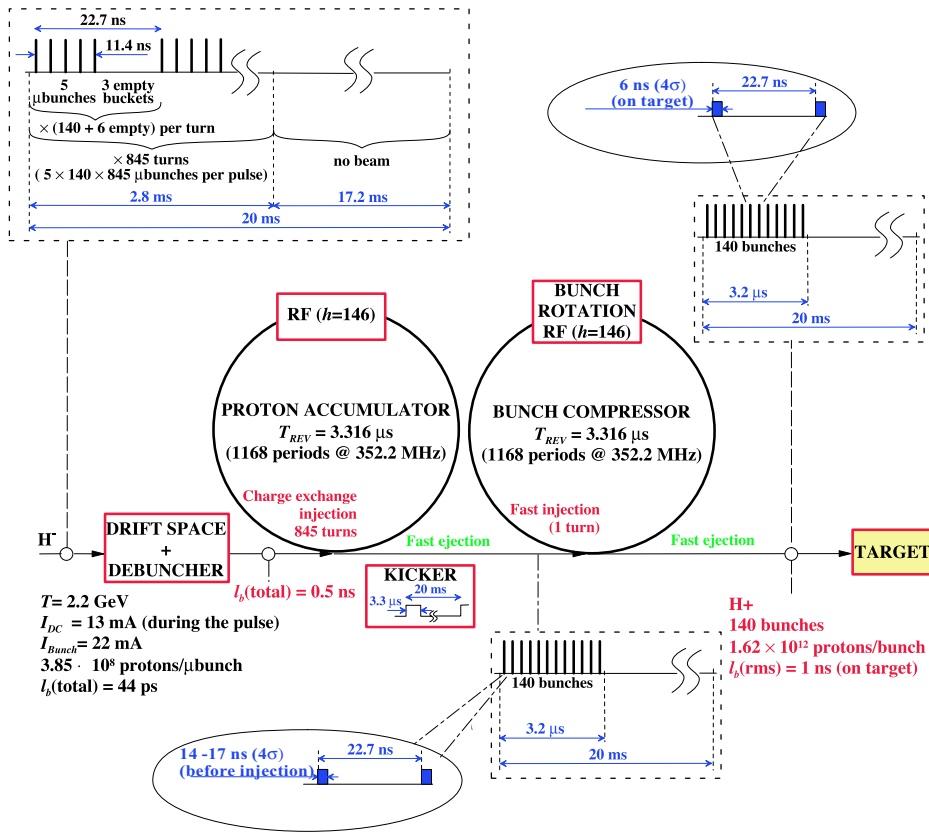


Figure 1.25: Proton driver detailed time structure.

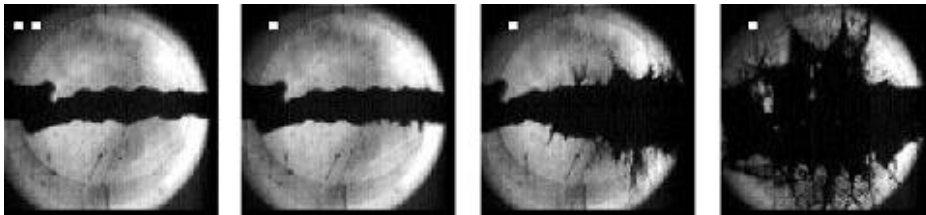


Figure 1.26: Mercury jet explosion due to proton impact. The time increases from left to right while protons are coming from the right part of each picture.

teraction cross section for the range of proton beam energies between some hundred MeV and few GeV. The data taken by the Harp experiment[64] will provide new measurements with a precision of a few percent and should allow a clarification of the best material to be used for a given proton energy. A more detailed description of the different targets proposed for the neutrino factory is discussed in chapter 2.

1.5.3 Horn

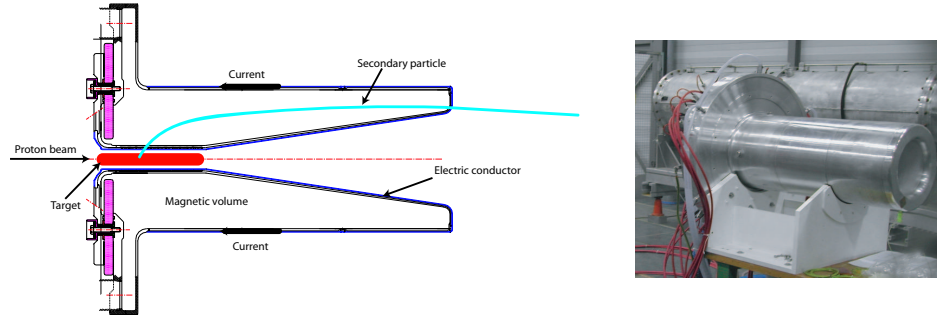


Figure 1.27: *Horn concept (left) and prototype of NuFact horn.*

A magnetic lens called a horn focuses pions produced in the target. A horn consists of two concentric conductors, which delimit a closed volume. The current of the order of few hundreds kA, pulsed at 50 Hz running in the conductors generates in that volume a toroidal magnetic field whose intensity decreases proportionally to the distance from the horn axis. Pions entering in the magnetic volume are bent by the field and focused in the direction of the decay channel section (see figure 1.27). The sign of pion charge is selected by the current polarity, changing in this way the sign of the muons in the machine. The major limitation of the system comes from its short life-time, estimated around 6 weeks, mainly due to thermal and mechanical stresses induced by the high repetition rate[24]. A more detailed description of the horn is presented in chapter 3.

1.5.4 Decay channel and phase rotation

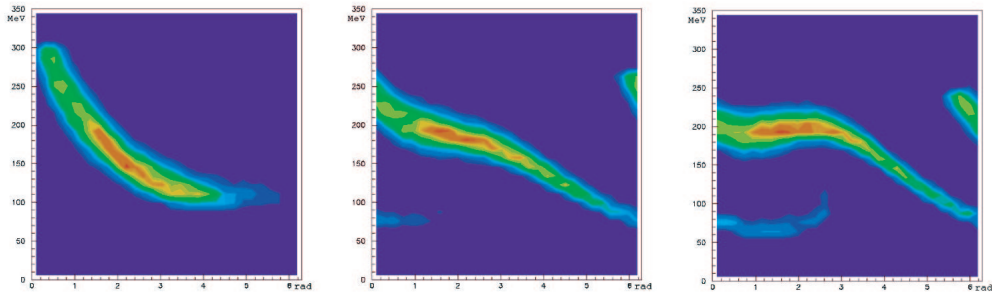


Figure 1.28: *Longitudinal phase space of muons during the phase rotation.*

Pions injected into a solenoidal decay channel have a large energy spread which will be transmitted after the decay $\pi^+ \rightarrow \mu^+ + \nu_\mu$ ($\pi^- \rightarrow \mu^- + \bar{\nu}_\mu$) in the energy distribution of the muons. Moreover pions are not ultrarelativistic, since the average energy is around 200 MeV, this means that to the energy spread corresponds to a velocity spread. At the end of the decay channel muons at higher energy will arrive before the less energetic ones. The building of the time-energy correlation can be used to reduce the energy spread with a series of RF. The RF phases are tuned to slow down the more energetic muons, which arrive earlier, and to accelerate the less energetic ones, which arrives later.

The typical result after 30 RF cavities at 44 MHz, 2 MV/m can be seen in figure 1.28: at the beginning of the channel pions have a banana distribution in the longitudinal phase space, and at the end of the channel muons are rotated around 200 MeV and the density of particles around 200 MeV is increased. A more detailed discussion of the phase rotation is presented in chapter 6.

1.5.5 Cooling

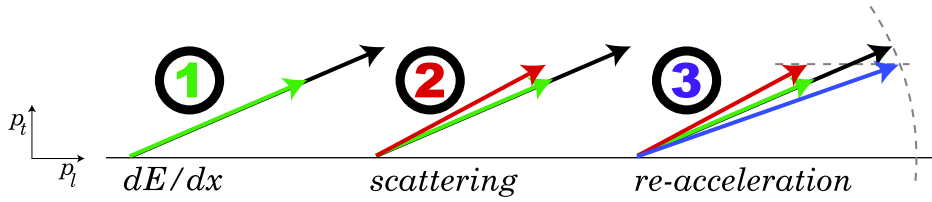


Figure 1.29: *Cooling principle sketch.*

After the phase rotation the transverse phase space dimensions (radius and angular divergence) are still too large to be accepted by a conventional accelerator: the beam has to be transversally cooled. Traditional techniques like stochastic cooling or the electron cooling are too slow compared to the mean life-time of a muon ($\tau = 2.19$ ms at rest), even for ultrarelativistic energies, and a faster process, called ionisation cooling, is used.

Ionisation cooling involves three elements: solenoids, absorbers, RF cavities. The beam is confined by a series of solenoids whose focal point is centered into an energy absorber of low Z material, like liquid hydrogen. Muons lose momentum in all directions passing through the material, while the accelerating RF system placed after the absorber restores only the longitudinal momentum, thus reducing the divergence of the beam (see figure 1.29).

As first approximation the relative reduction of the transverse phase space is

equal to the relative energy losses in the absorber. Liquid hydrogen is preferred for the absorber material, to keep the beam heating due to multiple scattering as low as possible.

The principle of ionisation cooling was invented 20 years ago [?], but no experiment was ever tried in the past to demonstrate the feasibility of a part of a cooling machine. The MICE experiment will test a section of the cooling channel of the NuFact [25].

1.5.6 Acceleration and storage ring

After the cooling section, muons are injected in a series of two recirculating linacs and accelerated to the final energy of 50 GeV. Then they feed into the triangular storage ring. This shape is chosen to have two preferred decay directions pointing towards two experimental sites, one at short distance (≈ 700 km), and the other at far distance (≈ 3000 km).

1.5.7 Detector and far location

Two locations are already identified inside Europe, namely the Gran Sasso Laboratories in Italy and the Canaria Island in Spain. The best detector candidates are a 40 kT iron magnetized calorimeter or a magnetized Liquid Argon TPC. The magnetic field of the order of 1 T will offer enough charge separation (roughly 10^{-4}) to distinguish the wrong sign muon signal from the background.

1.6 Superbeam

A first step before building the complete complex of the NuFact could be a neutrino SuperBeam, a conventional neutrino beam produced by the 4 MW SPL beam.

Existing man-made neutrino beam, described in the following, uses a proton driver of a delivered power of few kW to produce pions and kaons. After being focused by a horn, the decay of those mesons produces a neutrino beam suitable for oscillation experiments.

The K2K [26] project, for example, uses neutrinos at a mean energy of 1.4 GeV from the decay of pions and kaons produced by the KEK 12 GeV proton synchrotron to test the atmospheric oscillation $\nu_\mu \rightarrow \nu_\tau$. Two detectors located at different distances are used. The near one, located at the KEK site, studies neutrino beam spectra and cross sections, and the SuperKamiokande detector at 250 km verifies the oscillation hypothesis.

The neutrino energy is below the τ production threshold, hence it is not possible to search directly for τ appearance. The disappearance of ν_μ measured by the experiment so far is compatible with the atmospheric oscillation. K2K is presently in the process of data taking.

Future research on $\nu_\mu \rightarrow \nu_e$ oscillations is starting at Fermilab with Mini-BooNE (Booster Neutrino Experiment) [14] which is the first phase of the high sensitivity experiment BooNE. Neutrinos are produced using the 8 GeV high intensity proton beam from the Fermilab Booster synchrotron. The beam consists mainly in ν_μ from π^+ decay with a broad energy from 0.3 to 2 GeV. The MiniBooNE detector is installed at 500 m from the neutrino source.

Other experiments will start in the near future to test oscillations, in particular $\nu_\mu \rightarrow \nu_\tau$, at even longer distances.

The NuMI [27] project uses neutrinos from the decay of pions and kaons produced by the Fermilab Main Injector (MI), a 120 GeV proton synchrotron. The expected number of protons on target is $3.6 \cdot 10^{20}/y$. The detector of this experiment will be located in the Soudan mine at a distance of 730 km from the proton target.

The MINOS [27] experiment (Main Injector Neutrino Oscillations Search) will use two detectors, a near one at Fermilab and another one to be built at the Soudan site. Both detectors are iron-scintillator sandwich calorimeter with a magnetic field in the iron plates. The comparison between the fluxes measured by the two will be sensitive to neutrino oscillations.

The CNGS project consists in a neutrino beam from the CERN 450 GeV SPS to the LNGS (Laboratori Nazionali del Gran Sasso, Italy) at a distance of 732 km. The detailed description of the beam design can be found in [28]. However, none of those experiments has the sensitivity to measure from the oscillation $\nu_\mu \rightarrow \nu_e$ the angle θ_{13} or to give a first hint about leptonic CP violation as the SuperBeam.

As described above the SuperBeam is a conventional neutrino beam generated by the first part of the NuFact complex, which is composed by the SPL, the accumulator ring, the target, and the horn. The pion focused by the horn are sent to a 100 m long decay tunnel where a ν_μ neutrino beam of few hundred MeV is generated (see figure 1.30 for the spectrum). As explained in more details in chapter 4, the flux can be composed alternatively by neutrinos or antineutrinos, by selecting the charge of the pions focused by the horn. This allows the measurements of both oscillation probabilities $P(\nu_\mu \rightarrow \nu_e)$ and $P(\bar{\nu}_\mu \rightarrow \bar{\nu}_e)$, and it gives the possibility to have a first hint about leptonic CP violation. The detector is located at the place where the maximum of the oscillation occurs, which is between 100 km and 130 km for the neutrino Superbeam spectrum shown in figure 1.30. At 130 km from CERN, located

in the car Frejus tunnel, there is the Underground Modan Laboratory, which after an important enlargement, could host the new 1 Mton water Cerenkov detector which is required by the Superbeam physics. Table 1.2 summarizes

	ν_μ	$\bar{\nu}_\mu$
Neutrino flux ($\nu/\text{m}^2/\text{yr}$)	$4.78 \cdot 10^{11}$	$3.33 \cdot 10^{11}$
Neutrino average Energy	0.27 GeV	0.25 GeV
CC events	36698 (2 yrs)	23320 (8 yrs)
Oscillated	1279	774

Table 1.2: *Summary of the Superbeam parameters taken from [19]. Event rate calculated with 4400 kt-y exposure. The oscillated events are calculated with the same values used in section 1.2.5 but with $\theta_{13} = 10^\circ$.*

the parameters of the Superbeam.

The experiment is assumed to run for 10 years, two of which for neutrinos and eight for antineutrinos. This asymmetry in the running time comes from the fact that the beam of antineutrinos is produced by negative pions, which are produced less effectively compared to positive pions in the condition chosen for the experiment (see chapter 2). Moreover the antineutrino interaction, which at this energy is dominated by quasi elastic scattering, is a factor at least 2 lower compared to neutrinos.

Under this assumption, figure 1.8 shows the performances of the Superbeam for the measure of θ_{13} compared to NuFact.

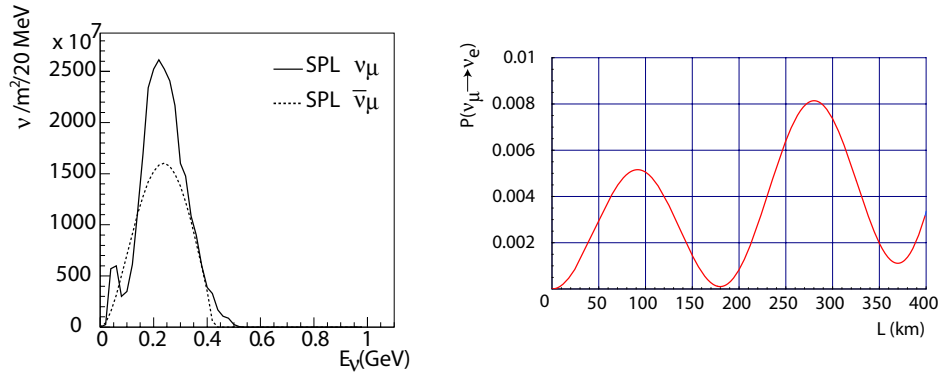


Figure 1.30: *Superbeam neutrino and antineutrino flux computed at 130 km from the SPL (left) and oscillation probability (right). The oscillation probability is calculated with the same values used in section 1.2.5 but with $\theta_{13} = 10^\circ$ and for 270 MeV neutrinos.*

1.7 Beta Beam

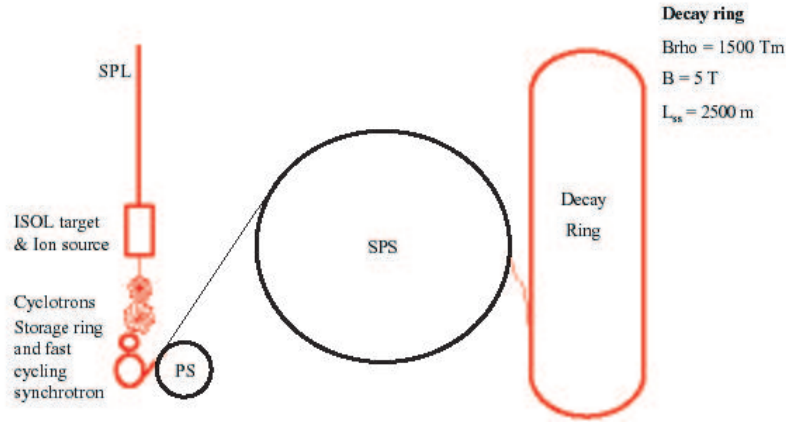


Figure 1.31: *Beta beam complex conceptual design.*

A novel concept for low energy ν_e and $\bar{\nu}_e$ production has been proposed in [51]. The idea is to produce a pure and well defined beam of high energy electron neutrinos (or antineutrinos) from beta decay of high energy radioactive isotopes.

The beta decay of the high energy nuclei, of $\gamma \approx 100$, creates a highly collimated low energy neutrino beam of few hundred MeV (see figure 1.32), which can be used for a medium base line experiment such as a SuperBeam. In par-

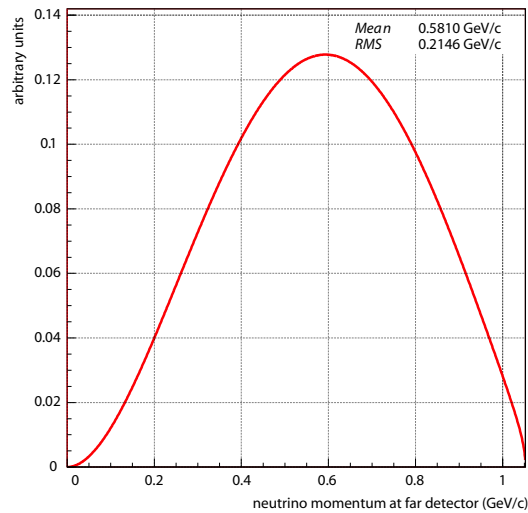


Figure 1.32: *Spectrum of ν_e generated by ${}^6\text{He}$ decay.*

ticular, the beta beam experiment aims to measure, with the same megaton

water Cerenkov detector as the Superbeam, the oscillation $\nu_e(\bar{\nu}_e) \rightarrow \nu_\mu(\bar{\nu}_\mu)$ which completes the measurement of the Superbeam $\nu_\mu(\bar{\nu}_\mu) \rightarrow \nu_e(\bar{\nu}_e)$. The combination of those two measurements can test at the same time the leptonic CP violation and direct T violation. The summary of the beta beam parameters is presented in table 1.3.

The beta emitters chosen to generate the electron neutrinos (antineutrinos) are the ${}^6\text{He}$ and the ${}^{18}\text{Ne}$, which decay according to



The beta beam complex is based on the existing CERN main accelerator

	${}^6\text{He}$	${}^{18}\text{Ne}$
Ions	$1.0 \cdot 10^{14}$	$4.5 \cdot 10^{12}$
γ	60	100
Neutrino flux ($\nu/\text{m}^2/\text{yr}$)	$1.97 \cdot 10^{11}$	$1.88 \cdot 10^{11}$
Neutrino average Energy	0.26 GeV	0.36 GeV
CC events	19710	144784
Oscillated	612	5130

Table 1.3: *Summary of the Beta Beam parameters taken from [19]. Event rate calculated with 4400 kt-y exposure. The oscillated events are calculated with the same values used in section 1.2.5 but with $\theta_{13} = 10^\circ$.*

chain completed with new accelerators for the radioactive isotope production, acceleration and storage (see figure 1.31).

Only 0.6% of the proton beam of the SPL, which can deliver at maximum 4 MW in pulsed mode, is needed on the target to produce the isotopes. The isotopes, generated as described in chapter 2, are accumulated before being injected into the CERN PS, then accelerated and injected into the CERN SPS. In the SPS ions reach the final γ of ≈ 100 and they are transferred into the decay ring.

The time structure of the ≈ 10 ns long bunches in the decay ring is imposed by the rejection of the atmospheric background for the neutrino detection. A more detailed description of the ions production for the beta beam, in particular of ${}^6\text{He}$ is presented in chapter 2.

Chapter 2

Target

The proton beam of 4 MW delivered by the proton driver impinges on a target and produces, together with all the other secondaries, pions. These pions are focused by the collection device, either a horn, according to the CERN reference scenario, or a solenoid, used in the US machine design.

The major issue for the target design is how to sustain the proton power of 4 MW, considering that roughly 1 MW remains in form of deposited energy inside the target material itself.

2.1 Target material for pion production

The requirements for the neutrino factory target from the particle production point of view are the following:

- large pion production to reach the intensity goal of 10^{21} muons per year;
- as many negative pions as possible for the CP violation study;
- compact target to simplify the focusing system design and minimize the amount of irradiated material.

From past experience, target materials for secondary particle production are usually: carbon (CNGS), tantalum (ISOLDE) or mercury (SNS) (see table 2.1), thus these materials have been chosen as candidates for the Nufact target.

Material	Z	A	Melting point (°K)	λ_I (cm)	density(g/cm ³)
C	6	12	3800	38.1	2.265
Ta	73	180	3290	10.4	16.650
Hg	80	200	628	13.0	13.570

Table 2.1: *Target material properties. The “melting point” for Hg stands for boiling point. λ_I is the nuclear interaction length for 2.2 GeV protons computed by MARS.*

The simulation of pion production is the first step to decide whether a material generates enough pions for the neutrino factory purposes. As described in the introduction chapter, the energy of the CERN proton driver has been chosen to be 2.2 GeV. For such a low energy the main process for pion production is the decay of a Δ resonance produced by the impinging of the primary protons on a target nucleon. The MARS Monte Carlo code[98] is used to simulate the pion production. In the range of energies between 0.5 MeV and 1 GeV, MARS contains a data driven model (see ref [39] for more details) to simulate the proton-nucleon interaction and the generation of pions.

The comparison between the three materials is performed considering cylindrical targets of one interaction length (λ_I) and with a radius of 0.75 cm. The impinging proton beam has a kinetic energy of 2.2 GeV, with a gaussian transverse size of 0.22 cm (1 sigma). The primary beam divergence is zero and all the protons are impinging at the same time. All particles, primaries and secondaries, are counted by fictitious detectors located on the sides of the cylinder.

The spectrum of positive and negative pions produced in the three different cases is presented in figure 2.1. The shape of the spectrum is very similar for the three materials: a peak at low momentum (low kinetic energy) which represents the Δ decay mostly at rest is followed by a shoulder for the case in which the Δ decays in flight. Even if pions at low momentum are more (around 100 MeV/c) abundant, the Neutrino Factory capturing device is designed to collect the higher energies (around 400 MeV/c), since the muons created by low energy pions will decay too quickly to be effectively manipulated before being accelerated. The transverse momentum distribution (see figure 2.2) presents again a similar distribution for the three cases, meaning that the focusing device required to capture pions can be in principle the same for the different materials.

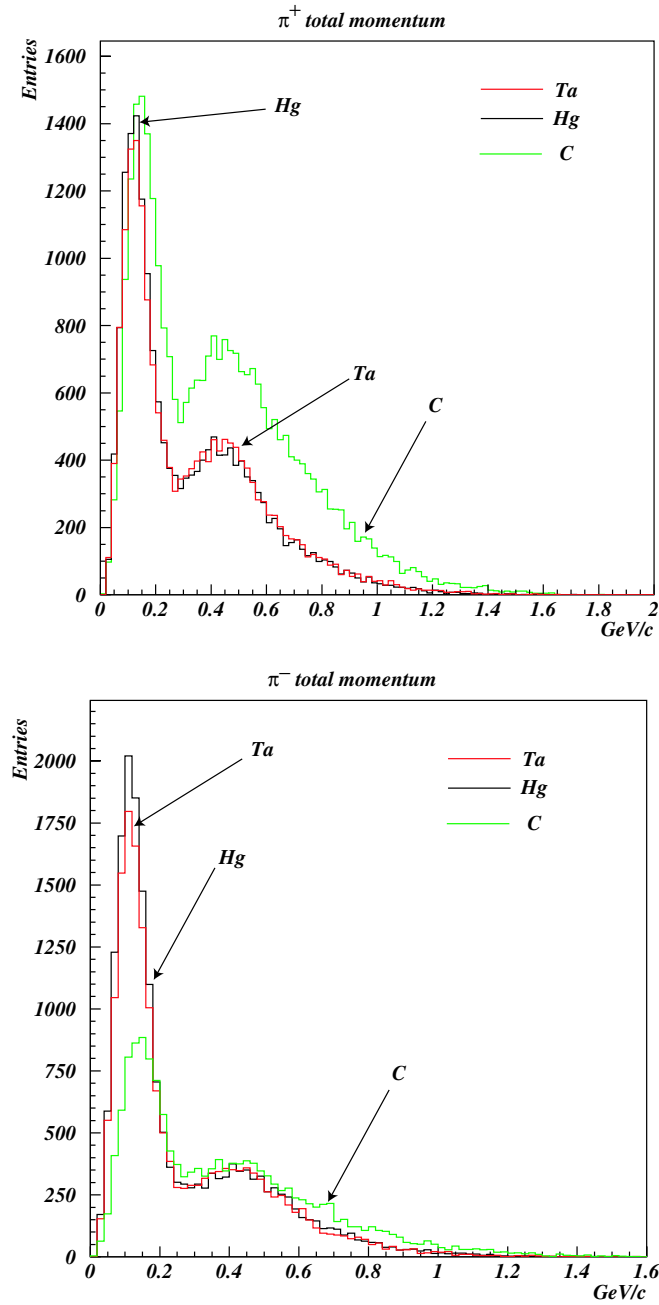


Figure 2.1: Total momentum spectrum for positive (top) and negative pions (bottom) for carbon, tantalum and mercury for 100000 impinging 2.2 GeV protons, on a target of $1 \lambda_I$

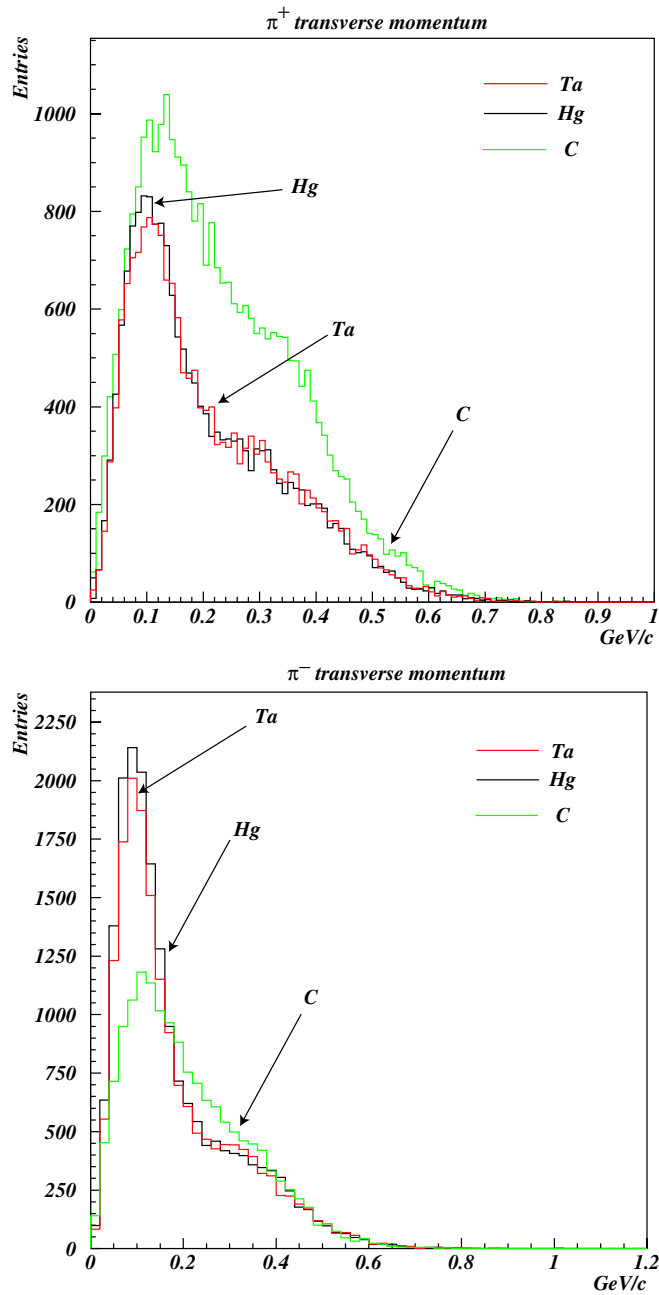


Figure 2.2: Transverse momentum for positive (top) and negative (bottom) pions for 100000 2.2 GeV impinging protons, on a target of $1 \lambda_I$.

As can be seen from table 2.2, carbon has the highest positive pion production. However, the ratio between negative and positive pions is different from

Material	π^+ per p.o.t.	π^- per p.o.t.
C	0.30	0.153
Ta	0.183	0.174
Hg	0.185	0.186

Table 2.2: Pion yields by 2.2 GeV protons computed by MARS. p.o.t. (p.o.t. = proton on target).

one: the negative pions are only half of the positive. There is an even more

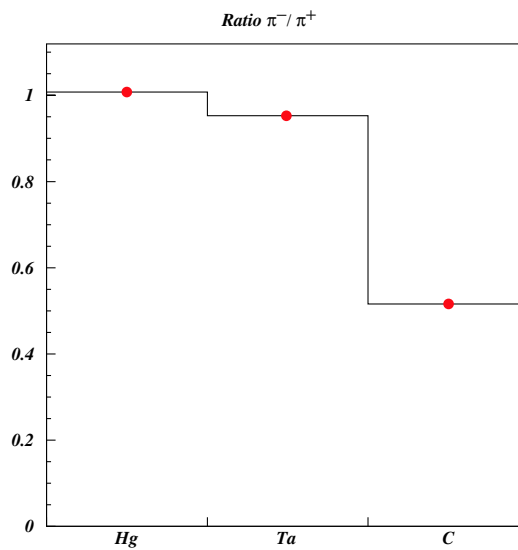


Figure 2.3: Negative over positive pions ratio for carbon, tantalum and mercury.

important disadvantage for the choice of the carbon. The carbon nuclear interaction length is 38.1 cm, while for mercury is 13 cm: in the first case pions are produced along a very long target. The time spread induced by a long target (see figure 2.4, where the width of the different curves represents time spread of positive pions), if larger than 0.5-1 nsec, will cause large muon losses during the phase rotation and the bunch to bucket injection, as described in chapter 6, would become less effective. The proton bunch length, which determines also the pion and hence the muon bunch length, is compressed in the second proton driver ring below 3 nsec (1σ) to reduce the effect of the pion drift and decay on the final muon time structure. A further muon bunch lengthening due to the target dimension requires a different design of the phase rotation from the one chosen in the CERN design.

However carbon could be considered as a good candidate for the superbeam

where the time structure is not such an issue even if a long target requires a long capturing device, causing an even more difficult design of the horn.

For these reasons mercury or tantalum are preferred as compact pion source.

The Monte Carlo simulation of the particle production and interaction can

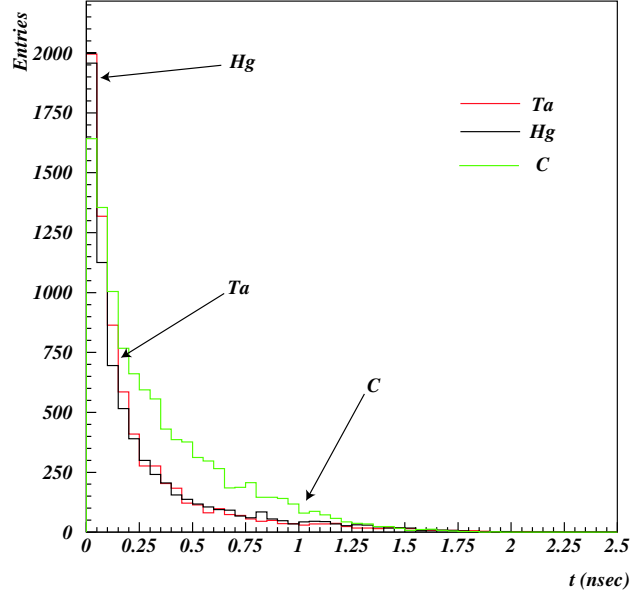


Figure 2.4: *Time distribution of positive pions for different materials selected in a total energy range between 0.2 and 0.5 GeV and for 100000 impinging protons.*

estimate the energy deposition inside the target.

For a 4 MW SPL, delivering macrobunches of 2.2 GeV, $2.26 \cdot 10^{14}$ in $3.2 \mu\text{sec}$, the power dissipated into the target is roughly 1 MW, causing a sudden temperature increase in the material. Figure 2.5 shows such increase from room temperature for carbon, tantalum and mercury, along the target axis, and it reveals a different behavior for the three cases. Tantalum and carbon have a high melting temperature, around 3500 degrees, and a single proton pulse cannot melt the material. However, for a proton pulse repetition rate of 50 Hz, an unavoidable pile up of the temperature causes a quick degradation of the material. For this reason the target has to be cooled, and even with cooling the believed upper limit for the allowed maximum deposited power remains below 100 kW[31]. For this reason, target composed either of steady carbon rod or tantalum spheres are considered for an entry level neutrino factory with a proton power limited to 1 MW.

For mercury the situation is different. Protons deposit enough power to locally vaporize the material even with just one pulse. In this case the material

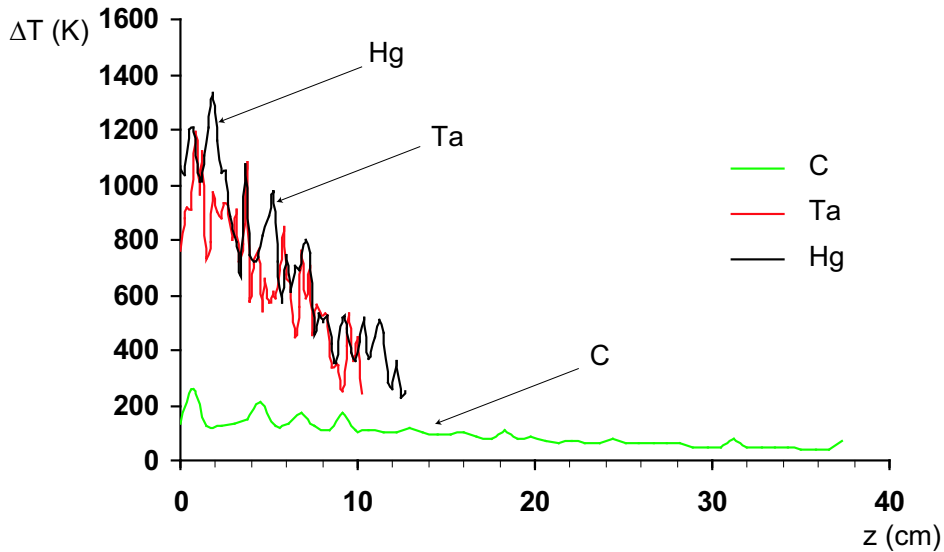


Figure 2.5: *Temperature increase from the room temperature after the impact of 2.2 GeV $2.26 \cdot 10^{14}$ protons on the different materials.*

collapses, causing a sort of explosion of the liquid due to the abrupt local phase transition. However, mercury has been chosen as the most appealing candidate for the CERN neutrino factory target, and the motivation for this choice is described in the following sections.

2.2 Target proposals

Starting from the choice of the materials described above, three main designs are proposed for the target of the Neutrino Factory:

- a liquid mercury jet.
The target is formed by a continuous jet formed like a fountain. In this way the target can be renewed with the same repetition rate as the proton pulses. Mercury is chosen for the baseline design of the CERN Neutrino Factory, and it will be discussed in more details in the next section;
- a rotating metal target[29] (figure 2.6).
The target is composed of a series of metal (Ti-Alloy or a Inconel-alloy) bands connected together to form a circle with a diameter of ≈ 5 m. The solid offered to the impinging proton beam is exchanged at every shot since the interaction region is displaced with the proper speed (at

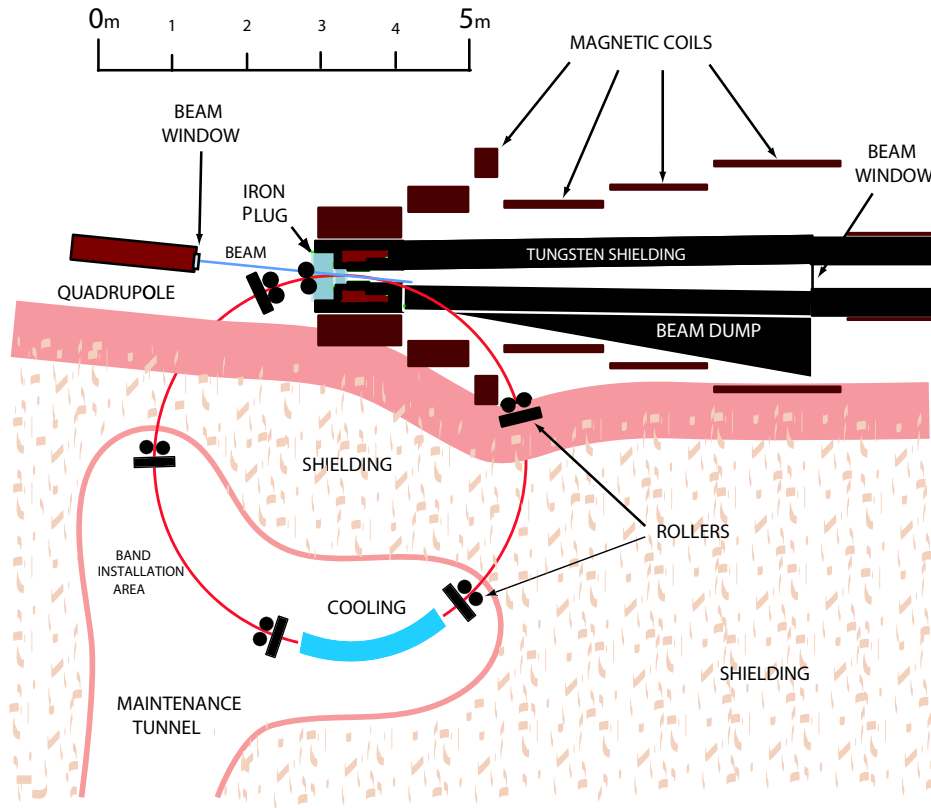


Figure 2.6: *Rotating metal band target.*

least few m/s for 50 Hz repetition rate). The deposited energy is diluted on a large volume.

The main disadvantages of such a target is the large dimension required to host the band and the mechanical stability during rotation. Moreover the rotating band seems to be difficult to integrate into a horn, hence it is not considered for the CERN Neutrino Factory study;

- a granular tantalum target[30].

The target is composed of small, 1 mm radius, tantalum spheres enclosed in a cylinder and cooled either by Superfluid Helium (see figure 2.7) or by liquid lithium.

This configuration would allow to cool the energy deposited by 1 MW proton beam, while the 4 MW case seems to be still an issue[30].

A conceptual design for the matching between the horn and the granular target has been proposed and is shown in figure 2.8.

This particular choice seems to be best the candidate for the four horn capture. This scheme, described in more detail in section 3.8, foresees

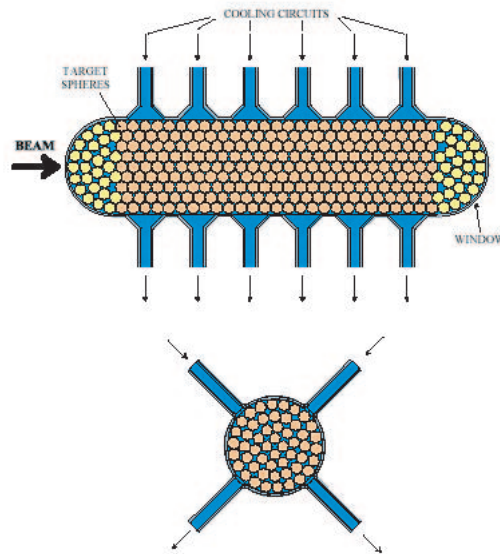
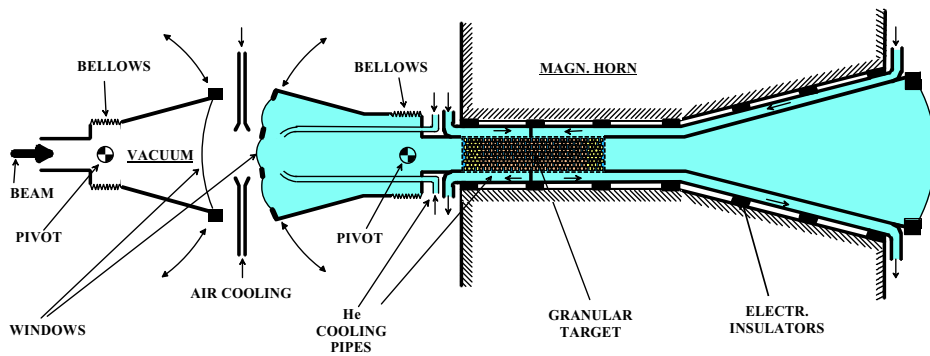


Figure 2.7: *Granular target conceptual design.*



P. SIEVERS - 23/05/2002

Figure 2.8: *Conceptual integration between the horn and a granular target.*

four target station and four horns. The proton beam is directed to a different target stations for every pulse. The main advantage for such a scheme is the reduction of the power losses per station, which is reduced by a factor of 4, since every target receives only a 1 MW proton beam.

2.3 Mercury Pros and Cons

The choice of mercury as favored target material comes from the a number of advantages over other materials as:

- high pion yield (high Z).
The pion production absolute rate is fundamental as a starting point for the total muon budget;
- high source brightness.
The dimension of the target has a major impact on the design of the focusing system. In the case of the horn, the perfect focusing is only possible using a point like source. For low primary proton energies and low energy pions, it is better to have a short target, hence a material with a short interaction length, like mercury.
In the case in which one prefers to use a solenoid for the capture, the length of the 20 T part has to increase according to the target length. The first practical problem encountered in this case is the increase in the cost of the solenoid, which scales in M\$ as $L^{0.662}$ [33] with L the solenoid length;
- flowing liquid metals have excellent power handling capabilities and have the capability to go to the highest power densities. This comes from the continuous renewal of the target material;
- no water radiolysis.
Since the target does not have to be cooled, the water radiolysis is limited to the water cooling system of horn, thus reducing the tritium production and the complexity of the installation;
- no target material fatigue limit caused by the radiation damage.
The radiation damage is together with the temperature rise the major limiting factor for the solid target life time. For example, in the case of the SNS target window, which can be considered as a solid target, the life time is limited to 5 dpa[†], which corresponds to two months of operation;
- no build up of dusty and pyroforic material.
From the nuclear reactor experience, where carbon is used as neutron moderator, one of the major concerns is to avoid a sudden energy release of the energy accumulated by atom dislocations. This kind of process can provoke carbon to take fire;

[†]dpa=displacement per atom

- liquid at ambient temperature thus no liquid-to-solid phase change issues;
- minimal waste stream compared to solid alternatives since the mercury is reused;
- most of the spallation products can be removed from the Hg by distillation;
- no confinement tubing or beam windows with lifetime limits caused by the radiation damage

The problem of mercury disposal can be solved by distillation to separate the most dangerous isotopes. The rest of the mercury left in liquid phase then can be solidified. The solidifying process is of common use and is similar to the process used to produce dental amalgams, which are a compound composed of 50% of mercury, 35% of Ag and the missing 15% is a mixture of Sn+In+Cu+Pd.

Mercury, however, presents also some disadvantages compared to a solid material:

- it is toxic;
- being a high Z material during irradiation will produce long-lived high Z radioactive isotopes;
- mercury is not compatible with a large number of materials. Mercury, for example, dissolves aluminum-oxides and hence cannot enter in direct contact with the conductors of a horn. The use of titanium or stainless steel windows or containers is required to solve this kind of issue;
- mercury is liquid at room temperature, hence one has to consider the unlucky case where a failure to the piping or pumping system occurs. This could be a major safety issue since radioactive losses, if uncontrolled, can cause serious damage to the target station and to the environment.

In the total budget between pros and cons, it seems that the advantages are so appealing to overcome the number of disadvantages. However, the construction of the mercury target station (see figure 2.17 for a conceptual design), which involves mainly the pumping system for the mercury jet formation, the pion focusing system, the mercury recuperation and the radiation shielding, requires careful design and a long R&D period, whose start is described in the next section.

2.4 Experimental measurement of Mercury explosion

An extensive series of measurements has been carried out to understand the dynamical behavior of mercury once exposed to a high current proton beam [34][†], to understand the feasibility of a liquid target and to test the results of the Monte Carlo calculation of the material heating.

As described in the previous section, the energy deposited by the high power proton beam and by the secondary particles causes the mercury jet explosion. The speed of the droplets generated by the jet disruption is a fundamental input for the design of the pion collection device. For this reason three different experiments, considered as three successive steps, have been realized to measure the dynamical behavior of a proton-induced mercury explosion.

The first two experiments were located at the ISOLDE target station at CERN. The proton beam accelerated by the BOOSTER up to 1.4 GeV impinges on one of the two ISOLDE front end (GPS or HRS on figure 2.10, top) where either a thimble target or a trough target is placed (figure 2.10, bottom). The third one, where a complete jet setup has been simulated, is not discussed here but can be found in [34]. A thimble target is composed of an explosion chamber enclosed by stainless steel walls and by two central windows (see figure 2.11, left). The 1.3 cm^3 of mercury are placed inside a cylinder with hemispherical base with a diameter of 1.2 cm, which is about 9% of the interaction length for protons at 1.4 GeV. The atmosphere is composed of Argon at the pressure of 1 bar.

The through target has the same configuration as the thimble target except that the 7.3 cm^3 of mercury are placed inside a 6 cm long gutter (about 46% of Mercury interaction length).

Both configurations are realized to study the vertical speed of the mercury explosion, with the advantage for the second case to measure also the displacement at different points along the proton axis. The second setup can

[†]Most of the plots of this section are taken from this reference

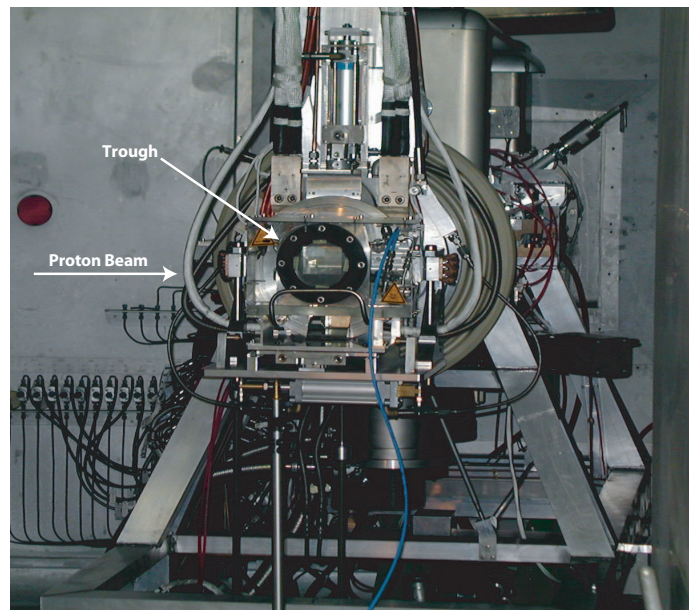
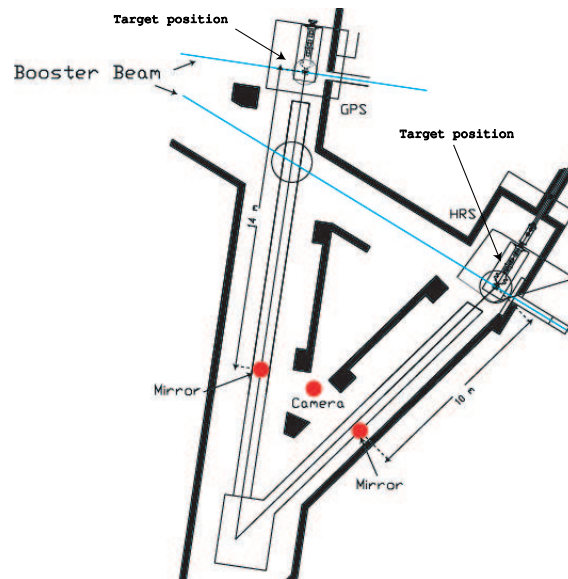


Figure 2.10: *ISOLDE facility target area with the experimental setup (top). The target is placed on one of the ISOLDE front-ends (bottom) with the BOOSTER proton beam coming from the left.*

be considered like a 2 dimension approach compared to the final behavior of a jet. The mercury droplet speeds are measured by a high speed cam-

2.4. EXPERIMENTAL MEASUREMENT OF MERCURY EXPLOSION 55

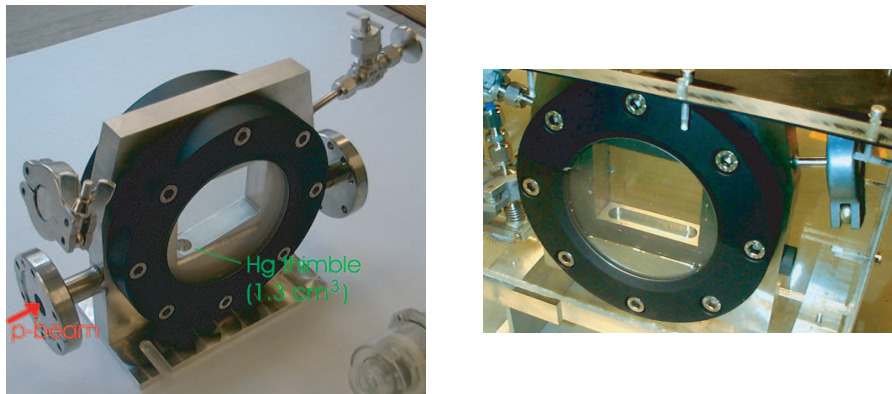


Figure 2.11: *Thimble empty target (left) and the trough empty target (right)*

era placed behind concrete blocks to reduce the risk of radiation damaging. The images of the mercury explosions are reflected by a system of mirrors to reach the hidden camera (see figure 2.10, bottom for a sketch of the experimental setup). The camera used is a Olympus Industrial Encore PCI 8000s which can record 8000 frame per second with a shutter opening time of $25 \mu s$. From the analysis of the images is possible to extract the displacement of the front of the mercury splash at each photo frame and extract the speed of the droplets.

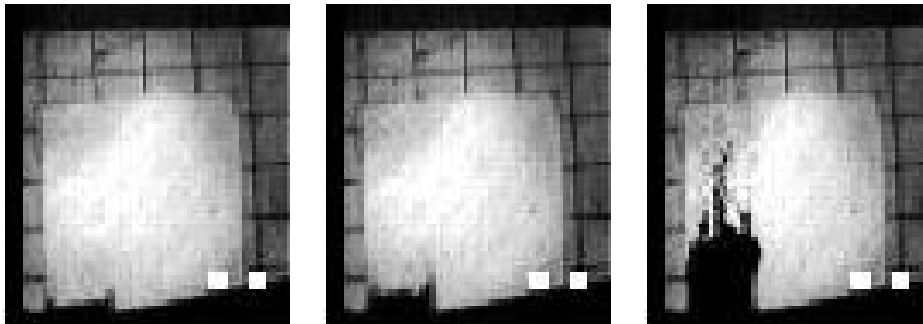


Figure 2.12: *Mercury splash at $t = 0.88, 1.25, 7 \text{ ms}$ after proton impact of $0.6 \cdot 10^{12}$ protons (thimble)*

The experiment with the thimble can be considered as the zero order case because it has provided the information about the behavior of the first part of the full jet. Figures 2.12 and 2.13 show the thimble explosion front once the mercury sample is irradiated by $0.6 \cdot 10^{12}$ protons at 1.4 GeV or by $3.7 \cdot 10^{12}$

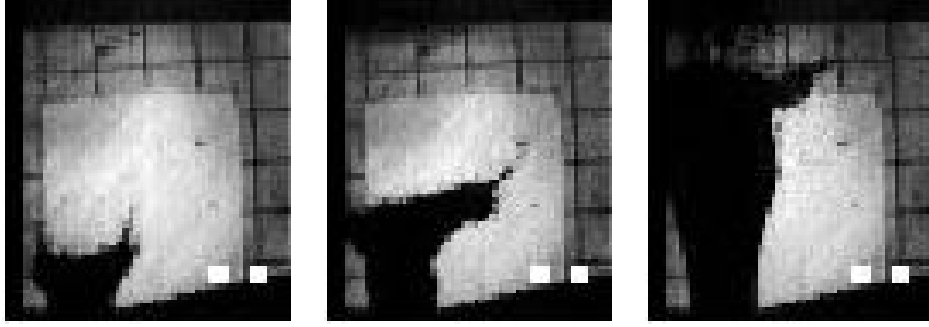


Figure 2.13: *Mercury splash at $t = 0.88, 1.25, 7$ ms after proton impact of $3.7 \cdot 10^{12}$ protons (thimble)*

protons. As it is clear from the images, mercury is expelled faster for higher proton intensity. The same experiment has been performed with different beam intensity from $0.6 \cdot 10^{12}$ up to $33 \cdot 10^{12}$ protons per pulse and the results, shown in figure 2.14, suggest that the splash velocity scales linearly with the beam intensity. In the case of the Neutrino Factory, the pulse intensity is 7 times larger than that of the ISOLDE beam and the spot size is two times larger. If no saturation in the velocity spectrum occurs, one can expect to have a typical velocity of the order of 50 m/s for the Neutrino Factory case.

A further upgrade of the experimental setup has been reached replacing, for the same beam condition, the thimble target with the trough. Figure 2.15 shows a typical explosion shape of the trough once the mercury sample is irradiated by 10^{13} protons at 1.4 GeV. The interaction between protons and the material of the trough has been simulated by MARS to understand the relationship between the mercury explosion parameters and the proton energy deposition. The results are shown in figure 2.16, where the experimental data, collected with a proton intensity of $2 \cdot 10^{13}$, are superimposed to the simulated temperature profile. The two continuous curves show the propagation of the mercury explosion front at two different times ($t_1 = 1.25$ ms and $t_2 = 3.25$ ms) along the beam axis. The dots are the measured velocities of the front along the same axis which is well followed by the simulated temperature distribution.

This result is considered as a first key point for the understanding of the mercury explosion, since the velocity distribution is proportional to the energy deposition distribution along the proton axis.

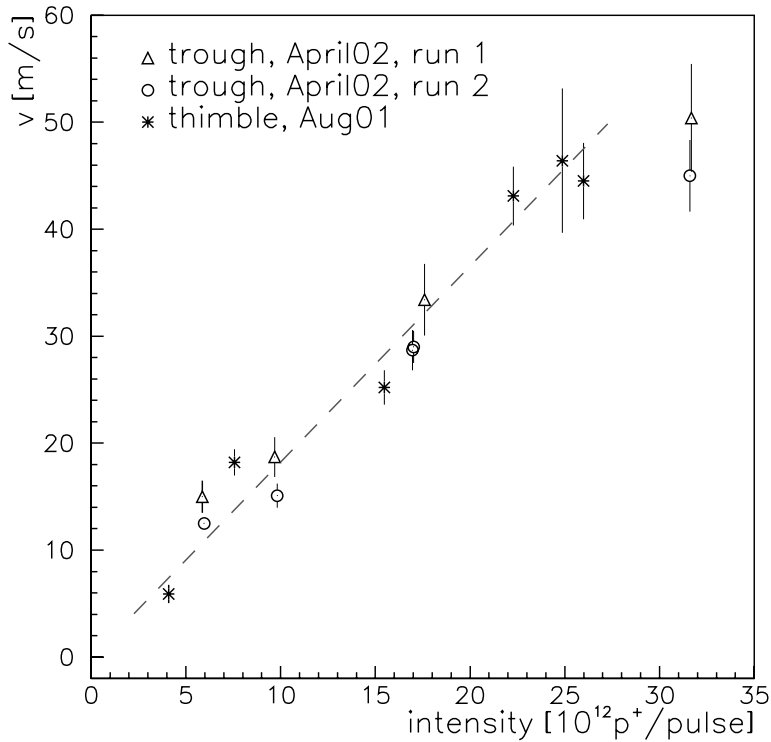


Figure 2.14: *Splash velocity measurements for different impinging protons intensities. The line is intended only to guide the eyes.*



Figure 2.15: *Trough splash at $t=0$, $t=2.5$ ms, $t=5.5$ ms after the impinging of 10^{13} protons arriving from the left part of the figure*

2.5 Conclusion

The conclusion of the target material study is that mercury is a valid option for the CERN NuFact design.

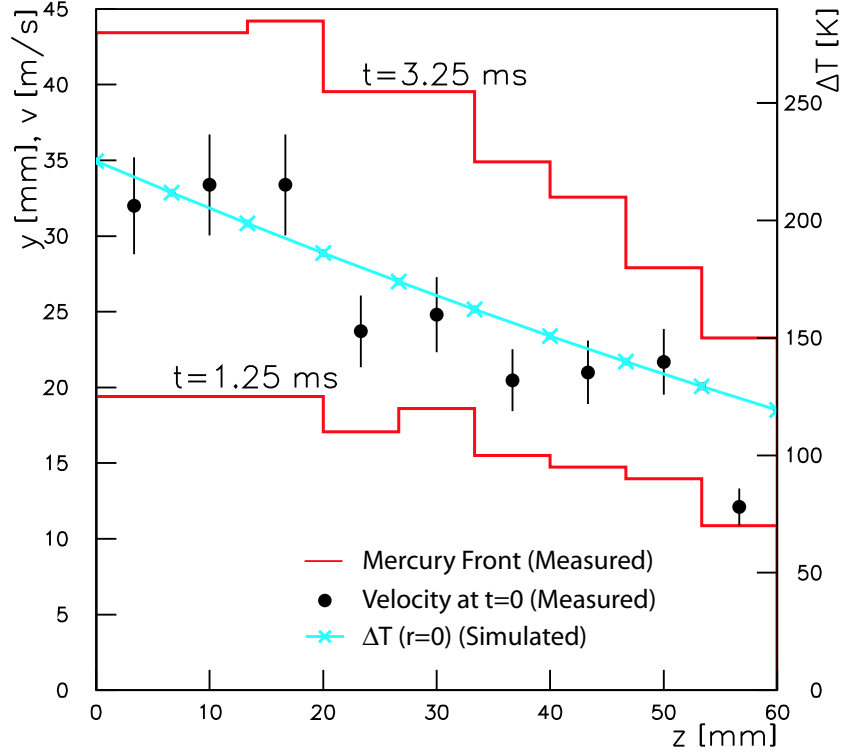


Figure 2.16: *Velocity (dots) and front distribution (red continuous line), taken at two different time, along z as measured the trough experiment compared to the simulated temperature increase (cyan line with crosses)*

From the experimental results presented in the previous sections it is clear that the design of the mercury jet and the matching between the pion focusing element, the horn, and the target requires more R&D than what has been done so far. However, for the first time, it has been shown that the Monte Carlo simulated energy deposition is in good agreement with the mercury explosion speed profile.

A major concern still unsolved is the amount of space to be left for the mercury to expand after the proton interaction without damaging the horn. Moreover the recuperation of the mercury is still a not completely solved issue. One possible solution could be to shoot the Mercury in the opposite direction to the proton beam. In this case a large part of the mercury droplets generated by the explosion would fly outside the neck of the horn in the direction opposite to the decay channel. At the first glance, it would be easier to accommodate a sort of explosion chamber outside in a zone where there are no restriction given by the presence of superconducting magnets or the horn. This situation is shown in figure 2.17 to be compared to the

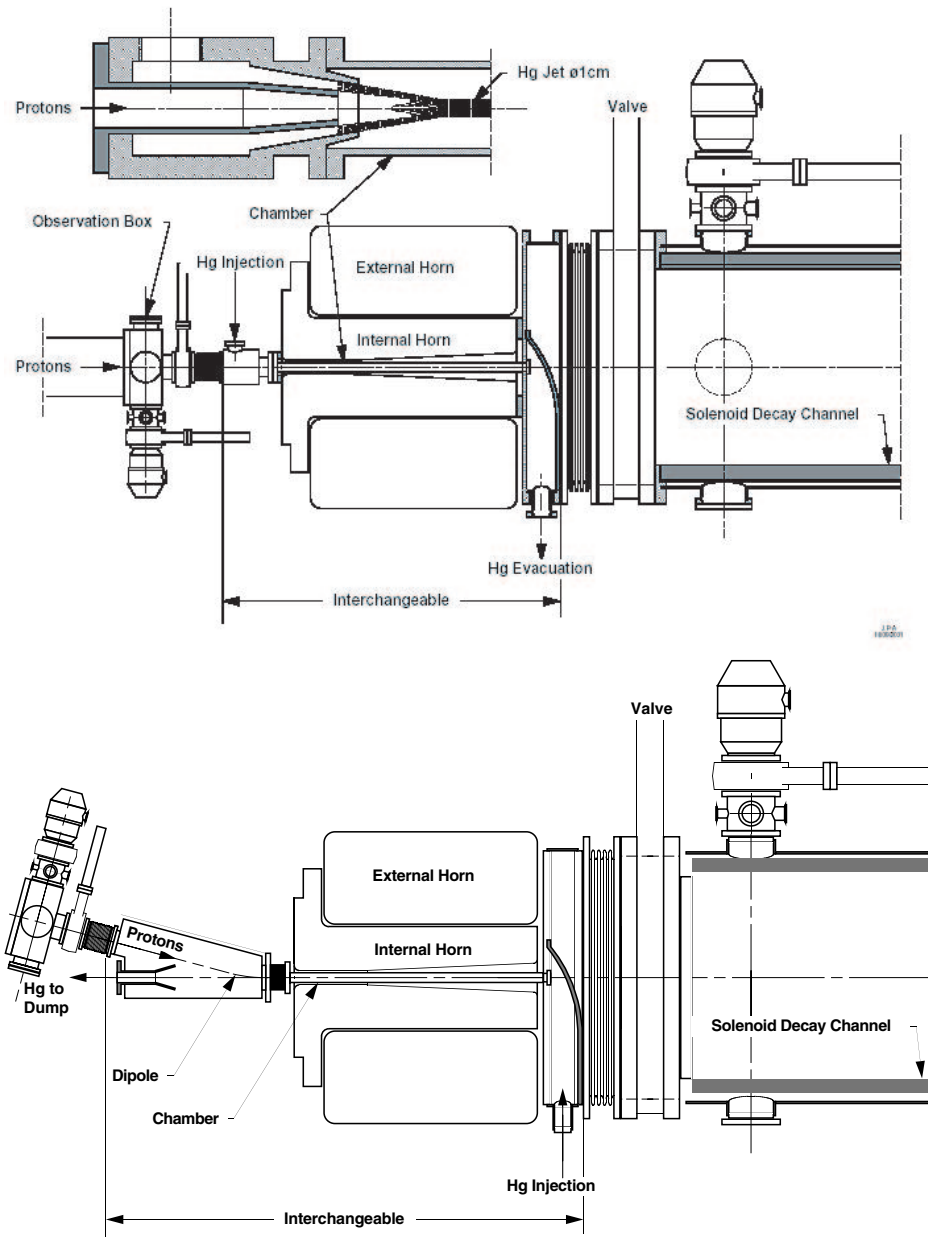


Figure 2.17: *Conceptual design of the horn target station with the mercury jet shot in the same direction as the proton beam and in the opposite direction.*

standard setup proposed for the target station.

2.6 A non conventional target concept: pulsed target

Generally the brilliance of secondary beams, defined as the beam transverse phase space density, is much lower than the one of primary beams. Resorting to cooling techniques is one way of increasing the brilliance but another way consists of acting on the secondary particles right at the time of their creation.

In passive targets, particles leaving the target follow straight lines and their phase space portrait at the end of the target is a polygon, the *butterfly*, drawn in figure 2.19. The downstream systems have to be designed to have a large acceptance, described by an ellipse, which must be circumscribed to the polygon to capture the largest possible part of secondary particles. It is clear that a large part of the ellipse does not contain any particle and that the phase space density, the brilliance, is poor. Improving the brilliance means transforming the butterfly so that the secondary particle portrait is better fitted to the acceptance ellipse or the acceptance ellipse can be reduced with tolerable losses.

In the case of pion production by the bombardment of heavy metal by a proton beam, as described in the previous sections, the brilliance of the secondary beam can be increased by pulsing a high intensity current through the target [35],[36],[37] (see figure 2.18). When a current of uniform density circulates through the target, the azimuthal magnetic field increases linearly with the radial position and focuses the pions (see figure 2.18). The trajectories of the particles contained in the target are then sinusoidal curves and the transverse phase space as it will be shown can become an ellipse of smaller size than that of a passive target. This gain of brilliance motivates the development of current carrying targets. However, the technological problems are very challenging and the experience with such devices is limited.

2.6.1 Target parameters

To determine the target parameters[†], the particle energy loss is neglected and the current density is supposed to be uniform. The field is then a linear function of the transverse coordinate x and the equations of a trajectory and of its slope for initial conditions x_0 and x'_0 for a given reference particle are

$$x = x_0 \cos(\sqrt{K_0}z) + \frac{x'_0}{\sqrt{K_0}} \sin(\sqrt{K_0}z) \quad (2.1)$$

[†]Here and in the following $c=1$

2.6. A NON CONVENTIONAL TARGET CONCEPT: PULSED TARGET61

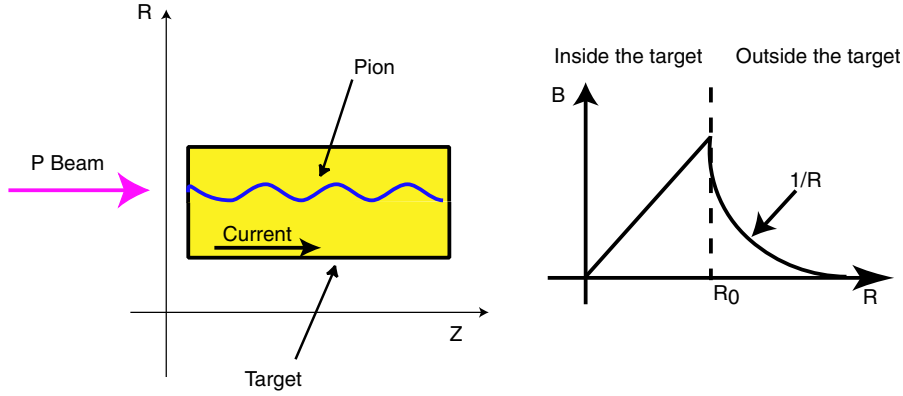


Figure 2.18: *Schema of magnetic field generated from a uniform current flowing inside the target.*

$$x' = \frac{dx}{dz} = -x_0\sqrt{K_0}\sin(\sqrt{K_0}z) + x'_0\cos(\sqrt{K_0}z) \quad (2.2)$$

where the focusing strength K_0 is related to the field gradient G , the momentum p_0 and the electric charge e through the expression

$$K_0 = \frac{e}{p_0}G \quad (2.3)$$

The particle emitted at the origin ($z = 0$) performs over the length l of the target an oscillation characterized by the phase φ :

$$\varphi = \sqrt{K_0}l \quad (2.4)$$

and

$$K_0 = \left(\frac{\varphi}{l}\right)^2 \quad (2.5)$$

At the end of the target, the transverse phase space of particles emitted on axis is an upright ellipse of semi-axes x'_0l/φ and x'_0 when φ is at least equal to π . The area of the ellipse, the *emittance*, decreases with φ . This property reflects the reduction of the radius and the constant collection angle.

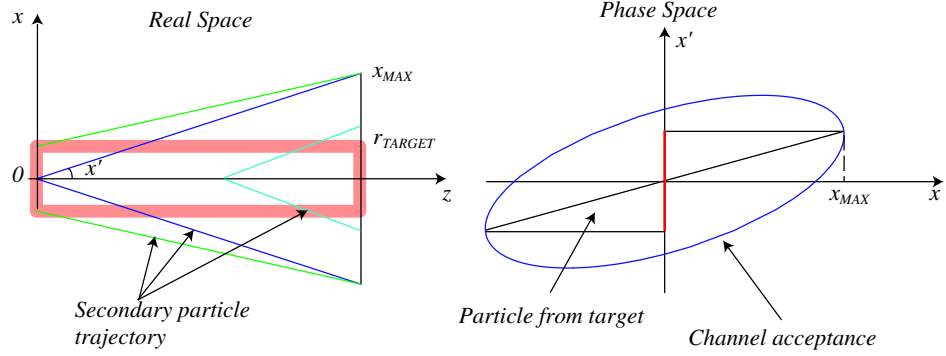


Figure 2.19: Trajectories of pions in a target of radius r (left) and associated portrait at the end of the target (right).

Assuming that the reabsorption length of the pions is the same as the nuclear interaction length λ , the optimum length of the target is chosen to be equal to λ . The field gradient G is thus only a function of φ

$$G = \frac{p_0}{e} \left(\frac{\varphi}{\lambda} \right)^2. \quad (2.6)$$

The radius r of the target is chosen equal to the maximum amplitude of the particle oscillation of a particle generated at the beginning of the target and on axis, $x_0 = 0$:

$$r = \frac{x'_0 \lambda}{\varphi} \quad (2.7)$$

deduced from equation 2.1 The magnetic field at the periphery of the target is Gr or

$$B = \frac{p_0 \varphi}{e \lambda} x'_0. \quad (2.8)$$

From Ampere's law, it can be derived that field gradient and current density are proportional:

$$G = \frac{\mu_0 j}{2}. \quad (2.9)$$

The current $I = jS$, with S the transverse surface of the target, needed to collect in a given emittance the particles born with an angle up to the tangent of x'_0 is then given by the expression

$$I = \frac{2\pi p_0}{\mu_0 e} (x'_0)^2 \quad (2.10)$$

considering all particles born at the same place $x_0 = 0$.

The current is proportional to the momentum and to the square of the tangent of the collection angle. The average power deposited in the target by an

2.6. A NON CONVENTIONAL TARGET CONCEPT: PULSED TARGET63

alternating current is $\frac{RI^2}{2}$ with R the total resistance of the target. However, if the current is pulsed at a frequency f with a pulse length τ and assuming that the current variation during the pulse is sinusoidal, then the expression of the power becomes:

$$P = \frac{1}{2}RI^2 f\tau. \quad (2.11)$$

From the experience obtained with lithium lenses [42], the radius r_{sk} through which the current flows equals twice the skin depth skd

$$r_{sk} = 2 skd = 2\sqrt{\frac{2\rho\tau}{\pi\mu_0}}. \quad (2.12)$$

where ρ is the resistivity of the material and μ_0 the vacuum permeability. The resistance R of the target is $\rho\lambda/S$ since $\lambda=1$ interaction length has been chosen before as the target length. The electrical power losses can be re-written:

$$P = \frac{1}{16}\mu_0\lambda f I^2. \quad (2.13)$$

The power, like the current, is basically a function of the collection angle.

	Mercury	Beryllium	Lithium
Power [MW]	3.18	9.95	33.6
Temperature rise per pulse [K]	160	83	142
Field [T]	22.04	21.12	20.84
Intensity [MA]	2.49	2.49	2.49
Frequency [Hz]	50	50	50
Phase [π]	1.	3.	10.
Pulse length [ms]	0.264	4.68	3.3
Target length= λ [m]	0.13	0.407	1.37
Target radius [m]	0.0226	0.0236	0.024

Table 2.3: *Parameters of three types of conducting targets.*

The method followed to derive the parameters consists of the following steps:

1. The momentum and the maximum transverse momentum define the reference particle used to design the collection system and provide the current via the tangent of the collection angle.
2. The phase of the oscillation described by the reference particle emitted from the origin gives the field gradient and the current density.
3. Using current intensity and density, the radius of the target is deduced.

4. The surface field is the product of the gradient and the radius.
5. The interaction length gives the length of the target.
6. Current, repetition frequency and target length give the electrical power.
7. The pulse duration is calculated from the skin depth expression.

A comparison between three target materials: lithium, beryllium and mercury is shown in Table 2.6.1. The particle momentum and transverse momentum are 500 and 240 MeV/c respectively. The phase has been chosen so that the radius and thus the beam emittance be roughly the same for the three targets.

2.6.2 Particle production

The pulsed target has been simulated using the **MARS** [98] code which includes pion production, interaction and transport in the magnetic field. Its parameters are listed in Table 2.6.1 for the mercury case. Pions are counted at the end of the target, within a radius of 2.26 cm. All the particles escaping from the side of the cylinder are considered as lost.

For comparison, the pion production in a target magnetized by a 20 T solenoid is also simulated. In this case, the target is 30 cm long, its radius is 0.75 cm and the angle between target and field axis is 50 mrad. The proton beam is collinear to the target. The solenoid is 30 cm long with an aperture of radius equals to 7.5 cm. The field of 20 T is constant and no radial component is considered. Particles are counted at the end of the solenoid within a radius of 7.5 cm. For both cases the proton beam energy is 2.2 GeV. The particles are collected in the transverse plane $x-x'$ (Fig.2.6.2) within a physical emittance of 1.7 cm rad corresponding to five times the *rms* emittance. It is to be noted that the physical acceptance of the first muon recirculator is 0.55 cm rad once the recirculator acceptance is rescaled for an average $\beta\gamma = 2.7$. Cooling is thus still required for this type of beam. Moreover the particles are counted in the (300, 600) MeV interval of total energy (Fig.2.21). This interval encloses the pion population that gives a muon in the longitudinal acceptance of the phase rotation. From the comparison given in Table 6.1, it turns out that, for the same 6D emittance, namely the one which contains all the pions produced by the conducting target, the conducting target produces more pions by a factor 1.4.

2.6. A NON CONVENTIONAL TARGET CONCEPT: PULSED TARGET65

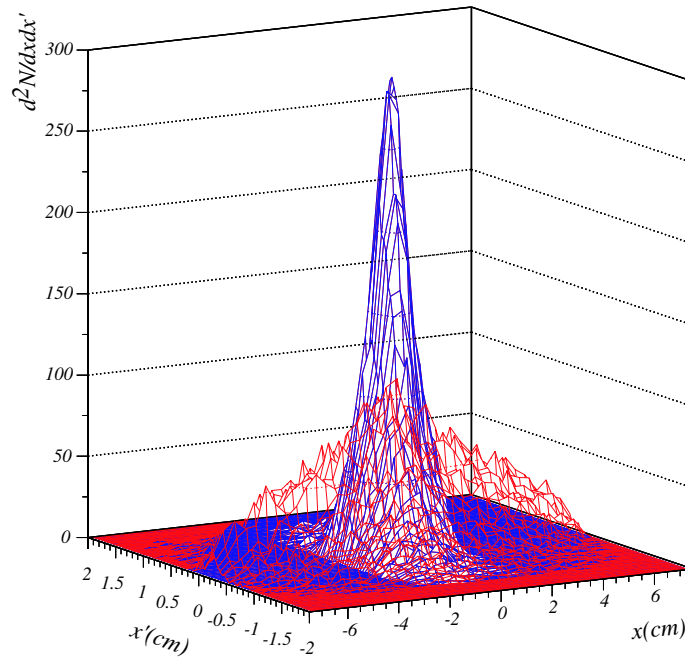


Figure 2.20: *Transverse phase space of positive pions for the conducting target (blue) and the target magnetized by a 20 T solenoid (red)*

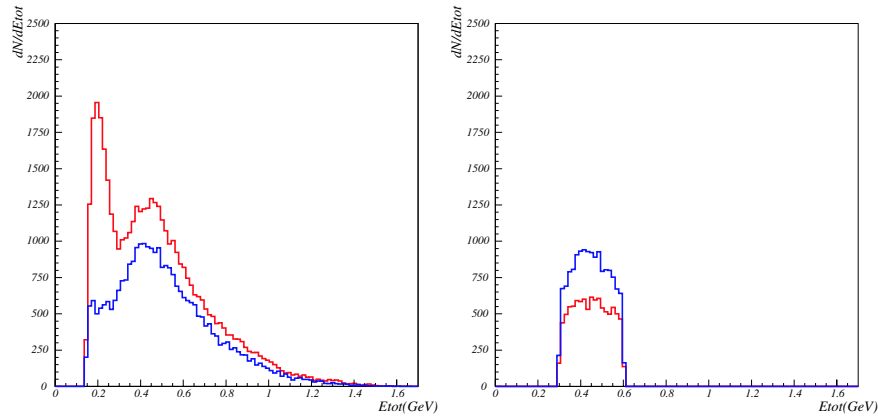


Figure 2.21: *Total energy distribution of pions without any particle selection (left) and with particle selected in a transverse physical emittance of 1.7 cm rad. The blue and red curves apply to the conducting target and to the target magnetized by a 20 T solenoid respectively.*

2.6.3 Technological aspects

The technical problems are related to the energy deposited by the pulsed current on one hand and by the beam on the other hand.

	no cut	p_t cut	p_t and energy cuts
Pulsed target	0.028	0.0267	0.014
Target magnetized by solenoid	0.044	0.0205	0.0095

Table 2.4: *Pion yield per proton.*

Temperature rises higher than $100\text{ }^\circ\text{K}$ per pulse present a severe load in any solid or even liquid material. The material must be free to expand to prevent an excessive pressure during the electrical heating. Moreover, electromagnetic forces exert a radial compression of the order of 100 MPa.

The temperature rise and pressure induced by the beam occur during the proton burst ($3.2\ \mu\text{s}$) and are of the same order of magnitude as those due to the electrical current.

In addition to the containment of the forces, the power deposited both by the current and the beam, about 4 MW in total, can only be handled by circulating the material rapidly through a closed loop with an external heat exchanger, as described in the previous section. A full mechanical and electrical design is far from completion (see figure 2.22 for a test circuit conceptual design).

Nevertheless, preliminary experience [40],[41] has been acquired at the time of the construction of p- $\bar{\text{p}}$ colliders but the targets were not tested in the beam. In the same line of development, a 1 MA lithium lens has been successfully used for beam collection [42]. Increasing the current by a factor 2 does not seem to be out of reach. Of more concern is the high repetition rate of 50 Hz. In the present study, the conducting medium is the secondary of a pulse transformer.

The robustness of the target would be obtained by metallic beads [44] which would act as *wave breakers* to avoid the destruction of the walls. The cooling would be made by circulating a liquid metal such as mercury. Creating n target stations and recombining the pion beams in a single transport line would reduce the repetition rate by n . Lattices of alternating gradient lenses for four beams are presently studied for this purpose [45].

2.6.4 Conclusion

For a conducting target, a heavy material such as mercury is preferable to light materials because it can produce pion beams of both signs in a small emittance with minimum electrical power. Conducting targets produce more brilliant pion beams than targets magnetized by a high solenoidal field, but the total number of particles produced is lower. The quadrupolar field di-

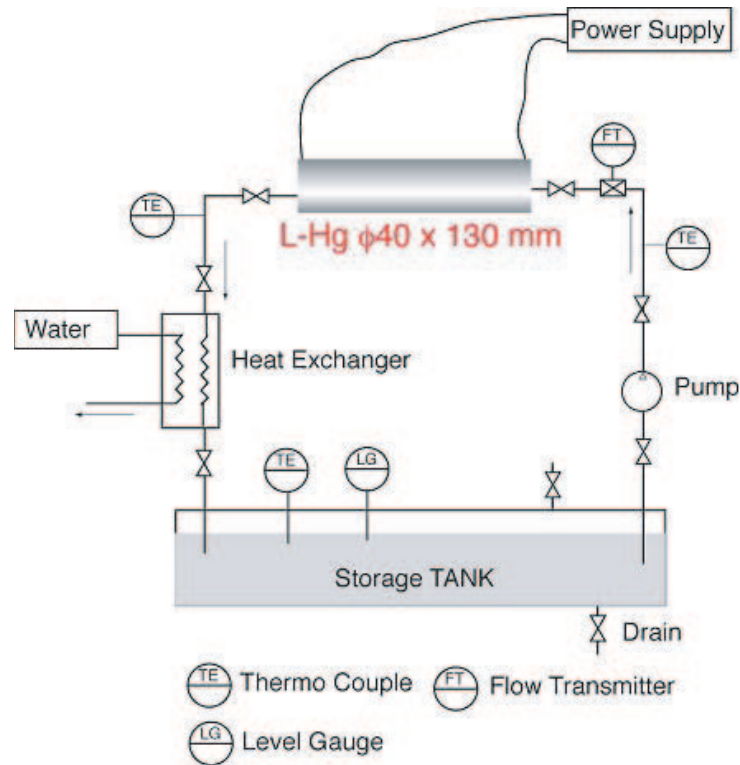


Figure 2.22: Mercury circuit and power supply connection conceptual design (taken from [43]).

rected in the radial direction associated with a uniform current density redistributes indeed the particles in phase space more efficiently than a long solenoidal field. However the production of negative pions is limited since protons are quickly defocused inside the magnetized target.

The ultimate issue is technological. The example considered in this paper is related to a special scenario of neutrino factory and may actually be the ultimate step in the development of pulsed targets. The K2K aluminum target is already used as pulsed target and the R&D in Japan is continuing[43].

2.7 Converter target for isotope production

One of the main limitations for the isotope production at the CERN ISOLDE (Isotope Separator On Line) is the maximum energy deposition of protons that the production target can sustain.

In this section a new technique is discussed for isotope production which can be applied to the isotope production for the Beta Beam.

2.7.1 Converter target

The typical isotope production target used at the CERN ISOLDE facility is a cylinder of Uranium Carbide (UC_2). Isotopes are produced by the proton beam of the CERN Booster, which can deliver a 1 GeV or 1.4 GeV nearly monochromatic beam, hitting a cylindrical target. The isotopes are then extracted from the target itself (for details see [46]).

The main limitation of a such a scheme is the maximum energy loss deposited by the proton beam in the UC_2 target and its container and the thermal shocks induced in those two elements. However, this limit can be bypassed if the primary target, hit by protons, is separated from a secondary target where isotopes are created. This separation function system, defined

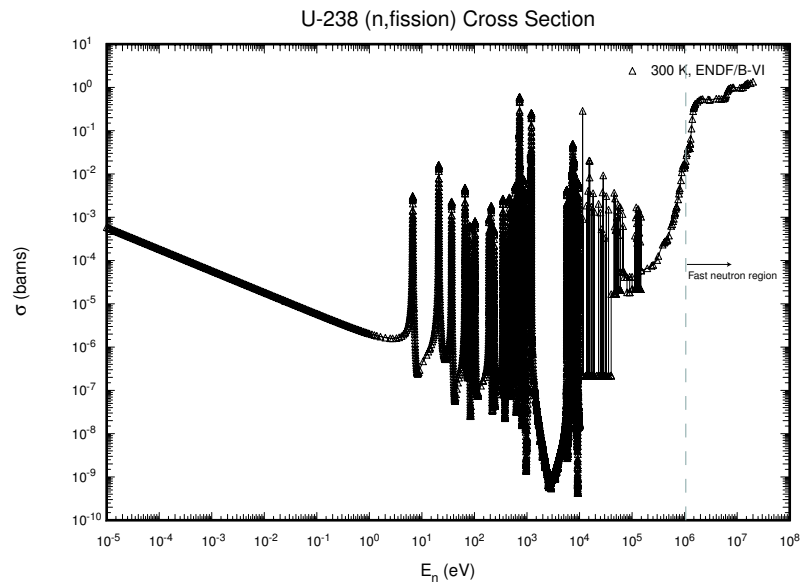


Figure 2.23: ^{238}U neutron-induced fission cross section as function of neutron energy.

as the target converter scheme, is made possible by the fact that the energy distribution of the spallation neutrons, shown in figure 2.25, has a maximum around few MeV, which coincide with a large cross section for the neutron induced ^{238}U fission (see figure 2.23). In the target converter scheme, as shown in figure 2.26, protons hit the converter to produce spallation neutrons and, since they are produced at large angle, they can interact in the surrounding production target.

Moreover, one can take advantage from the fact that a large part of neutron rich isotopes around $A = 100$ and $A = 140$ can be produced by neutron

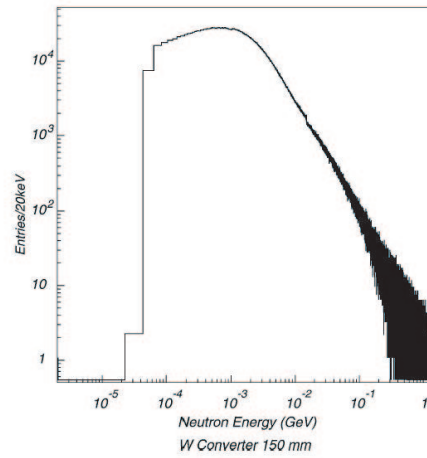
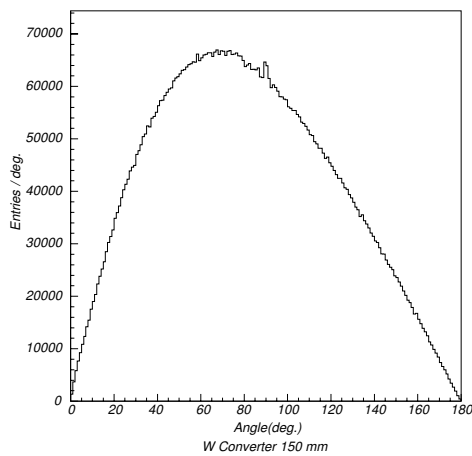


Figure 2.24: *Spallation neutron angular distribution*

Figure 2.25: *Spallation neutron energy distribution*

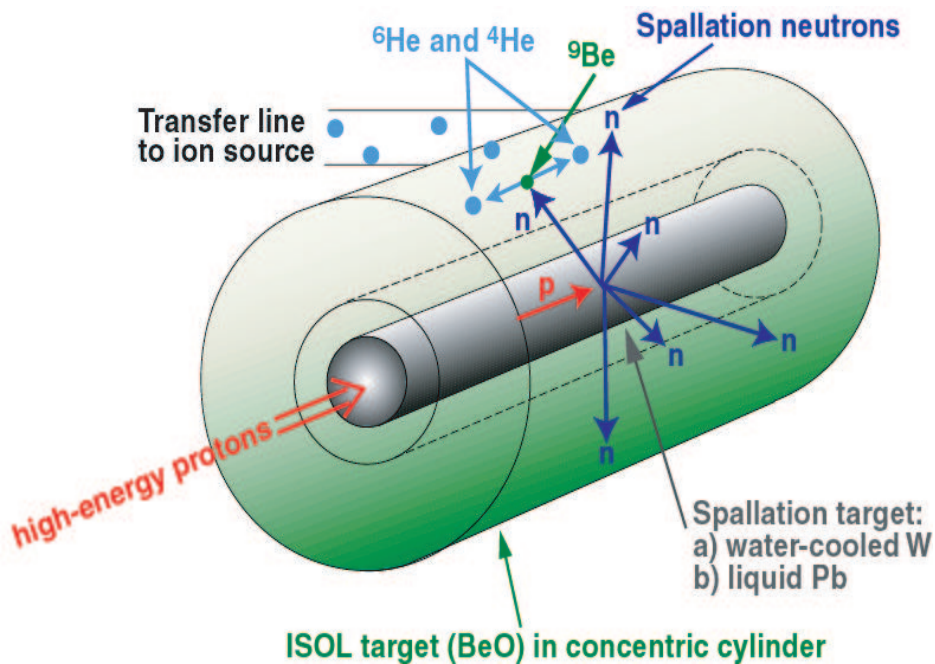


Figure 2.26: *Converter target conceptual scheme*

induced fission instead of proton induced fission or fragmentation (see figure 2.27) increasing considerably the production yields [48].

The proof of principle target (see figure 2.28) tested in 2001 at ISOLDE had a different geometry from the one shown in figure 2.26 because it is more practical to accommodate the converter outside the UC_2 container without

developing a complete new technology for the target assembly and a new channel for the isotope extraction. In this way a direct comparison with the isotope production yields with and without the converter is possible since the extraction and the ions channel are the same. Moreover, the UC_2 target operates at about 2000°C . Such a high temperature is necessary for the isotope extraction by effusion/diffusion processes. The insertion of the converter inside the production target would require a cooling circuit and a heat isolation between the two concentric cylinders.

The converter target is placed under the UC_2 target. This reduce the neutron flux for the isotope production, but is a much safer position in case of unforeseen converter behavior. This particular configuration, in fact, allowed to experience the situation when the proton focusing is too high and the local energy deposition is too high: the converter was destroyed but the UC_2 container remained intact (figure 2.29).

2.7.2 Converter Simulation

The simulation of the converter target neutron production for the geometry of figure 2.30 has been performed with MARS interfaced with the MCNP4C[47] neutron interaction and transport libraries.

The aim of the simulation is to understand the production of spallation neutrons, the influence of different converter target materials and different proton beam energies on the isotope yields. Four different converter target

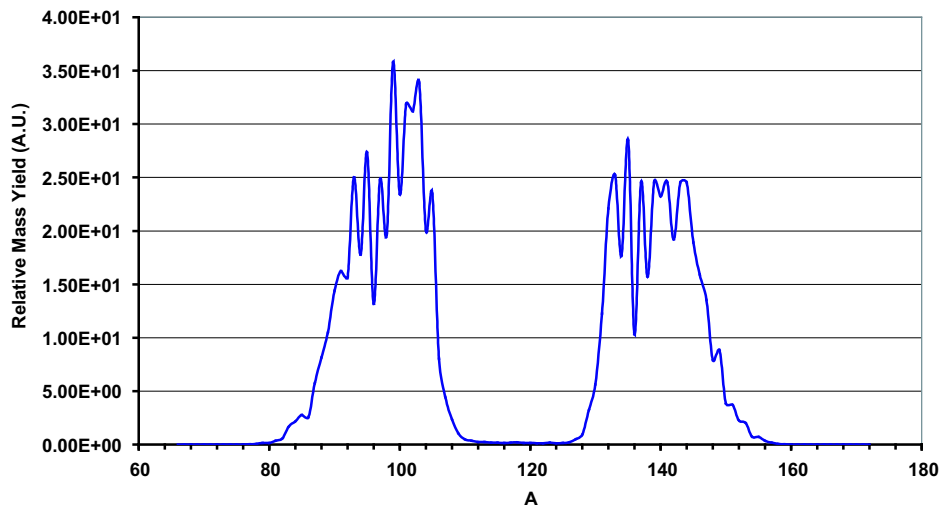


Figure 2.27: *Relative mass yields from ^{238}U fission induced by fast neutrons[31]*

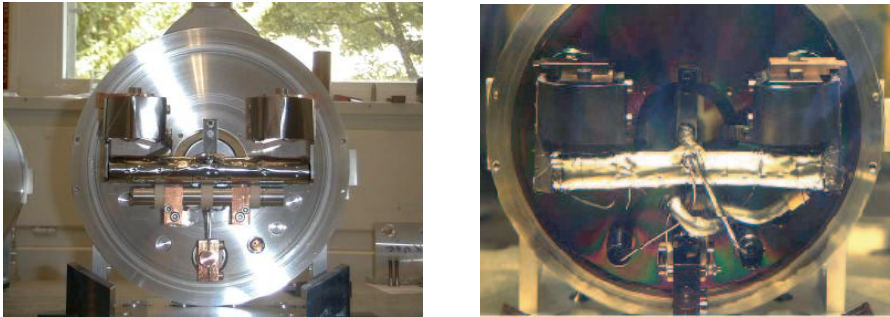


Figure 2.28: *Target converter* Figure 2.29: *Target converter mounted below the UC target be-melted after being irradiated 2.5 fore irradiation*
 10^{18} protons with $3 \cdot 10^{13}$ proton per pulse

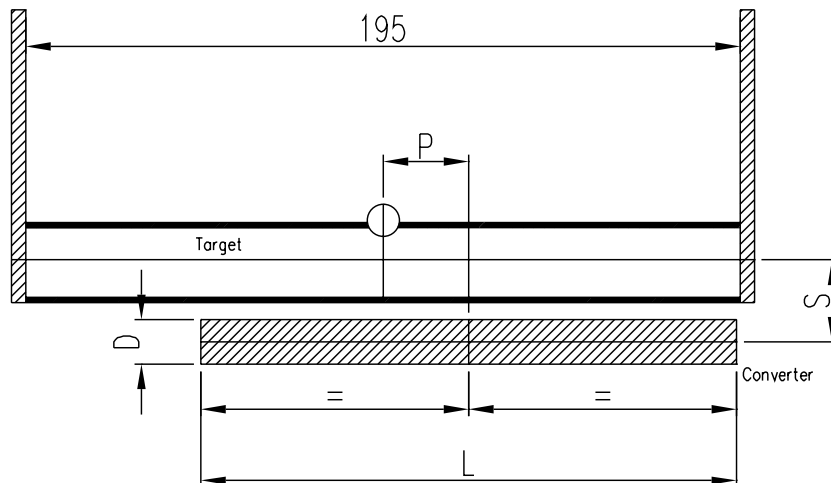


Figure 2.30: *Isolde target plus converter technical design*

settings have been simulated: two different materials (W and Ta) for two different proton energies (1 and 1.4 GeV).

The converter is 150 mm long, 12.5 mm radius and is placed below the UC_2 target (see figure 2.30). The results are normalized for 30 T_p (1 $T_p=10^{12}$ protons) with a sigma of 2.2 mm. Simulated neutron fluxes are compared with the measured yields for different isotopes, in particular with the yield for Cs and Kr. This is due to the fact that the experiment does not measure directly neutron fluxes but the yield of the isotopes produced by different fluxes, being the production yield proportional to the neutron fluxes.

Under this hypothesis, the Montecarlo ratio of neutron production between W and Ta has been estimated to be 1.39 and confirmed by the ratio of 2

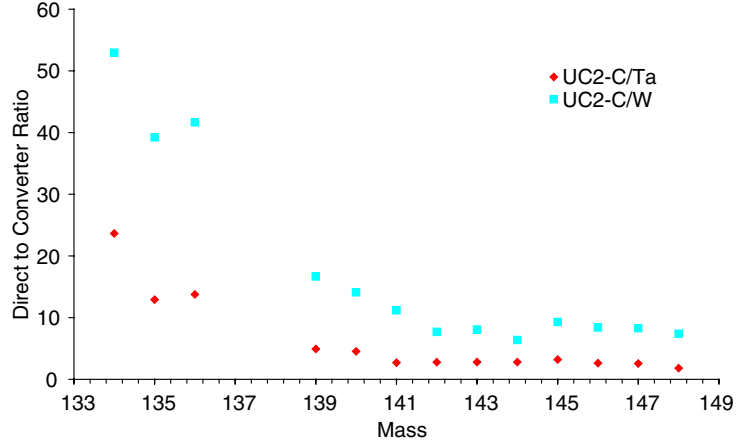


Figure 2.31: *Ratio of Cs yields obtained by 1) direct irradiation of proton on the target 2) use of a converter. Square dots are for Ta converter, diamond dots for W converter.*

measured from the Cs isotope data produced from the W and Ta converter. This result is shown in figure 2.31, in which the ratio of yields with and without a converter is compared for a Ta converter and W converter[49]. The Montecarlo ratio of neutron production between 1 and 1.4 GeV has been estimated around 1.4 and confirmed by the comparison of Xe isotope yields[48] measured for the two energies.

The energy deposition of the UC_2 target is reduced from 29.6 J/g for direct 1 GeV proton irradiation to 0.1 J/g when 1 GeV protons impinge on the converter.

2.7.3 Converter target for ${}^6\text{He}$ production

As described in section 1.7, ${}^6\text{He}$ is chosen as β^- emitter for the Beta Beam. The nuclear reaction used to produce ${}^6\text{He}$ is ${}^9\text{Be}(n,\alpha){}^6\text{He}$ (figure 2.32) which has a large cross section for the typical energy of the spallation neutrons (figure 2.33) of few MeV.

The production scheme is the same as the case of the converter. Primary proton incident on a W target to produce spallation neutrons. The converter can be a solid material since the energy deposition is estimated to be ≈ 100 kW (for $100\mu\text{A}$ protons at 2.2 GeV), which is the limit accepted for water cooled target.

The converter is surrounded by a BeO production target where the (n,α) reaction takes place. Then Helium is extracted from the target with an efficiency about $\approx 50\%$ [50].

Two different cases were studied: the first case uses the ISOLDE beam at 1.4

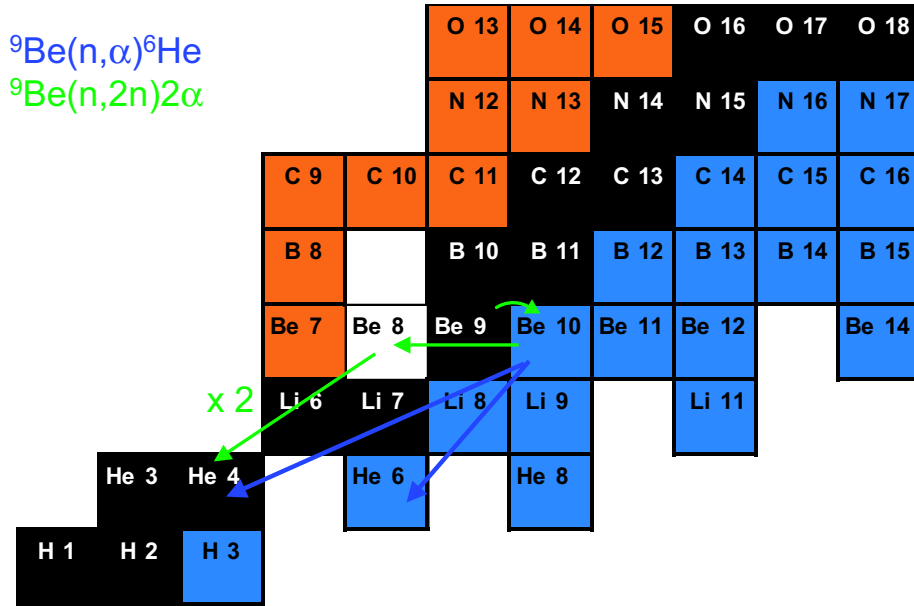


Figure 2.32: ${}^6\text{He}$ production reaction mechanism compared to ${}^4\text{He}$ production

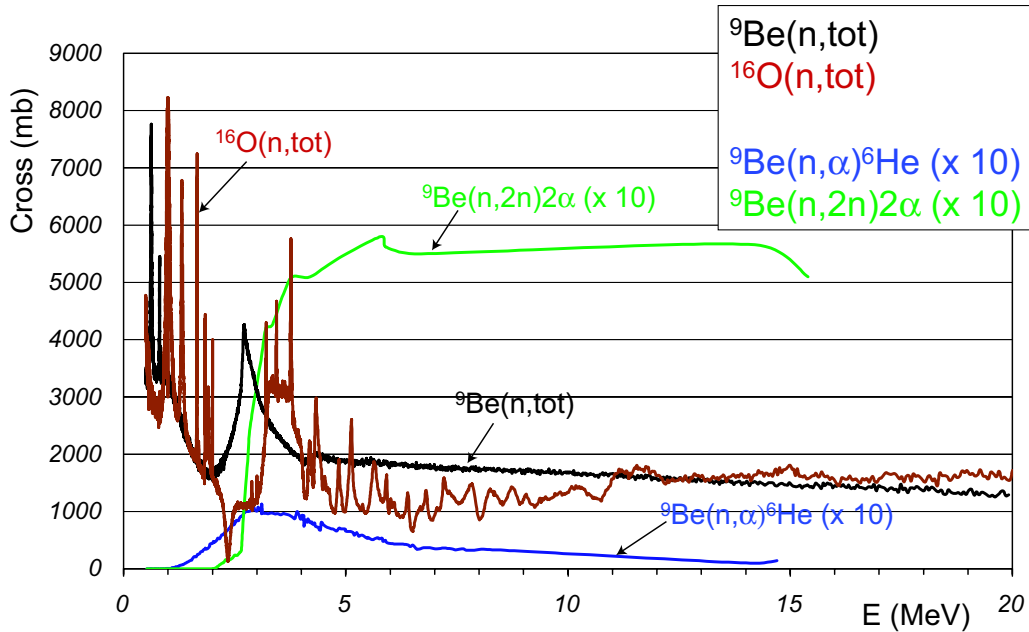


Figure 2.33: ${}^6\text{He}$ cross section production compared to the α production and total reaction cross sections[50]

GeV hitting on a W converter of radius of 1 or 2 cm. The latter is surrounded by a 4 cm thick BeO cylinder. As shown in figure 2.34 and reported in table 2.5 there is no gain in neutron flux for a thicker target, because the ${}^6\text{He}$ production cross section peaks around 3 MeV and from figure 2.34 the 1 cm radius flux is good as the 2 cm radius. Hence all the ${}^6\text{He}$ production rates

	All (n/pot)	E<16 MeV
Isolde 1 cm	15.1	11.3
Isolde 2 cm	16.5	13.2
2.2 GeV	23.6	17.8

Table 2.5: *Spallation neutron yield for different cases considered*

were calculated with a 1 cm target radius.

The results, reported in table 2.6, confirms that for the 2.2 GeV beam the goal of $5.5 \cdot 10^{13}$ ions per second using $100 \mu\text{A}$ protons is achieved. A design

	${}^6\text{He}$ (per pot)	${}^6\text{He}/\text{s}$ ($100\mu\text{A}$)
Isolde 1 cm	0.025	$1.56 \cdot 10^{13}$
2.2 GeV	0.088	$5.5 \cdot 10^{13}$

Table 2.6: *Production rate, not multiplied by the extraction efficiency*

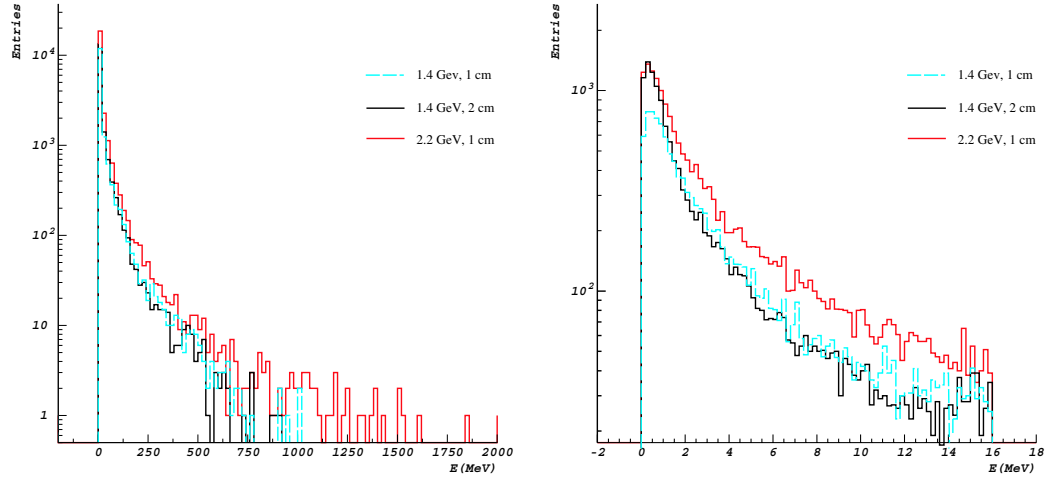


Figure 2.34: *Spallation neutron spectrum for the different case: a) 1.4 GeV, 1 cm radius (light dashed), b) 1.4 GeV, 2 cm radius (black), c) 2.2 GeV, 1 cm radius (light gray)*

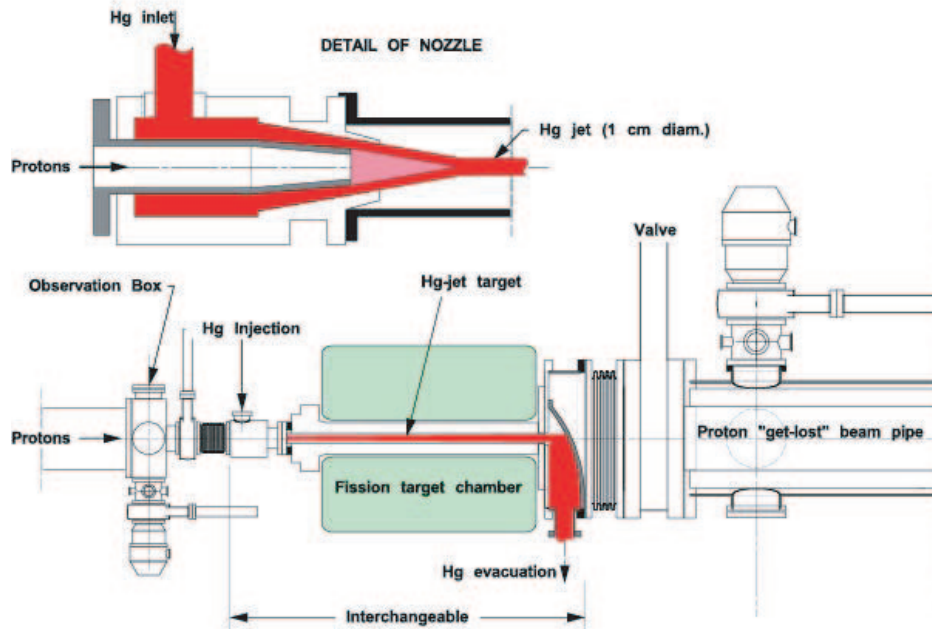


Figure 2.35: *Conceptual design of a 4 MW converter target station.*

concept for the target converter, which can handle beam power of up to 4 MW, has been proposed (see figure 2.35). The design is extrapolated from the neutrino factory target station.

Chapter 3

Horn

As described in the first chapter, in the CERN NuFact reference scenario, pions produced by the target are captured by a horn. The design of a first prototype, and its construction, the development of a test power supply are described in this chapter.

3.1 Horn

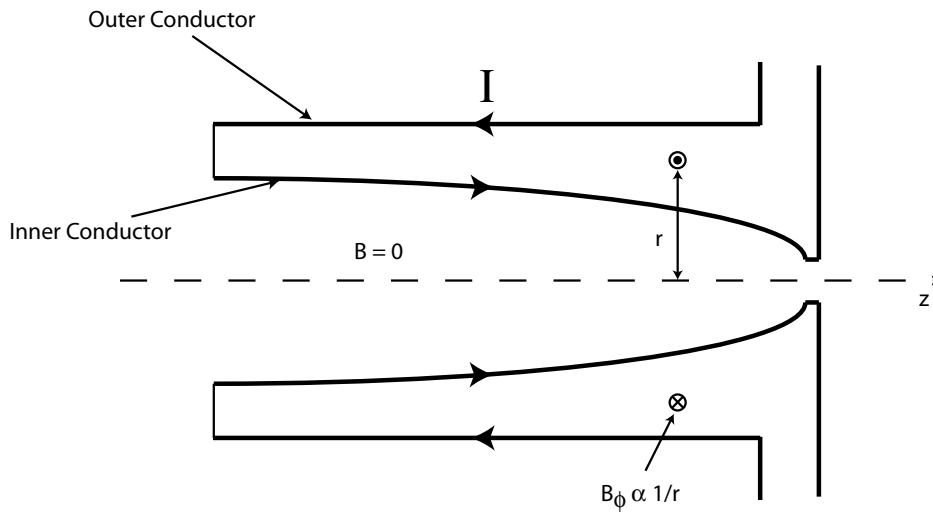


Figure 3.1: *Horn capture device scheme.*

A magnetic lens called horn is used to focus pions produced by protons impacting on the NuFact mercury target.

A horn consists of two concentric conductors, the inner and the outer conductor, which delimit a closed volume (see figure 3.1) generated by the revolution of the conductors around the z-axis. A longitudinal current produces a toroidal magnetic field in the volume between the two conductors.

The magnetic field intensity generated by the current can be determined directly from the Ampere's law considering the cylindrical symmetry of the geometry.

According to the Maxwell equation the relationship between the magnetic field \vec{B} and the current density \vec{J} is:

$$\vec{\nabla} \times \vec{B} = \mu_0 \vec{J} \quad (3.1)$$

where $\vec{\nabla}$ is the derivative operator ($\partial/\partial x, \partial/\partial y, \partial/\partial z$) and μ_0 is the vacuum magnetic permeability. Applying Stokes's theorem on a circular surface S perpendicular to the horn axis identified by the normal vector \vec{n} (see figure 3.2) one gets:

$$\int_S \vec{\nabla} \times \vec{B} \cdot \vec{n} \, ds = \mu_0 \int_s \vec{J} \cdot \vec{n} \, ds \quad (3.2)$$

Three different regions can be identified in the horn geometry: the first is enclosed by the inner conductor, the second is formed by the inner conductor and the first region, the third encloses the inner-outer conductor region.

In the first region, since there is no current, the magnetic field is constant and zero.

In the third region the magnetic field decreases proportionally to the inverse of the distance from the axis r , since from the application of the Gauss's law:

$$\int_{S_3} \vec{\nabla} \times \vec{B} \cdot \vec{n} \, ds = \oint_{c_3} \vec{B} \cdot d\vec{l} \quad (3.3)$$

$$\oint_{c_3} \vec{B} \cdot d\vec{l} = 2\pi r B_\phi \quad (3.4)$$

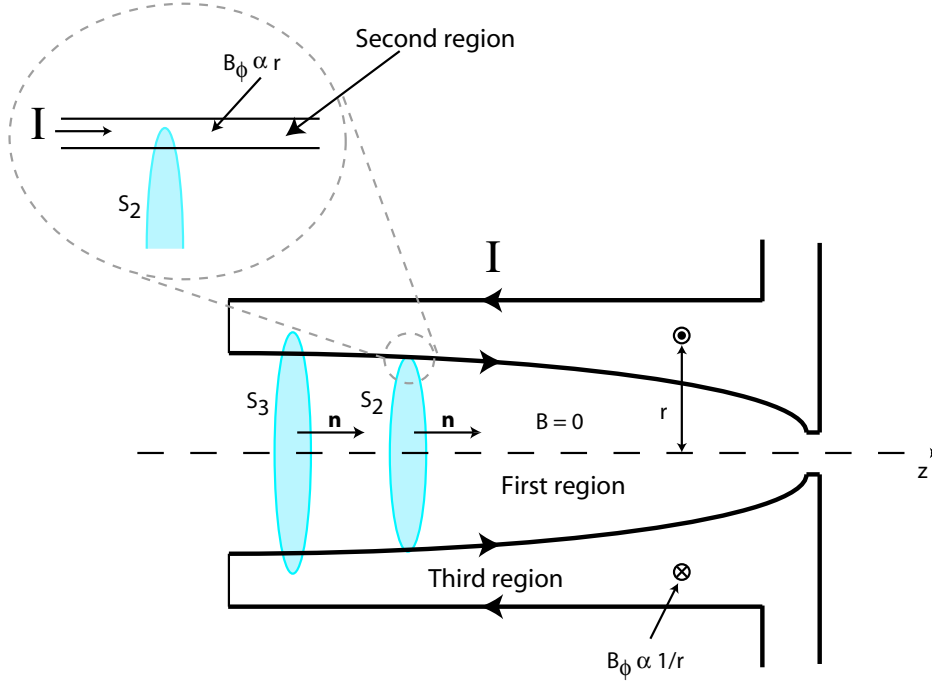
$$\mu_0 \int_{S_3} \vec{J} \cdot \vec{n} \, ds = \mu_0 I \quad (3.5)$$

where c_3 is the perimeter of the surface S_3 (see figure 3.2) and I is the total current flowing in the conductors.

The magnetic field intensity is deduced from the previous equations:

$$B_\phi = \frac{\mu_0 I}{2\pi r} \quad (3.6)$$

an it has only a toroidal component to respect the cylindrical symmetry and the current distribution.

Figure 3.2: *Horn magnetic field configuration.*

For the second region, since the current density \vec{J} is considered constant along the thickness of the inner conductor, the magnetic field increases linearly with the distance from the axis r , since:

$$\int_{S_2} \vec{\nabla} \times \vec{B} \cdot \vec{n} \, ds = 2\pi r B_\phi \quad (3.7)$$

$$\mu_0 \mu \int_{S_2} \vec{J} \cdot \vec{n} \, ds = \mu \mu_0 J \pi r^2 \quad (3.8)$$

with μ the magnetic permeability of the conductor material.

The magnetic field expression becomes:

$$B_\phi = \frac{1}{2} \mu \mu_0 J r \quad (3.9)$$

Particles entering in the magnetic volume are bent by the field and focused in the forward direction, since the Lorentz force points in the direction of the central axis z . The inner horn profile has to be properly shaped to obtain the focusing of the interesting particles.

The final inner horn profile is designed assuming a first guess profile according to the procedure of [52] and described in the following, starting from a point like source and a monoenergetic secondary beam. The focusing effect of the

raising part of the magnetic field inside the inner conductor is neglected, since the thickness of the conductor is small compared to the horn length. It should not exceed 2 cm to reduce the absorption of the secondary particles and to reduce the scattering of the going-through particles.

The equation of motion for particles inside the magnetic volume is deduced from the Lorentz equation:

$$\frac{d^2r}{dz^2} + \frac{A}{r} \left[1 + \left(\frac{dr}{dz} \right)^2 \right] = 0 \quad (3.10)$$

using the approximations that the variation in time of the trajectory along the radial coordinate is slower than the velocity of the particle v_z :

$$\frac{dr}{dt} \ll \frac{dz}{dt} = v_z \quad (3.11)$$

such that:

$$\frac{d}{dt} = v_z \frac{d}{dz} \quad (3.12)$$

In this approximation one has:

$$A = \frac{e\mu_0}{p} \frac{I}{2\pi} \quad (3.13)$$

with $p = m v_z$ the momentum of the particle of mass m , e the charge of the electron and I the total current flowing in the horn conductor.

Following the small angle approximation, $dr/dz \ll 1$, the equation of motion can be rewritten as:

$$r r'' = -A \quad (3.14)$$

with $r' = dr/dz$ and $r'' = d^2r/dz^2$. A particle which is produced by a pointlike target with an angle θ_1 enters in the magnetic region at $r = R_1$ and exit parallel to the z -axis for $r = R_m$ (see figure 3.3). The integration of the equation of motion with the latter conditions leads to:

$$r' = \sqrt{\theta_1^2 - 2A \log\left(\frac{r}{R_1}\right)} \quad (3.15)$$

Applying the condition $r' = 0$ for $r = R_m$, one gets the dependence of R_m from R_1 :

$$R_m = R_1 e^{\frac{\theta_1^2}{2A}} \quad (3.16)$$

The projection of the particle trajectory inside the magnetic field along the z axis corresponds to:

$$\Delta S_m = \int_{z_1}^{z_2} dz = \int_{R_1}^{R_m} \frac{dr}{\sqrt{\theta_1^2 - 2A \log\left(\frac{r}{R_1}\right)}} \quad (3.17)$$

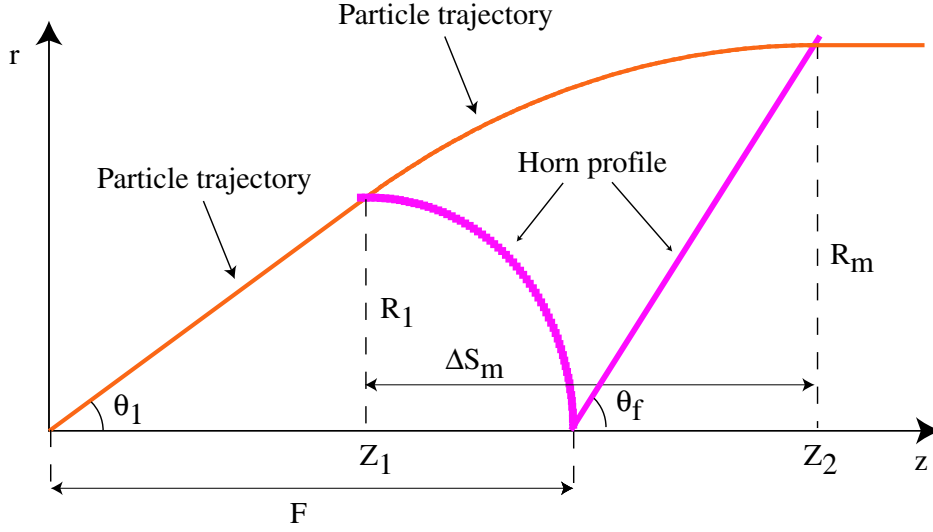


Figure 3.3: *Horn first-guess profile generated from a monoenergetic beam produced from a point-like source.*

which can be rewritten in term of error integral:

$$\Delta S_m = \frac{R_1}{\sqrt{A}} e^{\frac{\theta_1^2}{2A}} \int_0^{\frac{\theta_1}{\sqrt{A}}} e^{-\frac{t^2}{2}} dt = \frac{R_m}{\sqrt{A}} \text{Int}(\theta_1) \quad (3.18)$$

With the conventions of figure 3.3 and some trigonometrics, the dependence of R_1 versus the angle θ_1 , and hence the profile of the horn, takes the form of:

$$R_1 = \frac{F \tan \theta_1}{1 + \tan \theta_1 \left(\frac{\text{Int}(\theta_1)}{\sqrt{A}} - \frac{1}{\tan \theta_f} \right) e^{\frac{\theta_1^2}{2A}}} \quad (3.19)$$

The free parameters left in this formulation are three: the distance F , the angle of the exiting profile θ_f and the current through the conductors.

The current through the conductor fixes the maximum angle θ_1 of the particle of a given momentum which can be reduced to zero by the focusing effect of the horn. The relationship between the current I and the maximum angle θ_{MAX} is taken from ref [53], with the detailed discussion about how to deduce the following expression:

$$\theta_{MAX} = \sqrt{\frac{\mu_0 I}{2\pi B_\rho}} \quad (3.20)$$

with B_ρ the rigidity of the particle in Tm .

The other two free parameters, hence F and θ_f are chosen to maximize the focusing of secondary particles in the transverse phase space of interest. All

the description of the horn shape described so far is exact only for a point like source and for a monoenergetic beam.

However the target of the NuFact is pretty long, one or two interaction lengths of mercury, hence 13 cm to 30 cm long. Also the diameter required to accommodate the primary proton beam of ≈ 0.22 cm (1σ) radius has to be of two or three centimeters.

Moreover the NuFact horn should capture pions with a momentum of 250 MeV/c ($E_k \approx 146$ MeV) up to 600 MeV/c ($E_k \approx 476$ MeV), whereas the typical momentum acceptance of existing horn is around 3% [54]. Finally, the small angle approximation is certainly not sufficient to calculate the best horn profile.

The design of the NuFact horn to maximize the flux of pions in the mentioned momentum acceptance followed the procedure described in the next section.

3.1.1 Horn design

As described in the introductory chapter, the energy of the incoming proton beam in the CERN Neutrino Factory design is 2.2 GeV and the radius of proton spot size is assumed to be 0.22 cm (1σ). The target is a cylinder of mercury 30 cm long (\approx two interaction lengths) and 0.75 cm radius. The target is sitting inside the first section of the horn, parallel to the beam axis. The proton spot size, the target radius and the length are not optimized for the CERN scheme but taken from [56] which describes the choice for the US NuFact. The reason is that for proton beam at 2.2 GeV there is a lack of data for pion production to verify the Monte Carlo simulation and any optimization will suffer of an important systematic error.

However, even if the primary proton energy is typically of 20 GeV for the US scheme, one can consider in first approximation that the pion phase space useful for the NuFact does not depend too much on the proton primary energy. This would justify the choice of assuming the same parameters of the US design. A further justification of this assumption is shown in figure 3.4 [55] for the case of pion focused by the US solenoid described in section 3.2.

The efficiency factor for pion production plotted in the figure is defined as the ratio between the number of pion produced per proton divided by the primary proton energy. The efficiency factor is growing with the proton energy if one considers pions without selecting a particular kinetic energy. However, the NuFact phase rotation can accept muons only in a given energy range, which means pions in a selected energy range, for example between 80 MeV and 450 MeV. The efficiency factor computed for pions in this kinetic energy range remains approximately constant over a large range of primary

proton energy. In any case the optimization of the horn design would have to be repeated once the data for hadron production from the HARP experiment will be available [64]. The CERN horn design has been optimized and then

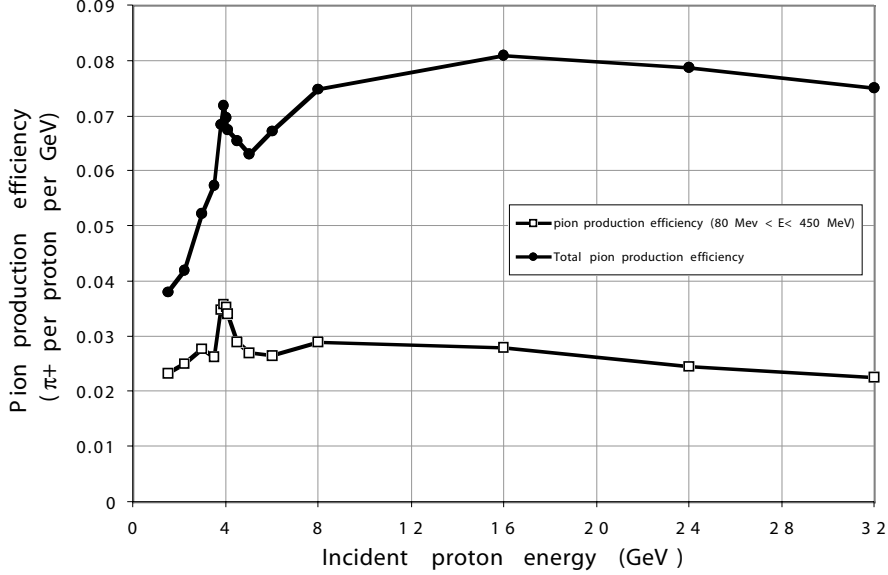


Figure 3.4: *Pion production efficiency for different primary proton energies. Pions are selected in the second curve according to their kinetic energy.*

its performance has been compared with the US capture system described in the following section. If one compares two focusing systems using the same production and transport code, the systematic error due to the pion cross section uncertainty will approximately cancel out, and the result, in first approximation, is a benchmark of the focusing systems. However, since the two focusing systems don't capture the same particles, the effect of the model used by the Monte Carlo particle production code is still not negligible. For this study the secondary particle production and the transport are simulated by MARS [98].

The procedure followed to design the final shape is the following:

- a first-guess shape starting with a point like source and monoenergetic beam is decided. The energy of reference pion to be focused point to parallel is chosen to be 500 MeV/c. For this momentum, as it is shown in figure 3.5, there is a broad maximum for pion production;
- the current is fixed to three different values, 150 kA , 300 kA or 400 kA. This last value is considered a conservative upper limits to reduce

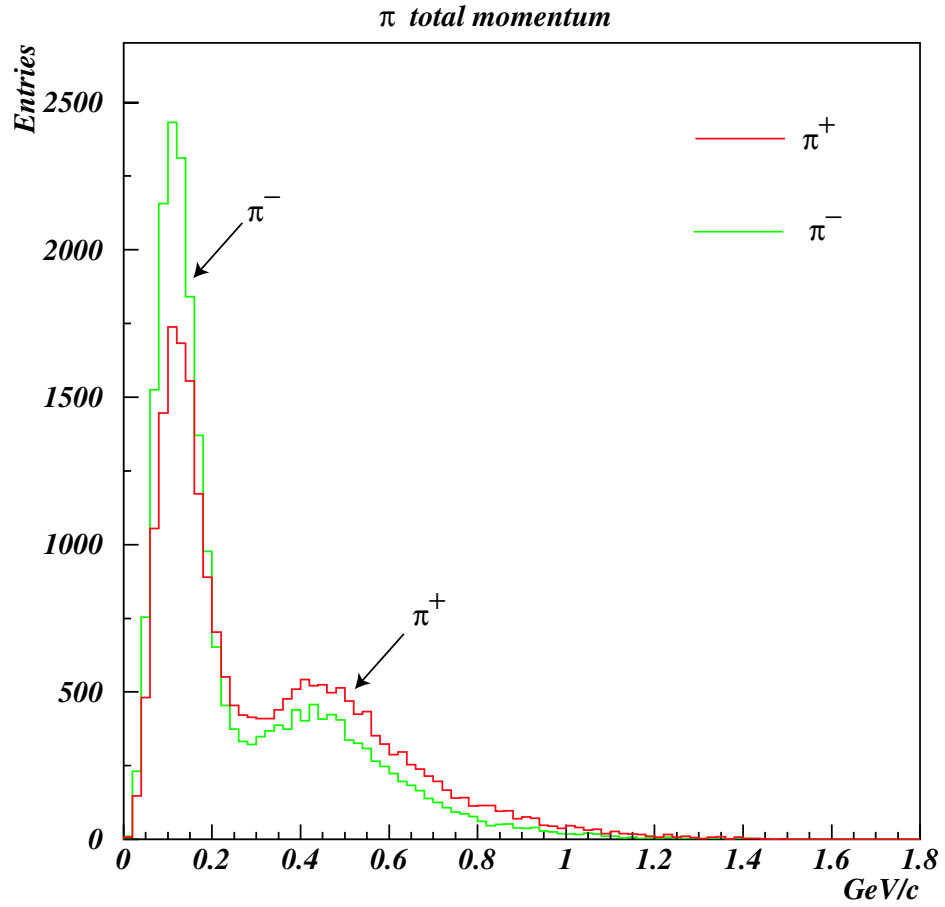


Figure 3.5: *Pion total momentum generated by the mercury target.*

the horn electric and magnetic stresses. For practical reason (see later), the operation value is chosen to be 300 kA;

- pions produced from the target are tracked through the material, the magnetic field of the horn and the magnetic field of the first part of the decay channel solenoid;
- the horn shape is adjusted until a maximum in the flux is reached.

The field configuration, hence the shape of the horn, is chosen to maximize the number of useful particles in the acceptance of the following sections of the machine, in particular for the energy acceptance of the phase rotation and the transverse acceptance of the first muon recirculating linac (μ RFA).

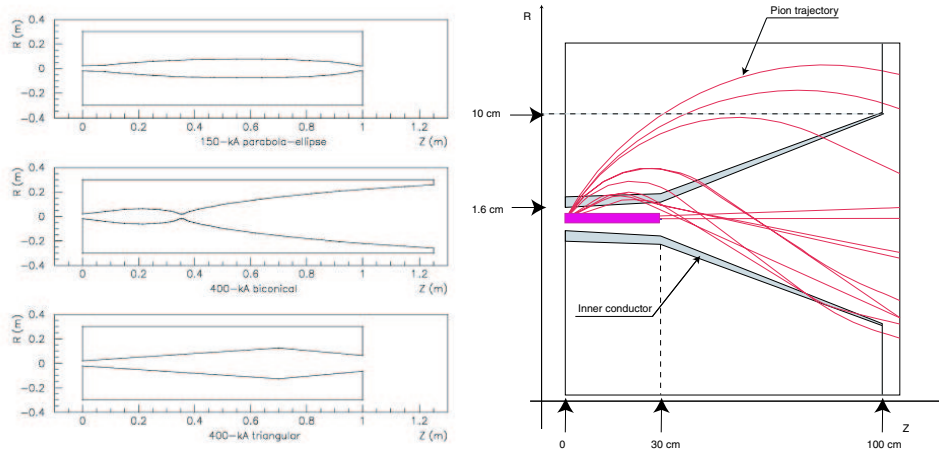


Figure 3.6: *Old Neutrino Factory horn different designs.*

The radius of the pion beam after the horn has to be smaller than 30 cm, otherwise most of the pions will be lost in the following elements, the solenoids of the decay channel, which have a radius of 30 cm. Moreover the decay channel only accepts pions with a transverse momentum smaller than 80 MeV/c.

For the longitudinal plane (E,t), one has to consider that the maximum pion energy that the horn can collect for a given production angle is set by the current, which is limited by mechanical and thermal stresses. A pion of given energy would produce a family of muons with different energies according to the 2-body decay kinematics. To fill the longitudinal acceptance of the phase rotation section, one is interested in muons between ≈ 100 MeV and ≈ 400 MeV kinetic energy. This is translated into a selecting window of pion energy between ≈ 100 MeV and ≈ 700 MeV. If pions with 500 MeV/c (kinetic energy of 379 MeV or total energy of 519 MeV) are focused point to parallel, pions with momentum below 500 MeV/c are over-focused.

Pions are injected in a solenoid positioned 50 cm after the end of the horn. Figure 3.9 shows the field B_z along the beam axis calculated by POISSON[99]. In the case of the horn the simulation of a solenoidal field map is fundamental, since pions are born in a region of zero field and then they traverse the toroidal horn field before going into the fringe field of the solenoid.

Figure 3.6 shows different horn designs tried during the optimization study before coming to the final design showed in figure 3.7. This design has been reached considering particle focusing together with three major technological constraints:

- only smooth angles in the horn shape. For this reason the section where the target is located, the first part of the horn, has a straight section

which reproduce the asymptotic behavior of the left curve of the shape presented in figure 3.3;

- large inner radius, at least 2.3 cm, for the section where the target mercury jet will flow
- no conductors in the forward direction to avoid the mercury deposition on the metal and to reduce the energy deposition from the protons that have not interacted in the target.

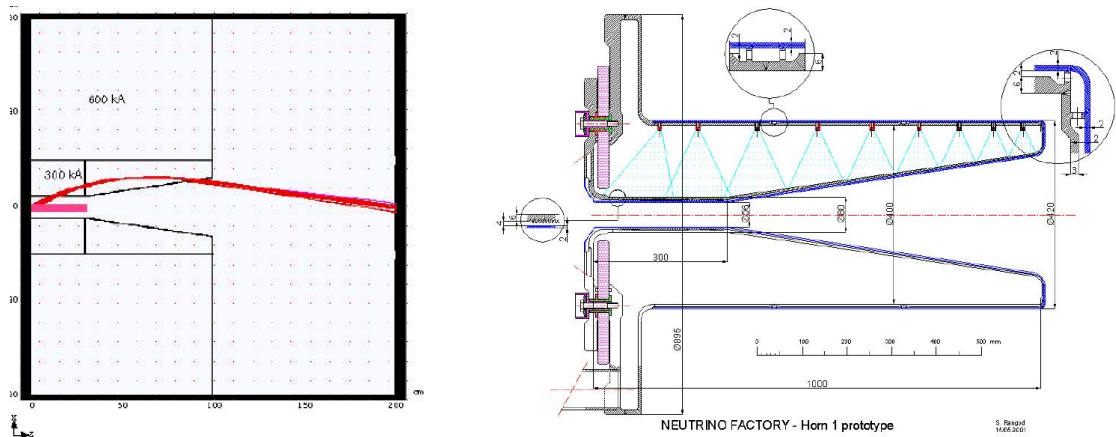


Figure 3.7: *Double horn shape (left) with some particle rays. On the right the prototype drawing taken from [67] for the inner horn.*

Starting from these constraints, in particular the second one, a new kind of horn or double horn has been proposed. The horn system is separated into two sub-devices:

- the inner horn: it focuses low angle particles at high energy and low energy particles. It has a conical shape;
- the outer horn: it focuses high energy particles with high transverse momentum. It is an hollow cylinder.

Those considerations, together with the limits imposed by the construction of the device, lead to the choice of 300 kA for the inner horn current, with a maximum field of 1.5 T, and 600 kA for the outer one, with a maximum field of 0.6 T. Figure 3.8 shows a sketch of the double horn concept and a photo of the first prototype of the inner horn built at CERN.

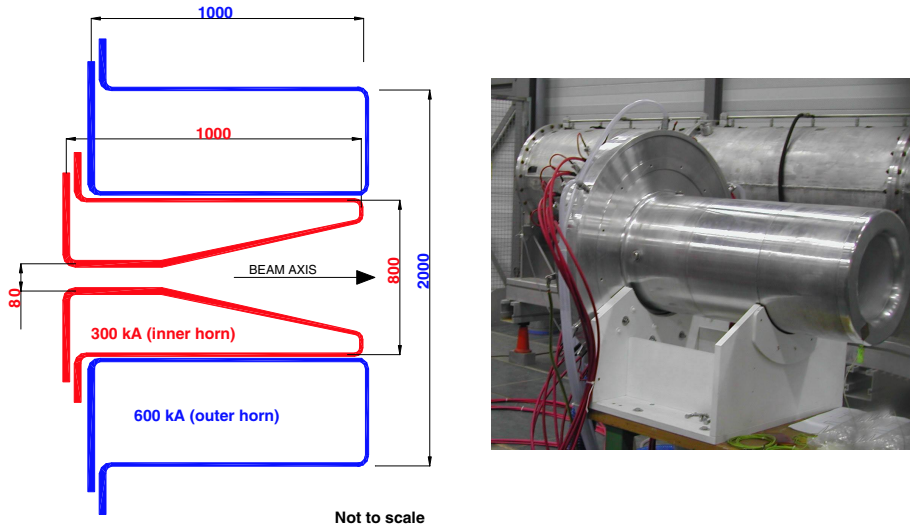


Figure 3.8: *Double horn conceptual design (left) and photo of the first prototype of the inner horn.*

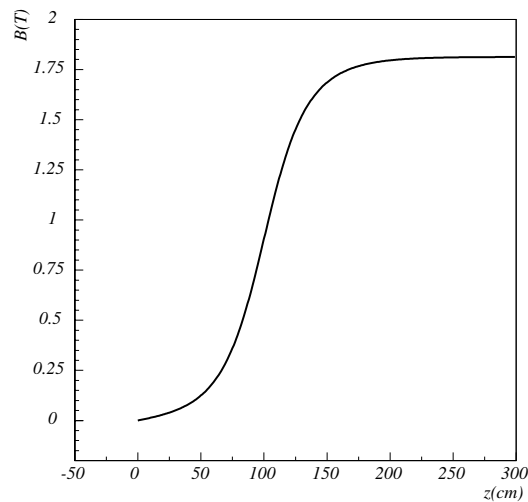


Figure 3.9: *B_z field along the beam axis of half of the first 1.8 T solenoid of the decay channel.*

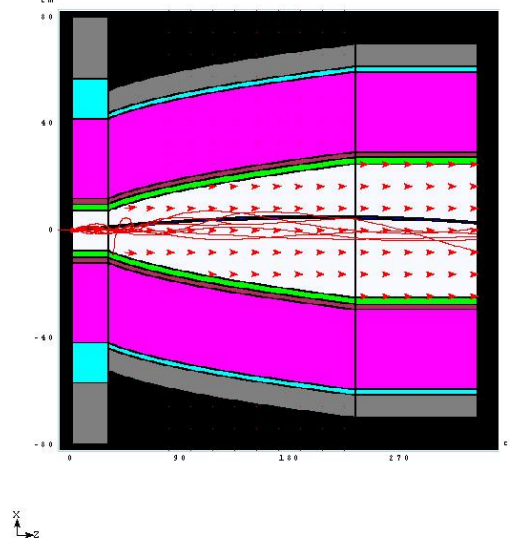


Figure 3.10: *Solenoid capture system. The different colors in the radial axis are for the different material simulated for the shielding of the coil. In blue is shown the trajectory of the mercury jet and in red some pion rays.*

3.2 The solenoid

A brief description for the solenoid capture is given below. For further details one should refer to [61]. The solenoid is composed of two parts (see figure 3.10):

- the straight section: the diameter (ϕ) is 15 cm, 30 cm long and the field (B) is constant along z at 20 T. This section will capture the pions with an average p_T according to:

$$p_T(\text{GeV}/c) \leq 0.075 \phi(\text{m}) B(\text{T}) \approx 0.225 \text{GeV}/c$$

- the tapered section. The field decreases adiabatically from 20 T to 1.8 T over 202 cm according to the formula [61]:

$$B_z(r, z) = \frac{B_0}{\zeta} \left[1 - 0.5 \left(\frac{kr}{\zeta} \right)^2 \right]$$

$$B_r(r, z) = 0.5B_0\left[\frac{kr}{\zeta^2}\right]\left[1 - 0.75\left(\frac{kr}{\zeta}\right)^2\right]$$

where $\zeta = 1 + kz$ and $k = 5$.

Since the action is conserved in an adiabatic varying field, one could show that [60]:

$$B\rho^2 = \text{const} \quad (3.21)$$

$$\frac{B}{p_T^2} = \text{const} \quad (3.22)$$

which are nothing else than magnetic flux conservation through a surface of radius ρ (the radius of curvature of a pion) and the angular momentum conservation. From those two relations one can observe that a reduction of a factor of four in the transverse momentum implies an increase of the same amount for the transverse dimension of the pion beam.

The target is placed in the 20 T solenoid with an angle of 50 mrad and the proton beam is collinear with the target. The angle is not necessarily optimum for the CERN scenario.

The system injects directly into the 1.8 T solenoid of the decay channel, represented in figure 3.10 by the 1 m long straight section after the tapered field.

3.3 Simulation and results

Pions are generated and transported through the magnetic field of the two systems by **MARS**.

Particles are counted at the same distance from the end of the target, namely at $z = 332$ cm, inside the 1.8 T solenoid of the decay channel for both the focusing systems. Figure 3.11 shows the transverse phase space for pions for the horn and the solenoid at the same z location. The ellipse plotted corresponds to a normalized emittance of 1.5 cm rad, namely the transverse acceptance of first μ RFA (Muon Recirculating Linac). The longitudinal plane underlines an important difference between the two systems. As one can notice from figure 3.13, the solenoid collects pions in a larger energy acceptance, while the horn was designed to have pions of 500 MeV/c produced with a transverse momentum of 162 MeV/c exiting from the horn with zero divergence (see figure 3.12 for the transverse momentum before and after the horn). Pions are selected in the transverse acceptance of 1.5 cm rad for both x-x' and y-y' plane and table 6.1 shows the yields for three different energy intervals.

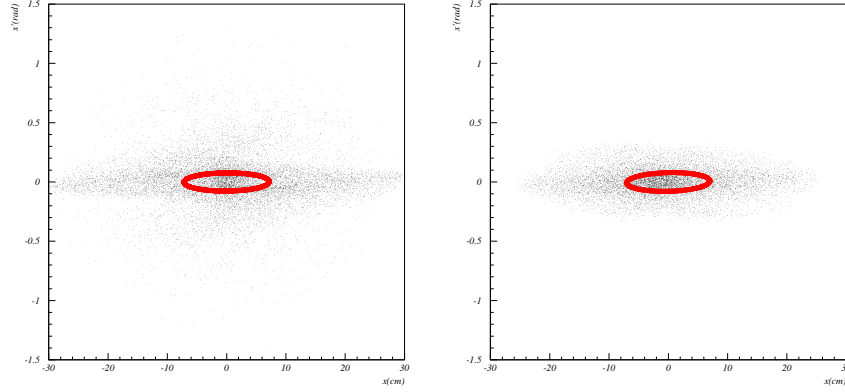


Figure 3.11: *Transverse phase space for pions focused by the horn (left) and by the solenoid (right). The ellipse shows the normalised acceptance of 1.5 cm rad.*

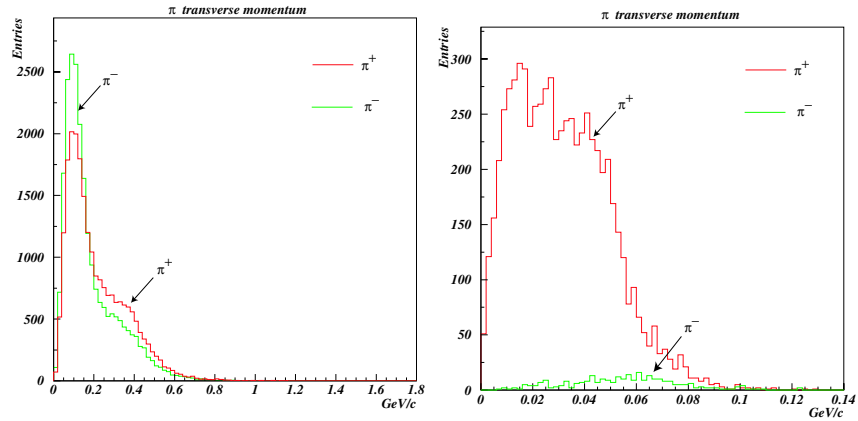


Figure 3.12: *Transverse momentum of positive and negative pions before the horn (left) and after the horn (right).*

Device	No Et cut	$0.2 < Et(\text{GeV}) < 0.8$	$0.3 < Et(\text{GeV}) < 0.6$
Horn	0.0015	0.0014	0.0013
Sol.	0.0045	0.0036	0.0015

Table 3.1: *Pions per P.O.T. (proton on target) after the cut in the transverse plane for the two systems in different windows of total energy Et .*

The solenoid yield should be corrected since the use of a real fieldmap for the tracking reduce the yield by 20-30% [62]. Moreover the separation of positive

and negative pions in the solenoidal capture would introduce another $\approx 20\%$ losses [63]. The solenoid captures more pions than the horn, but most of them are at too high momentum. The horn design provide enough flux to reach the 10^{21} muon per year, which is the final goal of the neutrino factory machine.

3.4 Conclusions

The comparison between two focusing systems, the horn and a superconducting solenoid, has been performed and the simulation shows, as presented in the last column of table 6.1, that the pion flux obtained by the horn is comparable to the solenoid in the energy window of interest for the CERN reference scenario[57].

The advantages of the horn compared to the solenoid capture can be summarized in the following points:

- the horn capture pions in a defined energy range, while the solenoid selects particles with a given transverse momentum. The horn shape can be hence tuned to capture only the interesting pion spectrum. This can be used to concentrate the pion losses at a precise section at the beginning of the decay channel;
- the horn focuses only one sign of pions, as it is shown in figure 3.12. The selected sign can be changed changing the polarity of the horn current. This is not possible with a solenoid, because the only difference between the two charges is the direction of their spiraling in the magnetic field. This horn property is fundamental for the SuperBeam, as described in the following chapter;
- the horn is cheaper than a solenoid, considering that a horn costs about 100 kCHF while the price of the solenoid system is 30 M\$[18] even if it has a shorter lifetime.

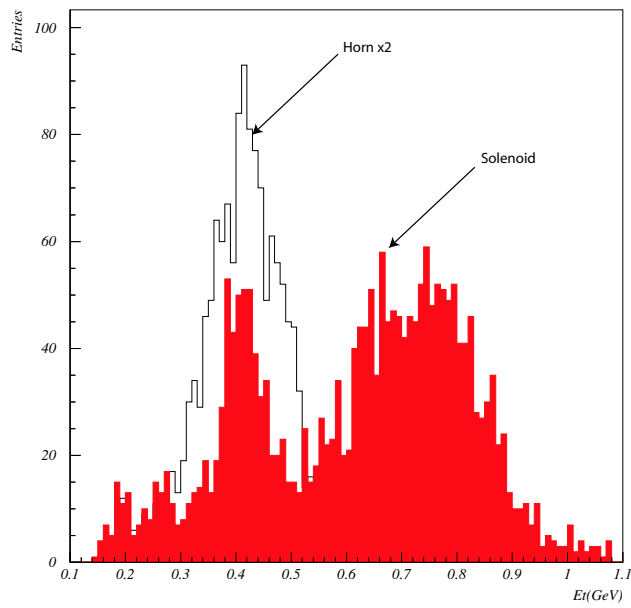
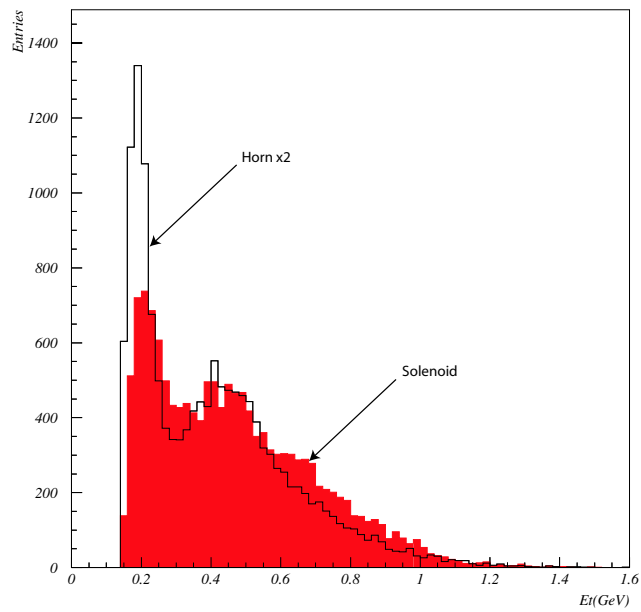


Figure 3.13: Total energy distribution for all the pions (left) collected by the horn (white and multiplied by two) and the solenoid (coloured), and the pions selected in the $x-x'$ and $y-y'$ normalised acceptance of 1.5 cm rad for both planes (right).

3.5 Horn power supply

The currents of the inner horn current (300 kA) and of the outer horn (600 kA) are pulsed at the same repetition rate of the proton driver, which is 50 Hz, with a pulse length longer than the proton pulse length, hence longer than $\approx 3.2 \mu\text{s}$.

Two successive prototypes of the power supply have been developed to test the design of some elements for the final power supply of 300 kA and to start the mechanical tests of the inner horn prototype [73],[74].

3.5.1 Basics of dumped current circuit

From the electrical point of view the magnetic horn is a mainly inductive load with a small resistance. The current through the horn is generated by discharging a set of capacitors connected to the horn through high power thyristor switches (see figure 3.14 for the simplified equivalent circuit). The

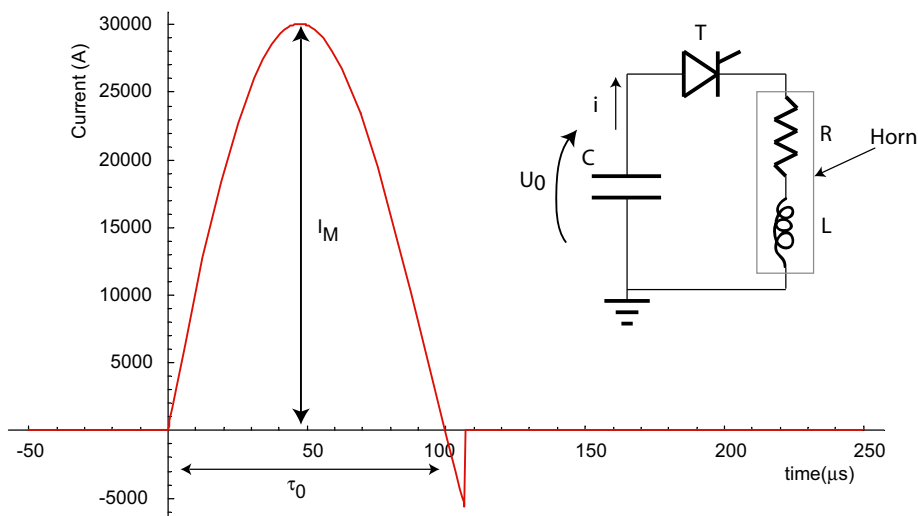


Figure 3.14: *Equivalent circuit of the horn power supply and the current pulse*

capacitor banks are charged by a high voltage and high current. Once the thyristors close the circuit, the voltage of the capacitors generates the high current which goes to the load, in this case the horn.

The dumped circuit shown in figure 3.14 is the equivalent circuit of the horn real power supply. In particular, R is the total circuit resistance, L the total

inductance, C the total capacitance and U_0 the capacitance charging voltage. The current pulse flowing in the circuit equals:

$$i = \frac{U_0}{\omega L} e^{-\delta t} \sin(\omega t) \quad (3.23)$$

where:

$$\begin{aligned} \delta &= \frac{R}{2L} \\ \omega &= \omega_0 \sqrt{1 - \gamma^2} \\ \omega_0 &= \frac{1}{\sqrt{LC}} \\ \gamma &= \frac{R}{2} \sqrt{\frac{C}{L}} \\ \tau_0 &= \frac{2\pi}{\omega_0} \end{aligned}$$

Assuming for the different components $L = 1 \mu\text{H}$, $C = 1000 \mu\text{F}$, $R = 5 \text{ m}\Omega$, which corresponds to the nominal value of the first power supply prototype, a charging voltage $U_0 = 1250 \text{ V}$, the current pulse $\approx 100 \mu\text{s}$ long has the shape shown in figure 3.14. Table 3.2 summarize the electric parameters of the final power supply.

The final power supply will have a pulse length of the order of $\approx 100 \mu\text{s}$ to limit the voltage of the horn conductors below 7 kV , which is considered a safety value deduced from previous experience [68].

3.5.2 Layout of the prototype power supply

The first horn power supply prototype has been built to deliver a total current of $\approx 30 \text{ kA}$. The repetition rate has been limited, for budgetary reasons, to 1 Hz instead of the nominal 50 Hz while the pulse length of $\approx 100 \mu\text{s}$ corresponds to the final design requirements. The electric circuit, shown by figure 3.15, is composed by two parallel units, each one delivering a current of 15 kA (see figure 3.16). Each unit is connected to the magnetic horn by 10 parallel 10 m long coaxial cables, as shown in figure 3.18, and both units are charged with one common capacitor charger (see figure 3.17). The circuit is controlled by a separated system (see figure 3.19) mounted on the same rack of the charging power supply, which contains the high voltage distribution box, the timing chassis, the pulse repeater chassis, the interlock chassis and

	Units	Value
Distance capacitor plus switching unit from horn	m	≤ 10
Peak current in horn	kA	300
Pulse repetition rate	Hz	50
Inductance of horn (max.)	μH	0.3
Additional inductance	μH	0.4
Total inductance (max.)	μH	0.7
Resistance of horn at 100°C (with skin effect)	$\mu\Omega$	180
Additional resistance	$\mu\Omega$	320
Total resistance (max.)	$\mu\Omega$	500
Total capacitance of capacitor bank	μF	≈ 1400
Pulse duration (half period)	μs	≤ 100
Skin depth	mm	1.25
Charging voltage	V	≤ 7000
Energy stored in capacitor bank	kJ	≈ 35
Stored energy recovery rate	%	86
Voltage on element	V	< 4000
r.m.s. current in horn	kA	15
Mean power dissipation in horn by current	kW	40
Water flow needed in horn for $\Delta T_w \leq 7^\circ\text{C}$	l/min	82
Number of pulses per month of operation		1.3×10^8

Table 3.2: *Horn and power supply summary table.*

the mains distribution box.

Once the capacitor charging voltage is set 1250 V, which is the maximum output voltage of the FuG[©] capacitor charger, the current through the horn reaches 31 kA. In particular the peak current of the first unit is 15 kA and of the second 16 kA. The pulse width is $\approx 105 \mu\text{s}$, which is slightly longer than the 100 μs aimed. This lengthening of the pulse has been corrected in the upgrade of the power supply: it was due to a too long current circuit inside the discharge units, generating a parasitic inductance.

In the second phase of the R&D program, the variation of the current path inside the discharge circuit and the exchange of the charging power supply allowed the increase of the current up to 100 kA, as shown in figure 3.20.

Unfortunately part of the discharge circuit has been built with electrical components refurbished from other circuits to keep the costs as low as possible. In the case of 100 kA, the repetition rate has been lowered to 0.5 Hz in order to avoid the breaking of some of those components, and to avoid the risk of breaking one of the thyristor from the pile up of heating from one pulse to

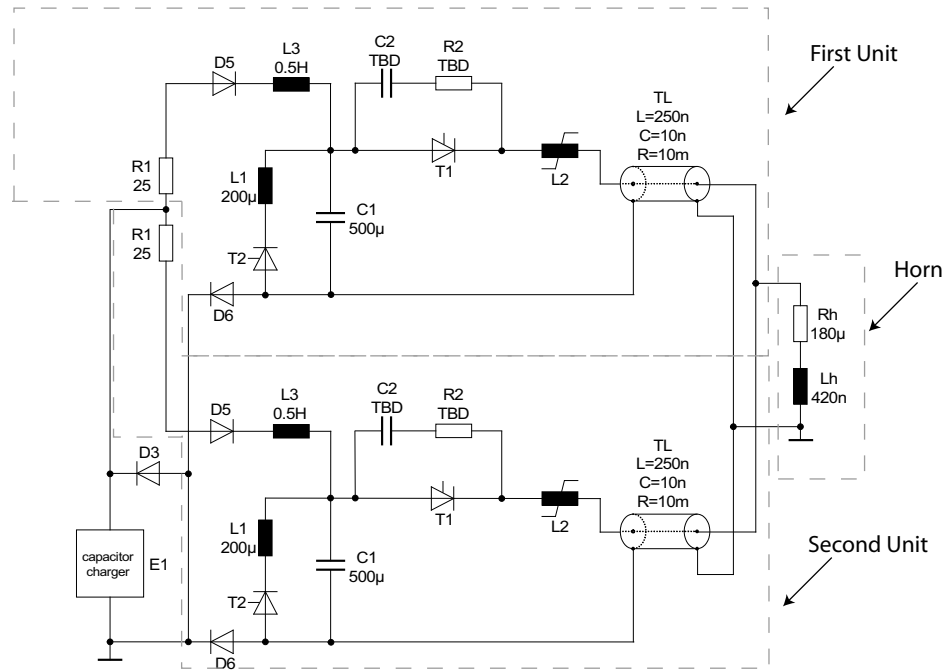


Figure 3.15: *Power supply electric scheme.*

another.

3.5.3 Horn lifetime estimate

The estimate of the horn lifetime is a key point for the design of the horn itself and the design of the target station.

Different effects contribute to the lifetime of the horn. The principal factors considered are:

- material property variation with temperature;
- material corrosion due to the water cooling;
- energy losses from the current;
- fatigue due to the current induced mechanical stresses;
- energy losses due to the interaction of primary and secondary charged particles with the conductors;
- radiation damage induced by neutrons.



Figure 3.16: *One of the two units of the discharging circuit. At the right bottom corner the red cables are connected to the horn. The capacitor banks are located behind this unit.*

The first factor which assure a long life time is the choice of the proper material for the horn construction. The material chosen for the NuFact horn



Figure 3.17: *Set of capacitor banks used for the discharging circuit. The discharging circuit is located in front of this unit.*

is the aluminium alloy 6082-T6, commonly used in nuclear reactors, whose chemical composition, compared to the ones of the Al 7075 and the Al 6061

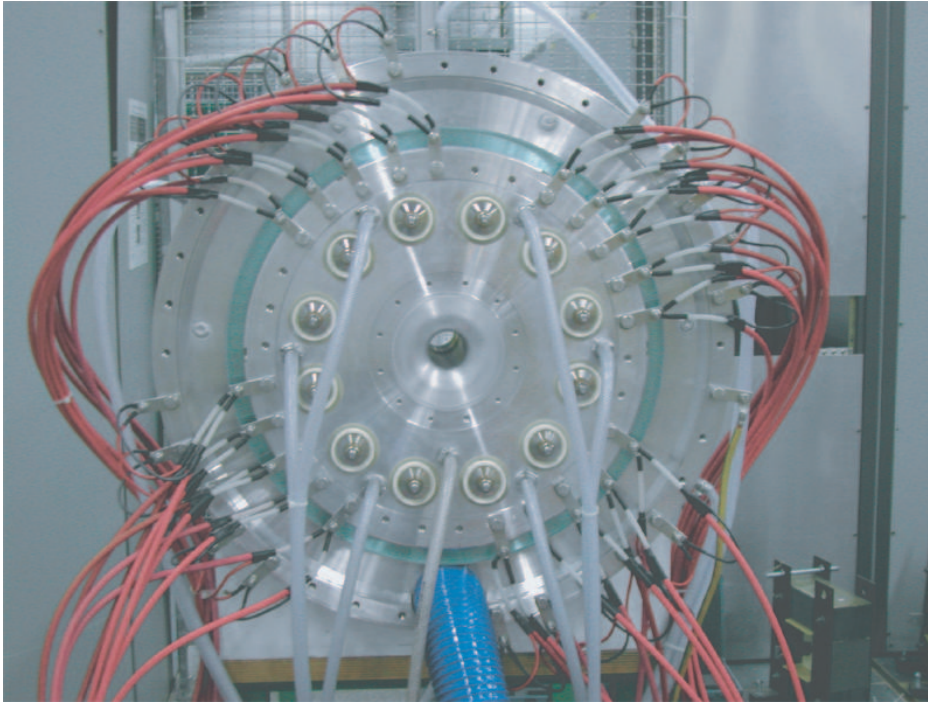


Figure 3.18: *Electric connection on the back of the inner horn prototype. The blue tube is the water cooling exhaust pipe.*

alloys, is reported in table 3.3. Those three alloys are used for the construction of horns, the first two at CERN and the last in the US.

These particular alloys are chosen because they are weldable, they have good corrosion resistance (even in marine atmosphere), they are well suited to most of the common surface treatment processes (anodising, chromating, phosphating, painting, plating etc.) and they have good strength properties to above 100 °C. In particular, as shown in figure 3.21, the ultimate tensile strength, the greatest longitudinal stress the material can bear without breaking apart, of the Al 6082-T6, starts to decrease after 100 °C, compared to the room temperature operating conditions.

For this reason the horn is equipped with a double cooling system to assure that the increase of the temperature in the horn conductors due to the current Joule losses and the particle energy deposition remains below 100 °C. The cooling system is composed of two elements. The first is series of nozzles which spray water inside the magnetic volume to cool the internal surface of

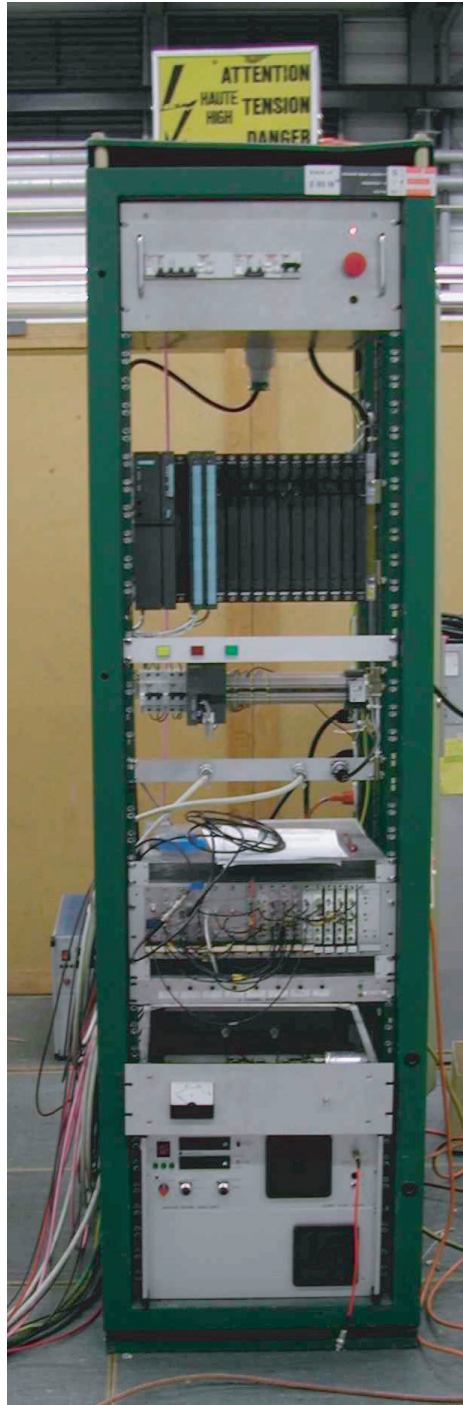


Figure 3.19: *Power supply controller rack. From the bottom to the top: high voltage charging unit, timing circuit, controller, electric switches.*

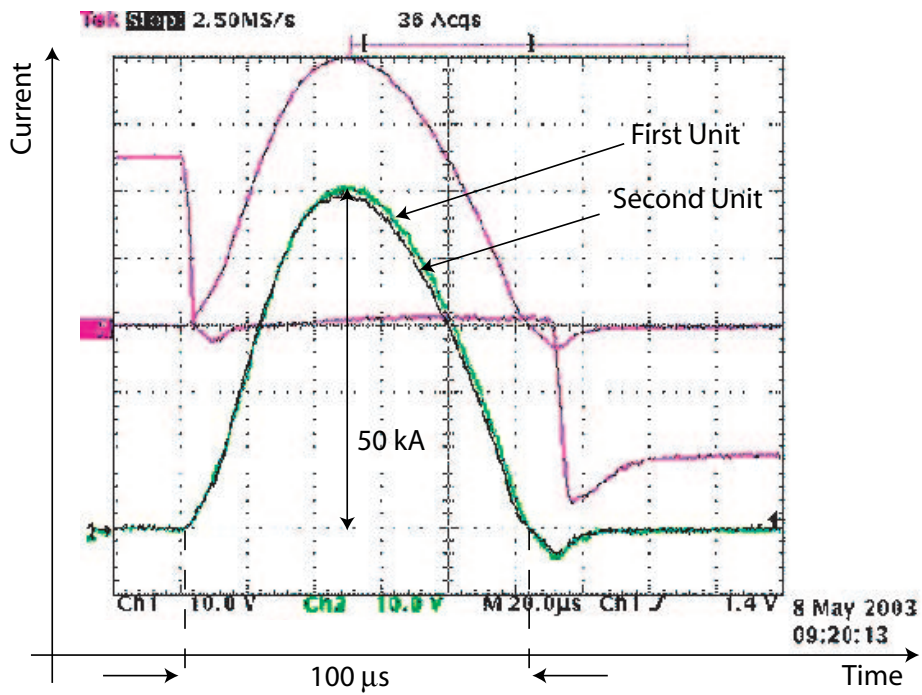


Figure 3.20: Power supply current discharge for 100 kA, signal recorded from the controller oscilloscope.

Al 6082-T6									
%	Si	Fe	Cu	Mn	Mg	Cr	Zn	Ti	Al
Min	0.7	0.0	0.0	0.4	0.6	0.0	0.0	0.0	Bal
Max	1.3	0.5	0.1	1.0	1.2	0.25	0.2	0.1	Bal
Al 6061-T6									
%	Si	Fe	Cu	Mn	Mg	Cr	Zn	Ti	Al
Min	0.4	0.0	0.04	0.0	0.8	0.04	0.0	0.0	Bal
Max	0.8	0.7	0.15	0.15	1.2	0.35	0.25	0.15	Bal
Al 7075-T6									
%	Si	Fe	Cu	Mn	Mg	Cr	Zn	Ti	Al
	0.40	0.50	1.60	0.30	2.50	0.23	5.60	-	Bal

Table 3.3: Al 6082-T6 alloy chemical composition compared to the Al 6061-T6 and the Al 7075-T6 alloy chemical compositions[69]. Bal=balance indicates the portion of Aluminium to reach the 100% material composition once the other chemical component fractions are chosen.

the conductors. Moreover a curtain of water flows in contact with the con-

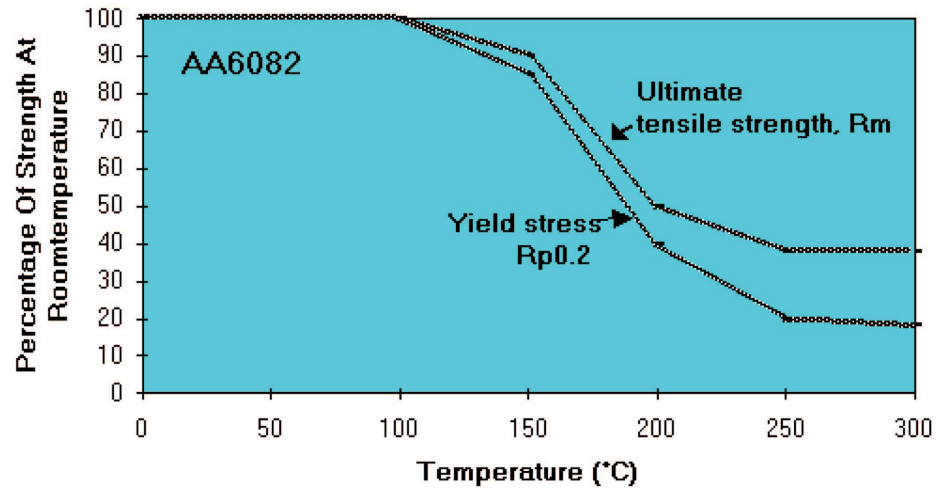


Figure 3.21: Material strength variation after operation at the given temperature. 100% indicate the material property at room temperature.

ductor to cool the conductor external surface, as shown in figure 3.22 (refer to table 3.2 for the total water flow and temperature rise). The water curtain

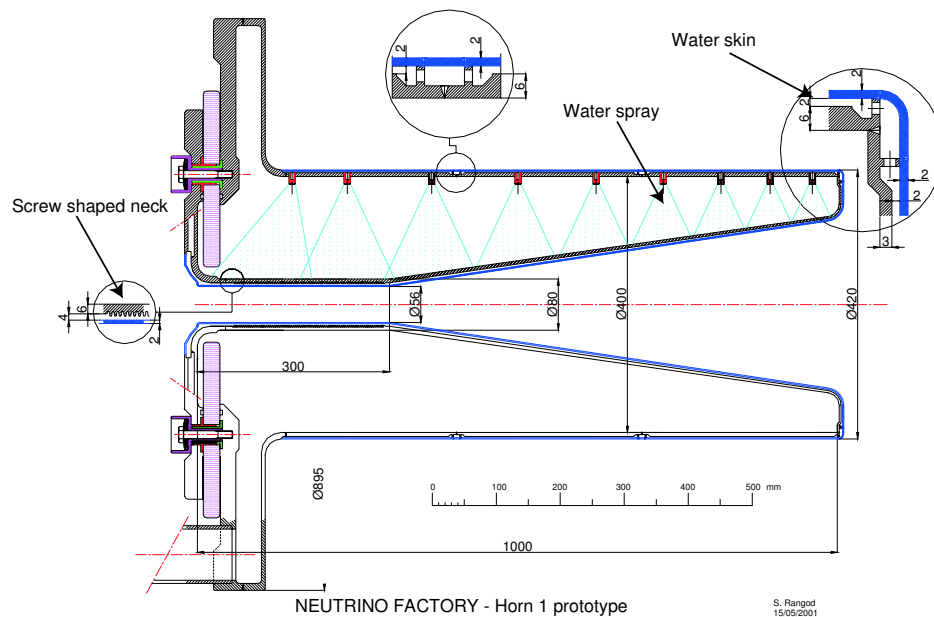


Figure 3.22: Horn prototype cooling system.

follows the shape of the conductors and, as shown in figure 3.22, the neck surface has been shaped like a screw to increase the heat exchange surface

in the weakest and hottest zone (see figure 3.23).

This arrangement seems to assure the proper cooling, even if the increase



Figure 3.23: *Horn neck conductor shaped like a screw to increase the thermal exchange surface.*

of temperature due to the particle energy deposition is uncertain.

The second limiting factor for the horn life time is given by the fatigue limit that the alloy can reach.

As described in the previous section, the inner horn current of 300 kA is pulsed at 50 Hz with a pulse length of $\approx 100 \mu\text{s}$. The maximum mechanical stress induced by the magnetic field is located in the neck of the horn. The stress has been evaluated to be 14.8 MPa for the peak current. Under this pressure, according to fatigue curve shown in figure 3.24, the material breaks after more than 10^7 cycles. With a meaningful extrapolation of the curve of figure 3.24, one can assess that the material will break after more 10^8 cycles. Assuming that the rupture limit is 2×10^8 cycles, which has to be considered a safe lower limit, the horn life time would be of 6 weeks pulsing at 50 Hz. Three caveats have to be mentioned about this life time limit.

The first is that the fatigue curve of figure 3.24 should be measured for a bigger number of cycles in order to assess the fatigue limit. For some materials, in fact, the fatigue curve flattens for low applied stresses, pushing the fatigue limit well above the 10^8 cycles considered. This is shown in figure 3.25 for the Al 6061-T6, from which one can argue that, for 14 MPa applied in the horn neck, the number of cycles can exceed 10^8 . Since the Al 6082-T6

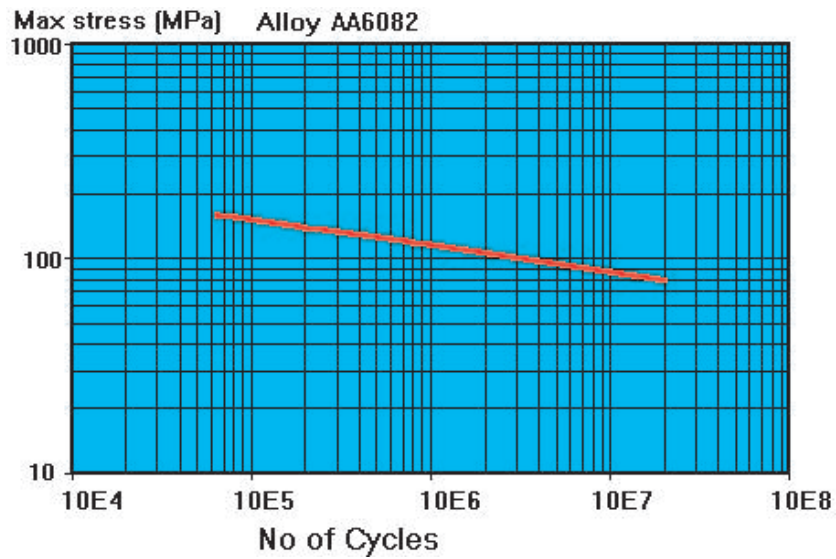


Figure 3.24: *Fatigue curve for the Al Alloy 6082-T6.*

is considered as a new and improved version of the Al 6061-T6, one can hope that the material would follow for a large number of cycles the same behavior of its predecessor.

The second caveat comes from the fact that the fatigue curves only apply

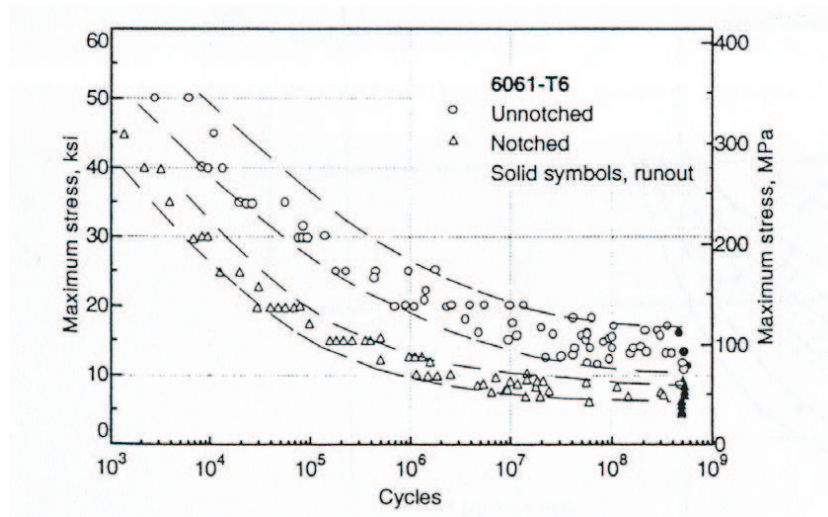


Figure 3.25: *Fatigue curve for the Al Alloy 6061-T6[70]. Solid points indicate runout (no failure).*

to the behavior of bulk material. However, the alloy has to be welded to

assemble the different components. The welding technique which assure the smallest degradation of the mechanical properties is the electron beam welding. Even with this technique the material strength at the location of the welding is reduced by 20%. The different parts of the horn are designed such that the welding points are subject of reduced stresses, well below the ≈ 14 MPa cited as the most intense pressure applied to the horn neck.

The third caveat is that the behavior of the material once irradiated by the particles produced by the target, which are mainly protons and neutrons, could be different than from unirradiated material. Under certain conditions, in fact, the irradiated material could reach the fatigue limit before or after the unirradiated fatigue limit. From previous experience coming from the CERN AD (Antiproton Decelerator) horn [71], see figure 3.26, it seems that the horn life time is reduced by a factor of two comparing the non irradiated case to the irradiated one. Even if it turned out that the AD horn



Figure 3.26: *AD horn (left) and view of a broken AD horn (right) during its replacement from the beam line.*

is not directly comparable to the NuFact horn because of its material and dimensions (see table 3.4 for the NuFact horn dimensions), it is useful to learn its failure modes and check if this would apply also to the NuFact case (see figure 3.26 for a broken horn).

The AD horn material is the aluminium alloy 7075 (see table 3.3 for its composition), which is commonly used for airplane construction or car bumpers. This material has been chosen because it has a high tensile strength which is needed to support the pressure induced on the 6 mm radius of the neck. This small neck radius and the use of a current of 300 kA are imposed by the focusing of the forward 3 GeV/c antiprotons.

The horn operates at a temperature of 60-130 °C and it is air cooled to keep the temperature below 160 °C, after which the unirradiated aluminium starts to degrade abruptly. Under these operating conditions, the fatigue limit is reached after $\approx 10^7$ cycles, corresponding to one year of operation.

Two factors gives the major contribution to the life time limit: the material

properties variation at high temperature under irradiation and the radiation damage induced by secondary particles.

Once a metal is irradiated with a high flux of particles, Hydrogen and Helium nuclei can be produced via the (n,p) and (n, α) reactions with the Aluminium. When the quantity of those two gases becomes large, for example under a neutron irradiation of more than 10^{26} n/m²⁰, one can observe the creation of bubbles of few micrometer diameter inside the material. This effect is known as swelling, which indicates the local material density variation due to the gas formation. For the Al alloys there is also a second form of swelling due to the precipitation of transmutation-produced Silicon. The swelling for different Al alloys, and in particular for the Al 6061-T6 is shown in figure 3.27. For

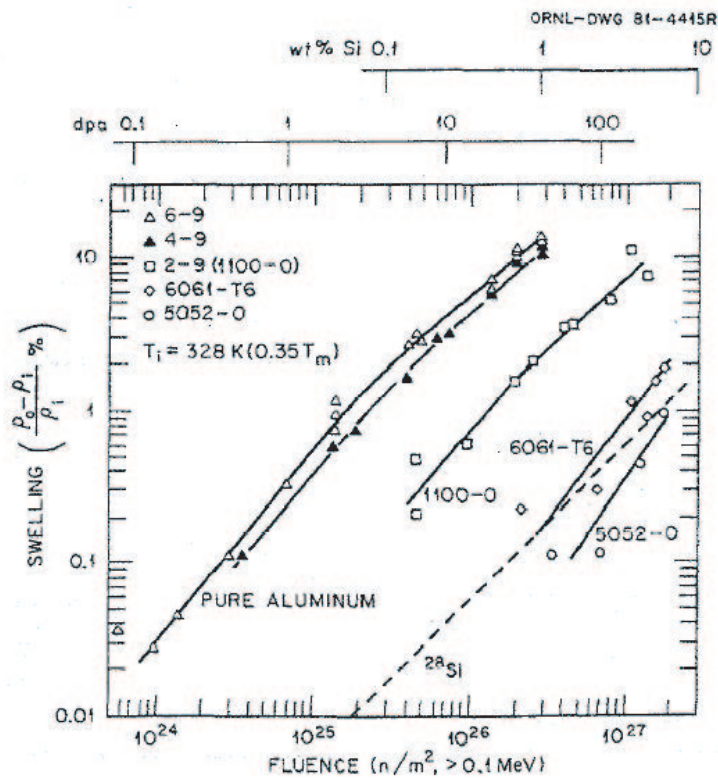


Figure 3.27: Swelling for Aluminium alloys after neutron irradiation at temperatures $60^\circ\text{C} < T_{IRR} < 100^\circ\text{C}$ [72].

intense neutron irradiation, bigger than 10^{26} n/m² which corresponds to at least 10 weeks of NuFact operation, the Al 6061-T6 shows a variation of the density of around 1%. This variation is considered negligible and becomes even smaller if the material is cyclically stressed at high frequency, as would

be the case for the horn material.

The density variation, however, is increased for operation temperature above 100 °C. The horn cooling system has been designed to keep the temperature below this limit, which is not the case for example for the AD horn, and this is considered the main reason for the AD horn failures.

The second effect due to the material irradiation is related to the fact that proton and neutrons passing through matter can lose energy without ionising the material. In particular particles can displace atoms of the material lattice from its normal position. If the number of displacements becomes important, the material mechanical properties can change, anticipating for example the elastic to plastic transition in the material behavior. The number of displacements produced inside a material is defined in terms of *dpa*, displacements per atom. The typical irradiation of the NuFact horn during six weeks corresponds to an irradiation which causes ≈ 10 dpa. This amount of damage is retained acceptable and it is not considered to be the trigger of a material failure. The horn material, in fact, operates in the elastic regime and the magnetic induced stresses are far below the elastic to plastic transition. A ≈ 10 dpa radiation damage is not intense enough to provoke an abrupt material failure. However, no data are available for Al 6082-T6 once irradiated and it would be interesting to evaluate the behavior of this alloy for large radiation damage, bigger than ≈ 100 dpa, to better assess the NuFact horn upper limit life time.

Once all these different factors have been analysed, it becomes clear that the best way to assess the final NuFact horn life time would be to pulse the horn while irradiating with beam. This experimental approach, however, requires the exposure of the only horn prototype build for a very long time until breaking, since no proton driver with high repetition rate is available to produce in short time the same integrated damage.

Instead of this, the horn life-time can be also deduced from existing horns operating in similar conditions, excluding the AD horn for the already mentioned reason. Figure 3.28 shows the existing horns operating in different neutrino experiments. The most similar to the NuFact horn is the MiniBoone horn, at Fermilab. The primary proton energy is 8 GeV, which produces a secondary particle beam comparable to the NuFact case, even if the flux is at least one order of magnitude less intense.

The horn material is Al 6061-T6, whose characteristics has been discussed above. This horn has been pulsing without any failure for $\approx 100 \times 10^6$ pulses, which corresponds to 3 weeks of the Neutrino Factory case, and it is still running. This allows to confirm the estimated lower life time limit of the NuFact horn to 6 weeks, and the upper life time to 60 weeks, namely one year of operation.

Dimension	
Total length	1030 mm
Outer diameter	420 mm
Max diameter (electrical connection flange)	895 mm
Free waist aperture	56 mm
Waist outer diameter	80 mm
Average waist wall thickness	6 mm
Double skin thickness	2 mm
Material	Al 6082-T6

Table 3.4: *Main mechanical dimensions of the inner horn.*

3.5.4 Cost of installation

The costs of the horn prototype together with the power supply prototype for 100 kA, 1 Hz described in section 3.5.2 are summarized in the following table:

Table 3.5 shows that the major costs come from the power supply and not

Item	Estimated value
Horn	77,898.00 CHF
Capacitor banks	16,432.00 CHF
Two discharger units (elements)	90,807.00 CHF
H. V. Control System	20,325.00 CHF
H. V. Power Supply (old one)	13,707.00 CHF
H. V. Power Supply (new one)	28,000.00 CHF
Cables	4,163.00 CHF
Racks	6,292.00 CHF
Total	257,625.00 CHF

Table 3.5: Cost of the first horn prototype and for the second prototype of the power supply

from the horn itself, even for a power supply which operates at 1 Hz and at one third of the current desired.

The cost for the final power supply, which should pulse a current of 300 kA at 50 Hz, with a pulse length of 100 μ s, is quoted at about 1.5 MCHF.

However, one has to consider that this power supply has a life time of at least 10 years, and it will not be changed every time a horn will break.

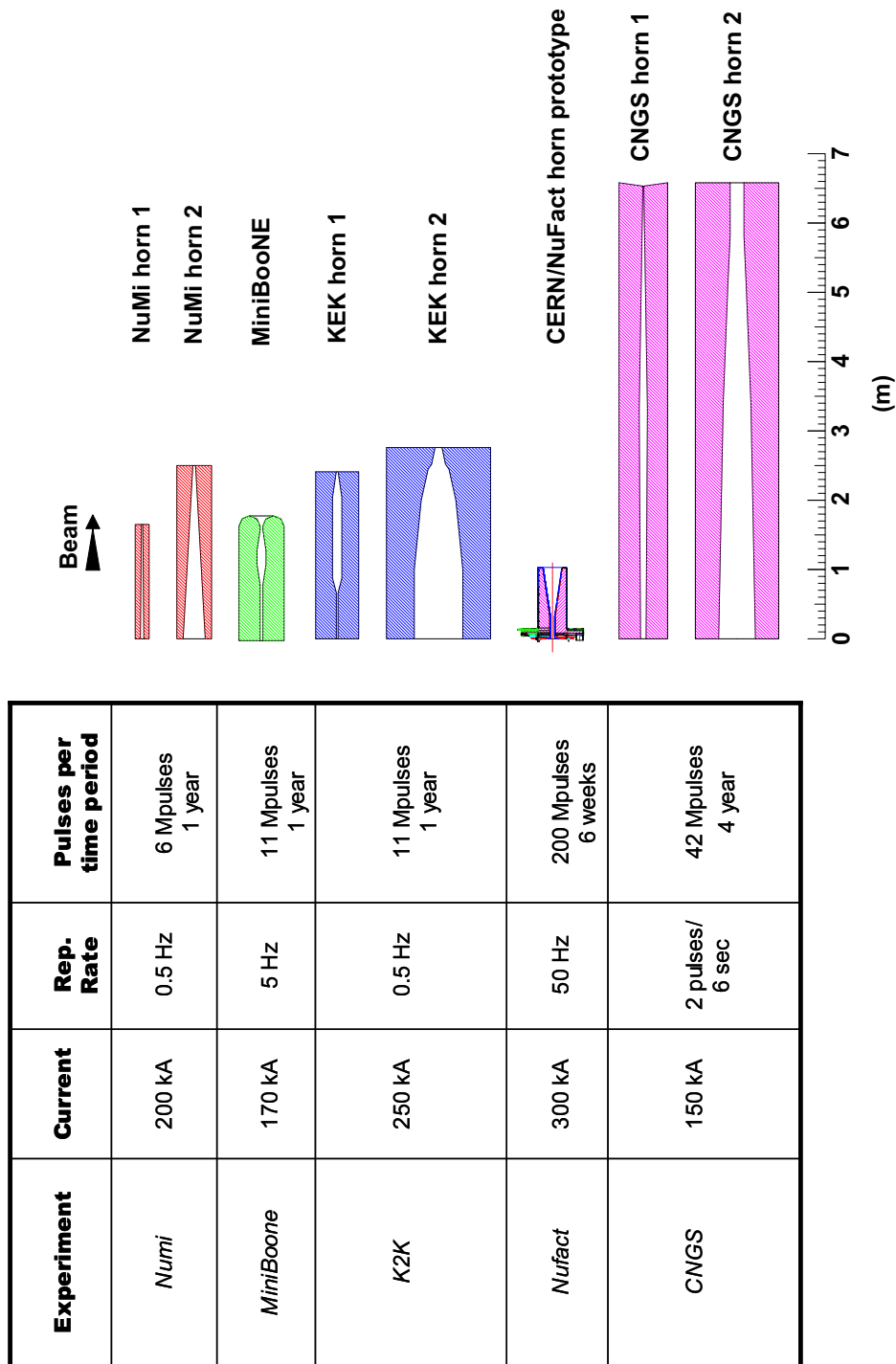


Figure 3.28: Summary of operating horns in different experiments with their operating parameters.

3.6 Horn vibration measurements

The knowledge of a horn vibration eigenfrequencies is fundamental to avoid resonant excitations via the power supply pulse during normal operations. The eigenfrequencies are usually determined by capacitance measurements [75] or via laser interferometry. For the measurement of the horn vibrations with the power supply running at 30 kA, an acoustic method was applied and it turned out to be accurate enough. The measurements have been repeated after the upgrade of the Neutrino Factory prototype power supply from 30 kA to 100 kA using a laser interferometer.

3.6.1 Generalities of the acoustic method

Mechanical vibrations are very often a source of sound which can be measured, for example, by a microphone, if the frequency range lies between ten of Hz to some ten thousands Hz.

The horn aluminum-alloy conductors excited either by a non-calibrated hammer or by its power supply, behave like a massive vibrating membrane, which produces a measurable sound like a percussion instrument. The Fourier analysis of the sound spectrum reveals the horn mechanical vibration eigenfrequencies.

3.6.2 Technical description of the method

The sound emitted by the excited horn is recorded by a directional microphone[†][78] directly connected to a PC and stored in a .wav[‡] file. A typical measured time series obtained from the recording is shown in figure 3.29 where the CNGS prototype horn is excited by a current of 100 kA with the time structure presented on the left diagram of the same figure. The .wav file is then post-processed via a Matlab[©][80] code or via Audacity program[81] to calculate the signal FFT (Fast Fourier Transform) and the power spectrum. The different eigenfrequencies are identified by the peaks in the power spectrum histogram (see figure 3.32), once the frequencies generated by the environment noise are rejected. For this purpose the noise is recorded without exciting the horn and placing the microphone in the same points where the data measurements are taken. Then the background is processed in the same way as the data.

[†]see Appendix for the microphone specifications

[‡]Wave files (.wav) are sound files with a specific format that can be found for example at [79]

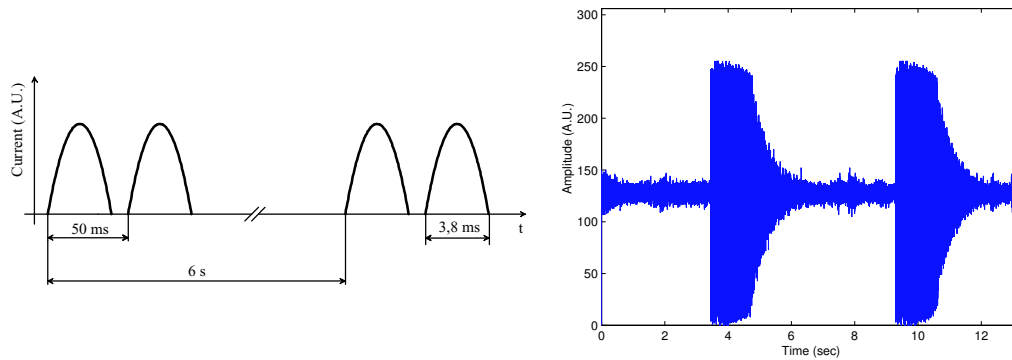


Figure 3.29: *Two current pulses with the time structure on the left excite the CNGS horn whose vibration generates the sound with the amplitude shown on the right picture.*

3.6.3 Validation of the method: CNGS and AA horn measurements

The acoustic method has been validated by comparing the measured eigenfrequencies with the results obtained by other techniques, such as measurements using accelerometers, for the CNGS and the AA horns.

The CNGS horn is the magnetic lens chosen to focus pions and kaons which generate the CERN-to-Gran Sasso neutrino beam (see figure 3.30 for the horn geometry). The microphone is placed in front of the endplate opposite to the strip line connection (see figure 3.30). The endplate (see figure 3.31) is excited by a non calibrated hammer for the first measurements. The

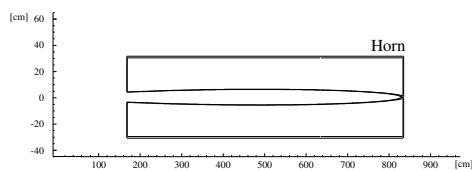


Figure 3.30: *CNGS horn layout and the photo of the first prototype connected to the power supply by a series of strip lines[75].*

environment noise is recorded in the same place without any excitation and processed as the signal to discard the noise eigenfrequencies. The signal and the noise FFT are shown in figure 3.32. The measured eigenfrequencies are



Figure 3.31: *The flange measured is at the opposite side of the power connection.*

Mode	Meas. Ref. (Hz)	Calc. Ref. (Hz)	Meas. Microp. (Hz)
1	111	139	107.66
2	392	364	398.36
3	424/426	-	-
4	568/570	-	570.63
5	744/746	-	742.9
6	882/884	-	904.39
7	916/914	-	-
8	956	-	958.22
9	1202	-	1200.00

Table 3.6: *Comparison between measured and calculated eigenfrequencies (taken from [75], second and third column) and those measured with the microphone.*

compared with the results published in [75] and reported in table 3.6. There is a slight discrepancy for the 3rd and the 7th modes (424 Hz and 916 Hz) which are hidden in the large peak of the previous harmonic (see figure 3.32). In the case of the acoustic method, the two modes at 260 Hz and 500 Hz are rejected since they are clearly coming from the background noise (see figure 3.32). Once the CNGS horn is excited with its power supply of 100 kA, two pulses 3.8 ms long separated by 50 ms every 6 s (see figure 3.29, left), the measure is repeated and the result is in good agreement with the previous one, as shown in figure 3.33.

The Antiproton Accumulator (AA) horn (see figure 3.34) is a small horn used at the beginning of the AA program to focus antiprotons produced at the PS target station for the SPPS proton-antiproton collision physics program. Its eigenfrequencies were calculated by a numerical model [82] and reported in table 3.7 together with the measured frequencies via the acoustic method.

The last two columns of table 3.7 reports the measured frequencies when horn is supported by a chassis with free boundaries (third column) and when

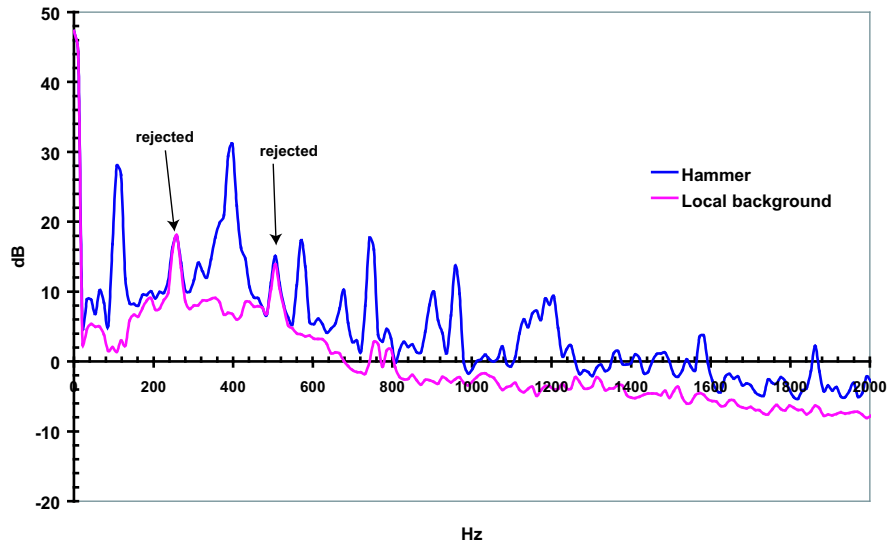


Figure 3.32: *CNGS horn FFT analysis of the non calibrated hammer excitation and signal compared to the background noise.*

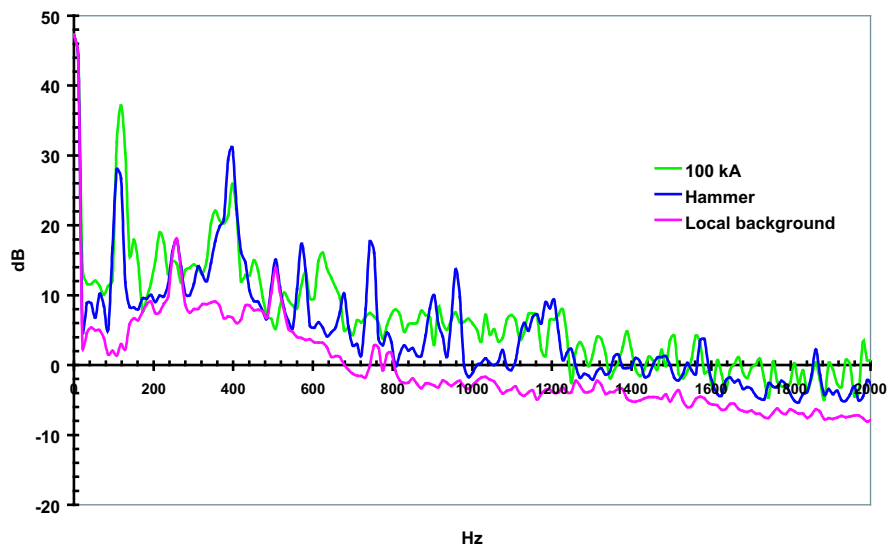


Figure 3.33: *Same as figure 3.32 with superimposed the measurement at 100 kA.*

the horn extremities are blocked (fourth column). The last case should better reproduce the calculated eigenfrequencies values since the numerical model was solved imposing no displacement for the two flanges as boundary condi-



Figure 3.34: The AA horn has a conic design very similar to the more recent neutrino horns scaled by a factor of 10 in every dimension.

Mode	Calculated (Hz)	Meas. Free (Hz)	Meas. Constr. (Hz)
1	1834	990.5	1765.72
2	3983	3531.4	3531.4
3	6055	6072.4	6072.4
4	8060	8333.3	8354.9
5	9934	9517.4	9517.6
6	11620	n.r.	10852.7
7	12150	n.r.	12230.8
8	14070	n.r.	13695.11
9	16030	n.r.	n.r.
10	17750	n.r.	n.r.

Table 3.7: Calculated eigenfrequencies taken from [82] (second column) versus the measured eigenfrequencies using the microphone. (n.r.=not registered, signal too low)

tion. The horn is hence fixed on a chassis and excited by a non calibrated hammer both on the longitudinal direction and radial direction. The signal FFTs for the two cases are shown in figure 3.35.

The eigenfrequencies found are in good agreement between the two different boundary conditions and with the calculated one as shown in the previous table.

3.6.4 Nufact Horn

The case of the Nufact horn is more complicated since it is very difficult to excite directly via a hammer the inner conductor. This is due to the

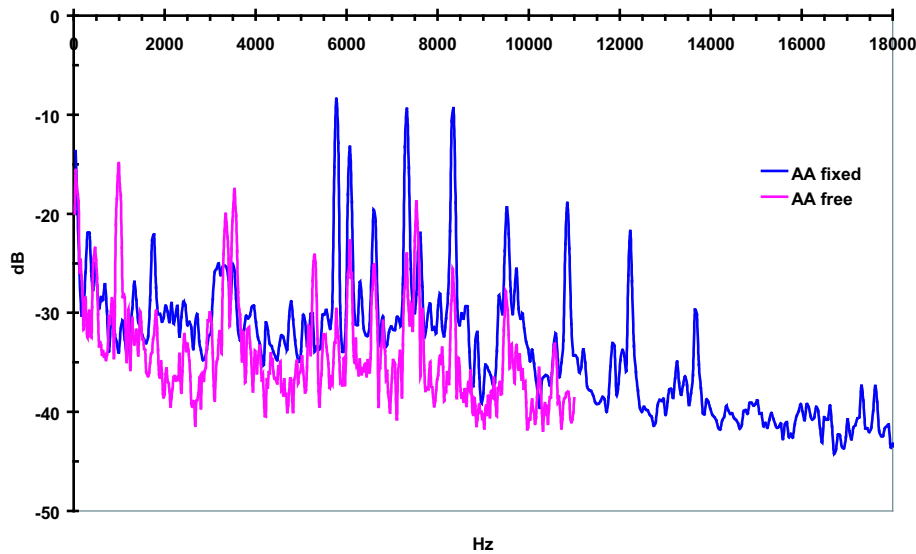


Figure 3.35: *AA horn FFT analysis for the horn endplate free and fixed by the chassis.*

particular horn design (figure 3.36). The inner conductor is enclosed into a water circuit to increase the heat evacuation and the circuit is closed in an Al alloy layer which is the external visible surface. The excitation with a non calibrated hammer doesn't assure the excitation of the inner surfaces, hence the best way is to use directly the main horn power supply. The first prototype of the power supply pulses at 1 Hz for $100 \mu s$ a current of 30 kA. Unfortunately at such low current the background noise is comparable with the horn signal, and even after the increase up to 100 kA the sound signal is still quite low. The three main noise sources are: the room ventilation, the cooling water flowing, the electric power supply discharge.

The main mode of vibration is expected to be in the longitudinal direction hence the microphone was placed in front of the horn opposite to the electric power connections. The first measurement was done with the cables of the power supply short-circuited, to determine the eigenfrequencies of the ventilation and the power supply noise. Then a second measurement is taken with the horn water cooling system running, to subtract from the data the water noise. For the last measurement the horn is properly connected to the power supply with the water running. The results for the three measurements are presented in figure 3.37 where the first two horn modes at 193.7 Hz and 549.1

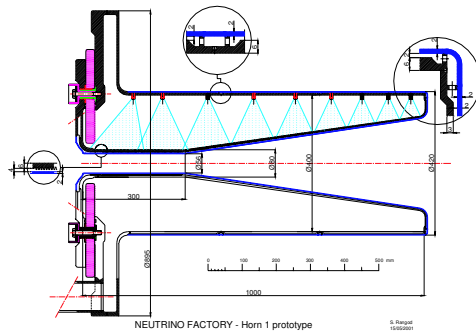


Figure 3.36: *Inner horn first prototype.*

Hz are indicated by two arrows. Those two peaks are not in common between the data taken with only the water running and the horn connected to the power supply.

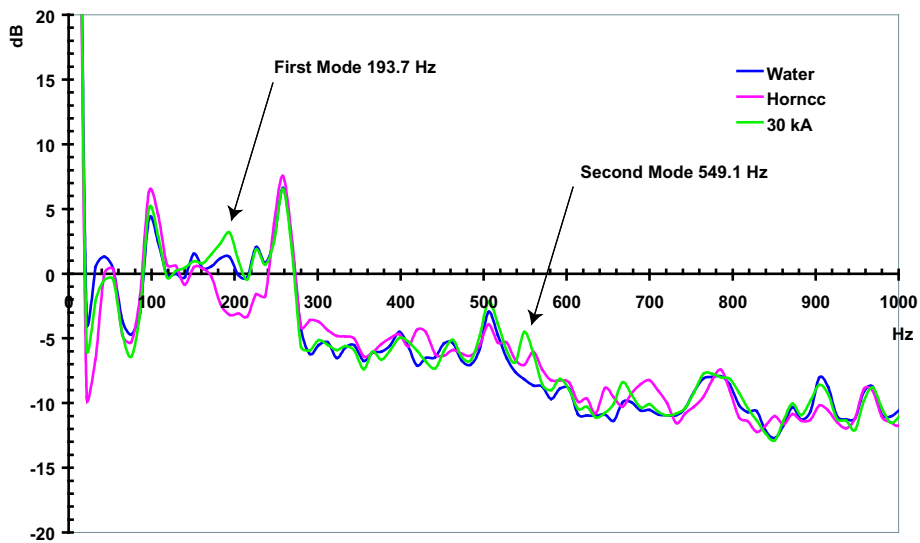


Figure 3.37: *NuFact horn spectrum analysis. The two arrows indicate the first two horn modes.*

3.6.5 Laser vibrometer measurements

The measurements of the NuFact horn described in the previous section have been repeated using a laser vibrometer. This technique, which is more expensive than the acoustic method, provides information about the displacement and velocity of a precise point, instead of the general horn behavior.

The laser measurements is based on the principle of the detection of the

Laser Vibrometer	OFV-3001-22/303
Laser Type	He-Ne
Laser Class	2
Light wavelength	632.8 nm
Power	1 mW
Frequency range	1 Hz - 1.5 MHz
Min. displacement	1 nm

Table 3.8: *Polytech[76] laser vibrometer main specifications.*

Doppler shift of the coherent laser light that is scattered from the test object, in this case the horn metallic surface, and detected by a sensor located inside the laser head.

The Doppler shift between the nominal laser wavelength and the scattered light provides the information about the velocity displacement of the measured point. For this purpose, an optical interferometer is used to mix the scattered light coherently with a reference beam and extract the Doppler frequency, which is proportional to the surface velocity, and the phase change with respect to the phase of a reference signal, which is proportional to the displacement of the measured point. The laser properties used for the measurements are reported in table 3.8. An example of NuFact horn measurement setup is shown in figure 3.38 where the the laser head is pointing to the end flange of the Nufact horn in the same position as the microphone for the previous measurement.

The validation of the laser vibration method has been done, as in the case of the acoustic method, by measuring the eigenfrequency of the CNGS horn. However, the results quoted in the following are different from the one reported in table 3.6 since the horn measured is an hybrid prototype towards the final horn version. This horn has the inner conductor which will be used for the CNGS beam but the same outer conductor of the first prototype.

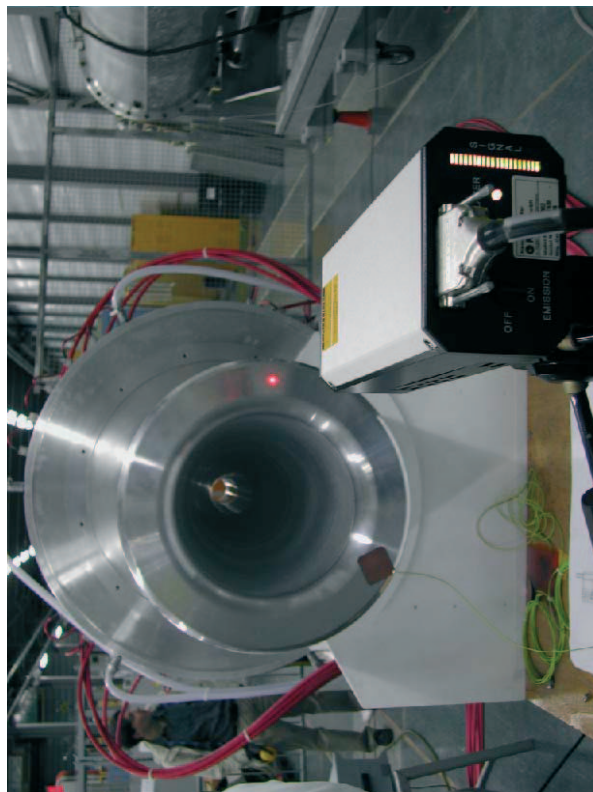
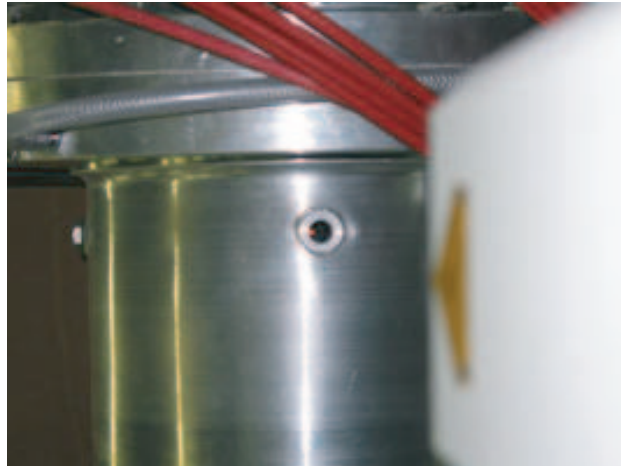


Figure 3.38: *Laser vibrometer head pointing to the end flange of the horn (right) and laser pointing on the neck inner conductor through the magnetic probe access hole (left).*

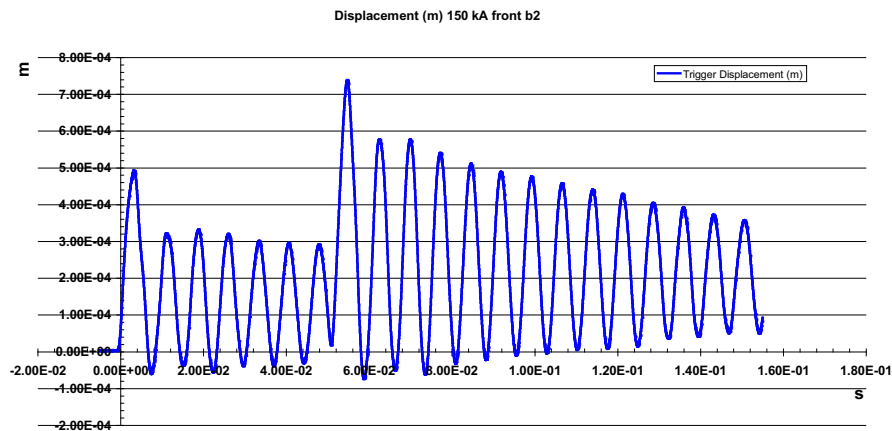


Figure 3.39: *CNGS horn displacement on short time scale. The second current pulse after 50 ms induces the second peak.*

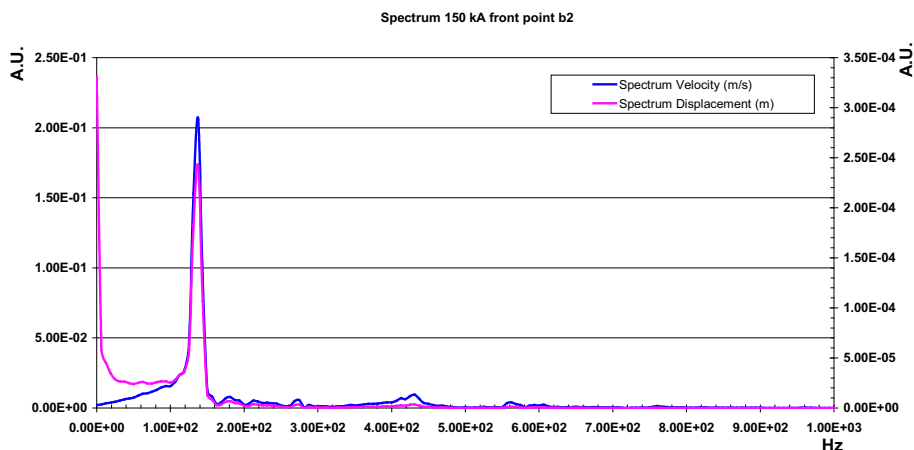


Figure 3.40: *Frequency spectrum of displacement and velocity of the CNGS horn measured point.*

The measurement point chosen is placed at 150 mm from the center of the side opposite to the bus bar connections (see figure 3.31). Figures from 3.39 to 3.42 show the displacement and the FFT transformation of the displacement and speed of the surface. The displacement has been measured for two different time windows. In the first case (figure 3.39), data are taken in a time window which contains the two current pulses separated by 50 ms, as it is visible from the second peak in the displacement intensity. In the

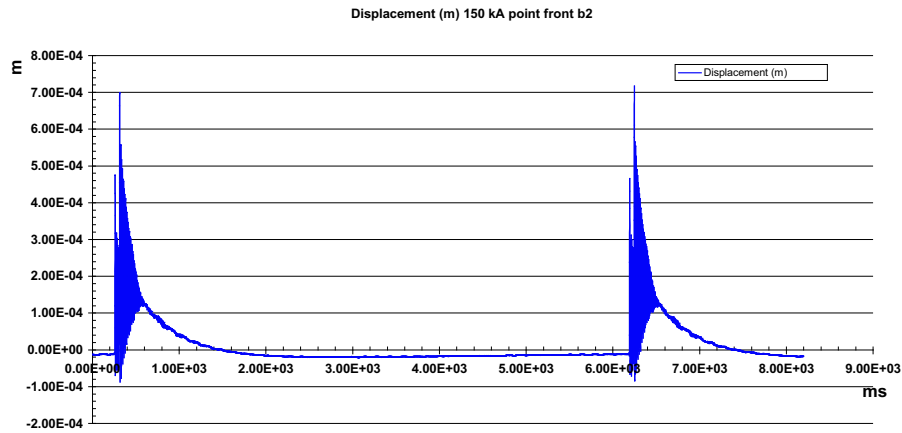


Figure 3.41: *CNGS horn displacement on long time scale. Two group of the two current pulses separated by 6 s. The thermal expansion after each group of two pulses provoke a material macroscopic deformation which is reabsorbed after few seconds.*

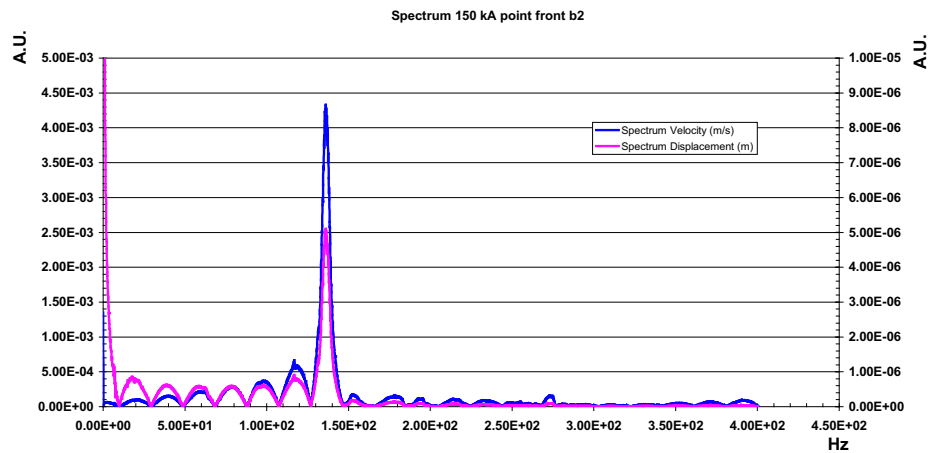


Figure 3.42: *Frequency spectrum of displacement and velocity of the CNGS horn measured point for the long time scale.*

second case the time window contains four pulses grouped in pairs separated by 50 ms, each pair separated by 6 s. Figure 3.41 reveals that after the first current pulse the flange starts to vibrate around a point which is not at zero displacement from the not-excited position. The current pulse, in fact, induces the vibration of the flange but also a macroscopic deformation

due to the sudden temperature rise in the conductors. This deformation is reabsorbed about 1 s after the end of the vibration.

From the analysis of the frequency spectrum of figures 3.40 and 3.42, the first vibration mode is at 137 Hz, as confirmed by the measurement done with accelerometers [77].

The same technique has been used to measure the NuFact prototype horn eigenfrequencies. For those measurements the NuFact horn has been pulsed at 102 kA. Between the different points measured shown in figure 3.43, three have been chosen as representative of the horn behavior. The first point

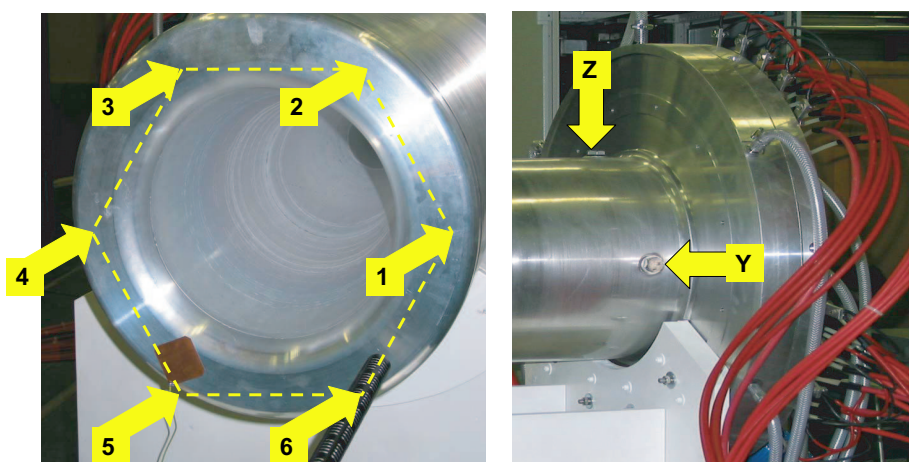


Figure 3.43: *Laser measurement points on the NuFact horn.*

is on the horn end flange, opposite to the electric connection, identified by the number 2. The spectra of point 2 displacement and velocity are shown in figure 3.44, for data taken with the water cooling turned off. The laser measurements confirms the vibration frequencies found with the acoustic method, being the first mode at 206 Hz and the second at 581 Hz (see table 3.9 for frequency summary). A new vibration peak appears in the measurement at 2470 Hz, which has not been clearly identified by the acoustic method.

Mode	Acoustic freq. (Hz)	Laser freq. (Hz)
1	193.7	206
2	549.1	581
3	-	2470

Table 3.9: *Frequencies of the modes identified by the acoustic method and by the laser vibrometer measurements.*

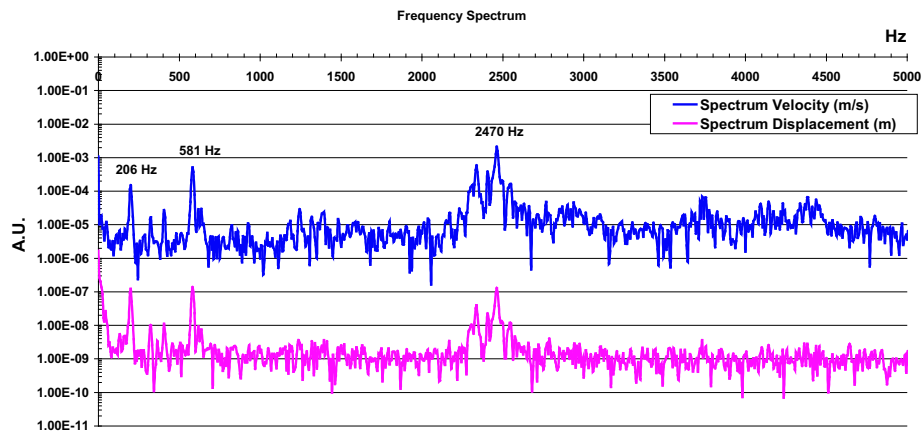


Figure 3.44: *Frequency spectrum of speed and displacement measured with no horn water cooling for point 2 (see figure 3.43).*

The vibration of the point 2, once repeated with the water cooling turned on, reveals that the cooling water flowing on the conductors dumps quite effectively the vibrations. The measurement results presented in figure 3.45 demonstrate the water dumping effect, since the vibration peaks decrease compared to figure 3.44. The vibration, however, is still present, as can be noticed by comparing the spectrum of figure 3.45 and the spectrum of a point located on the wall of the experimental hall of figure 3.46, used as reference fixed point.

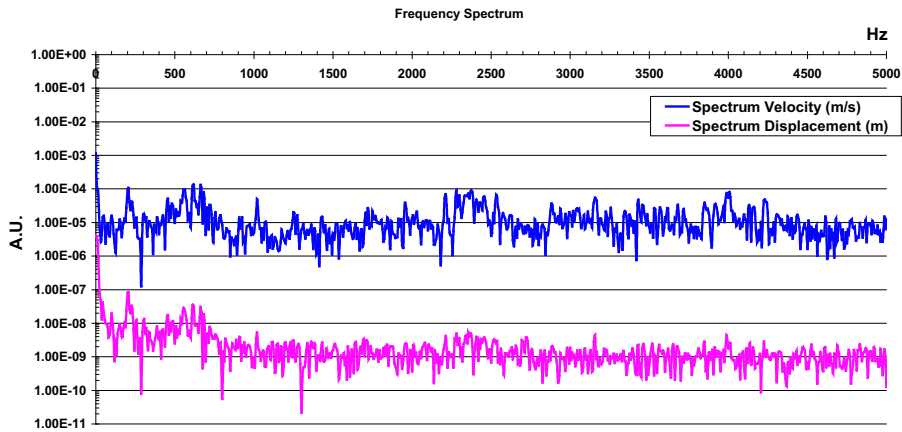


Figure 3.45: *Frequency spectrum of speed and displacement measured with the horn water cooling. The horn vibration are dumped nearly to zero by the water skin flows.*

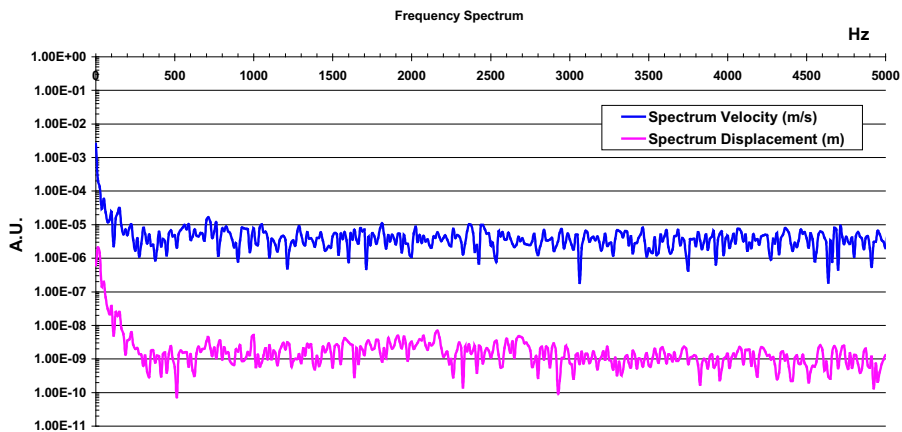


Figure 3.46: *Frequency spectrum of speed and displacement of a point of the wall of the experimental hall.*

The main advantage of using the laser is the possibility to reach the inner surface of the inner conductor via the holes of the magnetic probes. Two access holes are located one on top and the second on the side of the external conductor (see figure 3.43). In this case one expect to measure vibration modes which are a composition of longitudinal and radial vibration, while the measurement of the point 2 cannot provide information about merely radial modes.

The results are presented in figure 3.47 and the list of all the peaks identified as common to both points is resumed in table 3.10. However, the measure-

Mode	Frequency (Hz)
A	200
B	325
C	575
D	1330
E	2460
F	4410
J	6690
K	7030
L	8200
M	8640
N	8990
O	9860

Table 3.10: *Frequencies measured for the point Y and Z.*

ment in this case is more difficult than in the point 2 case since the laser light scattered by the inner conductor can be rescattered by the external conductor before reaching the laser sensor. In this case the frequency measured would be a composition of the vibrations of the external and internal horn conductors. For these reasons the frequencies quoted in table 3.10 are only the common ones to both points.

The frequencies found for the point 2 are present also in this case, meaning that those vibration mode are not merely longitudinal.

3.6.6 Conclusions of the vibration measurements

The method of horn eigenfrequency identification via acoustic method produced accurate enough results for a first measurements for the CNGS and AA horn.

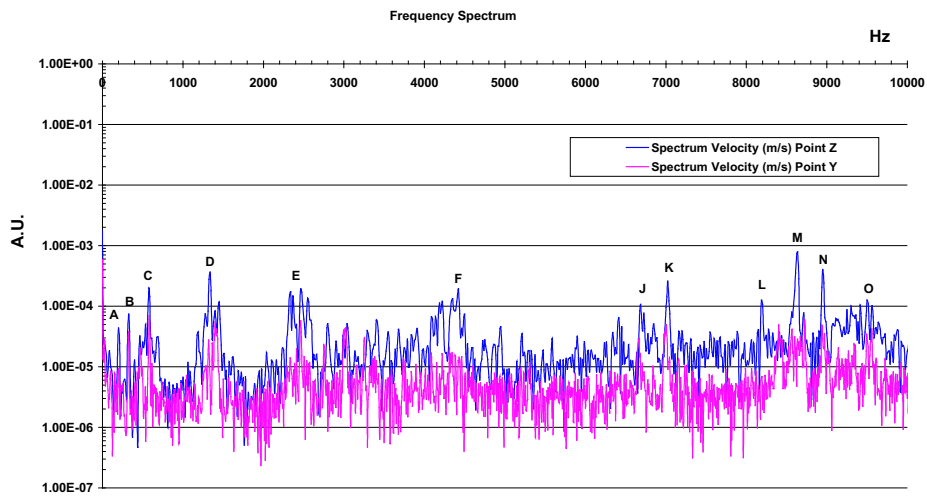


Figure 3.47: *Frequency spectrum of speed of the neck point Z and Y.*

For the case of the Neutrino Factory horn the results are not so evident since the available power supply excitation is too low, but nevertheless the measured eigenfrequencies are confirmed by the laser vibrometer method. The first two vibration modes are at ≈ 200 Hz and ≈ 581 Hz. A third frequency has been identified at ≈ 2470 Hz as a set of radial frequencies for the horn neck vibration.

3.7 Microphone Specifications

The microphone[78] used has the frequency response shown in figure 3.48, which is quite flat for the range of interest.

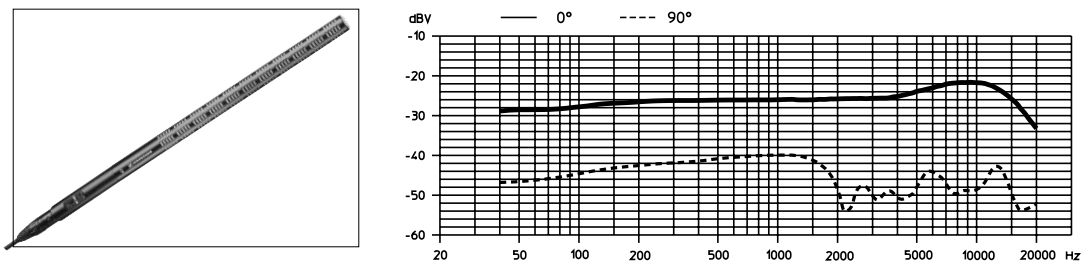


Figure 3.48: *The microphone chosen with its frequency response function.*

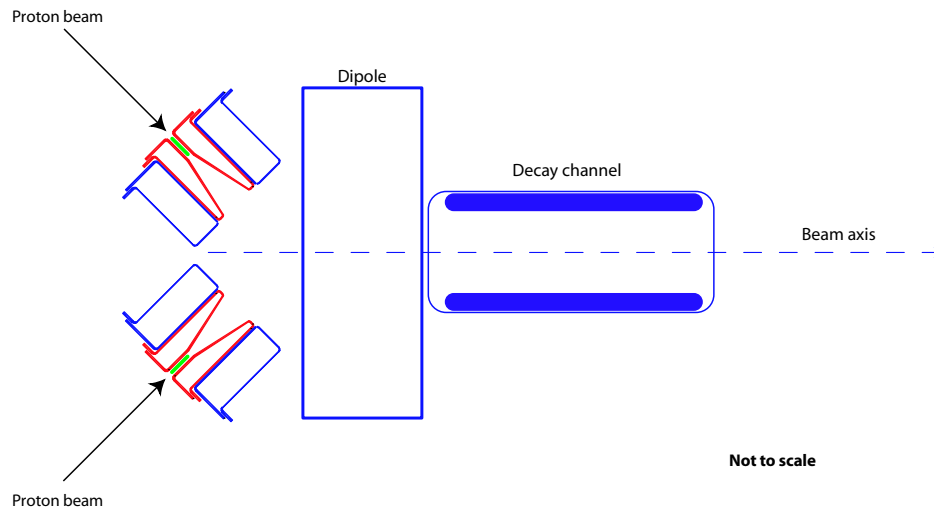


Figure 3.49: *The pion beam coming from one horn is corrected by the bend before the decay channel solenoid. The other two horns are not drawn and they are in the plane perpendicular to the one of the figure.*

3.8 Introduction to four horn capture scheme

The present pion capture scheme, as presented in the previous sections, uses a horn pulsed at 50 Hz which injects the beam directly into the solenoidal decay channel. The challenge in using one target and one horn is the high repetition rate required by the system and the high power to be handled by the system. This implies a limit in the lifetime of the horn and it imposes the use of the Hg target for the pion production.

In this section a system with four horns and four targets is proposed as a possible alternative to the traditional scheme. In this case the system repetition rate could be reduced to 12.5 Hz and the mechanical and thermal stresses would be more moderate having only 1 MW beam power per target. Moreover, this scheme could be used to increase the conventional neutrino beam proposed in [84] which does not suffer from the losses at the injection into the decay channel[†].

3.8.1 Proposed scheme

In Figure 3.49 the four horn scheme is presented. The proton beam coming from the proton driver is sent to one of the four lines and it impinges on one of the targets. The system target/horn is the same as presented in [83],

[†]In case of running the proton driver at 16 MW and having 4 MW per target.

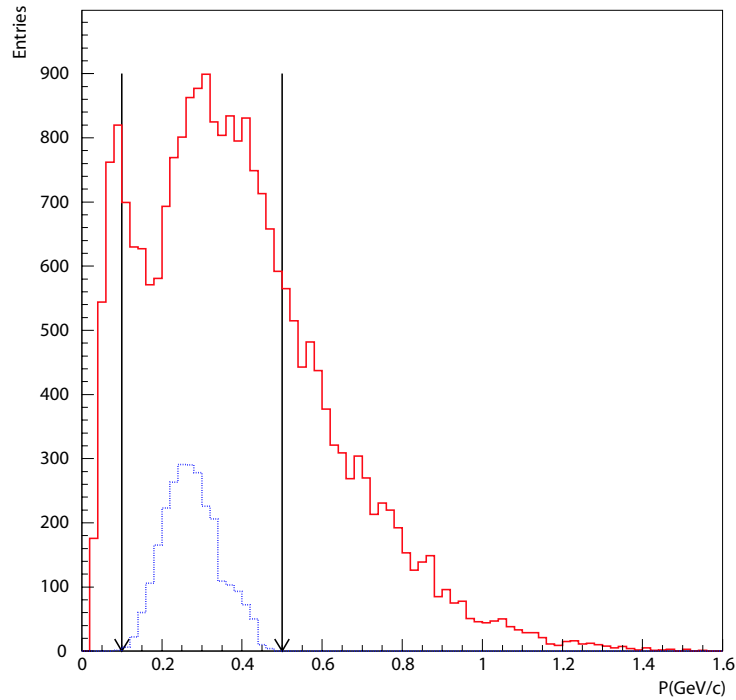


Figure 3.50: *Pion and muon momentum at the end of the decay channel. In red (continuous line) the distribution for the straight injection, in blue (dotted line) for the curved one with the four horns. The arrows limit roughly the momentum interval accepted by the phase rotation section. The bend introduces the selection in energy.*

except that the beam axis and the horn axis are inclined by 45 degrees with respect to the decay channel axis.

The pion beam is corrected by a pair of bending magnets, where the \mathbf{B} field direction is varied according to the direction of the incoming beam. The field in the dipole is 0.7 T and the dipole is 1 m long.

The beam is injected directly into the first decay channel solenoid, which is 4 m long with a radius of 30 cm and a field strength of 1.8 T. A complete field map of this solenoid and of the 30 m long decay channel has been computed by POISSON [85] and implemented into a MARS [98] simulation.

The same field map is also used for the injecting section in the one-horn scheme. In this case the decay channel starts 50 cm after the horn, and the toroidal field of the horn should be superimposed to the fringe field of the solenoid. This effect was considered negligible in first approximation, since the length of the radial field damping is comparable to the solenoid aperture.

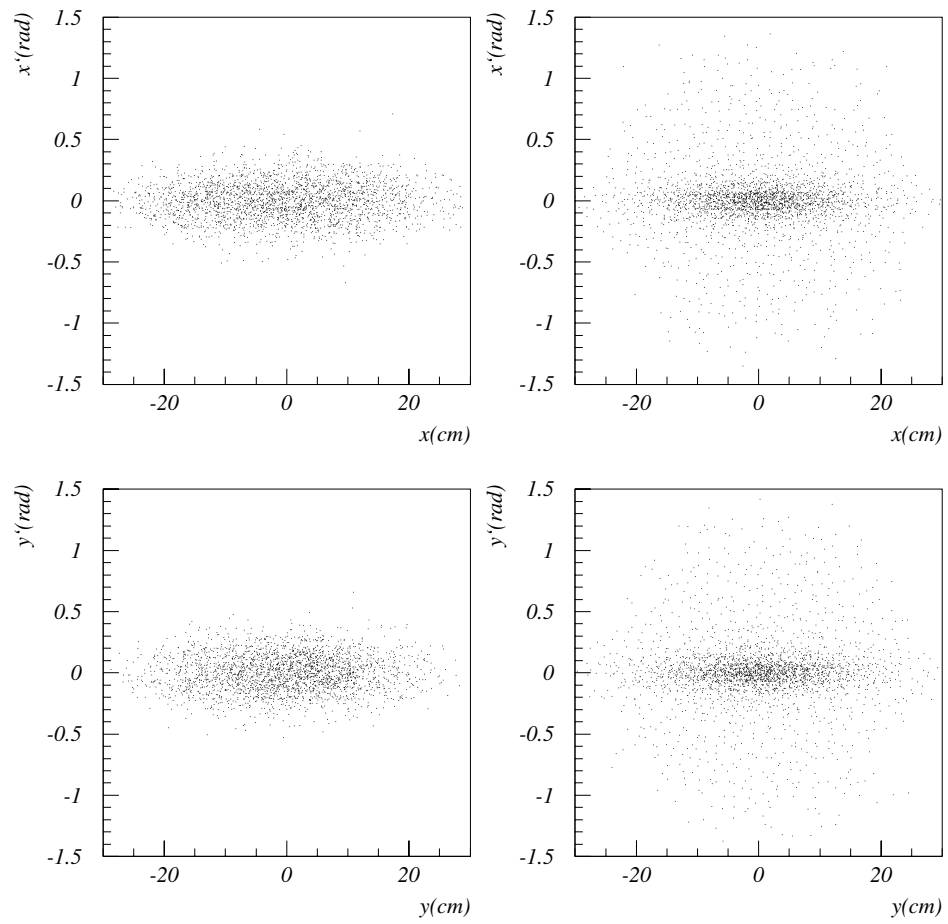


Figure 3.51: *The two transverse phase space planes for the curved injection (left) and the straight injection (right) at the end of the decay channel.*

3.8.2 Results

Pions and muons are counted at the end of the decay channel for both the straight injection and for the curved one. In the case of the curved injection, the bend introduces an energy selection in the beam, as is shown in Figure 3.50. In figure 3.51 the transverse phase space for both injections is presented. The results of the simulation are summarised as follows. It is more convenient to compare the yields in the momentum interval delimited by the arrows in Figure 3.50 between 0.1 GeV/c and 0.5 GeV/c. The phase rotation, in fact, will capture muons and pions in this energy range. In this case the rate between the two injection yields is 0.2. The losses come from:

- mismatch between the horn, the bend and the solenoid;
- the acceptance of the scheme is smaller compared to the straight injection.

The losses due to the transport in the decay solenoid are negligible.

3.8.3 Conclusions

The four horn scheme seems to be quite promising only from the point of view of the target and the horn lifetime, while for this preliminary study, it gives a lower limit to the yield that can be achieved with such a geometry. Various solutions are already under study. By varying for example the proton beam axis or the angle of the bending, one could hope to have improvement of the flux.

The main advantage of this scheme is the possibility to use a solid target, like a carbon rod or the Ta sphere target presented in chapter 2, instead of a liquid Mercury target. The reason is that the power per target is limited to 1 MW, instead of 4 MW.

Another advantage is that the life time of each horn is increased from one year to four years.

However, the target station infrastructure will be more complicated. The target station has to host four horns and four targets, increasing in first approximation the amount of irradiated material by a factor of four. Even if the material would be less irradiated than with only one horn, it is not clear from the point of view of the radiation safety and the decommissioning of the facility if this is an advantage or not. And the price to be paid is a factor of four less pion in the NuFact compared to the standard scenario.

Chapter 4

SuperBeam

As described in chapter 1 the SuperBeam is basically a conventional neutrino beam with higher intensity, which could be the first step towards a NuFact. It could be used for the study of the mixing angle θ_{13} and the CP violation. In this chapter the properties and the optimization of a low energy neutrino beam are discussed, in particular considering a possible CERN-Frejus Superbeam.

4.1 Introduction to the SuperBeam

The future generation of proton drivers will produce proton beams with a power of the order of a few MW, and the next generation of proton decay, atmospheric and solar neutrino detectors will require water Cerenkov detectors with masses of about a Mton. Those two ingredients, which at a first glance seem to be uncorrelated, are the main elements required by the second generation of the future neutrino long baseline experiments.

The next generation of long baseline neutrino beams, CNGS at CERN and NUMI at Fermilab, will use of the order of a half a MW proton beam to produce a ν_μ beam to test the $\nu_\mu \rightarrow \nu_\tau$ oscillation, observing in the CNGS case the appearance of ν_τ in the quasi-pure ν_μ beam and for the NUMI beam the disappearance of ν_μ . However, the oscillation probability $\nu_\mu \rightarrow \nu_\tau$ is driven by the atmospheric mixing angle $\sin \theta_{23}$, which is already known to be non zero from the atmospheric measurements.

These experiments are important nevertheless, since CNGS will observe for the first time the appearance of neutrinos of a different flavour from the one of the man-generated beam. But, as already mentioned in the first chapter, there are two parameters of the neutrino oscillation theory whose values are still unknown, the mixing angle $\sin \theta_{13}$ and the CP violating phase. The

angle $\sin \theta_{13}$ can be measured from the oscillation probability $\nu_\mu \rightarrow \nu_e$, if the neutrino beam is intense enough and the beam energy is high enough and/or detector is sufficiently massive.

The approach chosen by the NuFact is to produce an intense neutrino beam at high energy, 20 GeV, with a detector of 40 kT, which is considered a small detector. For such high energy the distance from the source to the detector required to have a large oscillation probability is of the order of thousands of kilometers.

A second approach, more similar to the conventional neutrino beams, uses the first part of the NuFact, the proton driver, target and horn, to produce an intense low energy, few hundreds MeV, ν_μ beam from pion decay. The neutrino detector in this case must have a mass of the order of hundreds kilotons up to one Megaton.

This is the design, for example, of the Japanese neutrino beam that will send neutrinos from Tokai to SuperKamiokande[87].

This experiment, named T2K, Tokaj to Kamioka, uses a 0.5 MW, 50 GeV proton beam to create a ≈ 0.8 GeV ν_μ beam directed to SuperKamiokande. The same approach can be studied using the first part of the CERN NuFact, as described in the next section. In this case the neutrino beam has a typical energy of few hundred MeV. For this energy the maximum of the oscillation probability for $\nu_\mu \rightarrow \nu_e$ is located at few hundred kilometers from the source and, with such low neutrino energy, an effective measurements requires a detector, for example a water Cerenkov, with a fiducial volume of at least half a Megaton.

The value of the oscillation probabilities, constrains the minimum mass of the detector.

Considering, for example, a neutrino monoenergetic muon beam of 250 MeV, which is the typical energy of the CERN Superbeam, the maximum of the oscillation is located at about 100 km. At this distance, about 99.5% of the ν_μ are transformed into ν_τ while only about 0.5% are transformed into ν_e . This, together with the low cross section of neutrino interaction in the MeV range, requires a Mton detector to produce the number of ν_e events required to measure $\sin \theta_{13}$. Even with all of this, $\sin \theta_{13}$ has to be larger than 1 degree, otherwise the only machine able to determine it is a NuFact, as shown in figure 4.1

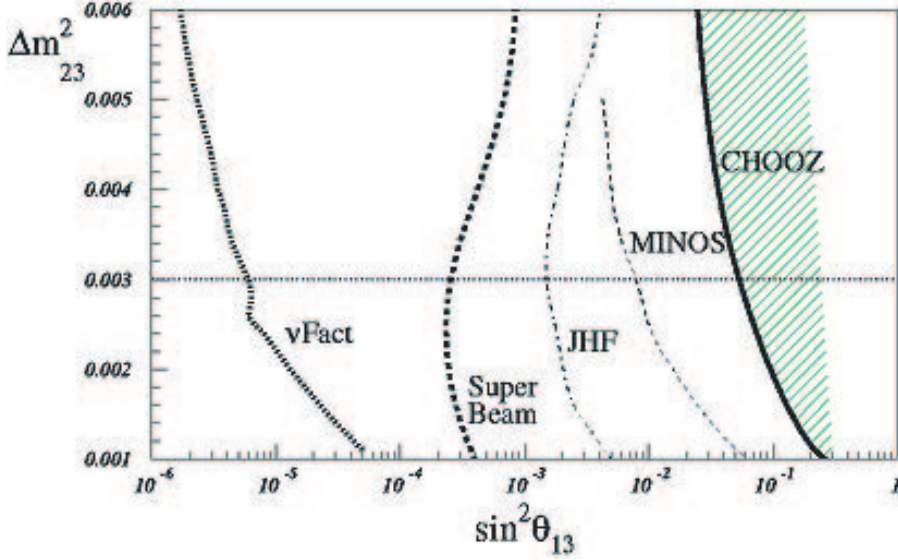


Figure 4.1: Sensitivity to $\sin^2 \theta_{13}$ for different conventional neutrino beams compared to the NuFact

4.2 Features of the CERN low energy neutrino SuperBeam

As described in the previous section, the CERN SuperBeam is composed of the first part of the NuFact. The 2.2 GeV proton beam from the SPL is accumulated into a single ring before being sent onto a mercury target (see figure 4.2).

Pion produced from the target are focused by a horn similar to that for the NuFact. These pions decay in some ten meters long decay tunnel according to:

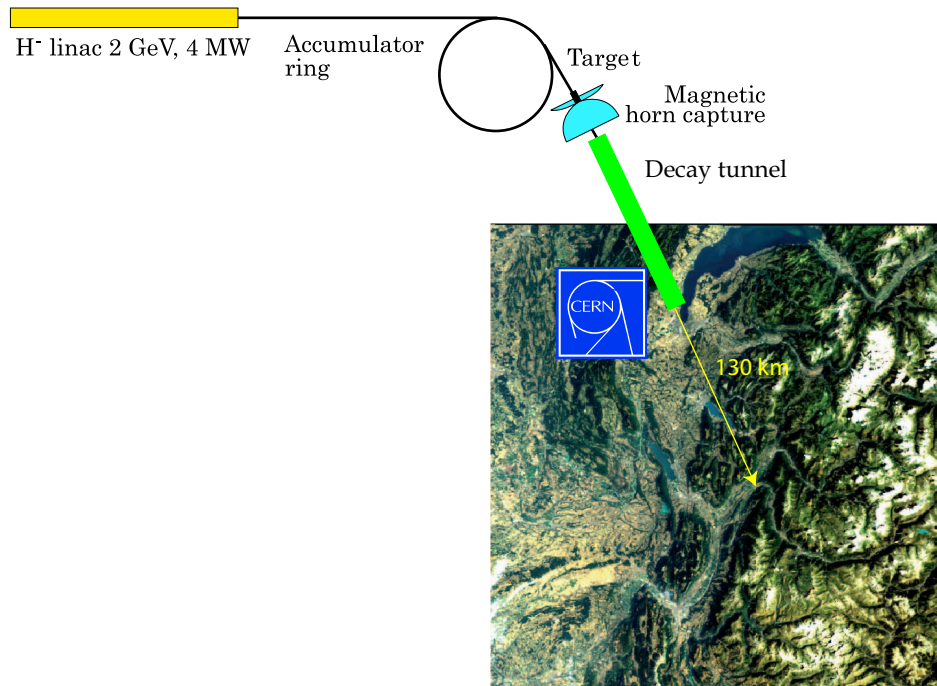
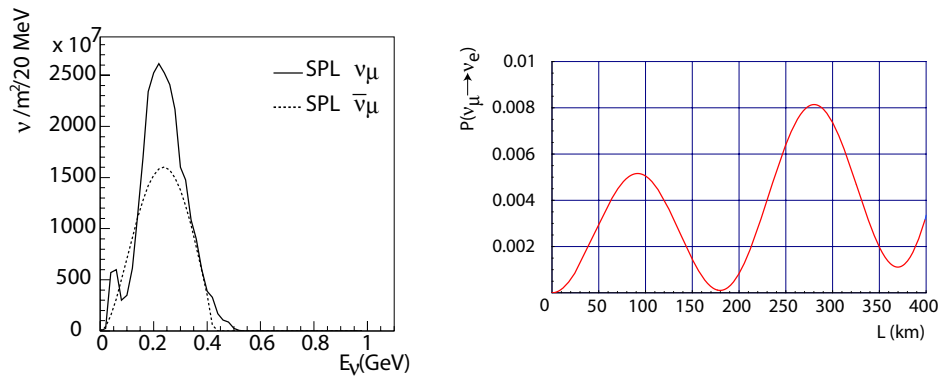
$$\pi^+ \rightarrow \mu^+ + \nu_\mu \quad (4.1)$$

and

$$\pi^- \rightarrow \mu^- + \bar{\nu}_\mu \quad (4.2)$$

A neutrino or antineutrino beam can be selected by the horn polarity, providing the two beams desired for the CP violation measurements.

The muon neutrino beam produced by the low energy pions (see previous chapter for the pion phase space description) has an energy spectrum which peaks typically at about 270 MeV, as shown in figure 4.3[88]. For this energy, the oscillation probability for the transition $\nu_\mu \rightarrow \nu_e$ has the first maximum at about a distance of 100 km, which would be the best distance to locate the

Figure 4.2: *Sketch of the CERN-Frejus SuperBeam.*Figure 4.3: *Neutrino and antineutrino flux at 130 km (right) together with the oscillation probability calculated with no CP violation for 250 MeV muon neutrinos.*

experimental detector. In particular, as a fortunate coincidence, located at 130 km from CERN there is the Laboratoire National de Modane. This laboratory occupies one cavern linked to the road tunnel which connects Italy to France. A significant enlargement of the laboratory, however, is necessary to host the some hundred kiloton detector required for the SuperBeam physics.

4.3 Optics design

The setup of the SuperBeam target is chosen to be the same as for the NuFact. The target is a mercury cylinder 30 cm long placed inside a magnetic horn, as described in the previous chapter for the NuFact.

However, the horn design is slightly different from the NuFact case. The NuFact decay channel, in fact, is composed by a series of solenoids whose acceptance is limited by their magnetic field and their aperture. Roughly, the NuFact decay channel acceptance in the transverse phase space, for example on the plane $x-x'$, is described by an upright ellipse with a maximum value of $x'=px/pz$ of the order of half a radian, and for x of the order of 30 cm (see figure 4.4).

The pion transverse phase space required by the SuperBeam is described

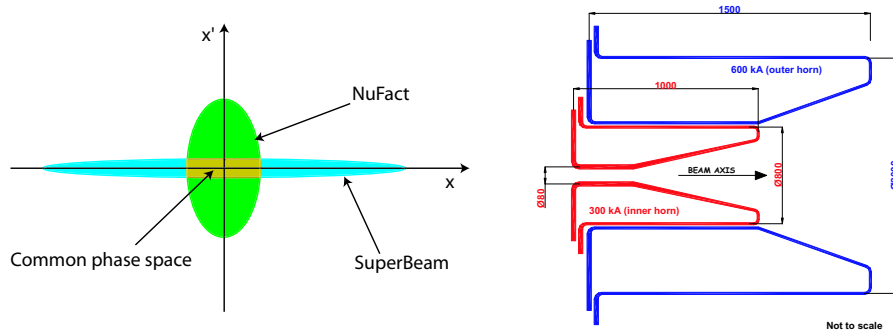


Figure 4.4: *Sketch of pion phase space required by a NuFact and a SuperBeam (left) and conceptual design of a double horn.*

by an ellipse with a large x , of the order of 1 m, which corresponds to the radius of the decay tunnel, and a very small x' , of the order of few mrad. The beam divergence has to be kept as small as possible, since the spot size increases due to the distance between the neutrino source and the detector considering that the typical height of the neutrino detector is between 40 m and 100 m.

For example, the distance between the CERN and Frejus is ≈ 130 km, and with a detector of half height 50 m, the maximum desired beam divergence is given by $50 \text{ m}/130 \text{ km} \approx 0.4 \text{ mrad}$.

The NuFact horn and reflector already focuses a part of the beam required by the SuperBeam, as shown in figure 4.4, considering the reflector placed around the inner horn.

A further optimization of the optics starting from the NuFact horn has been performed using the following constraints:

- the inner horn is the same as for the NuFact;

- the current of the inner horn is 300 kA and of the reflector is 600 kA;
- the horn and reflector are open in the forward direction to reduce the energy deposition produced by primary and secondary particles in the conductors;
- the optimization is done for a decay tunnel 30 m long and a neutrino detector located at the symbolic distance of 50 km;

The beam optimization has been studied by varying the length of the reflector and changing the slope of its endplate until a maximum of the flux is found. The details of the calculation of the fluxes are described in [89].

A longer reflector focuses particles at large radius, as shown in figure 4.5. The divergence of the pions shown in figure 4.5 is reduced for longer reflectors, and the resulting neutrino flux increases with the length of the reflector, as

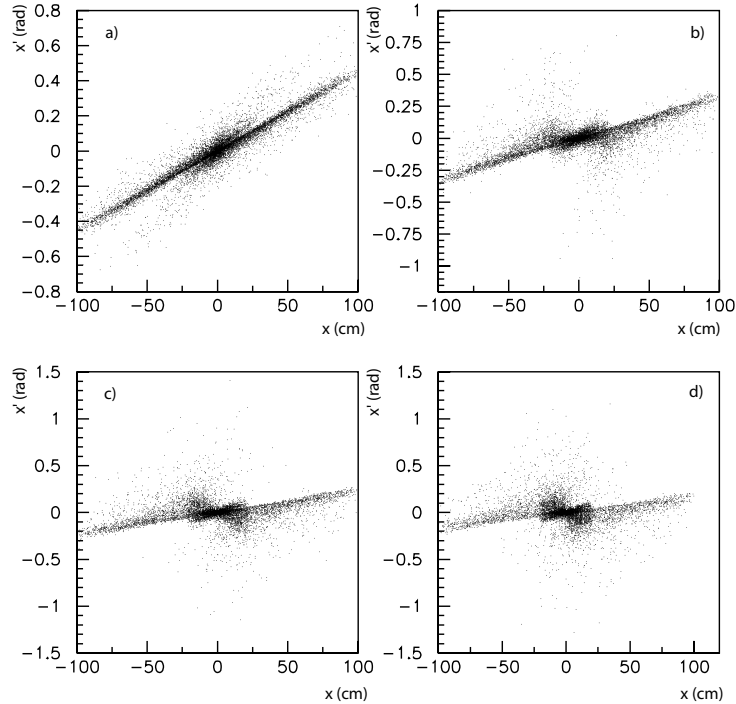


Figure 4.5: *Pion transverse phase space for different reflector length a) 1.5 m, b) 2 m, c) 3 m, d) 3.5 m at the end of the reflector.*

shown in figure 4.6. The reflector chosen is 3.5 m long with an angle endplate of 42 degrees to maximize the ν_μ flux.

The overall effect of the reflector is to increase the flux of neutrinos by a factor of 2 and to increase the energy of the flux peak from 230 MeV to about 260 MeV.

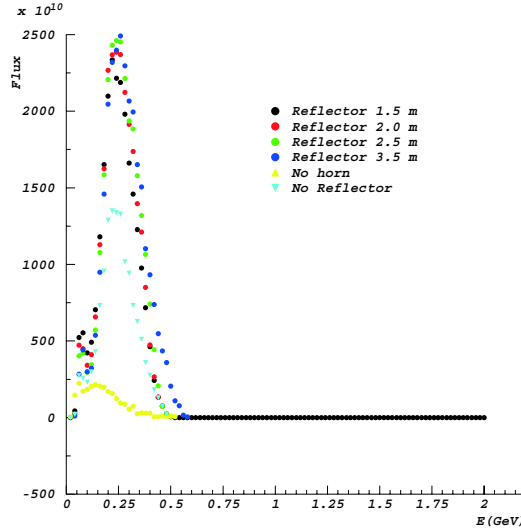


Figure 4.6: ν_μ fluxes from positive pions evaluated at 50 km in unit of $\nu/100 \text{ m}^2/20\text{MeV}$ for different reflector lengths and compared to the case without a reflector and the beam from the target alone. The decay tunnel is 30 m long.

4.4 Beam time structure

As described in the first chapter, the repetition rate of the CERN SPL proton driver is 50 Hz (20 ms). Inside this 20 ms there is only one proton macrobunch 2.8 ms long which is subdivided into groups of 5 microbunches separated by 22.7 ns (44 Hz, see figure 4.7).

The neutrino beam keeps the same time structure as the protons, and it would be the same as that of the SPL if the proton beam was sent directly onto the target. In this case it would be very difficult for the neutrino detector to distinguish neutrino interactions produced by the SPL beam and the interaction of atmospheric neutrinos, which is a source of background neutrinos which cannot be turned off.

To quantify the ratio between atmospheric neutrinos and SPL neutrinos produced with the SPL time structure, let us assume as detector a water Cerenkov detector. In this detector the rate of atmospheric electron neutrinos is approximately 100 evts/kton/year. With a 400 kton detector and an experiment which runs for 5 years, there will be of the order of 200000 atmospheric neutrino events, half ν_μ and half ν_e . In the same period and for the same detector the SuperBeam would produce of the order of tens of events for the $\nu_\mu \rightarrow \nu_e$ signal. One could use the proton macrobunch time window to distinguish between the atmospheric and the beam neutrinos. However, this would reduce the atmospheric events only by $\approx 86\%$, since $20 \text{ ms}/2.8$

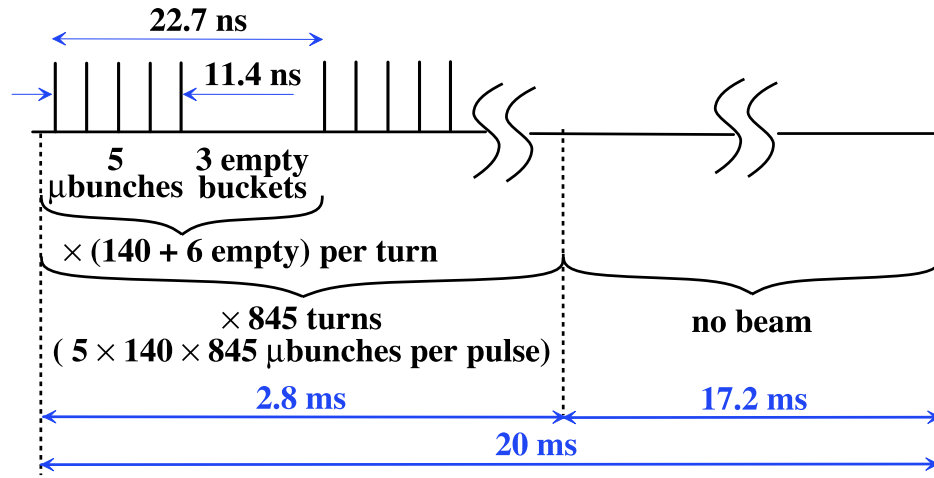


Figure 4.7: Proton time structure after the extraction from the SPL.

$\text{ms} \approx 7$, which is still not enough to enhance the SuperBeam neutrino events. For this reason the SPL protons are accumulated in a ring, the same ac-

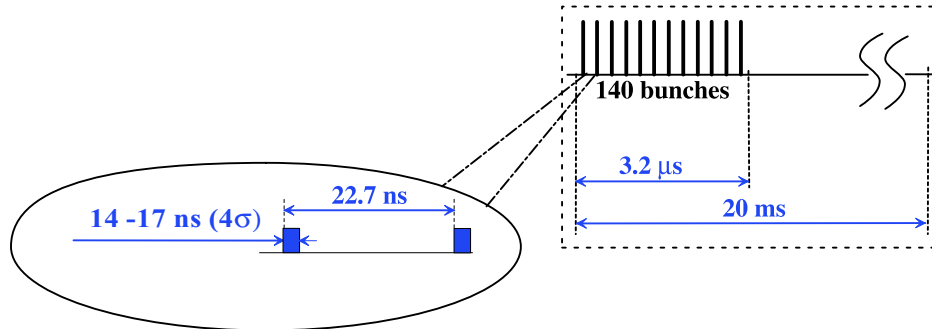


Figure 4.8: Proton time structure after the extraction from the accumulator ring.

cumulator ring as for the NuFact. In this way the protons, and hence the neutrinos, are concentrated into a shorter time window.

The proton time structure once extracted from the accumulator and sent to the target is shown in figure 4.8.

In this case the proton macrobunch has a length of $3.2 \mu\text{s}$, and the atmospheric background is reduced by 99.98%.

In this way the remaining atmospheric background can be furthermore reduced considering the direction of the neutrinos, since the beam neutrinos are coming only from a precise direction.

4.5 Decay tunnel length

Pions focused by the horn have an energy of the order of 500-600 MeV (see section) and their decay length is about 35 m. The minimum decay tunnel length is assumed to be 20 m and the maximum 100 m while the radius of the decay channel is assumed to be 1 m. Figures 4.9 and 4.10 show neutrino fluxes evaluated at 50 km from the horn for different decay channel lengths when positive and negative pions are focused. The length chosen is 60

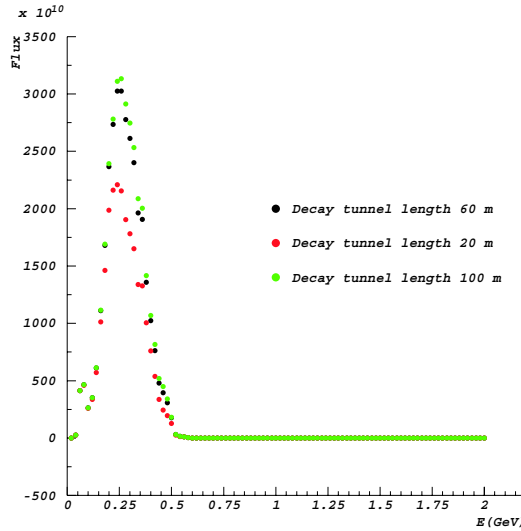


Figure 4.9: ν_μ fluxes from positive pion in unit of $\nu/100 \text{ m}^2/20\text{MeV}$ evaluated at 50 km from the target.

m, as a compromise between the maximization of the neutrino flux and the background produced from the muon decay.

One, in fact, should take into account the ν_e flux produced from muons in the decay tunnel, which is the main source of background since the kaon production is disfavoured by the low energy of the primary protons. As shown in figure 4.11, the ν_e flux increases with the increase of the tunnel length.

It is still argument of discussion if it would be better for the study of $\sin \theta_{13}$ to choose a short decay tunnel to control the muon decay, or a long decay tunnel to have the maximum ν_μ flux.

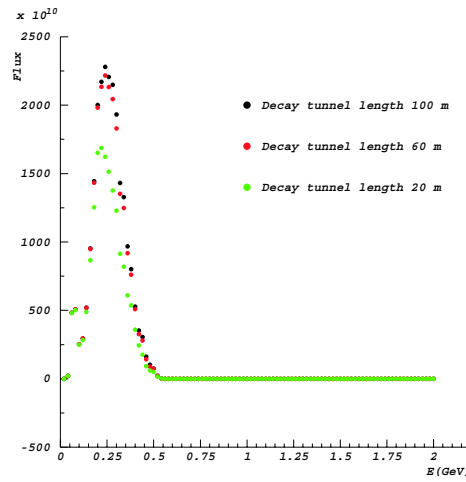


Figure 4.10: $\bar{\nu}_\mu$ fluxes from negative pions in unit of $\nu/100 \text{ m}^2/20\text{MeV}$ evaluated at 50 km from the target.

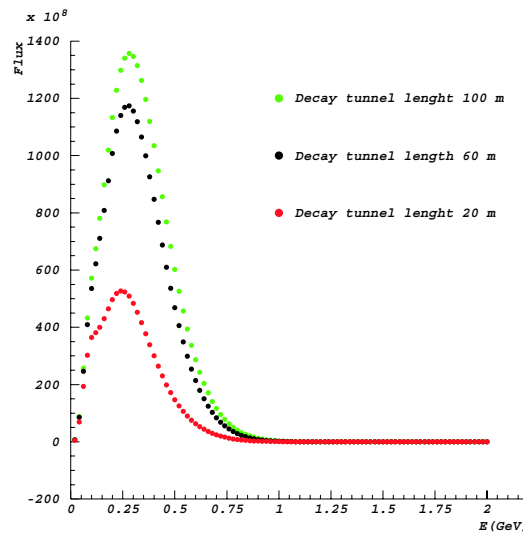


Figure 4.11: ν_e fluxes from muon decay in unit of $\nu/100 \text{ m}^2/20\text{MeV}$ evaluated at 50 km from the target.

4.6 Conclusions

The neutrino fluxes produced using the SPL proton beam have a promising physics possibility.

Some room to increase the neutrino flux is still available, since in this study some constraints has been considered to give a conservative estimation of the

neutrino fluxes.

The decision to keep the same inner horn as for the NuFact comes from the fact that this horn has also been deeply studied from the mechanical point of view, as presented in the previous chapter. However a different design, in particular a longer horn, could improve the integrated neutrino flux.

A second improvement could come from a different design of the reflector. A more complicated shape of the endplate, like a parabola or more similar to the theoretical one presented in the previous chapter, could improve the situation. However, since no mechanical study has been done in this case, a serious limitation in the life time could be a major issue for these kind of designs.

The optimization of the decay tunnel, both for the choice of the radius and its length should be repeated following the same philosophy presented in [89], once the HARP pion production data will be available[†].

[†]During the writing of this thesis the HARP experiment was still in the data analysis process.

Chapter 5

Solenoidal channel stability

The first part of the neutrino factory, defined as the front end, is composed mainly by two elements: solenoids for the beam focusing and RF (Radio Frequency) cavities for the manipulation of the longitudinal phase space. The stability of a linac composed only by solenoid as focusing elements can be discussed in terms of absolute values of the transfer matrix eigenvalues of one period of the channel. The same approach is used to study channels with solenoid alternating polarities and also for channels where the solenoids are described by fieldmaps. Once the lattice is chosen, the method allows to calculate the energy acceptance of the channel. Tracking simulations are used to check the stability conditions.

5.1 Matrix representation of a solenoid

The transport of particles in a solenoid is reduced to the solution of the equation of motion derived from the Lorentz force[†], namely:

$$\vec{F} = e\vec{v} \wedge \vec{B} \quad (5.1)$$

The magnetic field can be divided into three regions (see figure 5.1): the central section where the magnetic field is purely longitudinal ($\vec{B} = (0, 0, B_z)$), and the two end regions, where the field has a radial component ($\vec{B} = (B_x, B_y, B_z)$) due to the non vanishing gradient:

$$B_r = -\frac{r}{2} \frac{\partial B_z(z)}{\partial z} \quad (5.2)$$

[†]The non-relativistic case is considered for sake of simplicity. $c=1$ here and in the following.

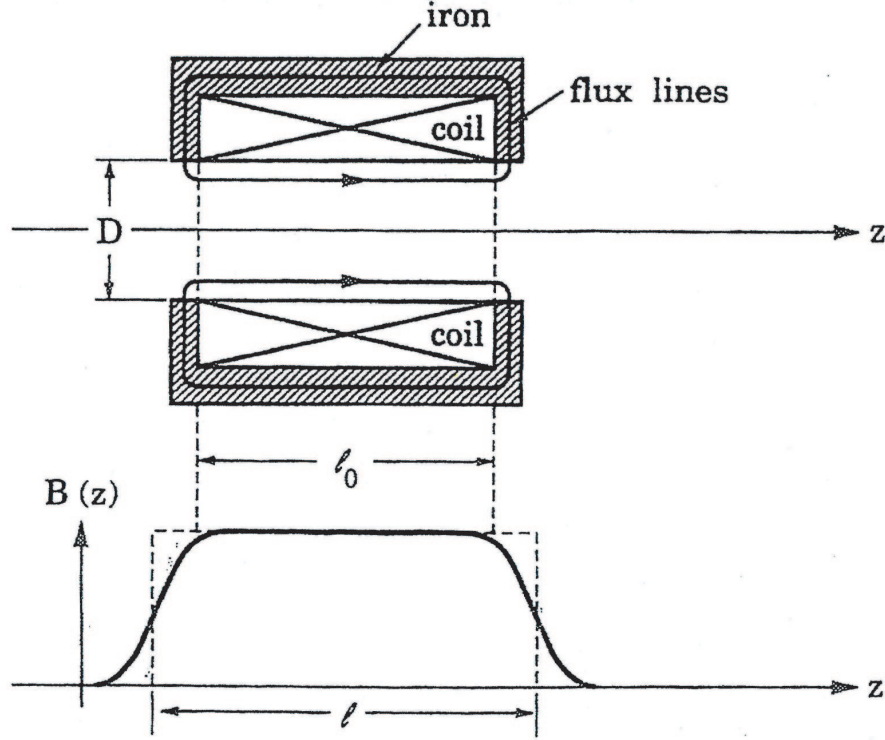


Figure 5.1: *Schema of a solenoid and the field along the z axis. D is the solenoid aperture, l_0 the solenoid physical length and l is the effective length used in the hard edge model*

In general a particle is not produced directly in the solenoid but has to cross the fringe field at the entrance and at the exit of the solenoid and its velocity is not parallel to the solenoid symmetry axis z ($\vec{v} = (v_x, v_y, v_z)$).

The presence of a radial magnetic field in the end regions causes a coupling between the transverse velocity and the longitudinal velocity. This can be shown developing equation 5.1 and considering only the z component:

$$mv_z \frac{dv_z}{dz} = e(v_x B_y - v_y B_x)$$

Moreover, even if a particle is parallel to the solenoid axis before entering the solenoid ($v_x = 0$ and $v_y = 0$), the presence of the transverse field forces the particle to start spiraling, since the radial field couples to the longitudinal velocity:

$$\frac{dv_x}{dt} = e(-v_z B_y) \quad (5.3)$$

$$\frac{dv_y}{dt} = e(v_z B_x) \quad (5.4)$$

The particle will continue spiraling in the pure longitudinal field region according to:

$$\frac{dv_x}{dt} = e(v_y B_z) \quad (5.5)$$

$$\frac{dv_y}{dt} = e(-v_x B_z) \quad (5.6)$$

conserving the velocity modulus.

The particle tracking in a solenoid can be approached in two different ways: in the first case the solenoid is described by its fieldmap, and the particle trajectories are calculated by a numerical method.

In the second case, the hard edge model, the solenoid is described as an optical element via its transfer matrix[90]. According to the three different magnetic regions cited above, and considering the linear approximation, the transfer matrix of a solenoid can be decomposed into three matrices:

- the matrix of the azimuthal kick given by the fringe field when a particle enters into the solenoid field, which is:

$$F_+^{in} = \begin{pmatrix} 1 & 0 & 0 & 0 \\ 0 & 1 & \frac{\theta}{2l} & 0 \\ 0 & 0 & 1 & 0 \\ \frac{-\theta}{2l} & 0 & 0 & 1 \end{pmatrix} \quad (5.7)$$

where $\theta = \frac{Bl}{B\rho}$, being B the magnetic field, l the effective length of the solenoid (see figure 5.1, where l_0 is the physical length and l is the effective length as described in the following) and $B\rho$ the magnetic rigidity of the particle;

- the matrix that represents the particle rotation given by the longitudinal magnetic field B_z , namely:

$$R_+ = \begin{pmatrix} 1 & \frac{l \sin \theta}{\theta} & 0 & \frac{l(1-\cos \theta)}{\theta} \\ 0 & \cos \theta & 0 & \sin \theta \\ 0 & \frac{-l(1-\cos \theta)}{\theta} & 1 & \frac{l \sin \theta}{\theta} \\ 0 & -\sin \theta & 0 & \cos \theta \end{pmatrix} \quad (5.8)$$

- the matrix of the azimuthal kick given by exiting from the fringe field at the end of the solenoid which is the inverse of (5.7):

$$F_+^{out} = (F_+^{in})^{-1} \quad (5.9)$$

The matrices of the same solenoid but with a reversed field have the following relations for the fringe fields:

$$F_+^{in} = F_-^{out} \quad (5.10)$$

$$F_-^{in} = F_+^{out} \quad (5.11)$$

and the matrix R_- has the same expression as R_+ but with the reverse sign for θ .

5.2 Solenoidal periodic channel

A solenoid with fixed length and bore aperture can be used as building block for two different channels. The first channel is composed by a sequence of

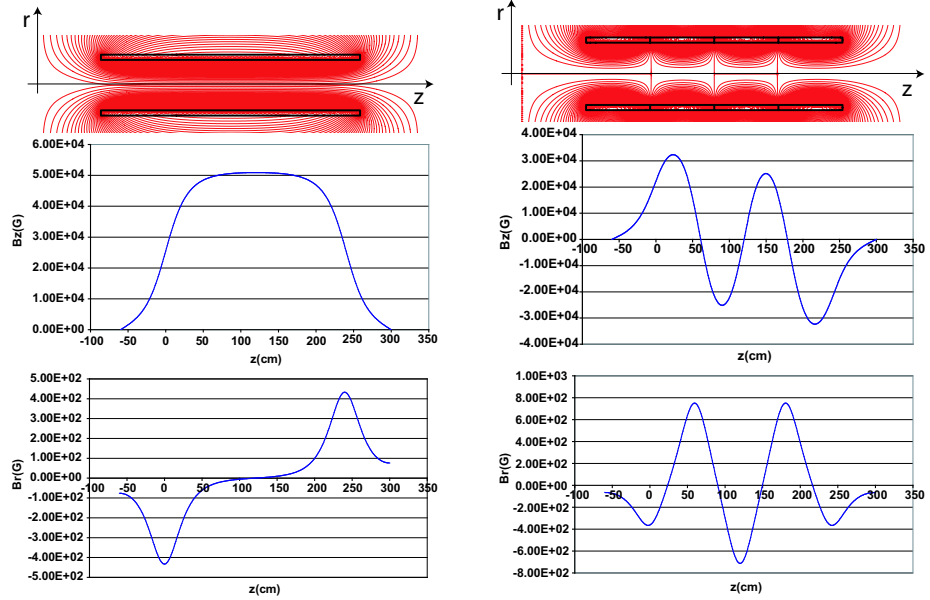


Figure 5.2: Example of two channels composed by the same series of solenoids with same current polarity (right) and with alternate polarity (left)

solenoids with the same current polarities see figure (5.2 left), while in the second the solenoid polarity is alternated (see figure 5.2 right).

The channel can be described by its period, which has been chosen to start in the middle of the positive solenoid. The transfer matrix for one period of the channel with solenoids of the same polarity is obtained by the following matrix multiplication:

$$T_+ = R_{+\frac{1}{2}} \cdot F_+^{in} \cdot F_+^{out} \cdot R_+ \cdot F_+^{in} \cdot F_+^{out} \cdot R_{+\frac{1}{2}} \quad (5.12)$$

where $R_{+\frac{1}{2}}$ is half of the rotation in the solenoid. The transverse phase space coordinates $\vec{x} = (x \ x' \ y \ y')^T$ of a particle after k periods equal to:

$$\vec{x}_f = T_+^k \cdot \vec{x}_i \quad (5.13)$$

where \vec{x}_i is the initial vector.

The stability of such linear system can be discussed in terms of absolute values of the T_+ matrix eigenvalues [91]. In fact, the solution \vec{u}_k of a difference equation like (5.13), if T_+ can be diagonalized as in this case, can be written as a linear combination of the eigenvectors \vec{e}_i times the k -th power of the associate eigenvalue λ_i :

$$\vec{u}_k = \sum_{i=1}^4 a_i \lambda_i^k \vec{e}_i \quad (5.14)$$

For increasing k the system is stable only if the absolute value of all the eigenvalues λ_i is less or equal to 1, otherwise one of the term of the sum (5.14) will diverge.

In the case of the fixed current polarity channel, the eigenvalues vector $\vec{\lambda}$ of T_+ corresponds to $(1, 1, e^{-\frac{2iBl}{B\rho}}, e^{+\frac{2iBl}{B\rho}})$ and since $|\lambda_i| \leq 1$ is verified the system is always stable.

The study of the solenoidal channel with alternating polarity uses the same formalism. The transfer matrix T_a is computed as:

$$T_a = R_{+\frac{1}{2}} \cdot F_+^{in} \cdot F_-^{out} \cdot R_- \cdot F_-^{in} \cdot F_+^{out} \cdot R_{+\frac{1}{2}}$$

with eigenvalues vector equals to $(e^{-\frac{iBl}{B\rho}}, e^{-\frac{iBl}{B\rho}}, e^{\frac{iBl}{B\rho}}, e^{\frac{iBl}{B\rho}})$. Also in this case $|\lambda_i| \leq 1$ is verified and the system is always stable.

Few considerations about the eigenvalues of T_+ and T_a can be deduced by the characteristics of the channel:

- two eigenvalues have to be complex conjugate[†];
- the product of the eigenvalues has to equal one because it corresponds to the determinant of the transfer matrix. The latter is the product of matrices with determinant equals to one, and the product of matrices has the same determinant as the product of the determinants of each matrix;

[†]This property comes from a theorem of squared real matrix. If one of the eigenvalues is complex, also its complex conjugate is an eigenvalue.

- considering the first two properties it follows that the absolute value of one eigenvalue is inversely proportional to the absolute value of the eigenvalue which is not its complex conjugate[†].

Two more questions can rise from the previous analysis, namely why the systems are always stable and if the stability of the fixed current polarity channel implies also the stability of the alternating polarity one.

A naive answer to the first question could be the following. Particles are always immersed in the magnetic field, and even if they are overfocused or underfocused they are always traveling in a magnetic field. The only restriction to a stable motion would come from a geometric limitation, like the one imposed by a beam pipe, which is not taken into account by this formalism. The answer to the second question can be deduced by observing that the focusing is the same for the two channels, since:

$$F_+^{in} \cdot F_+^{out} \cdot F_+^{in} \cdot F_+^{out} = F_+^{in} \cdot I \cdot F_+^{out} = F_+^{in} \cdot F_-^{out} \cdot F_-^{in} \cdot F_+^{out}$$

and the instability would only arise from the focusing. Moreover one could demonstrate the same property with a little algebra. The matrix T_a differs from T_+ for the inner negative solenoid, namely $F_-^{out} \cdot R_- \cdot F_-^{in}$. Using (5.10) and (5.11) one can show that:

$$R_{+\frac{1}{2}} \cdot F_+^{in} \cdot F_-^{out} \cdot R_- \cdot F_-^{in} \cdot F_+^{out} \cdot R_{+\frac{1}{2}} = \\ R_{+\frac{1}{2}} \cdot F_+^{in} \cdot F_+^{out} \cdot F_+^{in} \cdot F_+^{in} \cdot R_- \cdot F_+^{out} \cdot F_+^{out} \cdot F_+^{in} \cdot F_+^{out} \cdot R_{+\frac{1}{2}}$$

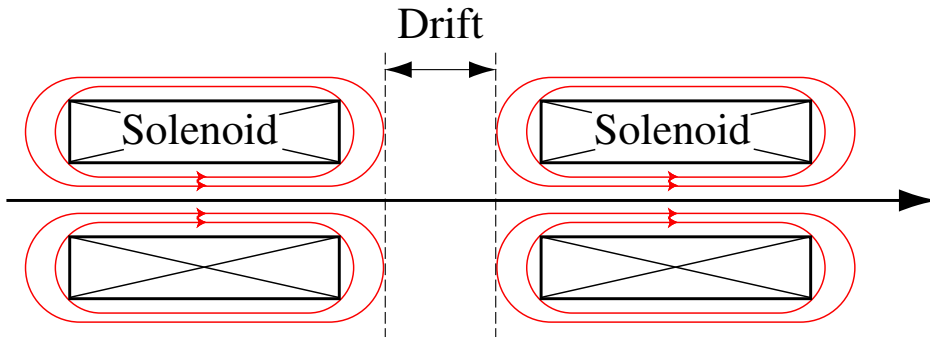
The inner term $F_+^{in} \cdot F_+^{in} \cdot R_- \cdot F_+^{out} \cdot F_+^{out}$ has the same eigenvalues of R_+ but different eigenvectors. In this way the only subsystem which is different in the two cases leads to the same stability conditions.

5.2.1 Periodic channel with a drift

A more realistic model of a periodic solenoidal channel is obtained by introducing a drift between each solenoid (see figure 5.3). The matrix D of a drift in 4 dimensions is block diagonal, since the coordinates of the two transverse planes are no more coupled like in a solenoid.

$$D = \begin{pmatrix} 1 & d & 0 & 0 \\ 0 & 1 & 0 & 0 \\ 0 & 0 & 1 & d \\ 0 & 0 & 0 & 1 \end{pmatrix}$$

[†]From this property it follows that the general condition for the stability, namely $|\lambda_i| \leq 1$, becomes $|\lambda_i| = 1$.

Figure 5.3: *Series of solenoid with an interposed drift*

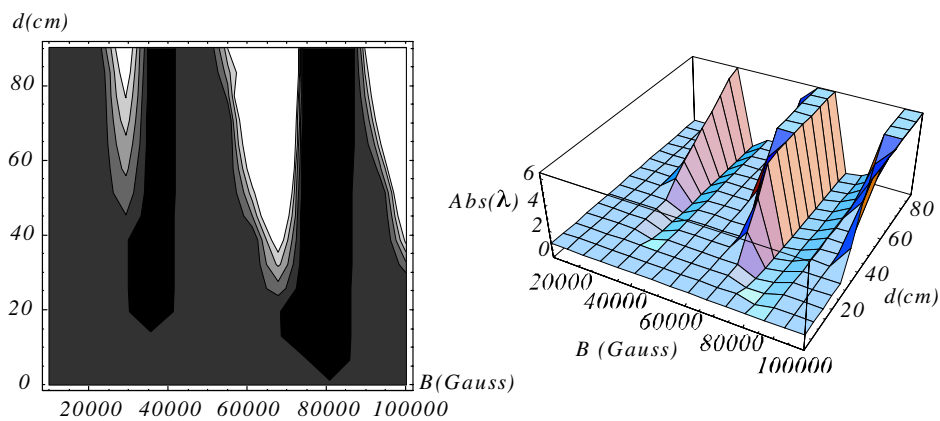
where d is the drift length.

The channel transfer matrix for positive solenoids for one period becomes:

$$T_+^D = R_{+\frac{1}{2}} \cdot F_+^{in} \cdot D \cdot F_+^{out} \cdot R_+ \cdot F_+^{in} \cdot D \cdot F_+^{out} \cdot R_{+\frac{1}{2}} \quad (5.15)$$

whose eigenvalues vector has a too complicated form to be written explicitly, but it can be calculated numerically by for example MATHEMATICA[®] [94].

The stability criterium presented in the previous section is still valid and also the eigenvalues properties. The stability conditions for the channel is defined again by the region where all the $|\lambda_i|$ are less or equal 1. Figure 5.4 and 5.5 show the eigenvalues $|\lambda_1|$ and $|\lambda_2|$ in function of d (drift between two solenoids) and the applied B field. Those two plots are generated for 100 MeV muons and a solenoid effective length of 90 cm.

Figure 5.4: *First eigenvalue plot as function of the applied magnetic field (in Gauss) versus the drift length (in cm)*

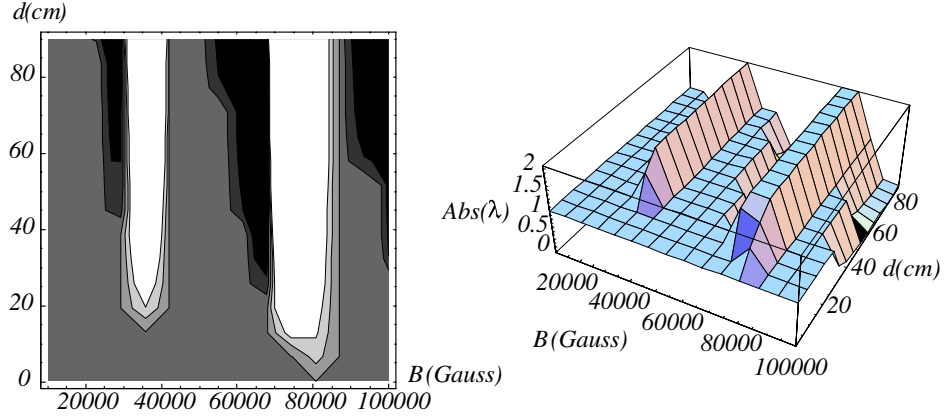


Figure 5.5: *Second eigenvalue function. The white zones are the unstable regions.*

The unstable regions are obtained by the sum of the light-gray and white zones of the two contour plots, which correspond to the condition of $|\lambda_i| > 1$.

A PATH[92] simulation of the same periodic channel has been used to check the theory. Two cases were considered, the first one is a stable channel ($d = 40 \text{ cm}$ and $B = 20000 \text{ Gauss}$) and the second is an unstable channel ($d = 40 \text{ cm}$ and $B = 35000 \text{ Gauss}$) and muons as beam particles. The beam energy equals to $E_k = 100 \text{ MeV}$ and the Twiss parameters for the transverse phase space are $\alpha = 0$ and $\beta = 10 \text{ m}$ and $\epsilon = 10^{-4} \text{ m rad}$ for both transverse planes. In the case of the stable channel the beam oscillates (figure 5.6) with a maximum amplitude that is constant, while in the case of the unstable channel this maximum increases (figure 5.7).

The same analysis can be repeated for the solenoidal channel with alternating polarity. The transfer matrix equals to:

$$T_a^D = R_{+\frac{1}{2}} \cdot F_+^{in} \cdot D \cdot F_-^{out} \cdot R_- \cdot F_-^{in} \cdot D \cdot F_+^{out} \cdot R_{+\frac{1}{2}} \quad (5.16)$$

and the eigenvalue functions are shown in figure 5.8 and 5.9. In this case the instability comes from the absolute values of the second eigenvalue, while the stability condition for the first eigenvalues is always fulfilled.

A PATH simulation is performed to check also in this case the theory. The beam parameters and the magnetic field have been kept the same as in the previous case, with the exception that the field sign was reversed after each solenoid. The results of this simulation are presented in figure 5.10 and 5.11, where the RMS beam envelope oscillates in the case of the stable condition (figure 5.10) and diverges for the unstable condition (figure 5.11).

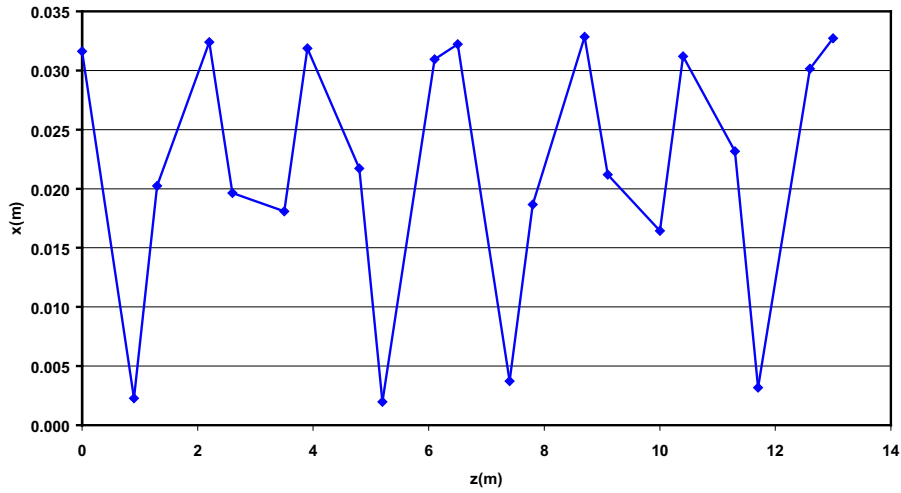


Figure 5.6: *The RMS envelope oscillates in the transverse plane along the channel but the oscillation remains bounded by a maximum value.*

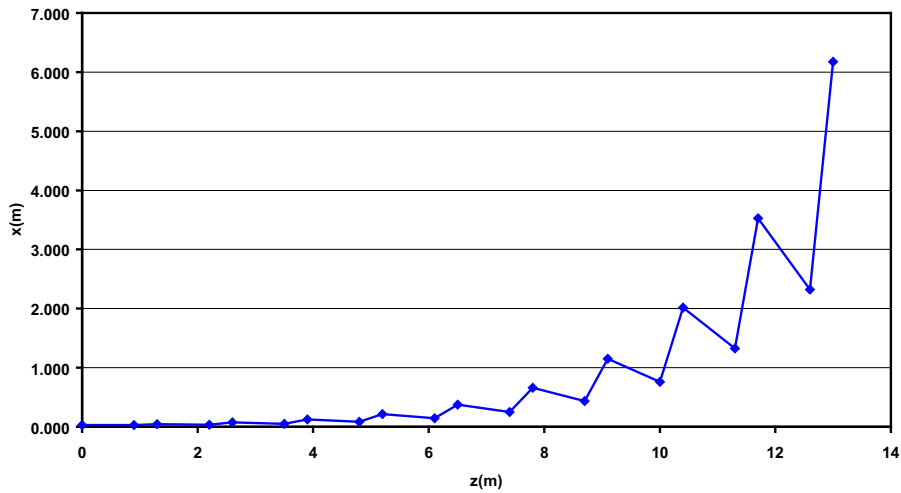


Figure 5.7: *For the unstable channel the RMS envelope starts to diverge after few cell.*

5.3 Stability versus energy acceptance

The method discussed in the previous section can be used also to determine the energy acceptance of a solenoidal channel. The expression for the eigenvalues is a function of four variables: the solenoid effective length l , the magnetic field B , the drift length d and the rigidity of the particle $B\rho$. As

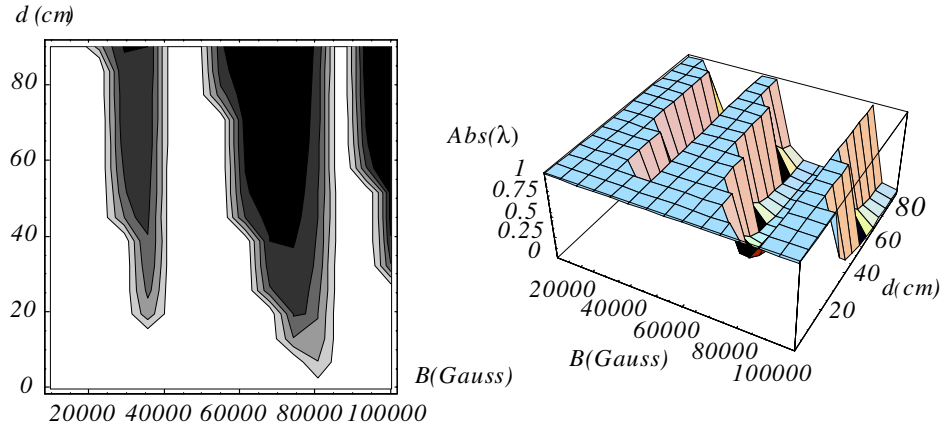


Figure 5.8: The absolute values of the eigenvalue is always less than one, so the white zones in this case don't represent the unstable regions.

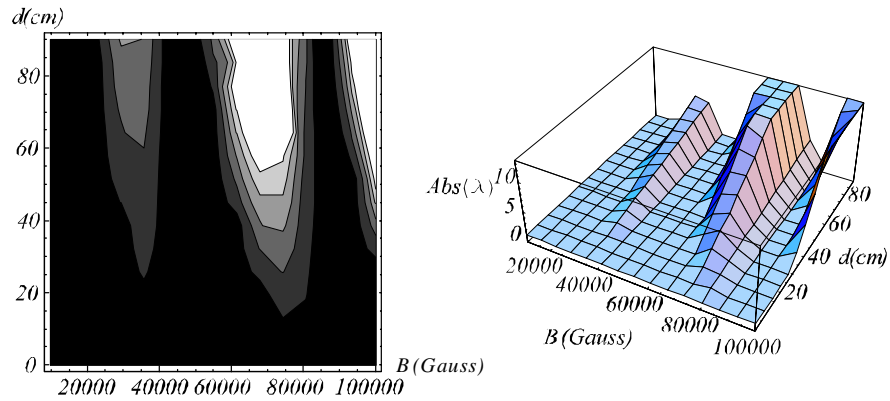


Figure 5.9: The absolute values of the second eigenvalue is greater than one in the white region, where the system becomes unstable.

$B\rho(\text{Gauss cm}) = 0.333 \cdot 10^4 p(\text{MeV}/c)$ (see figure 5.12) one can study the absolute values of the eigenvalues versus the rigidity, once the other three variables are fixed by the choice of the lattice, and study the momentum or the energy range accepted by the channel.

One application of this method is presented in figure 5.13. The channel chosen is composed by alternating polarity solenoids 90 cm long, 5 T field spaced by a 40 cm long drift. This channel can accept any particle with rigidity greater than $1 \cdot 10^6$ Gauss cm but there is also a band between $5 \cdot 10^5$ and $6 \cdot 10^5$ Gauss cm where the transport is stable.

5.4. HARD EDGE AND FIELDMAP EQUIVALENCE FOR THE STABILITY153

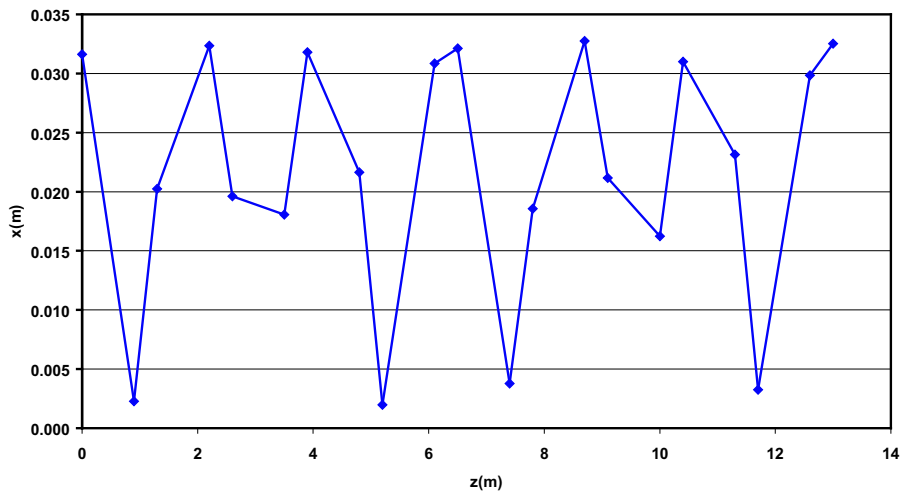


Figure 5.10: *RMS beam envelope versus the position along the channel in the case of stable field configuration..*

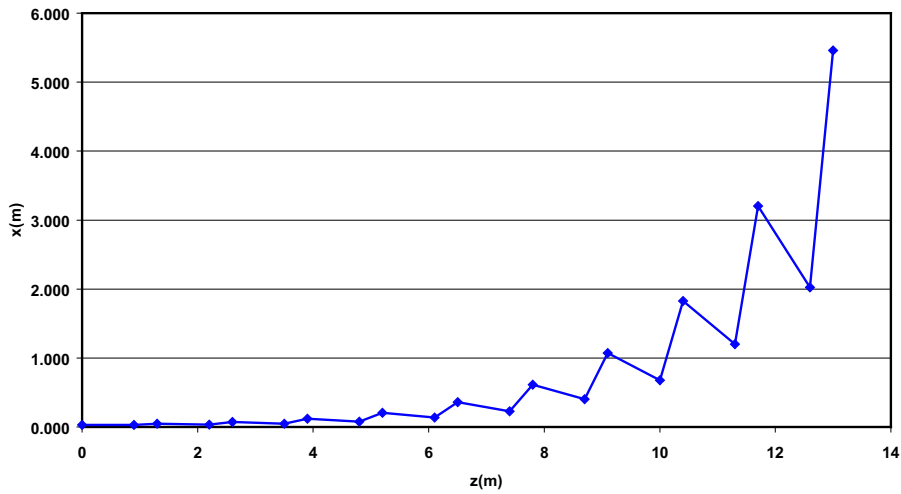


Figure 5.11: *RMS beam envelope for unstable magnetic field condition.*

5.4 Hard edge and fieldmap equivalence for the stability

In order to apply the results of the previous analysis to a field generated by magnetic coils it is necessary to establish an equivalence between the fieldmap and a solenoid described by the hard edge model.

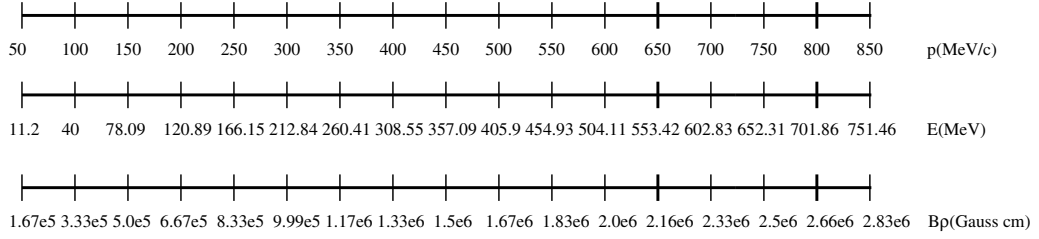


Figure 5.12: Conversion between momentum, kinetic energy and rigidity for muons.

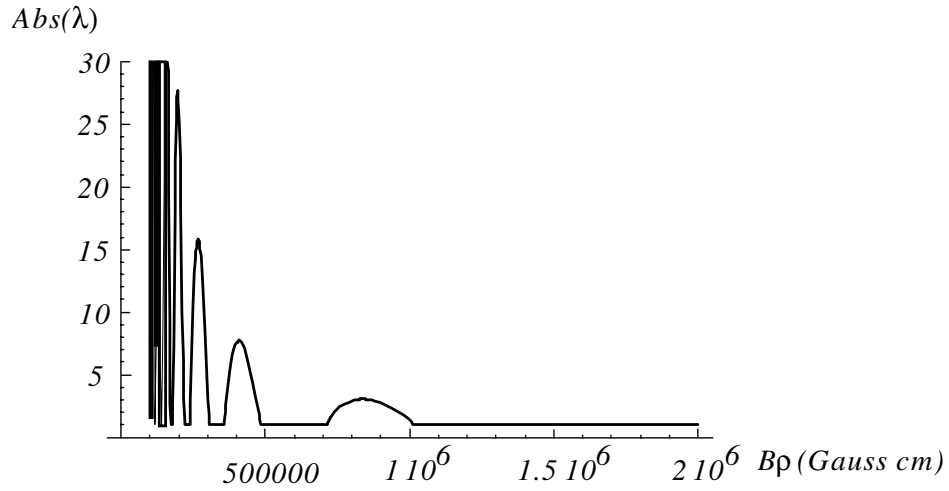


Figure 5.13: Absolute value of one eigenvalue versus beam rigidity for the described channel. The channel is unstable for absolute values greater than one.

In this case the fieldmap of a solenoid of length $L = z_f - z_i$ can be seen as a drift d followed by a solenoid of length l in the hard edge model, and then again another drift d , where $d = (L - l)$ and l corresponds to the effective length of the solenoid, namely:

$$l = \frac{1}{B_0^2} \int_{z_i}^{z_f} B^2(z, r = 0) dz \quad (5.17)$$

As example, a fieldmap of six solenoids of 410 cm length, 30 cm inner radius, spaced by 10 cm, is generated by POISSON[99]. Figure 5.14 shows the field along the beam axis of the central solenoid which is chosen as the element of the periodic lattice.

The solenoid fieldmap is considered equivalent to a 1.55 T solenoid in the hard edge model, 394.6 cm long preceded by a drift of 15.4 cm.

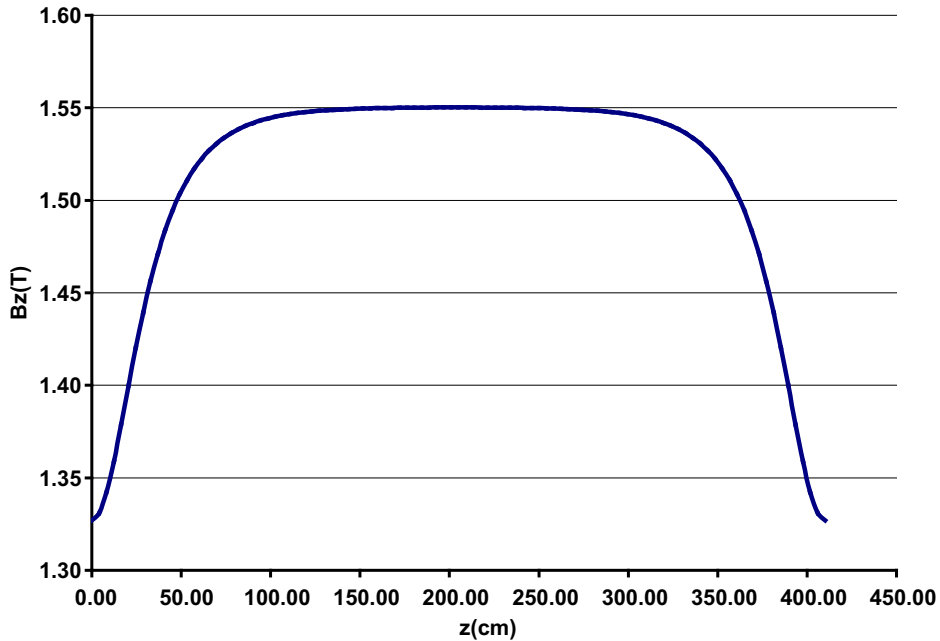


Figure 5.14: B_z along the beam axis. The effective length for this map is calculated taking $z_i = 0$ and $z_f = 410$ cm and $B_0 = 1.55$ T.

The plots for the absolute values of the two eigenvalues are shown in figure 5.15 and 5.16.

A PATH simulation that uses the fieldmap has been performed to check the results from the theory. Two cases are chosen, the first with a muon beam of 300 MeV/c momentum ($B\rho \approx 1 \cdot 10^6$ G cm) in the unstable region, the second one is the same beam but with a momentum of 391.65 MeV/c ($B\rho \approx 1.3 \cdot 10^6$ G cm).

Figure 5.17 and 5.18 show the transverse phase space $x - x'$ of the beam that results from the tracking in the case of unstable and stable conditions. In the unstable condition two large tails build up, while in the case of stable condition the beam rotates in the transverse plane.

5.5 Conclusions

A new procedure to identify the stability of a solenoidal channel has been discussed in this chapter.

The stability of a periodic solenoidal channel can be established by calculating the eigenvalues of the transfer matrix for one period and requiring that the absolute values of all the eigenvalues verify the condition $|\lambda_i| \leq 1$. This

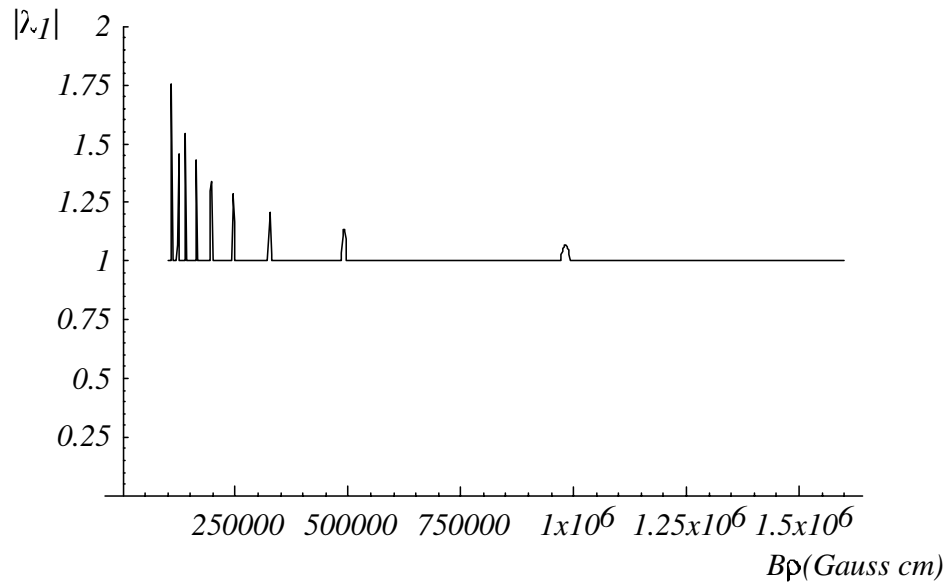


Figure 5.15: Absolute value of the first eigenvalue calculated for the equivalent hard edge solenoid plus a drift.

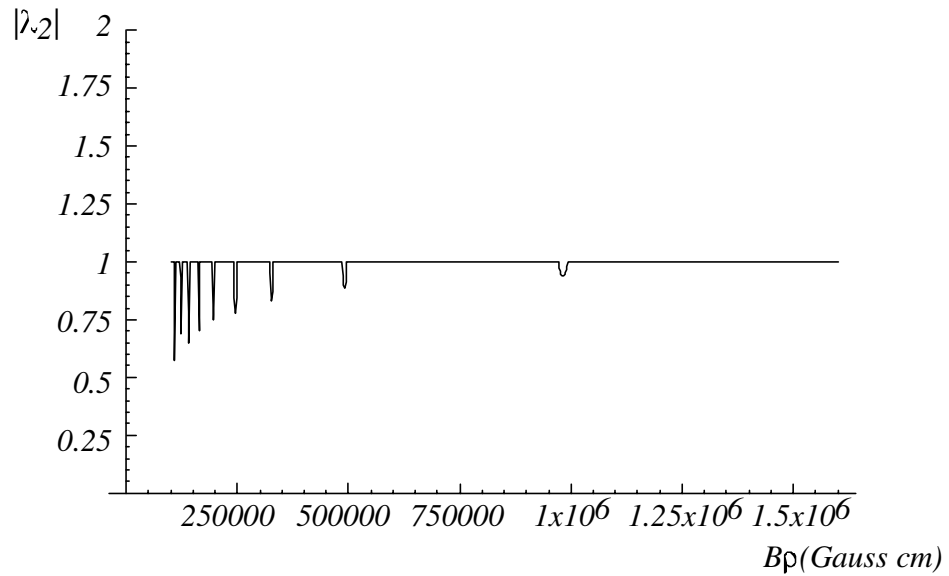


Figure 5.16: Absolute value of the second eigenvalue calculated for the equivalent hard edge solenoid plus a drift.

condition is also valid for the stability of channels computed from solenoid fieldmaps, if the equivalent solenoid in the hard edge model is used. The latter has been tested with the particle tracking code PATH.

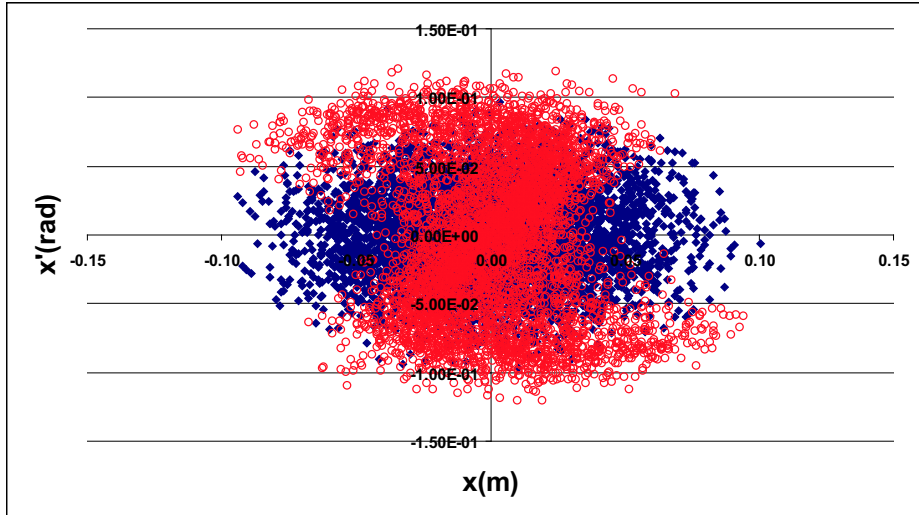


Figure 5.17: *The full dots are the muons generated at the beginning of the channel while the open dots the muons after 20 solenoids for unstable conditions.*

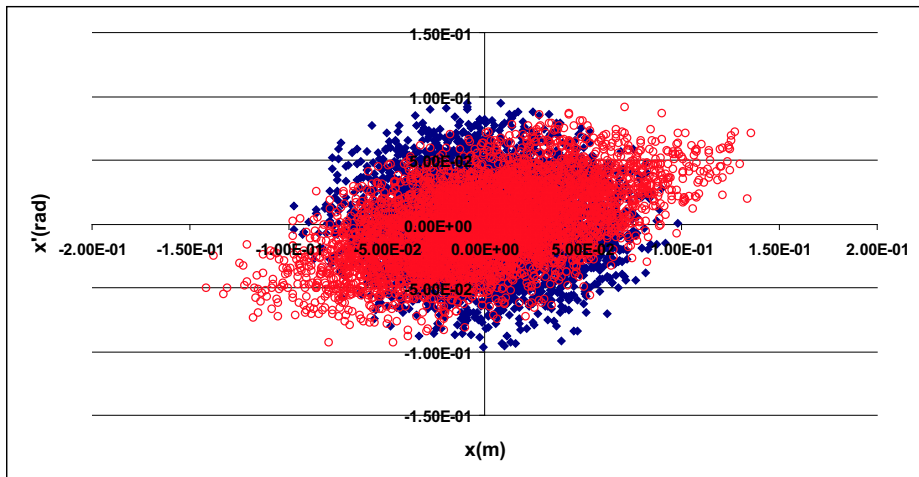


Figure 5.18: *The full dots are the muons generated at the beginning of the channel while the open dots the muons after 20 solenoids for stable conditions.*

Chapter 6

Phase Rotation

6.1 Phase Rotation

The phase rotation is the section of the Neutrino Factory whose aim is the reduction of the muon energy spread. Such a decrease of the energy spread is necessary for the injection into the following part of the machine, the cooling channel and the recirculating linacs for the acceleration.

As shown in figure 6.1, the energy distribution of pions after the focusing

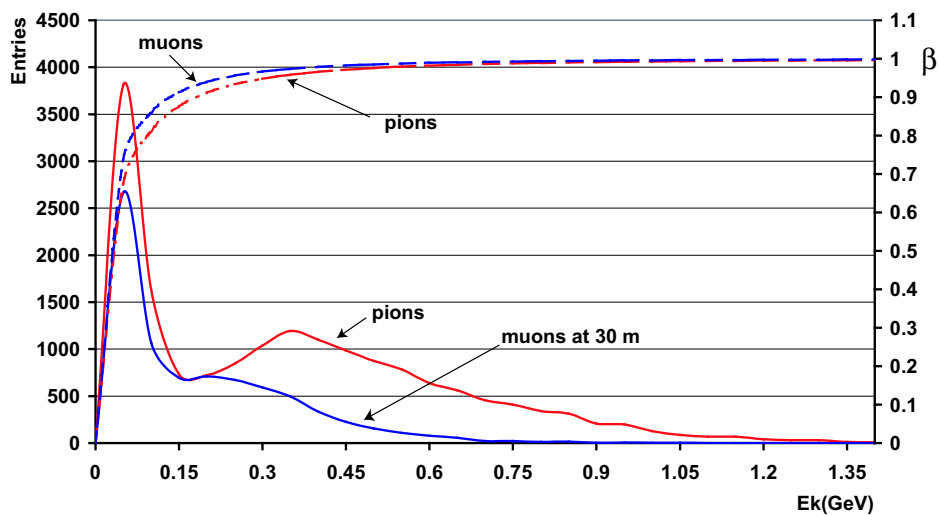


Figure 6.1: *Pion kinetic energy distribution after the collecting device and muon energy distribution after 30 m together with their respective relativistic beta.*

system or of muons after a 30 m long decay channel is quite broad. A possible choice for the injection into the accelerating section would be to capture

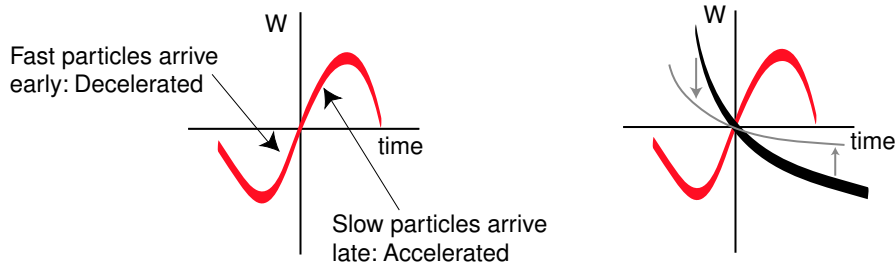


Figure 6.2: *Since muons in the energy window considered are not ultra-relativistic, an energy spread corresponds to a velocity spread. More energetic muons arrive early at the RF section and they are decelerated while low energetic muons arrive late at the RF and they are accelerated.*

particles longitudinally around the most populated energy, without any manipulation of the longitudinal plane. However, such a scheme loses most of the particles due to the large energy spread. A more effective solution is to reduce the energy spread around the most populated energy (200 MeV for muons and 400 MeV for pions) and for β larger than 0.85 by a phase rotation before injecting in the rest of the machine.

The phase rotation consists in a rotation of the particle longitudinal phase space[†]. This is realized by slowing down the high energy particles and by accelerating the low energy particles (see figure 6.2). This is possible because pions or muons produced by pion decay are spread in a kinetic energy interval between 1 GeV down to few MeV, and most of them are not ultra-relativistic (as shown in figure 6.1). This implies that, both for pions and for muons, to the energy spread corresponds a velocity spread: at the end of the decay channel, for example, muons of higher energy will arrive before the less energetic ones. This effect is shown in figure 6.3 where pions at the beginning of the channel, for $c * Time < 1000\text{ cm}$ (where c is the speed of light) decay into muons plotted at the end of the channel ($c * Time$ larger than 3000) where present a the strong time(or phase)-energy correlation.

Three different longitudinal manipulations have been discussed to obtain the same energy spread reduction:

- phase rotation of pions using RF cavities after the pion capture device;
- phase rotation of muons using RF cavities after 30 m;
- phase rotation of muons using induction linacs after 100 m.

[†]This process is not longitudinal cooling since the longitudinal phase space is conserved.

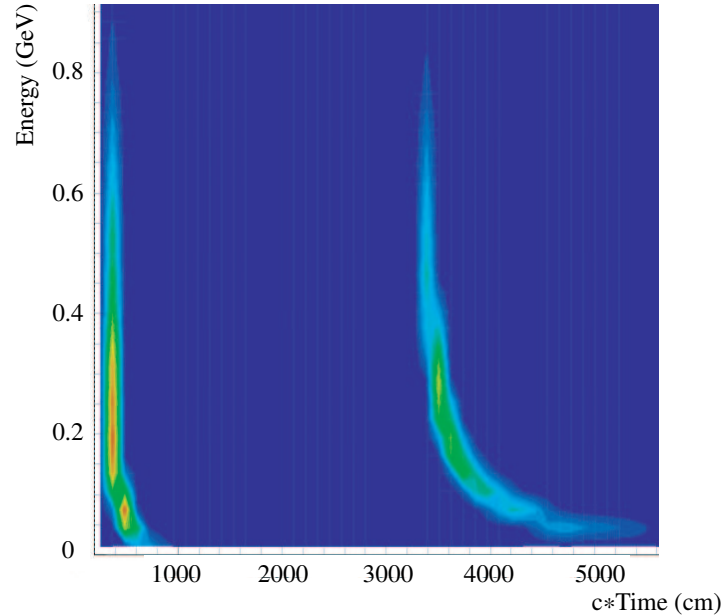


Figure 6.3: *Pions at the beginning of the decay channel, for $c * \text{Time}$ smaller than 1000 cm, with c the speed of light, have a large energy spread which is transmitted to the muons at the end of the decay channel ($c * \text{Time}$ larger than 3000 cm)*

These three approaches differ from the shape of the phase space that they manipulate (see figure 6.4).

After 1 m, as after 10 m from the target, the beam is composed mostly by pions (figure 6.4, two plots on top), which have a large energy spread but a small time spread (see figure 6.5). In this case the phase rotation can be applied by high-gradient (16 MV/m or 4 MV/m) high-frequency (200 MHz or 88 MHz) cavities. The main disadvantages come from the operation in a high radioactive environment and, moreover, from the complication of the time spread increase during the phase rotation due to pion decay. The decay, as shown from figure 6.4, enlarges the particle distribution in the longitudinal plane, pushing particles outside the bucket of the high frequency cavities.

The second possibility is to operate the phase rotation after 30 m. At such distance most of the pions are decayed into muons and the time spread (see figure 6.5) is still small enough to use RF cavities at middle frequency (44 MHz) and moderate gradient (2 MV/m). This is the CERN choice for the

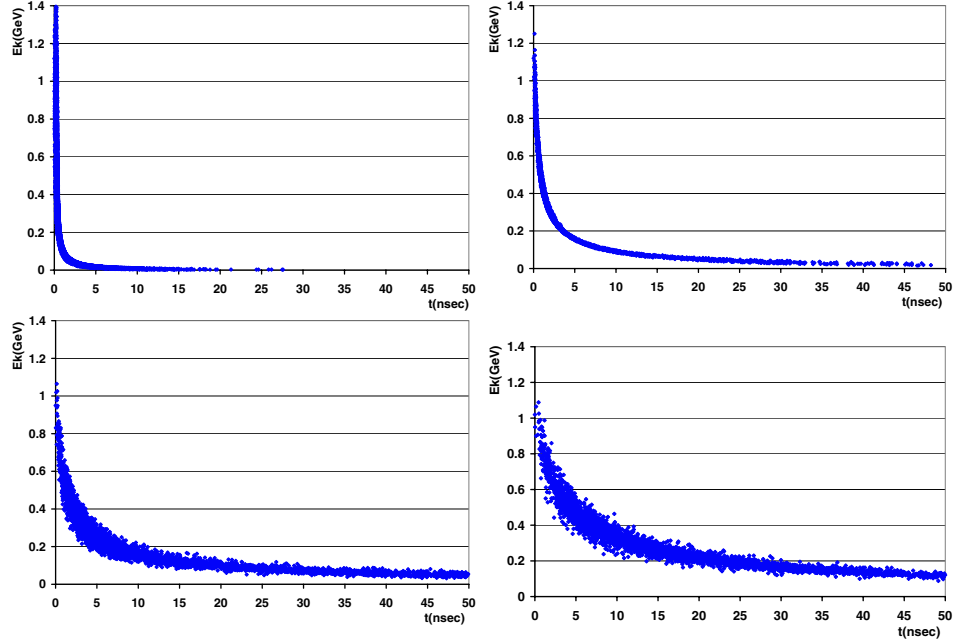


Figure 6.4: Longitudinal phase space for pions after 1 m and 10 m from the target (upper plots) and for muons after 30 m and 100 m (lower plots)

Reference Scenario and it will be discussed in the following.

In the last scheme, the one chosen for example in the US scheme [18], muons drift for 100 m to build a strong energy-time correlation (see figure 6.4) and the beam is quasi-continuous (see figure 6.5). The phase rotation is performed using a series of two induction linacs followed by a rebunching section at high frequency (200 MHz). The weak point of the scheme is the latter section, where most of the losses occurs.

6.2 CERN Reference Scenario

In the CERN Reference Design, phase rotation starts after a 30 m long decay channel where the beam is composed mainly by muons. At this distance muons preserve, with a 1 nsec time jitter due to the decay, the time structure of the pions and the latter have the same protons time structure (*bunch to bucket* technique for which the secondaries produced by the same bunch of protons fill the same bucket). As shown in figure 6.6, the proton beam has a macrobunch structure at 50 Hz (20 ms) and a microbunch structure at 44 MHz (22.7 ns). The phase rotation in the CERN scheme can hence be done with a set of 44 MHz RF cavities, since the 44 MHz bucket is long enough

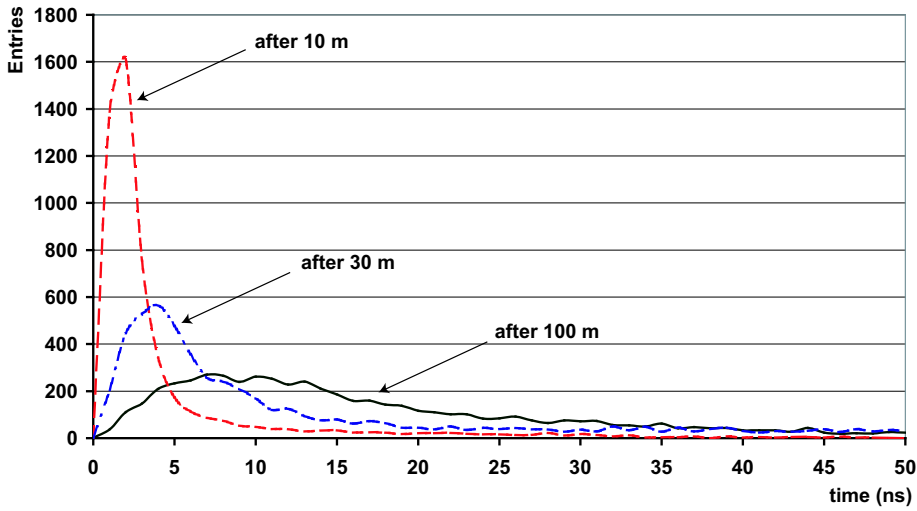


Figure 6.5: Time distribution for pions after 10 m from the collecting device and for muons after 30 m and 100 m from the collecting device

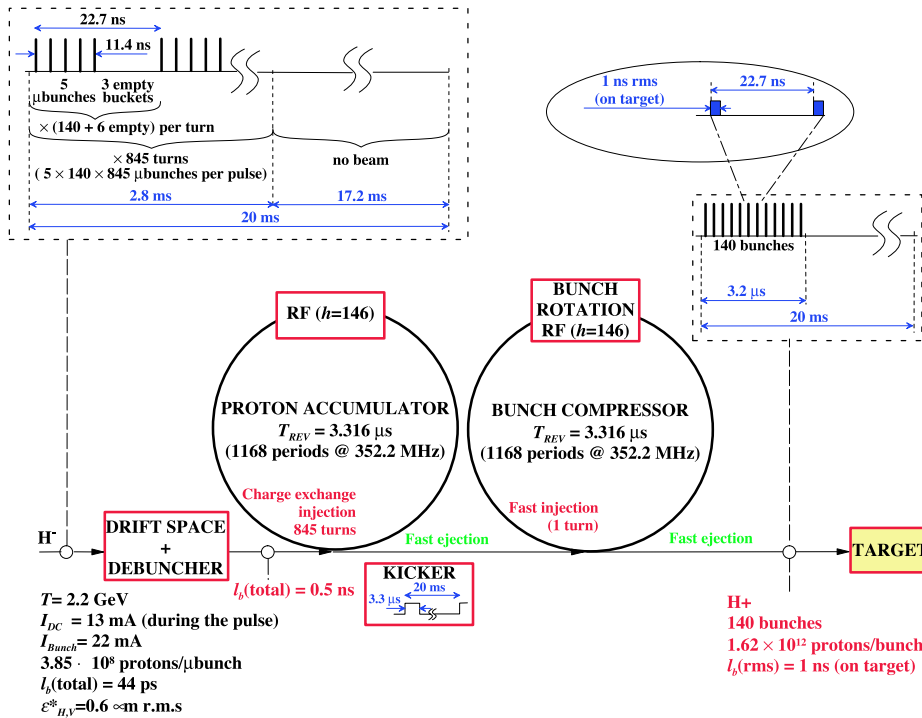


Figure 6.6: CERN proton driver time structure

(≈ 12 nsec to be compared with the time spread shown in figure 6.5) and high enough (≈ 100 MeV) to contains a large part of muons within an energy window of ± 50 MeV around the central energy of 200 MeV.

The total voltage required to rotate the beam is ≈ 60 MV (to achieve an average energy spread reduction of 50 MeV), and considering an average gradient of 2 MV/m, the channel is composed by 21 cavities 1.4 m long for a total length of 29.4 m.

6.2.1 Geometry and materials implemented in the simulation

The phase rotation channel has been simulated to calculate the muon transmission coefficient and the energy deposition in the superconducting solenoid cryostat due to beam losses or due to the electrons produced by muon decay. The phase rotation is composed of 21 44-MHz cavities with a gradient of 2 MV/m. According to the last design from [96](see figure 6.7) each cavity is 1.4 m long with a bore aperture of 30 cm. The total length of the channel 29.4 m and the maximum radius considered for the calculation of the beam energy losses is the external radius of the cryostat, which equals 1.3 m. The fieldmap of the solenoid surrounding one RF was generated by POISSON [99]. The field was normalized (normalization factor equals 1.7) to have the same integrated field as the one of a hard edge solenoid[†] of 2 Tesla and 1 meter long (see figure 6.8 for the un-normalised field distribution).

The free spaces inside the channel, like the beam pipe volume, were filled with air of the following contents (here and below everything is expressed in weight concentrations) $0.7537N + 0.2315O + 0.0128Ar$ at a pressure of 10^{-8} atm. This pressure roughly corresponds to technical vacuum that can be provided for large hermetical volumes. Each sections consists of stainless steel cover ($0.73Fe + 0.16Cr + 0.09Ni$) surrounding a cryostat filled with liquid helium. Inside the liquid helium a superconducting niobium solenoid generates the field of figure 6.8. A small gap of 1 micron was provided for touching surfaces.

6.2.2 Interactions of particles with materials

The incoming particle spectra were calculated by a MARS [98] simulation which includes pion production, interaction, focusing and decay, and only positive muons are considered for the energy deposition calculation. The simulation before the phase rotation includes the pion production with a

[†]The definition of hard edge solenoid is given in chapter 5

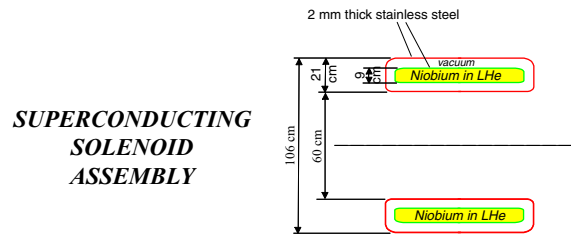
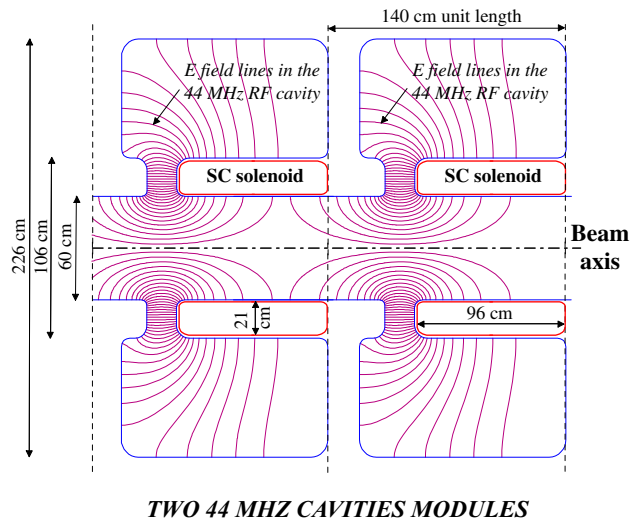


Figure 6.7: Cavity design from [96]. This geometry is described “as it is” in the GEANT4 simulation.

mercury target, the capture with a solenoid, and a solenoidal decay channel. The tracking of muons inside the phase rotation channel and all the interaction are calculates by GEANT4 [95]. Muons interact with matter by ionization energy loss, bremsstrahlung and pair creation. In addition they experience multiple scattering. Secondary electrons experience ionization energy loss, bremsstrahlung and multiple scattering. Secondary X-ray and gamma experience photoabsorption, Compton scattering and conversion.

6.3 Results of the simulations

The GEANT4 simulation was compared to a PATH [101] simulation of the phase rotation reference scheme [100] to validate the RF implementation in GEANT4 . Table 6.1 shows the nice agreement between the two simulations for transmission coefficients, while a small difference, discussed in the

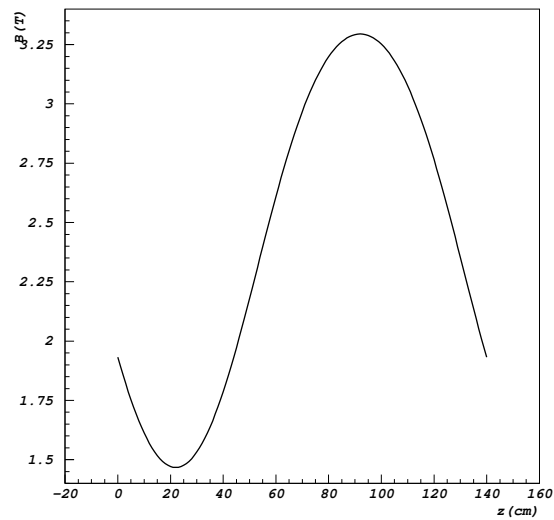


Figure 6.8: *Un-normalised longitudinal magnetic field component for along the beam axis of one RF cavity.*

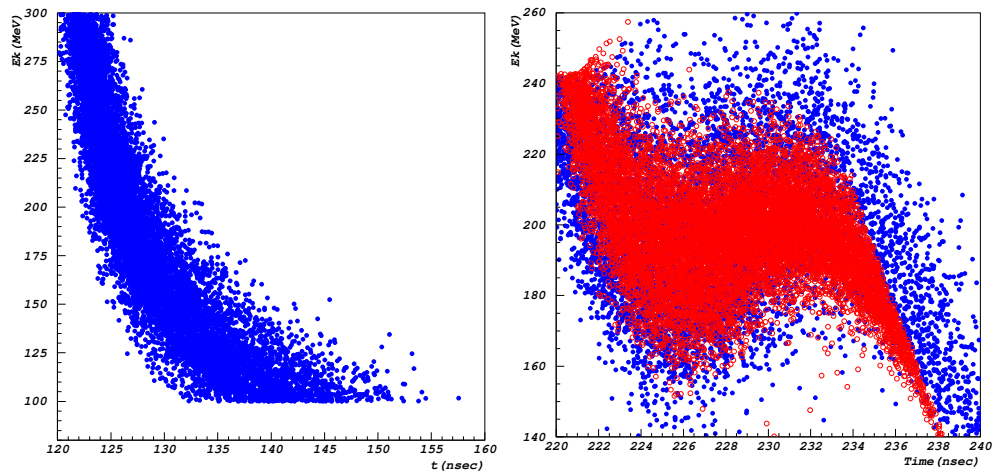


Figure 6.9: *Longitudinal phase space for muons produced by pion decay channel (left) at the beginning of the phase rotation. The right figure shows the GEANT4 simulation (full dots, blue), and PATH (open dots, red) after the phase rotation.*

6.4. ENERGY DEPOSITION IN THE SUPERCONDUCTING SOLENOIDS167

following, could be noticed in the longitudinal plane (figure 6.9).

	Input	Transmission	In cut
PATH	15222	100%	77%
GEANT4	10436	94%	79%

Table 6.1: *Particles “In cut” are calculated as the percent of the input muons selected in a window defined by $140 \text{ MeV} < E_{kinetic} < 260 \text{ MeV}$ and in one RF period of 44 MHz.*

The two distributions of figure 6.9 differ for the tail due to the following reasons:

- in the GEANT4 simulation the phase of the reference particle is chosen by injecting a 200 MeV muon in the center of the beam line. The arrival time of this particle at the different RF units is used as reference for the RF phase. This procedure is good enough only in first approximation, while codes like PATH calculate the time of the average particle before each RF. The average particle takes into account the evolution of the whole bunch in the channel, which is ignored by a single particle approach. To improve the GEANT4 RF implementation, one could imagine to use the GEANT4 stack facility. All the muons could be tracked just before one RF where the particles are stored into the stack. Once all the particles reach the RF, the average muon is evaluated and then the tracking restarts until the next RF, where this process is repeated.
- the particles used for the two simulations are not the same, but the average quantities like spot size, time and energy distribution are the same.
- the RF length was 1 m for the PATH simulation (as in the CERN reference scenario), while in the GEANT4 simulation the cavity is 1.4 m long, according to the very last design from [96]. The average gradient per meter was kept constant.

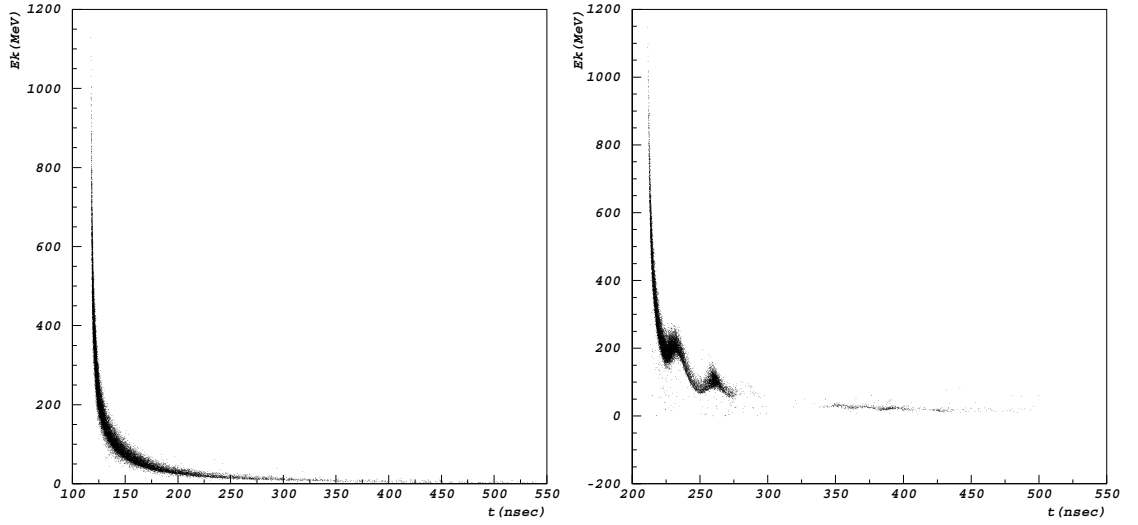


Figure 6.10: All muon spectra at the beginning of the phase rotation(left) and at the end of the channel(right)

6.4 Energy deposition in the superconducting solenoids

The energy deposition in the cryostat was calculated by the GEANT4 simulation using the full geometry shown in figure 6.7. All positive muons produced by pion decay (see figure 6.10) and accepted by the previous channel are tracked in the phase rotation, where part of them is lost due to mismatch. The phase rotation channel was optimised to transport with the higher possible efficiency the muons described in table 6.1. Only 6% of them are lost in the channel for mismatch or decay, while if one considers the whole muon distribution, then the transmission decreases from 94% to 69%. The energy deposited in the cryostat+solenoid is calculated by GEANT4. In figure 6.11 on left one could see the energy deposited versus the radius and integrated along the z coordinate. The spikes correspond to the energy deposited in the 2 mm thick steel surfaces of the cryostat, which are visible also in right histogram where the energy deposited is integrated along the radius and plotted versus the position along the beam axis. From this figure one could see that most of the power losses are due to the mismatch of the beam in the first four cells, after which it decreases and stays constant along the channel.

The energy deposition integrated versus the radius and z , normalised to one cell, gives 30.8 W/m, which is twice the recommended limit for a traditional cryogenic system. As solution, the beam losses could be diluted in the decay

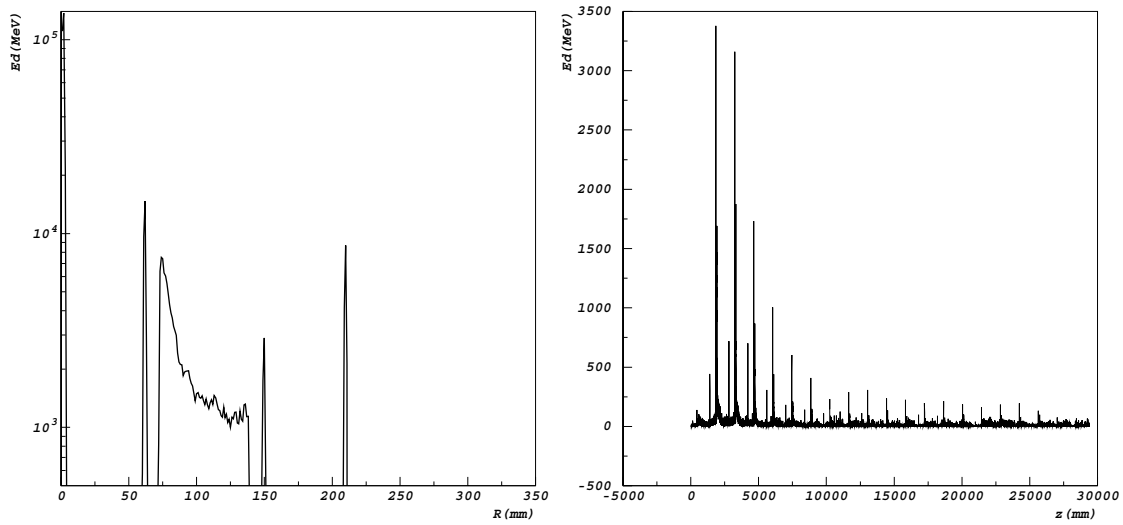


Figure 6.11: *Integrated energy deposited versus radius (left) and versus position in the channel(right)*

channel, of which a careful redesign could be envisaged.

6.5 Discussion and conclusions

A simulation of the CERN reference scheme for the phase rotation using GEANT4 was presented in this chapter. This can be considered as the first application of GEANT4 to accelerator simulation at CERN.

The RF implementation in GEANT4 is validated by the nice agreement with the simulation of the same channel using the PATH code.

The energy deposition in the cryostat+solenoid of the RF system calculated by GEANT4 is 30.8 W/m, which is a first input for further cryostat and channel in final design.

6.6 Appendix: Introduction to GEANT4

GEANT4 is an object-oriented toolkit for simulation in High Energy Physics, Space, and Medical applications [95].

The GEANT4 software has been developed by a world-wide collaboration of about 100 scientists from over 40 institutions and laboratories participating in more than 10 experiments in Europe, Russia, Japan, Canada and the United States. GEANT4 has exploited advanced software engineering techniques and Object Oriented technology to improve the validation of physics

results and in the same time to make possible the distributed software design and development in the world-wide collaboration. The first GEANT4 production version was released by the end of 1998, as it was scheduled in the DRDC P58 project proposal at the end of 1994. Since then, regular biannual releases have been performed, maintained and supported for the users. GEANT4 has a multi-disciplinary nature, providing functionality in a set of different scientific fields. The GEANT4 Object-Oriented design allows the user to understand, extend, or customise the toolkit in all the domains. At the same time, the modularity of the GEANT4 software allows the user to load and use only the components he needs. The main functionality of the different domains is outlined here.

The GEANT4 physics processes exploit Object-Oriented Technology to make transparent how physics results are produced. The way cross sections are calculated (via formulas, data files, etc. and eventually using different data-sets with restricted applicability by particle, energy, material) is clearly exposed via Object-Oriented design and it is separated from the way they are accessed and used in the algorithms. The user can overload both these features. The way the final state is computed is again separated from the tracking and is split into alternative or complementary models, according to, for example, the energy range, the particle type, the material. Multiple implementations of physics processes and models are possible and have been made available. No numbers should be hard-coded in formulas and algorithms, but only variables and constants should be used. An extensive set of units is defined in GEANT4 and all the numerical quantities are expressed through units explicitly, thus making the GEANT4 physics independent from the units chosen by the user.

The Electromagnetic physics manages lepton physics, gamma, x-ray and optical photon physics, and muon physics. It includes various implementation of ionization and Bremsstrahlung (both with differential treatment for energy loss and with integration of cross-sections in function of energy), the latter with LPM effect, as well as multiple scattering (with lateral displacement and without any path length restriction), and annihilation. It includes as well multiple implementations of the photoelectric (also with fluorescence) and Compton (also with polarisation) effects, pair conversion, synchrotron and transition radiation, scintillation, refraction, reflection, absorption and Rayleigh effect. Low energy extensions, down to 1 KeV and below, are implemented and will continue to be produced in the framework of a joint project with the European Space Agency. The validity range of all the muon processes (based on theoretical models) scales up to the PeV region, allowing the simulation of ultra-high energy and cosmic physics.

The Hadronic physics offers both a data parameterisation-driven set of

models, and a variety of theory-driven models for physics beyond test-beams energies, as well as treatment of low energy neutron transport. Parameterisation-driven models include high energy inelastic scattering, as well as low energy inelastic and elastic scattering, fission, capture and dedicated processes for stopping kaons and pions physics. The theory-driven models provide two string parton models in the high energy regime (with the possibility to interface to Pythia7 for the hard-scattering), as well as intra-nuclear transport models and pre-equilibrium, and a variety of de-excitation models, including evaporation, photo-evaporation, fission, Fermi break-up and multi-fragmentation. The low energy neutron transport is based on best selections of evaluated data (such as ENDF-B VI, JENDL, CENDL, ENSDF, JEF, BROND, IRDF, exploiting the file system to maximise a granular and transparent access to the data sets for the user) and it offers event biasing options, allowing radiation background studies. Lepton-hadron interactions, such as muon-nuclear interactions, photo-fission and general gamma-meson conversion are also implemented. Object-Oriented technology allows to plug-and-play models, for example a theory-driven evaporation model is also used by a parameterised stopping-pion model.

The Geometry provides an ISO STEP compliant solid modeller, allowing exchange of models from CAD systems, and provides the equation of motion solvers in different fields and geometrical boundaries conditions for the propagation of particles. Multiple solid representations, such as Constructive Solid Geometry, Boundary Represented Solids (including NonUniformRationalBSplines), Swept Solids, Boolean Operations, are supported according to the ISO STEP standard. Thus GEANT4 can perform physics simulation in CAD detector models. Different navigation algorithms in the geometrical data bases allow an high degree of automation in the optimisation of flat or hierarchical volumes structures. Different integrators, beyond classical Runge-Kutta, and including multi-turn perturbative methods, allow a correct treatment for various fields of variable non-uniformity and differentiability. A proper integration is also performed to update the particles time of flight during transportation.

The Tracking manages the evolution of the track's status determined by the physics interaction occurring at a given time, at a given location, or distributed in space-time. The tracking system manages any of these kinds of interactions, or any combination of them, leading to a closed generalisation of the traditional classification in discrete and continuous physics processes (which is found back as a special case). In order to fully exploit the validity ranges of the physics models, GEANT4 does not apply any tracking cuts, but relies only on production thresholds, thus all particles are tracked down to zero range. In addition, GEANT4 can ensure a consistent and material-

independent accuracy of the simulation because the production cuts are set in range, rather than in energy (and the tracking allows automatic correct treatment of near-boundary regions via the capability of processes to produce secondaries below threshold). Of course, the user can optionally define cuts in energy, path length, time-of-flight, for special treatment of selected areas in the experimental set-up.

The Run, Event and Track management allows the simulation of the event kinematics, together with primary and secondary tracks, and it provides the functionality to perform studies of anything from pile-up to trigger and loopers via a triple stacking mechanism. A fast parameterisation framework (which can be triggered on particle type, volume, etc.) is integrated with the full simulation, allowing independent and simplified detector descriptions and at the same time a correct treatment near cracks. Fast parameterisations allow the direct production of hits corresponding to a full shower development for several detector types. Finally the Hits and Digi domains provide the functionality to reproduce the read-out structure of the detector and its electronic response, independently from the geometry used for the tracking.

Visualisation and User Interface make use of abstract Object-Oriented interfaces to allow drivers of multiple standard and specialised graphics systems, and interaction with sophisticated GUIs or command line and batch systems. The implemented visualisation drivers allow the use of X11, PostScript, OpenGL, OpenInventor, VRML, and DAWN, which allows engineering quality drawings and automatic detection of volumes overlaps. The implemented user interfaces allow batch sessions (including the processing of macro files), interactive sessions based on command lines interfaces, as well as fully graphical user interface sessions such as with OPACS or MOMO, the latter including automatic code generation for detector description and materials definition. The VRML2 driver also allows interactive picking of physics objects, such as tracks and hits, visualising in real time the associated physics information. Particle Data Group compliant particle definitions, including hundreds of baryonic and mesonic resonances and ions) and decay processes and modes, have been implemented and are available. Extensive possibilities of interaction with the GEANT4 system are offered to the user via a kit of dedicated user-action classes. A wide set of utilities, including a complete set of random number generators, physics units and constants, as well as isotopes, elements, compounds definitions, and interface to event generators and to ODBMS, complete the toolkit.

Bibliography

- [1] W. Pauli, "Zur älteren und neueren Geschichte des Neutrinos", in Collected Scientific Papers, ed. By R. Kronig and V. F. Weisskopf (Interscience, New York, 1964), volume 2, p.1313
- [2] F. Reines et al., Science 124 (1956) 103
- [3] B. Pontecorvo, J.E.T.P. 33, 429 (1957), B. Pontecorvo, J.E.T.P. 34, 172 (1958)
- [4] R. Davis, Harmer and K.C. Hoffman, Phys. Rev. Lett. 21, 1205 (1968)
- [5] J. Bahcall home page, <http://www.sns.ias.edu/~jnb/>
- [6] SNO home page, <http://www.sno.phy.queensu.ca/>
- [7] SNO collaboration, hep-ex/0211013v1
- [8] SNO collaboration, nucl-ex/0309004v1
- [9] M. Apollonio et al., Eur. Phys. J., C 27 (2003) 331-374
- [10] The Kamland Collaboration, Phys. Rev. Lett. 90 (2003) 021802
- [11] NASA image, available from <http://visibleearth.nasa.gov/cgi-bin/viewrecord?1914>
- [12] Super-Kamiokande collaboration, hep-ex/0105023v1, Super-Kamiokande home page, <http://www-sk.icrr.u-tokyo.ac.jp/sk/>
- [13] The LSND collaboration, Phys. Rev., D 64 (2001) 112007
- [14] The Boone collaboration, hep-ex/0210020
- [15] As introduction Review, B. Kayser, hep-ph/0104147
- [16] G. Fiorillo, Nucl. Phys. B, Proc. Suppl. 118 (2003) 138-45

- [17] Review of physics at the Neutrino Factory, M. Apollonio et al., hep-ph/0210192
- [18] Feasibility Study-II of a Muon-Based Neutrino Source, ed., S.Ozaki, R.Palmer, M. Zisman, and J. Gallardo, BNL-52623 (2001)
- [19] J. Bouchez et al., Nufact03 proceedings, to be published
- [20] A. de Santo, hep-ex/0106089
- [21] M. Vretenar (ed.), CERN 2000-012
- [22] A. Fabich et al., J. Nucl. Mater. (2002) to be published
- [23] G. Catanesi et al., CERN-SPSC 2002/019
- [24] S. Gilardoni et al., Nufact02 proceedings, J. Phys. G (2002), to be published
- [25] MICE, <http://hep04.phys.iit.edu/cooldemo/>
- [26] K2K Collaboration, Phys. Rev. Lett. 90 (2003) 041801
- [27] <http://www.hep.anl.gov/ndk/hypertext/numi.html>
- [28] K. Elsener et al., CERN-98-02
- [29] B.J. King et al., A rotating metal band target for pion production at muon colliders, To be published on CD in Proc. Six Month Feasibility Study on High Energy Muon Colliders; Oct'00-Apr'01
- [30] P. Sievers, CERN-NUFACT-NOTE 121
- [31] Private communication
- [32] A. Fabich, private communication
- [33] Eur. Phys. J. C, Review of particle physics, pag. 160
- [34] A. Fabich, High Power Proton Beam Shocks and Magnetohydrodynamics in a Mercury Jet Target for a Neutrino Factory, CERN-THESIS-2002-038
- [35] G.I. Budker, T.A. Vsevolzhskaya, G.I. Silvestrov, A.N. Skrinsky, Generation Scheme of Antiprotons for a Proton-Antiproton Collider, *Proceedings of 1970 All Union Accelerator Conference, Moscow*, Nauka, vol. 1, p. 196 (1972).

- [36] T.A. Vsevolzhskaya, The Optimization and Efficiency of Antiproton Production within a Fixed Acceptance, NIM 190 (1981), 479-486.
- [37] B. Autin, Technical Developments for an Antiproton Collector at CERN, *Proceedings of the 12-th International Conference on High Energy Accelerators, Batavia (1983)*, CERN/PS-AA/83-35.
- [38] N.V. Mokhov, "The MARS Code System User's Guide", Fermilab-FN-628 (1995)
N.V. Mokhov, "MARS Code Development, Benchmarking and Applications" Fermilab-Conf-00-066(2000)
O.E. Krivosheev and N.V. Mokhov, "A New MARS and its Applications", Fermilab-Conf-98/43 (1998)
N.V. Mokhov, S.I. Striganov, A. Van Ginneken, S.G. Mashnik, A.J. Sierk and J. Ranft, "MARS Code Developments ", Fermilab-Conf-98/379 (1998)
- [39] N. V. Mokhov et al., FERMILAB-CONF-98-053
- [40] A. Ijspeert, T. Eaton, M. Ross, P. Sievers, Assessment of the further development of pulsed targets for ACOL, CERN/ABT/Technical Note 86-3 (April 1986).
- [41] R. Bellone, A. Ijspeert, P. Sievers, Targets for high intensity beams at CERN: design, operational experience and developments, CERN 86/ST/TE/A/113 (June 1986).
- [42] R. Bellone, C.D. Johnson, G. Le Dallic, M. Lubrano di Scampamorte, S. Maury, C. Metzger, F. Pedersen, T.R. Sherwood, P. Sievers, F. Völker, N. Walker, G. Silvestrov, Beam tests of a 36 mm lithium lens, *Proceedings of EPAC'90, 12-16 June 1990, Nice (France)*, Ed Frontières, pp 1303-1305, CERN 90-36-PS-AR.
- [43] K. Yoshimura, Talk presented at Nufact03 workshop.
- [44] P. Sievers, Stationary Target for the CERN Neutrino Factory, *These Proceedings*, CERN LHC/2001-1 (MTA), CERN NuFact Note 065.
- [45] F. Lemuet et al., Transmission of muons in an alternating gradient funneling system, PAC03
- [46] <http://isolde.web.cern.ch/ISOLDE/>
- [47] J.S. Hendrics, "MCNP4C" LANL Memo X-5; JSH-2000-3

- [48] J. Lettry et al., Effect of thermal shocks on the release of radioisotopes and on molten metal target vessels, NIM B 204(2003)251
- [49] R. Catherall et al., Radioactive ion beams produced by neutron-induced fission at ISOLDE, NIM B 204(2003)235
- [50] U. Köester, private communication
- [51] P.Zucchelli, A novel concept for a neutrino factory: the beta-beam, Phys. Let. B, 532 (2002) 166-172
- [52] E. Jones, CERN/PS-AA/83-46
- [53] S. Van der Meer, CERN 62-16
- [54] D. Möhl, CERN-PS-96-034-DI
- [55] J. F. Amand, CERN-NUFACT-Note-70
- [56] N. Mokhov, "PI/MU YIELD AND POWER DISSIPATION FOR CARBON AND MERCURY TARGETS IN 20-TESLA SOLENOID WITH MATCHING", Mucool Note 61
- [57] A. Blondel et al., CERN-2004-002
- [58] A. Ball et al., "Updated Results of the Horn Study For the NuFact" , proceedings of the NuFact'00 (to be published by Elsevier), Nufact Note 42
- [59] N.V. Mokhov, "The MARS Code System User's Guide", Fermilab-FN-628 (1995)
N.V. Mokhov, "MARS Code Development, Benchmarking and Applications" Fermilab-Conf-00-066(2000)
O.E. Krivosheev and N.V. Mokhov, "A New MARS and its Applications", Fermilab-Conf-98/43 (1998)
N.V. Mokhov, S.I. Striganov, A. Van Ginneken, S.G. Mashnik, A.J. Sierk and J. Ranft, "MARS Code Developments", Fermilab-Conf-98/379 (1998)
- [60] J.D. Jackson, Classical Electrodynamics, Second Edition, pag. 588.
- [61] R.J.Weggel et al., "Pion yield vs. geometry of target and ≈ 20 T pulse solenoid for a muon collider experiment", EPAC 99
- [62] N. Mokhov, private communication.

- [63] Mokhov, N. V., Noble, R. J., and Van Ginneken, A., 9th Advanced ICFA Beam Dynamics Workshop: Beam Dynamics and Technology Issues for $\mu^+ - \mu^-$ Colliders, Montauk, NY, October 15-20, 1995, pp. 61-86; also Fermilab Conf96/006 (1996)
- [64] Harp collaboration, "Proposal to study hadron production for the neutrino factory and for the atmospheric neutrino flux", CERN-SPSC/99-35
- [65] J.M. Maugain et al., "Technical Results of the Horn Study for the Nufact", Nufact Note 80
- [66] J. H. Billen et. al., "Poisson Superfish", LA-UR-96-1834
- [67] S. Rangod, Private Communication.
- [68] J. M. Maugain, Private Communication.
- [69] <http://www.howcogroup.com/>
- [70] S. Wallon, Talk available at <http://muonstoragerings.web.cern.ch/muonstoragerings/TC/meetings/20030709.html>
- [71] D. Boimond et al., CERN/PS 94-02(AR)
- [72] K. Farrell, "Material selection for the HFIR cold neutron source", ORNL/TM-99-208
- [73] G. Gräwer, CERN-NUFACT-Note-38
- [74] S. Gilardoni et al., CERN-NUFACT-Note-129
- [75] M. Konzien et al., *Dynamic and Fatigue Analysis of Gran Sasso Horn*, CERN-EST/ME/2001-008
- [76] <http://www.vibrometry.net/>
- [77] Cooseman, Private Communication.
- [78] Sennheiser web page, <http://www.Sennheiser.com>
- [79] <http://ccrma-www.stanford.edu/CCRMA/Courses/422/projects/WaveFormat/>
- [80] <http://www.mathworks.com>
- [81] <http://audacity.sourceforge.net/>

- [82] *Calculs de comportement dynamique de la corne AA sous charge impulsionnelle*, CERN-PS/AA/AP/81-1
- [83] A. Ball et al., “Updated results of the horn study for the Nufact”, Nufact Note 42, (2000).
- [84] A. Blondel et al., “Neutrino Fluxes from a conventional neutrino beam using CERN SPL”, Nufact Note 53 (2000).
- [85] Los Alamos Accelerator Code Group, “Poisson/Superfish Reference Manual”.
- [86] N.V. Mokhov, “The MARS Code System User’s Guide”, Fermilab-FN-628 (1995).
N.V. Mokhov, “MARS Code Development, Benchmarking and Applications” Fermilab-Conf-00-066(2000).
O.E. Krivosheev and N.V. Mokhov, “A New MARS and its Applications”, Fermilab-Conf-98/43 (1998).
N.V. Mokhov, S.I. Striganov, A. Van Ginneken, S.G. Mashnik, A.J. Sierk and J. Ranft, “MARS Code Developments”, Fermilab-Conf-98/379 (1998).
- [87] <http://neutrino.kek.jp/jhfnu/>
- [88] J. Bouchez, M. Lindroos and M. Mezzetto, Beta-beams: Present design and expected performance, In the proceedings of Nufact 03, New York, 2003
- [89] M. Donega, Master Thesis, available at <http://mdonega.home.cern.ch/mdonega/lowe/homepage.html>
- [90] A.P. Banford, *The Transport of Charged Particle Beams* (E. & F. N. Spon Ltd., London 1966), p. 129
- [91] G. Strang, *Linear Algebra and its application* (Harcourt Brace Jovanovich College Publishers, 1988, third edition), p. 266
- [92] A. Perrin, *PATH Reference Manual*
- [93] J. H. Billen et al, *Poisson Superfish*, LA-UR-96-1834
- [94] S. Wolfram, *The Mathematica Book (4th Edition, Mathematica Version 4, Wolfram Media/Cambridge University Press, 1999*

- [95] GEANT4 Collaboration, CERN/LHCC 98-44, GEANT4 : An Object-Oriented Toolkit for Simulation in HEP; see also the web site: <http://wwwinfo.cern.ch/asd/geant4/geant4.html>
- [96] F. Gerigk, Private Communication
- [97] CERN Program Library Long Write-up, W5013 (1993).
- [98] N.V. Mokhov, “The MARS Code System User’s Guide”, Fermilab-FN-628 (1995)
N.V. Mokhov, “MARS Code Development, Benchmarking and Applications” Fermilab-Conf-00-066(2000)
O.E. Krivosheev and N.V. Mokhov, “A New MARS and its Applications”, Fermilab-Conf-98/43 (1998)
N.V. Mokhov, S.I. Striganov, A. Van Ginneken, S.G. Mashnik, A.J. Sierk and J. Ranft, “MARS Code Developments”, Fermilab-Conf-98/379 (1998)
- [99] J. H. Billen et. al., “Poisson Superfish”, LA-UR-96-1834
- [100] L. Lombardi, “A 40-80 MHz System for Phase Rotation and Cooling”, CERN Neutrino Factory Note 37 (2000)
- [101] A. Perrin, “PATH Manual”